N°:2012-04 YEAR 2012

THESIS

presented at
VON KARMAN INSTITUTE FOR FLUID DYNAMICS

submitted to
ÉCOLE CENTRALE DE LYON

to obtain
the degree of DOCTOR in ACOUSTICS

by

Korcan KUCUKCOSKUN

PREDICTION OF FREE AND SCATTERED ACOUSTIC FIELDS OF LOW-SPEED FANS

Presented on March 22nd, 2012 in front of the Jury:

Prof.	Michel ROGER	(Thesis advisor)
Prof.	Christophe SCHRAM	(Co-advisor)
Dr.	Michel TOURNOUR	
Prof.	Thomas CAROLUS	(Reviewer)
Dr.	Alain GUÉDEL	(Reviewer)
Prof.	Stéphane MOREAU	(Reviewer)

Contact informations :
Korcan Kucukcoskun
Ecole Centrale de Lyon
Avenue Guy de Collongue, 36
69130 Ecully
FRANCE
email: korcan.kucukcoskun@ec-lyon.fr

Abstract

This thesis proposes to predict the sound emitted from low-speed fans and its scattered-field by installation effects related to industrial applications. Both tonal and broadband components of fan noise are investigated.

Methods existing in the literature contain assumptions and simplifications in order to deal with fan noise problems in analytical manner, such as consideration of an observer located in the far-field of the source. Firstly, the effect of far-field assumption in the tonal fan noise formulation is addressed. Using artificial blade sources, a comparison between two closed-form analytical solutions and a numerical technique is performed for validation in free-field.

Secondly, the scattered field of the tonal fan noise is investigated using numerical and analytical techniques. The acoustic field of a rotor operating in a finite duct is first investigated combining the closed-form analytical formulations with the Boundary Element Method (BEM). Since BEM would be computationally demanding for high frequency applications, analytical scattering techniques are also introduced. Reflection and scattering of sound waves by a large plane are first addressed replacing the plane with an image source. Secondly, an exact analytical solution considering scattering of the tonal fan noise by a rigid corner is derived.

Another point addressed in this thesis is the prediction of the broadband noise generated by a low-speed axial fan operating in turbulent stream. Amiet's theory of turbulence-interaction noise for a stationary airfoil is considered. One of the key points proposed in this thesis is an extension of Amiet's method, allowing prediction of the acoustic field of the airfoil in its geometrical near-field in a semi-analytical perspective. The extended formulation is compared with Amiet's classical solution and a reference solution obtained with numerical integration involving no geometrical far-field assumption. Experiments are also performed in anechoic chamber using an isolated airfoil located in grid generated turbulence. Another assumption made in Amiet's theory is the consideration of uniform flow impinging onto the airfoil. However this assumption is not valid for most industrial applications. Different methods exist in literature to deal with this problem. A new approach is proposed in order to take the spanwise varying flow conditions into account. Including all the improvements, the broadband acoustic responses of a stationary airfoil located in the developing region of a jet and of a low-speed axial fan operating in a turbulent stream are investigated and validated against measurements.

Finally, scattering of the sound generated by the considered airfoil and fan by benchmark obstacles is addressed numerically and analytically. Since BEM is not capable to handle statistical source fields directly, an innovative approach obtained by re-formulating the deterministic BEM method is employed. The final model is compared to the numerical, analytical and experimental solutions for validation purposes.

Résumé

Cette thèse propose de prédire le bruit émis par des ventilateurs à basse vitesse et sa diffraction par des obstacles liés aux contraintes d'installation dans les applications industrielles. Les composantes tonale et à large bande du bruit sont étudiées.

Les méthodes existant dans la littérature considèrent des hypothèses et des simplifications afin de traiter le problème du bruit des ventilateurs de façon analytique, comme par exemple l'approximation de champ lointain. Tout d'abord, l'hypothèse de champ lointain dans la formulation du bruit tonal est relaxée. En utilisant des sources artificielles, une comparaison entre deux expressions analytiques et une simulation numérique est effectuée pour la validation en champ libre.

Ensuite, la diffraction du bruit tonal est étudiée par des techniques numériques et analytiques. Le champ acoustique d'un rotor fonctionnant dans un conduit fini est d'abord pris comme exemple en combinant les formulations analytiques avec la méthode d'éléments de frontière (BEM). Etant donné que cette dernière serait trop coûteuse en temps de calcul pour des applications haute fréquence, des techniques analytiques pour le problème de diffraction sont également présentées. La réflexion et la diffraction des ondes sonores par une plaque infinie sont d'abord considérées en remplaçant la plaque par une source image. Ensuite, une solution analytique exacte pour la diffraction du bruit tonal par un coin rigide est formulée.

Un autre point abordé dans cette thèse est la prévision du bruit à large bande produit par un ventilateur axial à basse vitesse évoluant dans un écoulement turbulent. La théorie d'Amiet pour le bruit d'interaction de turbulence sur un profil fixe est considérée. Nous en proposons dans cette thèse une extension permettant de prédire le bruit du profil dans son champ proche géométrique l'aide d'outils semi-analytiques. La nouvelle formulation est comparée à solution classique d'Amiet et à une solution de référence obtenue par intégration numérique sans hypothèse de champ lointain géométrique. Des expériences sont également menées dans une soufflerie anéchoide où la turbulence est générée en amont du profil par une grille. Une autre hypothèse du modèle d'Amiet concerne l'écoulement uniforme arrivant sur le profil. Cette hypothèse n'est pas vérifiée dans la plupart des applications industrielles. Différentes méthodes existent dans la littérature pour traiter ce problème. Nous proposons une nouvelle approche pour prendre en compte des conditions d'écoulement variables en envergure. En intégrant toutes ces améliorations, la réponse acoustique large bande d'un profil fixe placé dans un jet turbulent et d'un ventilateur axial à basse vitesse placé dans un écoulement turbulent est étudiée et validée par comparaison avec l'expérience.

Dans une dernière partie, la diffraction des ondes acoustiques générées par le profil et le ventilateur par des obstacles est déterminée numériquement et analytiquement. Puisque la méthode BEM n'est pas prévue pour résoudre directement le champ d'une source aléatoire, une approche innovante obtenue par la reformulation de la méthode déterministe de BEM est utilisée. Le modèle final est comparé aux solutions numériques, analytiques et expérimentales pour la validation.

Acknowledgements

Foremost, I offer my sincere gratitude to my advisor Prof. Michel Roger for his academic experience and his support during my PhD studies. His patience and kindness have been invaluable to me. His guidance helped me greatly during both the analytical and experimental parts of my research and the writing of this thesis.

I am extremely grateful to Prof. Christophe Schram for the encouragement he gave me starting from the first day of my PhD research. It would not have been possible to write this thesis without his help and support. His support and friendship have been invaluable in my academic, professional and personal lives.

I am also grateful to Dr. Michel Tournour for his support during my stay in LMS and for acquainting me with the ATV approach. I am thankful to him for his partition in my jury. I would like to thank the rest of my jury and reviewers: Prof. Thomas Carolus, Prof. Stéphane Moreau and Dr. Alain Guédel, for their enlightening comments.

I would like to acknowledge the financial support of the European Commission during my PhD studies. This work is supported in the framework of the Marie Curie projects SIMVIA2 (contract no MEST-CT-2005-020263) and AETHER (contract no MRTN-CT-2006-035713) and the FP7 Collaboration Project ECOQUEST (grant agreement no 233541).

My sincere thanks also go to Dr. Julien Christophe for the fruitful collaboration on Amiet's extensions. I am also thankful to all the co-authors of the papers, some of whom have already been named.

I thank my colleagues at LMS (as the Poker Champion), my Marie Curie fellow friends (as an axe-thrower) and my labmates at VKI and ECL for making the academic and professional lives easier and funnier. I also thank my friends Hakan, Onur K., Asim, Zeynep, Onur A., Thomas, Paula and Arnulfo for their informal support and encouragement which have been priceless. I am also thankful to Jessica for her support and patience during the time of writing my thesis. I am lucky to meet all of many good friends in my stay in Belgium and France. Life would not have been the same without them.

Last but not least; I would like to thank my mother Nazire, my father Omer and my family, for supporting me throughout my life.

Contents

Chapter 1.

Introduction

Aerodynamic noise emitted from rotating machinery is a concern in several industrial applications in terms of comfort and regulations. In aeronautical industry, the sound generated by aircraft propellers [53] and turbofans in engine nacelles [94] is a matter of interest. The sound emitted from rotor blades of a helicopter is also investigated by many authors [43, 72, 119]. In the automotive industry it is a point of interest since the noise generated by the cooling fan [91, 18] and its radiation towards the air-conditioning unit may be inconvenient for passengers. In the energy sector, the noise emitted from wind turbine blades [46] is a matter to be dealt with for the comfort of inhabitants and regulated by certification where the noise pollution is hindering their landside development. Also the low noise level emitted from other domestic appliances [124, 61] is an important parameter demanded by the customer hence the acoustic comfort becomes an important commercial asset. It is known that for such rotating machinery applications, flow induced sound is not the only noise source [50]. Additional mechanisms due to vibration or installation effects also exist. This thesis only focuses on fan noise in the aeroacoustical perspective.

1.1. Aeroacoustic Analogies

The attention paid on aeroacoustical problems is associated with the start of common usage of jet engines in the 50s. Lighthill is known to be the pioneer of aeroacoustics [73]. He reformulated the continuity and momentum equations in the non-homogeneous wave equation format, dealing with jet noise without the presence of solid boundaries [74]. The free space Green's function therefore can be used to solve Lighthill's equation. His work on jet noise only points out an equivalent quadrupole contribution. However, it is known that solid boundaries reflect and diffract the sound generated by the volume quadrupole sources to produce sources of other nature. Curle re-derived Lighthill's equation considering stationary solid boundaries [33]. His model contains both quadrupole and dipole sources where the strengths depend on the turbulence stress tensor and the unsteady forces exerted on the surface by the fluid, respectively. Finally Ffowcs Williams and Hawkings (FW-H) considered moving surfaces with respect to the medium [40]. Their formulation contains all three types of acoustic sources, quadrupoles, dipoles and monopoles. The sound components generated by the dipoles and monopoles are called loading and thickness noise, respectively. Thickness noise results from the displacement of the fluid and the advancing surfaces. The current aeroacoustic derivations, including fan noise problems, are mostly based on these analogies.

Theoretically, aeroacoustic problems can be described by the compressible continuity and momentum equations. They can therefore be solved using only CFD methodology. Several studies performed using so called direct methodology [14, 89] to deal with aeroacoustic problems including low-speed fan noise computations [29, 100]. However, a direct approach

requires a computational domain extending from source to observer and may become highly computationally demanding.

A more common approach is to use a hybrid method where the sound generation and the sound propagation are solved separately from each other [78]. Incompressible CFD techniques can now be applied to identify and quantify the noise sources[128] including fan noise problems [95, 15, 115]. Compared to the direct methodology, hybrid methods are mostly used in industrial applications due to less demanding computational efforts. This thesis employs hybrid approaches in order to compute the sound emitted by considered fans.

1.2. Review of Fan Noise Sources

As the most general statement, the FW-H analogy considers monopole, dipole and quadrupole components of the noise radiated by a fan. It applies in particular to low to moderate Mach number fan noise problems. However, it was shown that for the low-Mach number flows, the quadrupole term becomes negligible [54]. Later, the monopole component is shown to be less efficient compared to the dipole one in terms of acoustic radiation [92] for low-speed fan applications especially for thin blade design and significantly distributed flows. Therefore, only the dipole component, due to aerodynamic forces acting on the blade surface, is considered for most low-speed fan problems. Gutin was the first person who developed the first successful theory of propeller noise [51]. He was also the first recognizing the dipole like radiation pattern in the presence of a solid surface. He considered the force distribution on a disk swept out by the propeller during the rotation. The theory was based on a uniform inflow. The blade forces are therefore steady and the dipoles have constant absolute strength. This type of noise, referred to as steady-loading noise, becomes significant when the peripheral Mach number exceeds 0.7 [82]. However, in most of the applications the propellers and fans are operated under non-uniform flow conditions. Especially for low tip Mach number fans, due to the non-uniformity of the flow-field, Gutin's model fails to predict the acoustic field accurately [41].

Depending on the periodic or random aerodynamic forces applying on the blade surface, the acoustic spectrum may consist of tones or humps. A chart of the forces applying on the blade and their contribution on the acoustic spectrum is given in Figure 1.1 [30]. If the force is periodic, the aerodynamic noise generated by the fan is a combination of discrete frequencies, related to the number of blades and rotational speed, the blade passing frequency (BPF) and its harmonics. Several studies addressed the tonal noise emitted by fans. Lowson extended the model of Gutin and re-derived his analogy using model analytic results [77, 76]. The empirical theory was applied to helicopter main-rotor noise only considering the dipole contribution. Farassat proposed a time domain solution for fan noise based on the derivations of the FW-H and Kirchoff formulation [37]. The model, known as "Formulation 1A", was applied to predict the noise generated by a helicopter rotor considering both dipole and monopole sources. The monopole contribution becomes non-negligible for such applications due to the high rotational speed and the significant blade thickness. Later, a simplified model called "Formulation 1B" was proposed by the same authors considering only the dipole contribution [20]. Goldstein re-derived the FW-H equation in the frequency domain and extended the model for the presence of an upstream stator [47]. However the model is based on the geometrical and acoustical far-field assumptions. Therefore it is not able to predict the acoustic field accurately in the near-field of a fan.

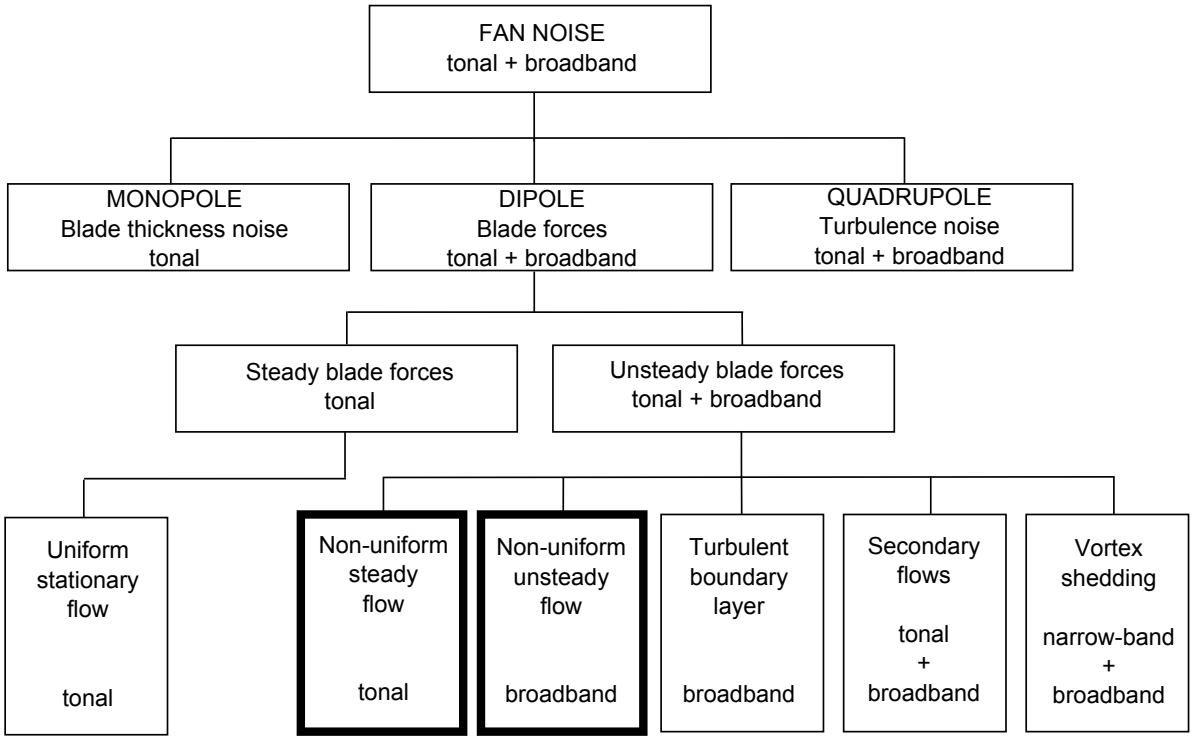

Figure 1.1.: Fan noise source mechanisms [30]

The sound pressure field in the immediate neighborhood of the blades can reach levels beyond the limits of linear acoustics. In such cases, applying a linear propagation method can yield a substantial overprediction of the acoustic field. An alternative strategy was proposed to deal with the near-field acoustic problems for rotors. For this, the near-field acoustic field around the sound generating surfaces can be solved with the full compressible CFD [81]. For rotors operating in ducts, the pressure field is evaluated at a given distance from the fan blades, where its level has decreased to the linear regime, and is expanded on the duct modes [94]. This method presents significant advantage in aeronautical turbomachinery applications characterized by high Mach number and sound levels, however it suffers from robustness issues in HVAC applications. The sound generated by the fan and its radiation through an engine exhaust is also investigated solving Linearized Euler Equations (LEE) in the near-field and combining it with the far-field FW-H solution for the acoustic propagation [105]. Another asymptotic approach for large blade number applications was proposed [99] in order to deal with the near-field terms. These approaches were found to be promising but do not apply to the engineering fan noise problems due to the geometrical and blade number limitations, respectively. Finally, Roger introduced a closed-form analytical solution reconsidering the derivations of FW-H and Goldstein by introducing auxiliary functions [108]. The compact rotating source now takes the near-field terms into account in the definition of these function.

Besides the periodic forces applying on blades, random forces also result from turbulence in the flow and generate the broadband component of the sound spectrum. For example, vortex-shedding downstream the trailing edge results in so called vortex-shedding noise. Several empirical studies performed in order to predict that noise in the aeronautical community [75, 62]. For centrifugal fans, vortex shedding noise is more likely in narrow band whereas,

due to the spanwise varying relative velocity, the vortex shedding noise is broadband [50]. Random pressure fluctuations on blades result from turbulence within attached or separated boundary layers. They produce what is called blade self-noise. Several approaches have been proposed to address this problem, ranging from semi-empirical methods [16] to highly accurate and CPU intensive transient CFD calculations [23]. Semi-analytical methods also exist in the literature addressing self-noise problems [57, 119]. Finally due to turbulence carried by the incoming flow, interaction with the blades generate turbulence-impingement noise, also called leading-edge noise [96, 97, 19]. Most industrial applications involve a fan operating downstream of obstacles which are responsible for installation effects, hence the incoming flow is already disturbed. The primary attention is therefore given to the turbulence-interaction noise in this thesis for the broadband noise prediction. Linking the analytical turbulent spectra to the sound spectra, a direct relationship was proposed by Homicz [56]. Amiet and co-workers [5, 8] proposed a theory assuming statistical turbulence models combined with the application of Curle's analogy for a distribution of point dipoles [33] and derived semi-analytical Green's functions for the acoustic response of an airfoil subjected to incoming turbulence. Amiet's theory is employed in the broadband framework and is extended for the applicability for industrial purposes including near-field correction and consideration of non-uniform flow conditions [64, 65, 67].

1.3. Acoustic Scattering

Another contribution of the installation effects is the scattering of the sound waves emitted from the fan by surrounding surfaces. In free-field radiation problems, only the sound field emitted by the source needs to be determined. However in scattering problems, besides the free-field, the effect of reflected and scattered sound waves also needs to be determined [35]. Based on the free-field prediction methods, numerical or analytical scattering techniques exist in literature [90, 101].

The most commonly used numerical approach for finding an approximate solution of the Helmholtz partial differential equation and the associated boundary conditions is based on the transformation of the mathematical problem into a set of approximating equations [35]. Finite Element Method (FEM) [36] and Boundary Element Method (BEM) [34] are the most common approaches addressing acoustic scattering problems in a numerical perspective. However, classical BEM and FEM solutions are restricted to problems where the source is defined deterministically. In this thesis, dedicated to statistically defined random noise sources, the deterministic BEM formulation is re-addressed.

Additionally, applicability of FEM and BEM is practically restricted to low-frequency problems depending on the nature of the problem and on the available computer resources. They would require a prohibitively large amount of computational effort and memory resources to get an acceptable level of accuracy [35]. Other numerical methods can deal with the acoustic scattering problem numerically at high frequencies such as statistical energy acoustics [79, 80] and ray acoustics [93]. Recently, a time domain solution based on equivalent source method also been used in scattering problems [71]. It is worth noting that solving Helmholtz equation using BEM is based on a stationary medium assumption.

Further, exact analytical solutions for relatively simple geometries also exist in the literature. The presence of an infinite flat plate [103] or a semi-infinite plate [39] can be taken into account analytically for scattering problems. MacDonald also proposed an analytical

solution addressing acoustic scattering from a rigid corner [83]. In this thesis, his theory is extended in order to be applied to compute the scattered field of a low-speed fan by a corner.

1.4. Structure of the Thesis

The scope of this thesis is mainly shared on the tonal and broadband components of low-speed fan noise. One main concern is also the acoustic scattering of the noise generated by the fan. Each component is then considered from a double point of view; the free-field and the scattered-field. Since the scattering obstacles are mostly present in the very vicinity, the far-field assumption is also examined and released.

In Chapter 2, the free-field tonal fan noise is investigated. Two closed-form exact analytical approaches, one with far-field assumption and another one without, are introduced. A non-closed form numerical method based on equivalent stationary sources is also addressed. A free-field comparison of these methods is performed on a benchmark low-speed axial fan equation to address the effect of the far-field approximation.

Chapter 3 contains the information on numerical and analytical acoustic scattering techniques and their application to tonal fan noise. A numerical scattering technique already in use in industry is introduced. Combining the model with two closed-form analytical approaches for low-speed tonal fan noise, the scattered acoustic field of a fan operating in an open duct is computed. Analytical methods accounting for relatively simple scattering obstacles, such as infinite plate or wedge, are also introduced in this chapter. A model of acoustic scattering from an infinite corner and its application to tonal fan noise are proposed.

Chapter 4 deals with the free-field broadband noise emitted from a fan located in turbulent stream. The theory employed in order to predict the broadband noise generated by fan blades [8] is based on the one for a stationary airfoil [5]. Hence, the theory for the airfoil is first applied in a benchmark problem with extensions for validation purposes. An intermediate level of geometrical near-field correction is proposed to the theory. As a second step, the non-uniform flow field that needs being introduced along the span of a rotating blade is taken into account with a segmentation technique. A new technique considering correlation between adjacent segments is proposed. Finally, the theory is implemented in the free-field acoustic response of a low Mach number axial fan and validated against measurements performed in anechoic chamber.

In Chapter 5, the acoustic scattering methods introduced in Chapter 3 are applied to the broadband noise sources in both cases of a stationary airfoil and of a low-speed axial fan. A benchmark scattering obstacle is first introduced to the stationary airfoil test-case. The scattered field problem is dealt with the numerical method for deterministic sources. An innovative method for the acoustic scattering of non-deterministic source field is proposed. The model is validated against the measurements and the other analytical solutions detailed. Finally, the scattered-field of the broadband fan noise is computed combining the analytical and numerical methods.

Chapter 2.

Free-Field Tonal Fan Noise

This chapter addresses the derivation of the free-field tonal fan noise formulation. Two closed-form analytical approaches are presented for rotating sources. Depending on the position of the observer with respect to the source, the analytical solutions are named far- and near-field formulations. If the source to observer distance, R, is much longer than the acoustic wavelength at the frequency of interest, such as $R/\lambda \gg 1$, the observer is assumed to be located in the acoustical far-field. If R is larger compared to the geometrical extent of the source, such as the radius of the rotor, r', making $R/r' \gg 1$, the observer is assumed to be located in the geometrical far-field. Another method, based on using an equivalent array of fixed sources rather than rotating ones is also investigated. Finally, all three models are compared numerically for the acoustical free-field radiation of a low speed axial fan.

2.1. Tonal Fan Noise: Fundamental Equation

Acoustic disturbances are usually regarded as small amplitude perturbations in addition to the ambient state [101]. The state of the acoustic radiation field is characterized by the ambient variables, such as pressure, p_0 and density, ρ_0. The overall pressure and density fields then obtained summing the disturbances to the ambient variables

$$\begin{aligned} p &= p_0 + p' \\ \rho &= \rho_0 + \rho', \end{aligned} \tag{2.1}$$

where the acoustic contributions are represented as p' and ρ'. For isentropic flows where the ratio ρ'/ρ_0 is sufficiently small, the acoustic pressure fluctuations are related to the density fluctuations with the following equation

$$p' = c_0^2 \rho'. \tag{2.2}$$

For aeroacoustic problems, where the sound field is not influenced by any solid boundaries in the flow, the density fluctuations can be computed with the inhomogeneous wave equation formula using Lighthill's analogy [73],

$$\frac{\partial^2 \rho'}{\partial^2 \tau} - c_0^2 \nabla^2 \rho' = \frac{\partial^2 T_{ij}}{\partial y_i \partial y_j}. \tag{2.3}$$

The term on the right hand side of the equation is Lighthill's stress tensor equivalent to distributed volume quadrupoles, defined as

$$T_{ij} = \rho u_i u_j + (p - c_0^2 \rho)\delta_{ij} - \tau_{ij}. \tag{2.4}$$

$\mathbf{u}$ is the velocity of the fluid. Indices i and j are representing the $i-$th and $j-$th component of the related parameter, respectively. τ_{ij} is the viscous stress tensor. Choosing ρ' as the acoustic variable is convenient for prediction of sound prediction by turbulence for example [106]. For consistency of derivations, p' is chosen as the acoustic variable.

The solution of Equation (2.3) can be expressed in terms of Green's functions [47]

$$p' = \int_{V(\tau)} \left[\frac{\partial^2 \mathrm{G}}{\partial y_i \partial y_j} T_{ij}(\mathbf{y}, \tau) \right] \mathrm{d}^3\mathbf{y}. \tag{2.5}$$

The square bracket is computed in the retarded time, $\tau = \mathrm{t} - R/c_0$ where $R = |\mathbf{x} - \mathbf{y}|$ is the linear distance between the source and the observer. Since there is no solid boundaries influencing the sound field to any appreciable extent, the free space Green's function can be employed [47]

$$\mathrm{G}(\mathbf{y}, \tau | \mathbf{x}, t) = \frac{1}{4\pi R} \delta(\tau - t + \frac{R}{c_0}). \tag{2.6}$$

In its initial form, Lighthill's analogy considers a sound field not affected by the solid boundaries present in the flow-field, hence its only important application is the jet noise problems. However, it is known from the classical acoustics, that the sound generated by the volume quadrupole sources are reflected and diffracted by solid boundaries [33]. Ffowcs Williams and Hawkings introduced moving surfaces in Lighthill's model [40].

Governing moving surfaces, the fundamental equation for the sound field then writes (see the related reference [47] for further derivations)

$$\begin{aligned} p' = & \int_{-T}^{T} \int_{V(\tau)} \frac{\partial^2 \mathrm{G}}{\partial y_i \partial y_j} T_{ij} \, \mathrm{d}^3\mathbf{y} \, \mathrm{d}\tau \\ & + \int_{-T}^{T} \int_{S(\tau)} \frac{\partial \mathrm{G}}{\partial y_i} f_i \, \mathrm{d}^2\mathbf{y} \, \mathrm{d}\tau \\ & + \int_{-T}^{T} \int_{S(\tau)} \rho_0 V_n \frac{\partial \mathrm{G}}{\partial \tau} \, \mathrm{d}^2\mathbf{y} \, \mathrm{d}\tau \end{aligned} \tag{2.7}$$

where T is a large but finite interval of time.

Equation (2.7) is an exact solution applied to any region $V(\tau)$ bounded by impermeable surfaces $S(\tau)$. The first term in the right hand side of the equation denotes the volumetric distribution of the quadrupole term, triggered by the stress tensor as shown above. The second term is the dipole term generated by the unsteady forces, f_i. Finally the third term is the monopolar term resulting from the volume displacement of the fluid due to the surface motion.

As seen in Equations (2.3) and (2.7), if one wants to compute the acoustic field of a source, the flow-field has to be solved first in order to obtain the source terms, $\rho_0 V_n$, f_i and T_{ij}. A convenient implementation of the method relies on unsteady CFD simulations to provide the transient pressure field [69, 95], that is integrated to yield the source field such as unsteady forces. Measurements can also provide the required source data [115].

For a low-speed fan application, it was shown that dipolar terms are dominant and monopolar and quadrupolar terms shown to be negligible [54, 92]. Therefore the sound field can be approximated via only the dipole contribution

$$p' \cong \int_{-T}^{T} \int_{S(\tau)} \frac{\partial \mathrm{G}}{\partial y_i} f_i \, \mathrm{d}^2\mathbf{y} \, \mathrm{d}\tau. \tag{2.8}$$

Because the presence of solid boundaries is already accounted for in the source terms, the free-field Green's function can be employed for the free-field acoustic propagation [47]. Introducing the free field Green's function, Equation (2.8) becomes

$$p' \cong -\frac{\partial}{\partial x_i} \int_{-T}^{T} \int_{S(\tau)} \frac{1}{4\pi R} \delta(t - \tau - \frac{R}{c_0}) f_i \, \mathrm{d}^2\mathbf{y} \, \mathrm{d}\tau. \tag{2.9}$$

The minus sign appears since $\partial \mathrm{G}/\partial y_i = -\partial \mathrm{G}/\partial x_i$. The integral on the right hand side is computed as

$$\int_{-T}^{T} \frac{1}{R} \delta(t - \tau - \frac{R}{c_0}) f_i \, \mathrm{d}\tau = \left[\frac{f_i}{R|1 - (\mathbf{R}/R) \cdot \mathbf{M}|} \right] \tag{2.10}$$

where the square brackets indicate that the quantity is evaluated at the retarded time. The term in the denominator is the so called Doppler factor

$$D = 1 - (\mathbf{R}/R) \cdot \mathbf{M}. \tag{2.11}$$

Introducing the notation D, the acoustic pressure fluctuations finally become

$$p' \cong -\frac{1}{4\pi} \frac{\partial}{\partial x_i} \int_{S(\tau)} \left[\frac{f_i}{R \; D} \right] \mathrm{d}^2\mathbf{y}. \tag{2.12}$$

Equation (2.12) requires the integration of the distributed sources on the boundary surface, $S(\tau)$ [41]. At this stage, it becomes convenient to assume that the extent of the source domain is much smaller than the acoustic wavelength, $l \ll \lambda$. Hence, the surface can be represented as a point dipole whose strength is equal to the integration of the distributed sources. In such a case, the source is said acoustically compact. If the source domain is not acoustically compact, it can be decomposed as a sum of compact sources by dividing the surface $S(\tau)$ in compact sub-domains [59]. The overall acoustic field is then obtained with summing their contributions. For reader's information, as the blade thickness is also compact at the frequencies of interest, the difference of retarded times between the suction and pressure sides is also neglected in the derivations [47]. The acoustic pressure generated by a compact dipole source then becomes

$$p'(\mathbf{x}, t) = -\frac{1}{4\pi} \frac{\partial}{\partial x_i} \left[\frac{F_i}{R \; D} \right] \tag{2.13}$$

with the point dipole strength given by

$$F_i(t) = \int_{S(\tau)} f_i \, \mathrm{d}y^2. \tag{2.14}$$

R and M now designate the coordinate and Mach number at the center of the surface $S(\tau)$ where the dipole is assumed to be located. The space derivative yields

$$\frac{\partial}{\partial x_i} \left[\frac{F_i}{R \; D} \right] = -\frac{R_i}{c_0 R^2 D} \frac{\partial}{\partial \tau} \left(\frac{F_i}{D} \right) - \frac{F_i R}{R^3 D} + \frac{F_i R_i}{R^3 D^2} \left(M_i R - \frac{\mathbf{M} \cdot \mathbf{R} R_i}{R} \right). \tag{2.15}$$

For the tonal noise generated by rotating machinery applications, the periodic motion of the sources is considered [51]. It is therefore convenient to compute the acoustic field in the Fourier domain [77, 41].

$$p'(\mathbf{x},\omega) = \frac{1}{2\pi}\int_{-\infty}^{\infty} p'(\mathbf{x},t)\mathrm{e}^{-\mathrm{i}\omega t}\,\mathrm{d}t \tag{2.16}$$

Taking the Fourier Transform of Equation (2.15) writes

$$p'(\mathbf{x},\omega) = \frac{1}{8\pi^2} \int_{-\infty}^{\infty}\left[\frac{R_i}{c_0R^2D}\frac{\partial}{\partial\tau}\left(\frac{F_i}{D}\right) + \frac{F_iR}{R^3D} - \frac{F_iR_i}{R^3D^2}\left(M_iR - \frac{\mathbf{M}\cdot\mathbf{R}R_i}{R}\right)\right]\mathrm{e}^{-\mathrm{i}\omega t}\,\mathrm{d}t. \tag{2.17}$$

Using the identity $\partial t/\partial\tau = D$, and integrating Equation (2.17) by parts, the acoustic pressure generated by the rotating dipole then becomes

$$p'(\mathbf{x},\omega) = \frac{\mathrm{i}k}{8\pi^2}\int_{-\infty}^{\infty}\frac{\mathbf{F}\cdot\mathbf{R}}{R^2}\left(1+\frac{1}{\mathrm{i}kR}\right)\mathrm{e}^{-\mathrm{i}\omega(\tau+R/c_0)}\,\mathrm{d}\tau. \tag{2.18}$$

It is worth to note that expression 2.18 is quite general and it does not introduce any assumption on the periodicity of the forces nor trajectory of the dipole. Considering a rotating point source, the fan and listener coordinates are specified in the coordinate system illustrated in Figure 2.1. The dipole is rotating with a constant angular speed Ω. Introducing $\beta = \Omega t + \varphi'$, coordinates read

$$\begin{aligned}
\mathbf{x} &= (x\sin\theta\cos\varphi, x\sin\theta\sin\varphi, x\cos\theta)\\
\mathbf{y} &= (r'\cos\beta, r'\sin\beta, \zeta_3)\\
\mathbf{F} &= (-F_D\sin\beta + F_R\cos\beta, F_D\cos\beta + F_R\sin\beta, -F_T)
\end{aligned}$$

where F_R, F_D and F_T are the radial, drag and thrust forces acting on the blade, respectively. Using $\mathbf{R} = \mathbf{x} - \mathbf{y}$, the $\mathbf{F}\cdot\mathbf{R}$ product in Equation (2.18) becomes

$$\mathbf{F}\cdot\mathbf{R} = -F_Dx\sin\theta\sin(\beta-\varphi) + F_R(x\sin\theta\cos(\beta-\varphi) - r') + F_T(\zeta - x\cos\theta). \tag{2.19}$$

Equation (2.18) is a general solution for fan noise prediction. Once the source field is determined, the acoustic field of the fan can be computed via such a formulation. However, integration in the time domain is computationally demanding and requires a high resolution of the flow field at the higher frequencies of interest [104].

Knowing the source, and hence the sound field, is periodic with angular frequency Ω, the acoustic field of the fan can be computed only for the harmonics. Computation at the harmonics will reduce the computation time when only the tonal components are needed. The nth harmonic of the density fluctuations then becomes

$$p'_n = \frac{\Omega}{2\pi}\int_0^{2\pi/\Omega} p'(\mathbf{x},t)\mathrm{e}^{-\mathrm{i}n\Omega t}\mathrm{d}t. \tag{2.20}$$

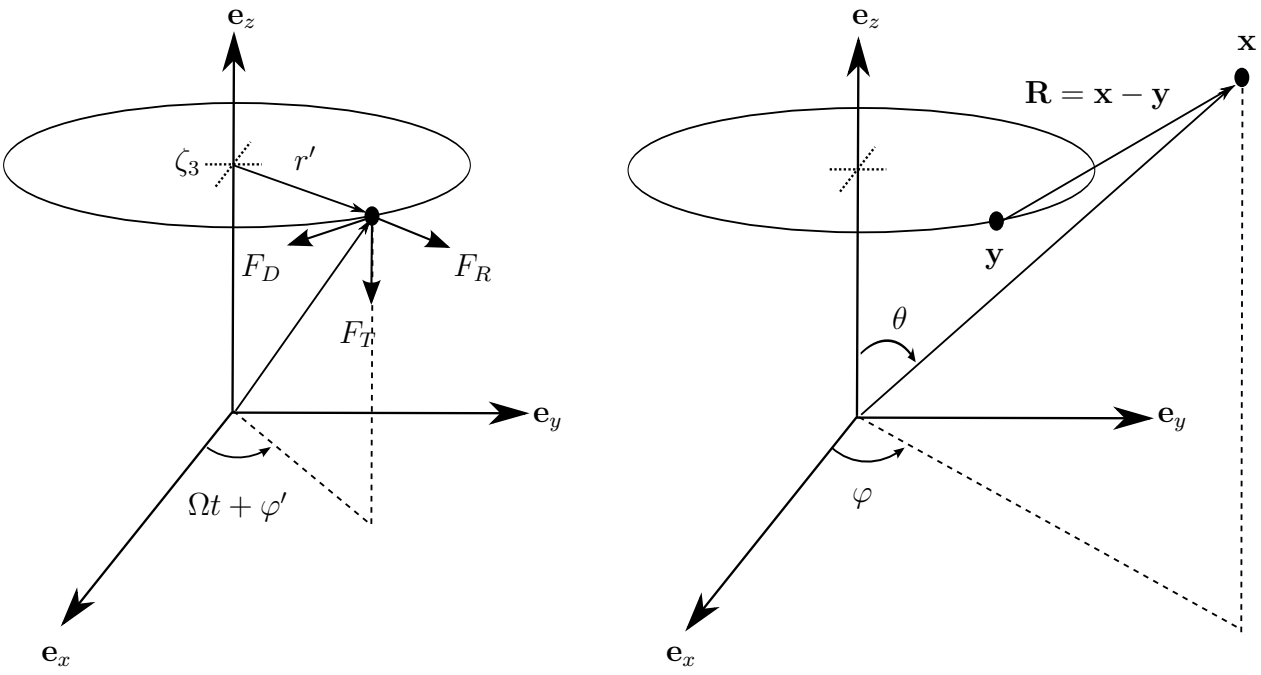

Figure 2.1.: Source and listener coordinates

2.1.1. Far-Field Approximation

For some of the fan noise applications, the free-field acoustic field is needed to be computed for the observers located in both geometrical and acoustical far-field of the fan. The far-field assumption then allows making simplifications in the derivations. For large values of R, Equation (2.15) approaches

$$\frac{\partial}{\partial x_i}\left[\frac{F_i}{R\ D}\right] \sim -\frac{R_i}{c_0 R^2 D}\frac{\partial}{\partial \tau}\left(\frac{F_i}{D}\right). \tag{2.21}$$

Introducing Equation (2.21) into Equation (2.20) and considering the periodicity of the function R with the period $2\pi/\Omega$, the acoustic field becomes

$$p'_n \sim \frac{\Omega}{8\pi^2 c_0}\int_0^{2\pi/\Omega} \frac{x_j}{x^2 D}\frac{\partial}{\partial \tau}\left(\frac{F_i}{D}\right) \mathrm{e}^{-\mathrm{i}n\Omega t}\mathrm{d}t. \tag{2.22}$$

where the R_j/R^2 term is replaced with its asymptotic value x_j/x^2. The new scalar product is then equal to

$$\mathbf{F}\cdot\mathbf{x} = -F_D \sin\theta \sin(\beta-\varphi) + F_R \sin\theta\cos(\beta-\varphi) - F_T\cos\theta. \tag{2.23}$$

Since the integrand in Equation 2.22 is evaluated at the retarded time τ, it is convenient to change the integral variables from t to τ. Acoustic pressure perturbations then read

$$p'_n \sim \frac{\Omega}{8\pi^2 c_0}\frac{x_j}{x^2}\int_0^{2\pi/\Omega} \frac{\partial}{\partial \tau}\left(\frac{F_i}{D}\right) \mathrm{e}^{-\mathrm{i}n\Omega(\tau+R/c_0)}\mathrm{d}\tau. \tag{2.24}$$

Using the identities relating the Bessel function to the modulation of the frequency shift due to the relative motion between the source and the observer,

$$\mathrm{e}^{-\mathrm{i}Z cos\beta} = \sum_{m=-\infty}^{\infty} (-\mathrm{i})^m J_m(Z)\mathrm{e}^{-\mathrm{i}m\beta} \tag{2.25}$$

$$-\sin\beta \mathrm{e}^{-\mathrm{i}Z\cos\beta} = \frac{1}{Z}\sum_{m=-\infty}^{\infty} (-\mathrm{i})^m J_m(Z)\mathrm{e}^{-\mathrm{i}m\beta} \tag{2.26}$$

$$\cos\beta \mathrm{e}^{-\mathrm{i}Z\cos\beta} = \sum_{m=-\infty}^{\infty} (-\mathrm{i})^{m-1} J'_m(Z)\mathrm{e}^{-\mathrm{i}m\beta} \tag{2.27}$$

the acoustic field of a rotating compact dipole becomes

$$p'_n \sim \frac{-\mathrm{i}k_n}{4\pi x}\mathrm{e}^{-\mathrm{i}k_n x}\sum_{p=-\infty}^{\infty} \mathrm{e}^{-\mathrm{i}(n-p)(\varphi-\pi/2)} \left[J_{-n+p}(-k_n r'\sin\theta)\left(\cos\theta F_p^T - \frac{n-p}{k_n r'}F_p^D\right) - \mathrm{i}J'_{-n+p}(-k_n r'\sin\theta)\sin\theta F_p^R\right]. \tag{2.28}$$

Equation (2.28) is general and applies even if every blade is different from every other. However, the low speed fans used usually consist of B identical and equally spaced blades. The force acting on the $s = 1$ blade at time τ is the same as the force which acts at the time $\tau + (2\pi/(\Omega B)(s-1))$ on the blade which is displaced by angle $2\pi(s-1)/(\Omega B)$. Using the identity,

$$\sum_{s=1}^{B} \mathrm{e}^{\mathrm{i}n2\pi(s-1)/B} = \begin{cases} B & \text{for } n = mB, \\ 0 & \text{for } n \neq mB. \end{cases} \tag{2.29}$$

where m is an integer, the pressure fluctuations read [47],

$$p'_{nB} \sim -\frac{\mathrm{i}Bk_{nB}}{4\pi x}\mathrm{e}^{-\mathrm{i}k_{nB}x}\sum_{p=-\infty}^{\infty} \mathrm{e}^{-\mathrm{i}(nB-p)(\varphi-\pi/2)} \left[J_{-nB+p}(-k_{nB}r'\sin\theta)\left(\cos\theta F_p^T - \frac{nB-p}{k_{nB}r'}F_p^D\right) - \mathrm{i}J'_{-nB+p}(-k_{nB}r'\sin\theta)F_p^R\sin\theta\right] \tag{2.30}$$

where $k_{nB} = nB\Omega/c_0$ is the wave number of the nBth harmonic. Taking only the $p = 0$ contribution into account considers only the steady forces acting on the blades as addressed in Gutin's model [51]. Once again this is recognized as not being a significant contribution for low-speed fans.

In some of the industrial applications, the rotor operates downstream of a stator or inlet guide vanes. In presence of a stator upstream of the rotor, the periodicity of the forces F^α on the reference rotor blade is $2\pi/(\Omega V)$ instead of $2\pi/\Omega$. Simply changing the index p by pV, the nBth harmonic becomes

$$p'_{nB} \sim \frac{\mathrm{i}Bk_{nB}}{4\pi x}\mathrm{e}^{-\mathrm{i}k_{nB}x}\sum_{p=-\infty}^{\infty}\mathrm{e}^{-\mathrm{i}(nB-pV)(\varphi-\pi/2)} \left[J_{-nB+pV}(-k_{nB}r'\sin\theta)\left(\cos\theta F^T_{pV}-\frac{nB-pV}{k_{nB}r'}F^D_{pV}\right)-\mathrm{i}J'_{-nB+pV}(-k_{nB}r'\sin\theta)\sin\theta F^R_{pV}\right]. \tag{2.31}$$

Expression (2.31) provides a closed form solution for the incident field in a numerical acoustics context, provided the listener is placed in both geometrical and acoustical far-field. Taking apart this limitation, the FW-H approach is very attractive, given the source field is restricted to the blade surfaces [40, 41].

The theory mentioned above has been used in many industrial applications where the observer position is located in both geometrical and acoustical far-field [53]. The common denominator of the application cases is that they all consider acoustical free-field radiation. However, for some of the industrial configurations where the observer is located in the vicinity of the fan or acoustic scattering takes part due to installation effects [94, 105], the acoustic quantities are required to be computed in the near-field of the fan. The far-field assumption then becomes invalid. A complete closed-form exact analytical solution was proposed by Roger without making the far-field assumption for the rotating machinery [108]. The derivations are described in the next section.

2.1.2. Near-Field Correction

Rewriting Equation (2.18) reads

$$p'(\mathbf{x},\omega)=\frac{\mathrm{i}k}{8\pi^2}\int_{-\infty}^{\infty}\big(-G_2(\tau)F_D x\sin\theta+ G_3(\tau)F_R x\sin\theta+G_1(\tau)(F_T(\zeta_3-x\cos\theta)-F_R r')\big)\mathrm{e}^{-\mathrm{i}\omega\tau}\,\mathrm{d}\tau \tag{2.32}$$

where the auxiliary functions G_1, G_2 and G_3 are defined as

$$\begin{aligned} G_1(t) &= \frac{\mathrm{e}^{-\mathrm{i}kR}}{R^2}\left(1+\frac{1}{\mathrm{i}kR}\right)\\ G_2(t) &= \sin(\Omega t+\varphi'-\varphi)\;G_1(t)\\ G_3(t) &= \cos(\Omega t+\varphi'-\varphi)\;G_1(t) \end{aligned} \tag{2.33}$$

including the acoustical near-field contribution $1+1/(\mathrm{i}kR)$. Due to its periodicity, the sound field can be again expanded as a Fourier series

$$p'_n=\frac{\mathrm{i}k_n\Omega}{8\pi^2}\int_0^{2\pi/\Omega}\big(-G_2(\tau)F_D x\sin\theta+ G_3(\tau)F_R x\sin\theta+G_1(F_T(\zeta_3-x\cos\theta)-F_R r')\big)\mathrm{e}^{-\mathrm{i}n\Omega\tau}\,\mathrm{d}\tau. \tag{2.34}$$

Since the sources have the same periodicity they can be represented as Fourier series

$$F_\alpha(\tau) = \sum_{p=-\infty}^{\infty} F_p^{(\alpha)} \mathrm{e}^{\mathrm{i}p\Omega\tau} \tag{2.35}$$

where $\alpha = T, D, R$ is the thrust, drag and radial components of the source strength.

Combining Equations (2.34) and (2.35) leads to

$$\sum_{p=-\infty}^{\infty} F_p^{(\alpha)} \int_0^{2\pi/\Omega} G_N(\tau) \mathrm{e}^{-\mathrm{i}(n-p)\Omega\tau} \, \mathrm{d}\tau = \frac{2\pi}{\Omega} \sum_{p=-\infty}^{\infty} F_p^{(\alpha)} G_{n-p}^{(\alpha)} \tag{2.36}$$

where G_m^N is the mth Fourier component of the auxiliary Green's functions G_N (N=1,2,3). Finally, the acoustic field becomes

$$p'_n = \frac{\mathrm{i}k_n\Omega}{4\pi} \sum_{p=-\infty}^{\infty} \big(-G_{n-p}^{(2)} F_p^D x \sin\theta + G_{n-p}^{(3)} F_p^R x \sin\theta + G^{(1)}(F_p^T(\zeta_3 - x\cos\theta) - F_p^{(R)} r')\big) \tag{2.37}$$

Using the same assumptions as in the previous section, the model can be applied for instance to B equally spaced identical blades and the presence of a upstream stator with V vanes as

$$p'_{nB} = \frac{\mathrm{i}k_{nB}\Omega}{4\pi} \sum_{p=-\infty}^{\infty} \big(-G_{nB-pV}^{(2)} F_{pV}^D x \sin\theta + G_{nB-pV}^{(3)} F_{pV}^R x \sin\theta + G^{(1)}(F_{pV}^T(\zeta_3 - x\cos\theta) - F_{pV}^{(R)} r')\big). \tag{2.38}$$

Equation (2.31) and Equation (2.37) both contain one summation of a set of modes. However the near-field extension requires computation of the Fourier Transform of the auxiliary Green's function, additionally.

2.2. The Continuous Array of Stationary Dipoles

Another modeling strategy to simulate the rotation of the sources of fan tonal noise is using circular distributions of phase-shifted dipoles. Instead of one single rotating dipole (see Figure 2.2 (left)), infinite number of but fixed dipoles can be used to reproduce equivalently the rotation (right). In this methodology, the rotation of the fan is provided by the phase difference of the dipoles which is directly linked to their azimuthal position, β_{dipo} [88]. Since it represents a numerical integration of the source field, the integral resolution –the number of dipoles here– required for an accurate representation also needs being determined.

Assuming the source is acoustically compact in radial direction, the area integral in Equation (2.12) vanishes. However, since the source will be represented by a continuous distribution of dipoles, the azimuthal variations of the dipole positions are kept with a radius equal to r'.

The integral from 0 to 2π can now be replaced by the summation of the dipoles,

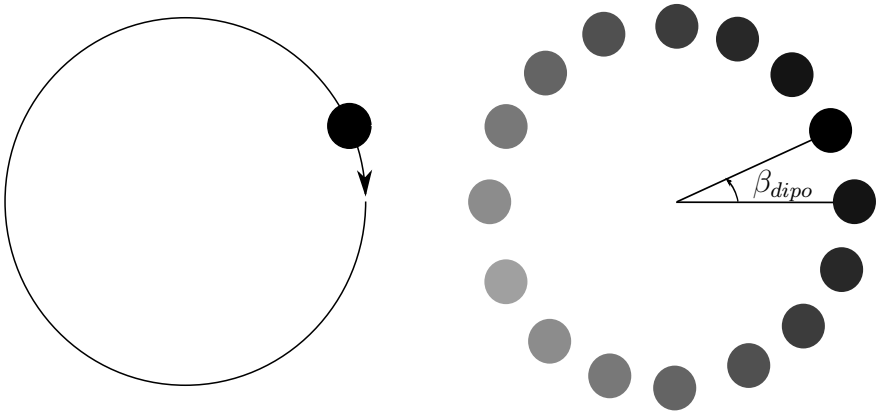

Figure 2.2.: Fan source modeling strategies; (left) single rotating dipole, (right) continuous array of phase shifted dipoles.

$$\int_0^{2\pi} \mathrm{d}\varphi' = \sum_{N_{dipo}} \int_{\beta_{dipo}-\frac{2\pi}{N_{dipo}}}^{\beta_{dipo}+\frac{2\pi}{N_{dipo}}} \mathrm{d}\varphi' \tag{2.39}$$

where N_{dipo} is the number of dipoles used. Since the dipole sources are compact in the azimuthal direction, the azimuthal integral over φ' is replaced by a summation of the variables over β_{dipo}. The strength of the phase shifted dipole is related to the initial dipole as

$$F(\beta_{dipo}, t) = F\left(0, t - \frac{n\beta_{dipo}}{\omega}\right). \tag{2.40}$$

The source strength $F(0,t) = |F|\mathrm{e}^{-\mathrm{i}\omega t}$, where $|F|$ stands for the dipole amplitude. The force strength of each dipole then becomes

$$F^{\alpha}_{n,dipo} = \sum_{p=-\infty}^{\infty} F^{\alpha}_{p}\mathrm{e}^{\mathrm{i}(n-p)\beta_{dipo}}. \tag{2.41}$$

Using the same assumptions described above for a fan containing B equally distributed blades, the source strength becomes

$$F^{\alpha}_{nB,dipo} = \sum_{p=-\infty}^{\infty} F^{\alpha}_{p}\mathrm{e}^{\mathrm{i}(nB-p)\beta_{dipo}}. \tag{2.42}$$

Similarly, the stator-rotor configuration can be implemented as

$$F^{\alpha}_{nB,dipo} = \sum_{p=-\infty}^{\infty} F^{\alpha}_{pV}\mathrm{e}^{\mathrm{i}(nB-pV)\beta_{dipo}} \tag{2.43}$$

where V is the number of upstream stator vanes.

Introducing the source strength to the acoustic pressure formulation, the total acoustic field of the continuous array of the circular oriented phase shifted dipoles finally becomes

$$p'_{nB} = \frac{B}{N_{dipo}} \sum_{N_{dipo}} p'_{nB,dipo}. \tag{2.44}$$

2.3. Acoustic Free-Field Validation

In order to make a comparison between the models described in preceding section, a benchmark axial fan is defined including artificial source strengths. The blade surface is considered as acoustically compact and represented as a point dipole. The fan has 3 uniformly distributed blades. The fan rotates with a fixed angular speed equal to 1000 rpm without the presence of an upstream stator. The blade loading frequency is then equal to $1000/60 = 16.33$ Hz where the blade passing frequency is 50 Hz. The radius of the fan is selected as 0.5 m making the tip Mach number, $M_{tip} \cong 0.3$. Hence, the low-speed fan condition is satisfied.

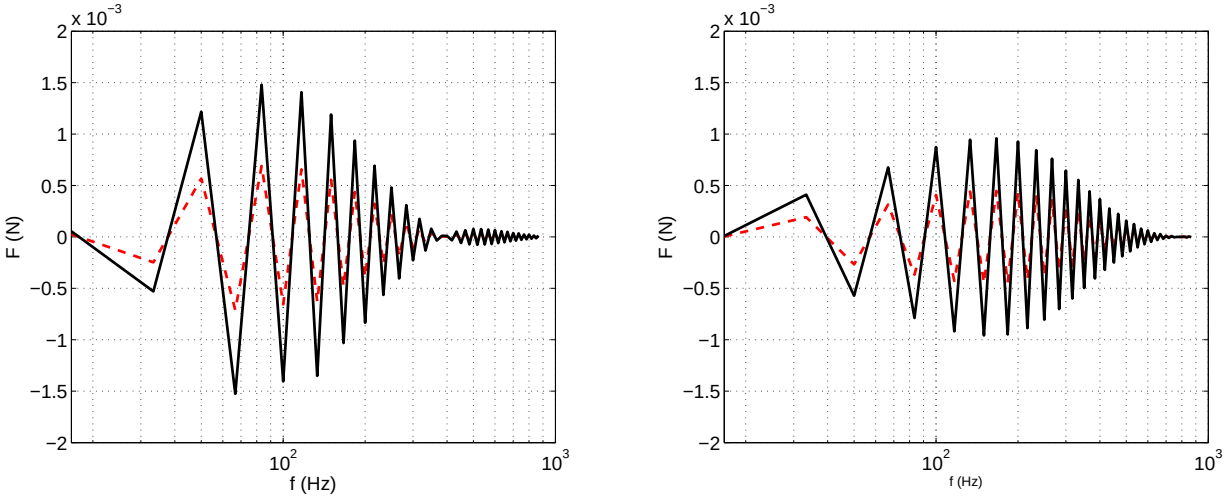

Figure 2.3.: Real (left) and imaginary (right) components of the artificial unsteady blade forces; thrust (plain) and drag (dashed).

Figure 2.3 shows the real and imaginary components of the force strengths of the dipoles at the blade loading harmonics. As mentioned above, since the radial force is known to be negligible for axial fans, only the drag and thrust components are taken into account. Thrust (plain) forces are considered higher than the drag (dashed) forces.

A first comparison is made in the acoustical far-field of the fan. The fan is assumed to rotate on the xy plane with a rotation axis aligned with the z axis. Observers are located where the non dimensionlized wavelength, $r_{obs}/\lambda \approx 3$ satisfying the far-field condition.

Figure 2.4 shows the directivity at the first BPF on yz, xz and xy planes, respectively. The plots are the acoustic pressure amplitude at the observer points. Dot symbols represent the far-field solution obtained with Equation (2.31) where the plain curve represents the near-field solution using Equation (2.37). Plus represent the circular array of phase shifted dipoles. In four lines of the figure, $16, 32, 64$ and 720 point dipoles are compared, respectively. It is seen that a convergence is satisfied using 64 stationary point dipoles at all three directions for the given configuration. It is also seen that solutions (2.31), (2.37) and (2.44) converge in the far-field since the near-field terms (R^2 decay) are negligible.

A second comparison is performed in the acoustical near-field of the fan. The same fan is considered with observers located where the non dimensionlized wavelength is, $r_{obs}/\lambda \approx 0.3$.

Directivities of pressure amplitude in the near-field of the benchmark fan are shown in Figure 2.5. Dots, solid line and plus represent the far-field solution (2.31), near-field ex-

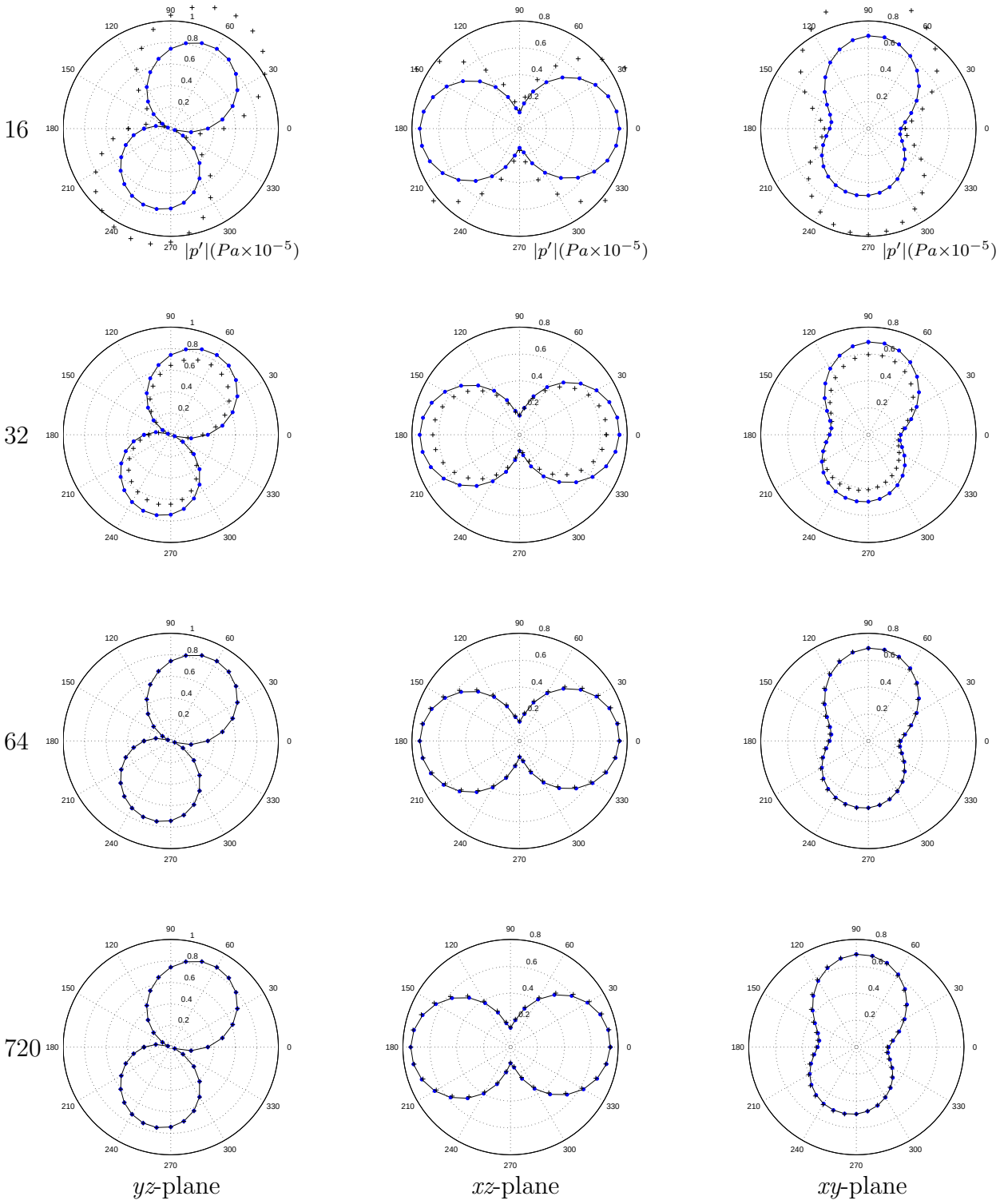

Figure 2.4.: Free-field directivities of the low-speed axial fan in its far-field at 50 Hz, observers located at $r_{obs}/\lambda \approx 3$: Solution (2.31) (dot symbols), solution (2.37) (solid line) and formulation (2.44) (cross symbols). 16, 32, 64 and 720 dipoles are used in order to represent an equivalent fan source using formulation (2.44).

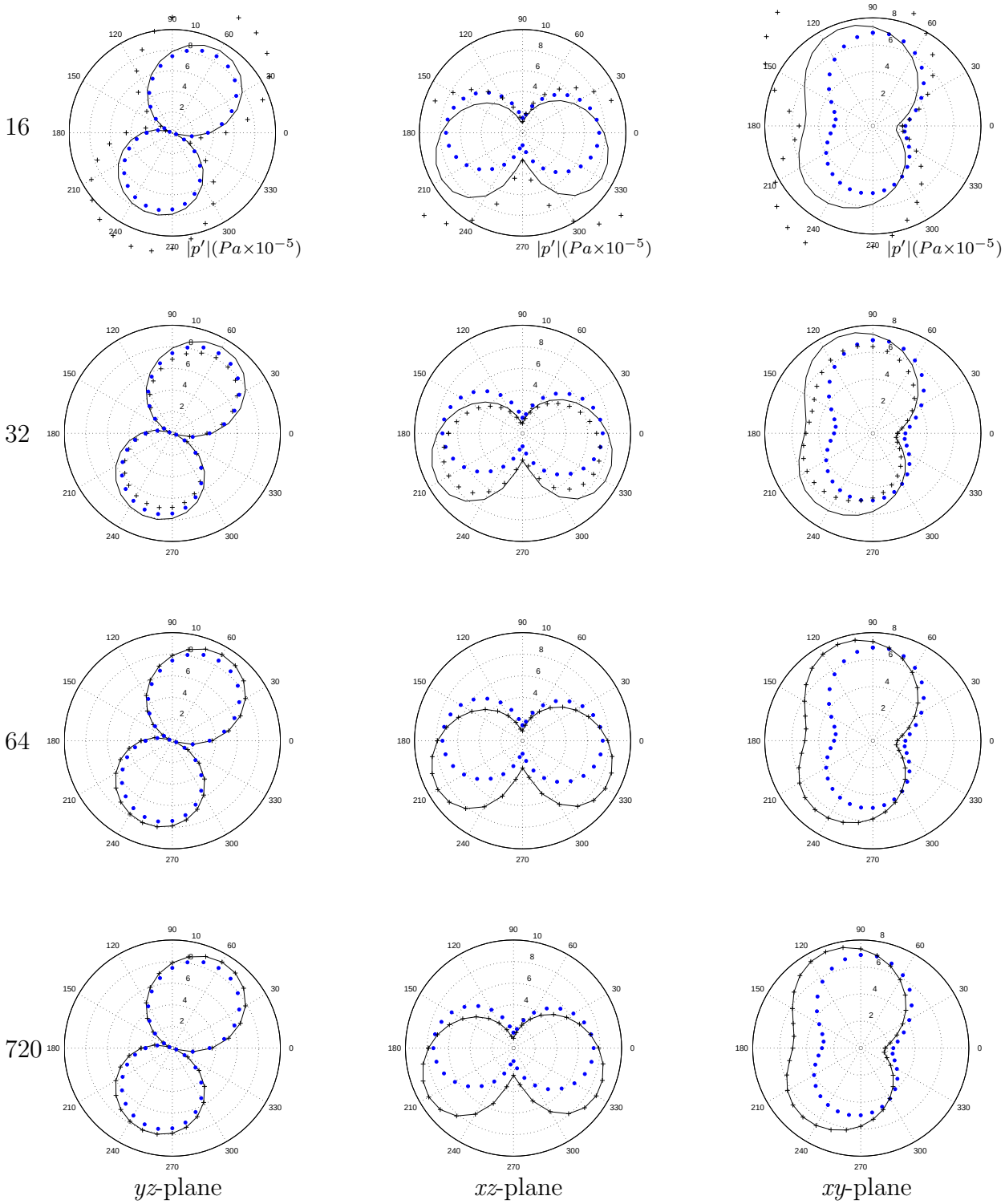

Figure 2.5.: Free-field directivities of the low-speed axial fan in its near-field at 50 Hz, observers located at $r_{obs}/\lambda \approx 0.3$: Solution (2.31) (dot symbols), solution (2.37) (solid line) and formulation (2.44) (cross symbols). 16, 32, 64 and 720 dipoles are used in order to represent an equivalent fan source using formulation (2.44).

pression (2.37) and the dipole array formulation (2.44), respectively. A convergence is again satisfied employing 64 fixed point dipoles in all given directions for the benchmark configuration. Solution (2.37) and solution (2.44) converge at the near-field of the fan. However, for the current observer positions, a deviation is observed with the solution (2.31). The difference between solution (2.31) and solution (2.37) addresses the effect of the near-field terms detailed above.

2.4. Conclusion

In conclusion, solution (2.37) provides accurate prediction for the acoustic field of the fan where the observer is located in its acoustical and geometrical near-field. It is more elegant than formulation (2.44) since it is an exact solution and does not involve resolution issues, such as the number of dipoles used in expression (2.44). However, formulation (2.44) is a useful solution to predict the acoustic field of the fan for complex problems where it is not possible to obtain an exact analytical closed-form solution. It will be used for sound-scattering problems to define the equivalent fan tonal source in the following chapter.

Furthermore, solution (2.31) may be useful where the observer is located at the far-field of the fan. Since it does not require the computation of the Fourier components of the Green's functions as in the near-field solution (2.37), it provides a faster prediction in terms of computation time.

As a result, depending on the configuration of the problem, the tonal acoustic free-field response of a low speed axial fan can be predicted by choosing a method described above. These methodologies will be extended in order to compute the scattered field of the tonal fan noise in the following chapter.

Chapter 3.

Tonal Fan Noise Scattering

This chapter deals with numerical and analytical acoustic scattering techniques and their applications to low-speed fan noise. A numerical approach based on the solution of the Helmholtz equation, called Boundary Element Method (BEM) is first introduced. The scattered acoustic field of a ducted axial fan is computed using the closed-form fan noise formulation combined with the BEM approach. Both far and near-field formulations are investigated. The results are compared with experiments.

In a second step, two analytical methods are introduced for relatively simple scattering geometries; an infinite plane and an infinite corner. Both methods are compared with the numerical solutions based on the BEM approach, as an introduction to scattering by non-axisymmetric surfaces.

3.1. Introduction

In most industrial applications, the acoustic waves generated by a fan are reflected and scattered due to installation effects [94, 105]. The acoustic free-field condition assumption then becomes invalid and the scattered acoustic field of the fan needs being taken into account. Several methods have been proposed to deal with the scattered acoustic field problems based on analytical, empirical and numerical models [35, 93, 79, 71].

As mentioned in the previous chapter, the acoustic free-field of a low-speed axial fan can be predicted by exact closed-form analytical formulas [47, 108]. However, computing the scattered-field of the sound emitted from a fan source in an exact analytical solution only exists for a very limited number of acoustic problems, involving scattering structures with simple geometrical shapes. Prediction of reflected and scattered acoustic waves emitted from an axial fan by a large flat plate is one of the simple problems that could be solved analytically [103]. Additionally, a low-speed axial fan operating in the vicinity of a rigid corner is also addressed analytically using the Green's function of a corner [83] and the description in terms of a continuous array of stationary dipoles [88]. Possible applications for this problem could be the scattering of the noise generated by a cooling unit located on the top of a locomotive from the point of view of one side of the locomotive, or a small wind turbine located on the top of a building and its scattered-field by the building itself. For complex configurations approximate solutions of the Helmholtz equation can be obtained using the associated boundary conditions with numerical techniques.

3.2. Numerical Acoustic Scattering Techniques

The most popular numerical approach dealing with engineering problems based on solution of the partial differential equations is the Finite Element Method (FEM) [21]. In acoustical

perspective, it is based on the solution of the Helmholtz equation in a domain with a set of boundary conditions. A derivation of the FEM approach can be found in the related references [58].

Even though it is the most common approach to deal with scattered acoustic fields, FEM has some disadvantages [35, 36].

- Generally, the entire domain needs being discretized in FEM in order to solve the numerical model [9], therefore it is restricted to bounded, so-called interior, acoustic domains. Several schemes have been suggested to extend the FEM algorithm in order to solve exterior acoustic problems, which contain unbounded acoustic domain. They are mainly based on construction of an artificial surrounding surface and using impedance boundary conditions [31], damping elements [13, 12] or infinite elements [3] on this surface.

- In principle, at least 10 elements per acoustic wavelength are required in order to obtain an accurate prediction [35]. The required number of elements will increase as frequency increases, since the acoustic wavelength decreases. Additionally, since FEM requires the entire volumetric domain discretizated, the number of equations to be solved and the model size will increase [9]. Therefore, larger domains and higher frequencies are more challenging and they require a large amount of memory and computational sources for constructing and solving the problem [35].

- Predictions of secondary field variables such as fluid velocities are obtained by a derivation of the primary field variables, the acoustic pressure for example. The primary variables are usually expressed in terms of polynomial expansions up to some order, hence the derived variables are expressed only up to a lower order [35]. The prediction accuracy for derived secondary variables is therefore smaller than the one for primary field variables [36].

3.3. Boundary Element Method (BEM)

In the field of linear acoustics, the Boundary Element Method (BEM) is an important alternative to the FEM [63]. BEM is based on the solution of the unknown boundary variables on the bounding surface. The rest of the acoustic domain is then computed as a post-processing step [9]. BEM can therefore handle problems with unbounded, so-called exterior, acoustic domains easily. Additionally, since only the boundary surface of the acoustic domain is discretized into elements, the size of boundary element models is substantially smaller that that of finite element models [63, 9]. Beside its benefit on solving unbounded problems, BEM has additional advantages.

- Since only the boundary of the domain is considered, BEM significantly reduces the mesh generation effort for the numerical domain [9]. However, construction of these models requires a considerable amount of computational effort, since the matrices in acoustic boundary element models are fully populated and complex [35, 34].

- The secondary variables are derived from the boundary integral formulations in BEM. Since an analytical expression is available for Green's kernel function, the differentiation of the boundary integral formulations involves no additional accuracy loss for the secondary variables in comparison with the accuracy for the primary predictions [34].

In the benchmark configurations investigated in this chapter, the fan source is located in unbounded acoustic domain in the presence of scattering obstacles. Since only the boundary surface of the acoustic domain is discretized into elements for BEM, it is a more suitable scattering technique for such configurations. Its benefit includes reducing the time spent for

both mesh preparation and computation of the numerical problem, compared to the FEM approach [63].

The Boundary Element Method follows a two-step procedure in which scattering surfaces are interpreted as secondary sources [34]: In the first step, the boundary variables are determined. In the second step, using the boundary surface results of the first step, the acoustic field variables are obtained from the boundary integral formulation.

3.3.1. BEM Theory

Depending on the boundary type of the fluid domain, the BEM model can be defined as interior or exterior. BEM is capable of handling both acoustic problems. The benchmark configurations addressed in this section are exterior acoustic problems, therefore only the unbounded BEM definition is considered [59].

Exterior acoustic problems can be grouped in two sets, with a closed boundary surface and with an open boundary surface. An exterior acoustic problem with an open boundary surface maybe regarded as a special case of an exterior problem with a closed boundary by considering both sides of the open boundary surface as two separate parts of a closed boundary surface such as $\Omega_a = \Omega_a^+ \cup \Omega_a^-$. The positive/negative sign of Ω corresponds to the positive/negative orientation of the surface normal, n as shown in Figure 3.1.

For inhomogeneous acoustic problems, such as when non-zero external source distribution F is applied –unsteady blade forces here–, the total acoustic pressure field p_{tot} may be regarded as the superposition of a so-called homogeneous (scattered) pressure field p_{scat} and an inhomogeneous (incident) free-field pressure p_{inc},

$$p_{tot} = p_{inc} + p_{scat}. \tag{3.1}$$

In a fluid domain V (see Figure 3.1), the steady-state acoustic pressure p_{inc} due to a time-harmonic external source distribution F at a location (x, y, z) at angular frequency $\omega = 2\pi f$ is governed by the Helmholtz equation,

$$\nabla^2 p_{inc}(\omega, x, y, z) + k^2 p_{inc}(\omega, x, y, z) = -\mathrm{i}\rho_0 \omega F(\omega, x, y, z) \tag{3.2}$$

where $k = \omega/c_0$ is the acoustic wave number. For the scattering problems including a fan source, the incident pressure addresses the free-field solution of the fan noise, as defined in Equations (2.31) and (2.37). The homogeneous pressure field p_{scat} is defined as the solution of the homogeneous Helmholtz equation

$$\nabla^2 p_{scat}(\omega, x, y, z) + k^2 p_{scat}(\omega, x, y, z) = 0. \tag{3.3}$$

In order to obtain a unique solution of the pressure field in domain V, the boundary conditions must be specified at any position of the boundary surfaces of the domain, such as pressure, p, normal acoustic velocity, v, and normal impedance, Z. The parameters must be specified at each position of the boundary surface of the domain. Decomposing $\Omega_a^+ = \Omega_p^+ \cup \Omega_v^+ \cup \Omega_Z^+$ and $\Omega_a^- = \Omega_p^- \cup \Omega_v^- \cup \Omega_Z^-$, the boundary conditions for the imposed pressure then read

$$p = \bar{p}, \ on \ \Omega_p^+ \tag{3.4}$$

$$p = \bar{p}, \ on \ \Omega_p^-. \tag{3.5}$$

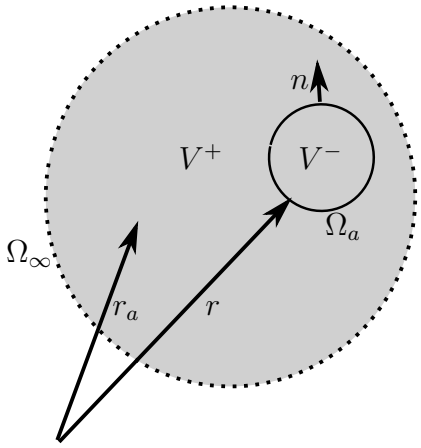

Figure 3.1.: Sketch of the BEM problem

Similarly, the boundary conditions for the imposed normal velocities and for the imposed normal impedances are defined as

$$\frac{\mathrm{i}}{\rho_0 \omega} \frac{\partial p}{\partial n} = \bar{v_n}, \ on \ \Omega_v^+ \tag{3.6}$$

$$\frac{\mathrm{i}}{\rho_0 \omega} \frac{\partial p}{\partial n} = \bar{v_n}, \ on \ \Omega_v^- \tag{3.7}$$

$$p = \frac{\mathrm{i}\bar{Z}^+}{\rho_0 \omega} \frac{\partial p}{\partial n}, \ on \ \Omega_Z^+ \tag{3.8}$$

$$p = \frac{\mathrm{i}\bar{Z}^-}{\rho_0 \omega} \frac{\partial p}{\partial n}, \ on \ \Omega_Z^-. \tag{3.9}$$

The acoustic pressure field in the unbounded domain V must satisfy the Sommerfeld radiation condition [35] for large values of r,

$$\lim_{|r| \to \infty} |r| \left(\frac{\partial p}{\partial |r|} + \mathrm{i}kp \right) = 0. \tag{3.10}$$

Since the incident pressure field p_{inc} may be obtained via an analytic solution using the source distribution F as a combination of acoustic point sources, as shown in Chapter 2, a numerical solution is needed only for the homogenous subproblem. Equation (3.3) can be solved using Green's second identity,

$$\int_V \left(\varphi \nabla^2 \psi - \psi \nabla^2 \varphi \right) \ \mathrm{d}V = \int_{\Omega_s} \left(\varphi \frac{\partial \psi}{\partial n} - \psi \frac{\partial \varphi}{\partial n} \right) \ \mathrm{d}\Omega. \tag{3.11}$$

Assuming thin boundary surfaces, the boundary integral equation becomes,

$$p(\vec{r}) = \int_{\Omega_a} \left((p^+(\vec{r}_a) - p^-(\vec{r}_a)) \frac{\partial G(\vec{r}, \vec{r}_a)}{\partial n} - G(\vec{r}, \vec{r}_a) \left(\frac{\partial p^+(\vec{r}_a)}{\partial n} - \frac{\partial p^-(\vec{r}_a)}{\partial n} \right) \right) \ \mathrm{d}\Omega(\vec{r}_a). \tag{3.12}$$

The single layer potential, $\sigma(\vec{r}_a)$, is the difference in normal pressure gradient between both sides of the boundary surface Ω_a

$$\sigma(\vec{r}_a) = \frac{\partial p^+(\vec{r}_a)}{\partial n} - \frac{\partial p^-(\vec{r}_a)}{\partial n} \tag{3.13}$$

which can also be regarded as the monopole sources on the boundary surface. Similarly, the double layer potential, $\mu(\vec{r}_a)$, is the pressure difference between both sides of the boundary surface

$$\mu(\vec{r}_a) = p(\vec{r}_a^+) - p(\vec{r}_a^-) \tag{3.14}$$

and represents a distribution of equivalent dipole sources on the boundary surface.

Combining Equations (3.12), (3.13) and (3.14), the boundary integral equation becomes [34],

$$p(\vec{r}) = \int_{\Omega_a} \left(\mu(\vec{r}_a) \frac{\partial G(\vec{r}, \vec{r}_a)}{\partial n} - \sigma(\vec{r}_a) G(\vec{r}, \vec{r}_a) \right) \, \mathrm{d}\Omega(\vec{r}_a). \tag{3.15}$$

Formulation (3.15) is known as the indirect boundary integral equation [59]. The term 'indirect' indicates that the boundary variables such as monopoles and dipoles on the boundary surface do not represent any direct physical quantity of the acoustic pressure field.

As in the FEM approach [36], the boundary surfaces are discretized into small patches called 'boundary elements'. Acoustical nodes are then located on the surface of elements. The most common types of elements are known as triangular and quadrilateral element and the nodes are located at the corners of each element. In the following problems considered in this chapter, only the quadrilateral elements are used.

In each element, the distribution of the single and double layer potentials are approximated in terms of a number of prescribed shape functions. The details of computing the shape functions are not addressed in this thesis. The reader is referred to technical notes [34, 58] for a detailed derivation of the BEM formulation and the geometrical quantities. Once the single and double layer potentials are determined, the pressure field in the domain is obtained using the boundary integral equation above.

3.3.2. Application to a benchmark ducted fan

Combining the tonal fan noise prediction methods mentioned in Chapter 2 and the Boundary Element Method described above, the scattered acoustic field of a low-speed axial fan can be computed. In order to make a comparison, a low-speed benchmark axial fan with $B = 6$ blades has been selected [69] in the scope of the IWT Project CAPRICORN. The fan is operated downstream of 5 guide vanes. The rotational speed is fixed to $N = 1600$ rpm. The tip and hub radii of the blades are selected as 0.2m and 0.05m, respectively. The tip Mach number is then around 0.1, satisfying the low Mach number axial fan condition, $M \ll 1$.

The Blade Passing Frequency (BPF) and Blade Loading Harmonics (BLH) for the current configuration are then computed as

$$\begin{aligned} BPF &= \frac{NB}{60} = 160 \ Hz \\ BLH &= \frac{NV}{60} = 133.33 \ Hz. \end{aligned} \tag{3.16}$$

The Ffowcs Williams and Hawkings approach [40, 47, 108] detailed in Chapter 2 is very useful, since the source field is restricted only to the blade surfaces. In order to define the

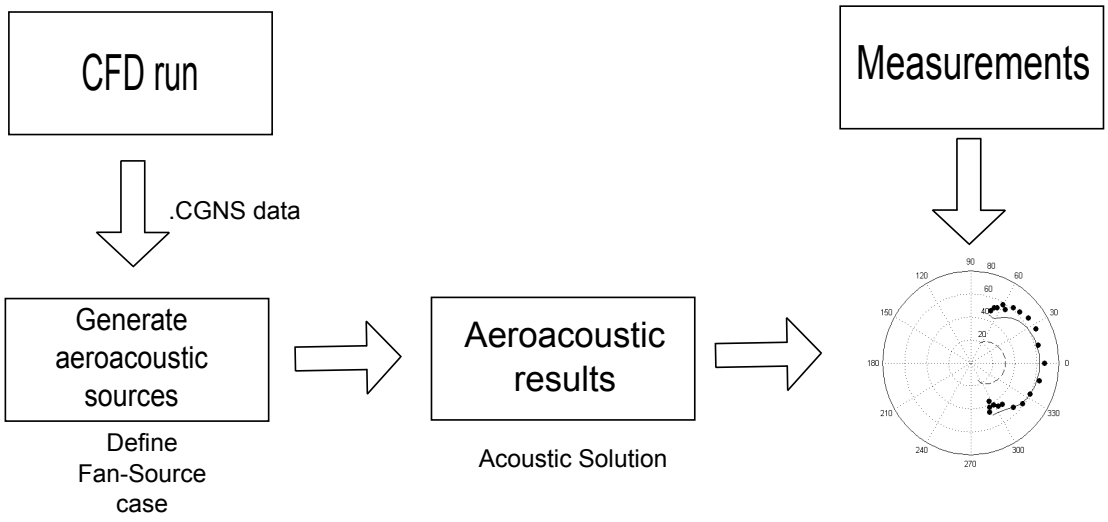

Figure 3.2.: Flowchart of the application of the hybrid approach to the tonal fan noise problem.

blade loading forces, an unsteady CFD simulation is required, such as Large Eddy Simulation (LES) [104], Unsteady Reynolds Averaged Navier Stokes (URANS) [132] or Non-Linear Harmonic (NLH) [126] models. Figure 3.2 shows the flowchart of the validation model. In this validation problem NUMECA provided the CFD data for one single blade of an axial fan which is calculated with an NLH model in frequency domain [69]. A snapshot of the blade loading pressure amplitude at the 5th BPF is shown in Figure 3.3.

The LMS software Virtual Lab. and the solver Sysnoise are used in order to defined the fan source case and solve the BEM problem [59]. Unsteady blade loadings provided are imported in Virtual Lab. within the *.CGNS* format. A fan source set is created in an external Virtual Lab. Analysis file where the effect of number of blades, guide vanes, radius and the rotational speed are defined. For reader's information, the fan source model used in the Virtual Lab. is based on the rotating dipole formulation.

The imported unsteady pressure distribution on the blade surface is first integrated and the entire blade is reduced to a point dipole. This assumption is only valid if the blade is acoustically compact at the frequency of interest [41], BPF or higher harmonics in the tonal fan noise case. If the compactness condition is not satisfied for the blade surface, the blade surface can be split into spanwise (or chordwise) compact segments and separate fan sources are then defined for each segment [108, 59]. Although applying segmentation multiplies the computation time by the number of segments, it provides a better representation of the blade geometry for the integration of the surface pressure and it is required in order to ensure acoustic compactness. In the validation model, the blade is split into two spanwise segments [69] so that the aspect ratio of segments is around 1. Figure 3.4 shows the integrated blade loading harmonics for two segments. Plain and dashed represent drag and thrust forces applied on the blade surface, respectively. The thin line stands for the segment close to the tip of the fan. The ratio of the thrust and drag components is seen to be around two. Using the given source strengths, the tonal fan noise formulation is then applied to both segments. Both far-field and near-field fan noise models implemented in the solver are used in the comparison [59].

Figure 3.5 shows pictures of the fan and the duct geometry imported in Virtual Lab.

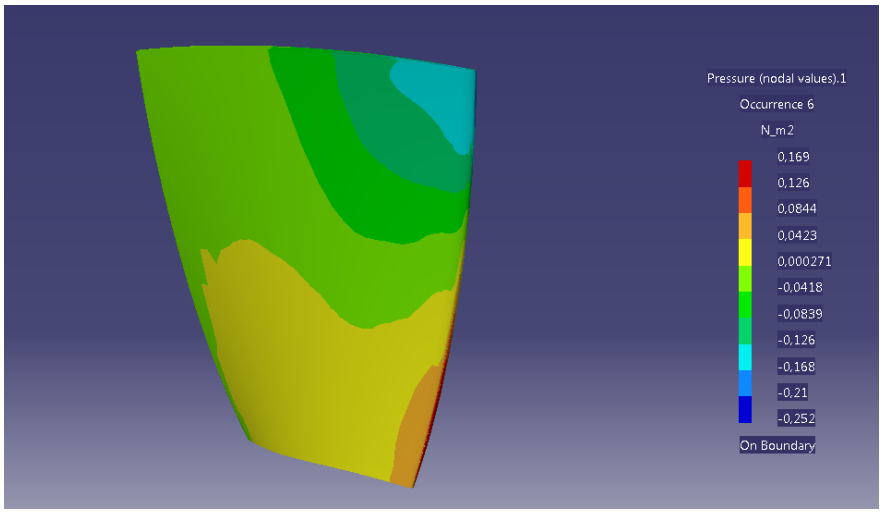

Figure 3.3.: Snapshot of the blade loading pressure amplitude at the 5th BPF.

The fan is located 0.2m downstream of the duct inlet. The two segmented fan sources (yellow circles) can be seen in the duct. The acoustic scattering by the guide vanes is neglected in computations. Due to the periodicity of the CFD problem, the flow field is solved around single rotor blade in the NLH technique [126]. The 3-Dimensional duct model is then obtained by revolving the nodes provided by the CFD mesh. The acoustic mesh is then created using the resulted surfaces.

Due to the finite structure of the duct and the presence of the hub, it is not possible to use exact analytical scattering techniques such as based on propagating duct modes [101, 125].

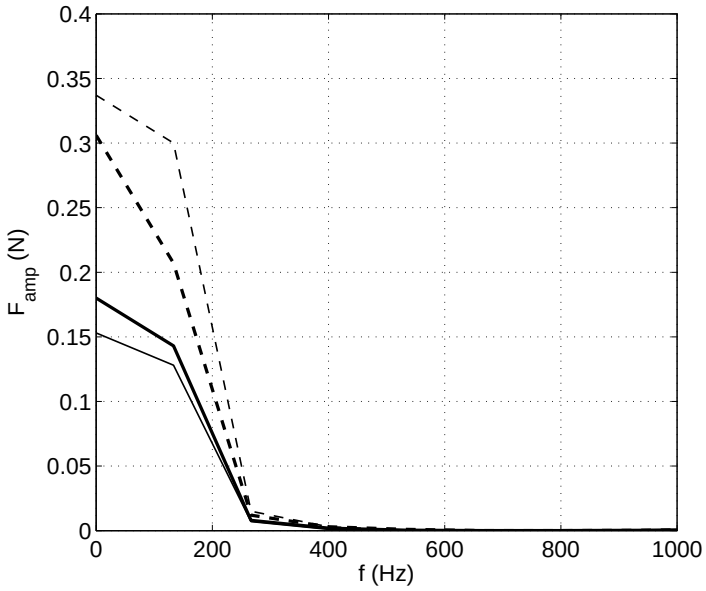

Figure 3.4.: Integrated blade loading forces, thrust (dashed) and drag (plain) over fan blade for two segments. Thick; segment close to the hub, thin; segment close to the tip.

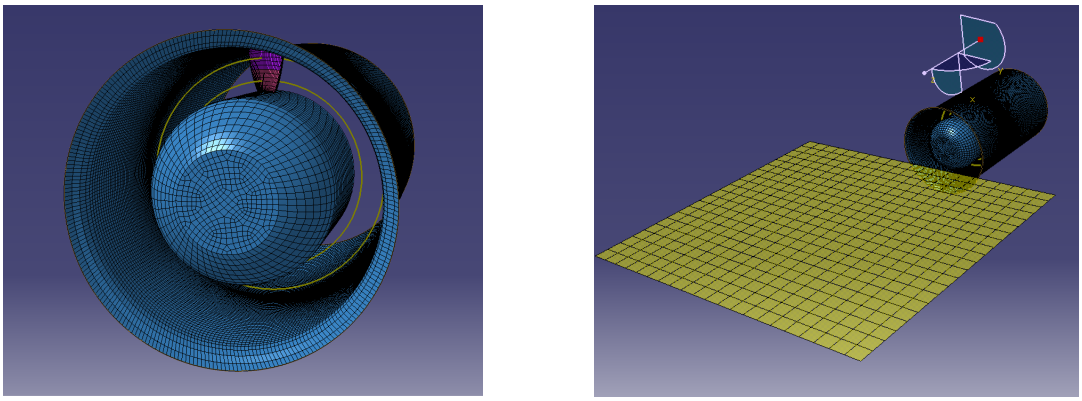

Figure 3.5.: Numerical representation of the benchmark ducted fan validation case; (left) duct and rotor, (right) distribution of upstream field points. (Snapshot taken from Virtual Lab.).

It is therefore required to solve the problem numerically. Since the field points are located in the unbounded fluid domain, BEM is a suitable method to compute the scattered acoustic field for the current ducted fan configuration [35]. Hence, only the meshes of the duct and hub surfaces are enough for the BEM model. The final acoustic mesh contains 27100 hexagonal acoustic elements. The size of elements close to the rotation plane is decreased in order to keep the sufficient distance-element size ratio in order to prevent numerical errors in the BEM formulation [34].

A first comparison is performed using the unsteady blade forces provided for the fan operating in the duct but assuming the fan is operating in free-field for the acoustic propagation. Although it is not a realistic prediction of the noise generated by the fan, since the effect of the duct was already taken into account in the aerodynamic computations, it is a good exercise to compare the effect of the near-field terms up to the far-field of the fan. Figure 3.6 shows the distribution of the sound pressure level for both analytical approaches at a microphone array located upstream of the fan. The acoustic field is plotted in dBs. The array consists of 441 microphones covering $1m \times 1m$ area. The array is oriented symmetrically in a lateral plane (yz-plane) starting from 0.25m upstream of the fan center (see Figure 3.5). Both far-field solution (2.37) and near-field formulation (2.31) are compared with the selected field point configuration. Since the unsteady pressure field on the rotor blades is triggered by five upstream guide vanes, the 5th BPF becomes dominant [125]. Therefore the results at the 5th harmonic, $f = 800Hz$, are focused on. It is seen that both methods provide similar results, with only differences up to 1 dB at all the considered field point locations. The near-field terms become negligible since field points are located somewhat in the far-field of the fan where l/λ varies from 0.6 to 3.

In a second step, an exact comparison is performed using the same unsteady blade forces provided for the fan operating in the duct but including the duct geometry in the acoustic field computations. Figure 3.7 shows the distribution of the total sound pressure level on the same microphone array for both simulations based on the far-field and near-field incident pressure, respectively. Now, the difference between both predictions reaches 30 dB, proving that the effect of the near-field terms in the scattered-field computations is essential.

Series experiments have been performed in Vrije Universiteit Brussel (VUB), for the same ducted fan configuration [69]. The acoustic measurements are taken on the same microphone

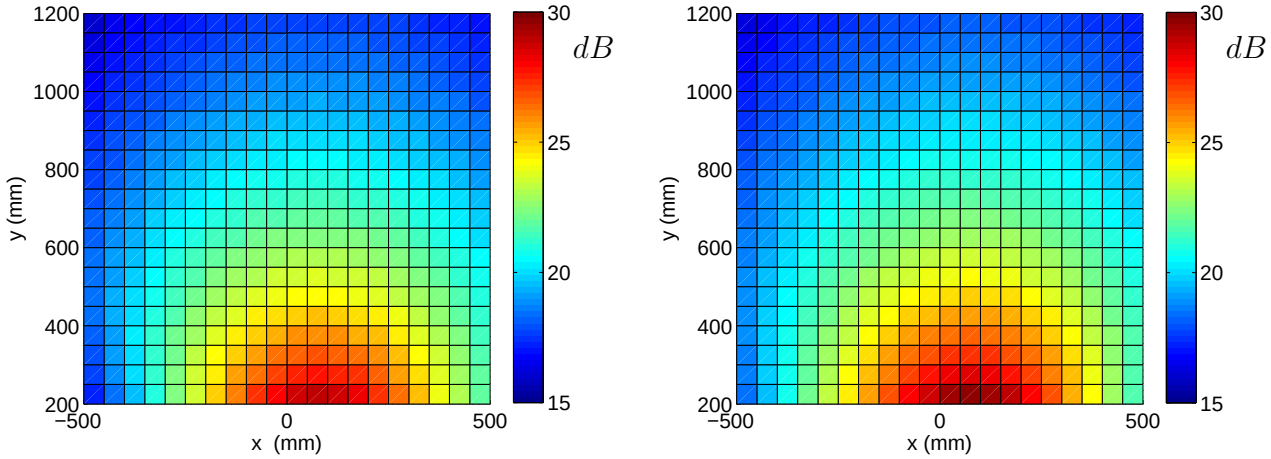

Figure 3.6.: Computed free-field response of the fan at 5th BPF at observers located at $l/\lambda = 0.6$ to 3. Results obtained using (left) far-field formulation (2.31), (right) near-field formulation (2.37).

array in the presence of the duct. Figure 3.8 (left) shows the measured sound pressure level for the microphone array at the 5th BPF. The order of magnitude of the sound pressure levels shows a fair agreement with the ones obtained with the near-field tonal fan noise formulation combined with the BEM approach compared with the ones obtained with the far-field ones.

In order to compare all three estimations, the directivity at $l/\lambda \approx 1.2$ upstream of the fan center is plotted in Figure 3.8 (right). The far-field solution (2.31) (dashed) is found to underpredict the acoustic field by 30 dB. The far-field consideration is not an accurate assumption for the current model since the near-field terms in the scattered-field computations are not negligible anymore. In contrast, the difference between the measurements (dots) and the near-field fan formulation (2.37) combined with BEM (plain) is less than 5 dB for the

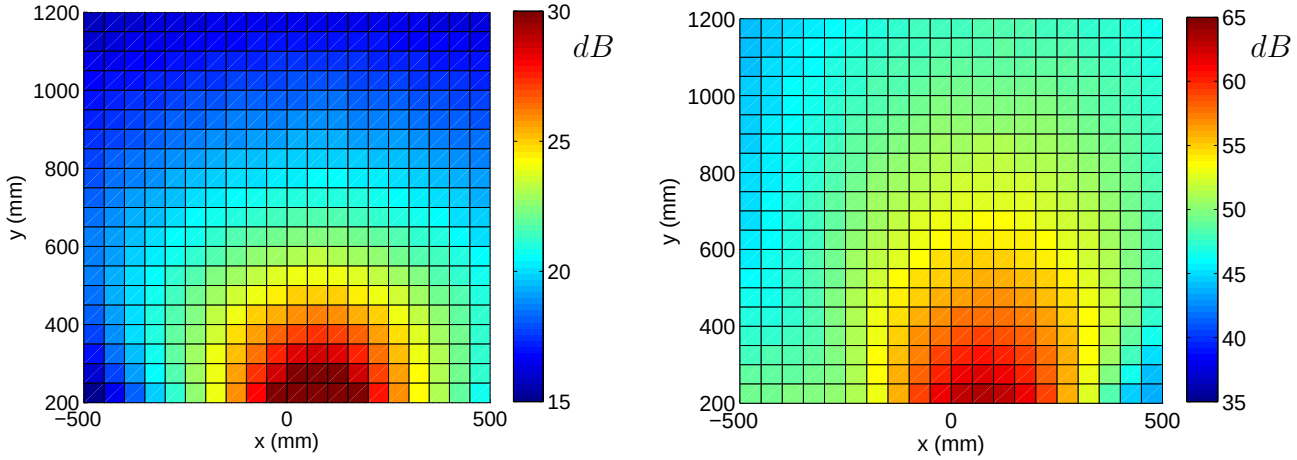

Figure 3.7.: Computed total acoustic field of the ducted fan at 5th BPF at observers located at $l/\lambda = 0.6$ to 3. Results obtained using (left) far-field formulation (2.31), (right) near-field formulation (2.37) combined with BEM.

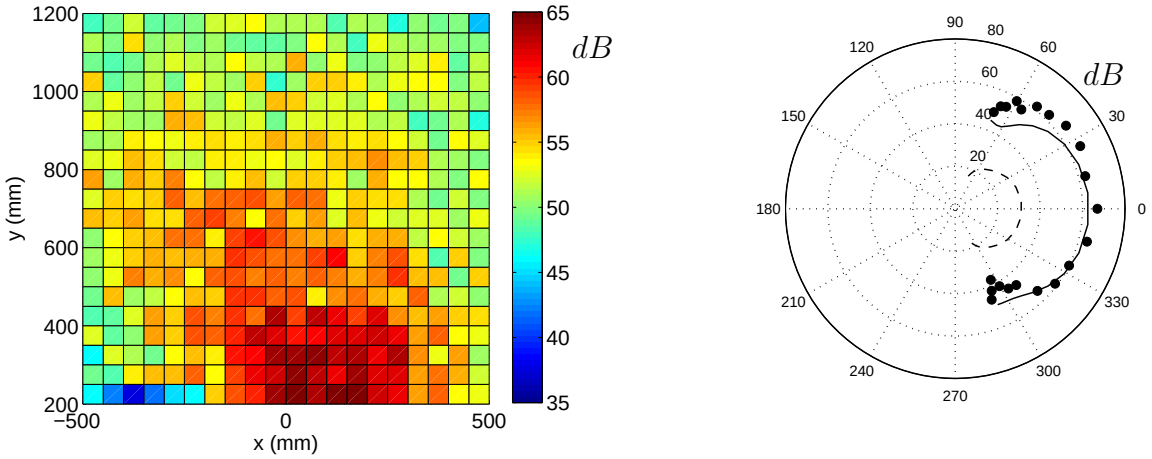

Figure 3.8.: Measured acoustic field of the ducted fan at 5th BPF at observers located at $l/\lambda = 0.6$ to 3 (left). Directivity at $l/\lambda \approx 1.2$ far-field solution (2.31) (dashed), near-field formulation (2.37) (plain), and measurements (symbols).

given observer locations. The near-field formulation combined with the BEM approach is therefore a useful tool to predict the scattered acoustic field of a low-speed axial fan.

Since BEM approach is based on the boundary integral equation, it can be applicable to complex geometries. It is also useful for both bounded and unbounded domains. However, BEM is a suitable model for low frequency problems [35]. At higher frequencies of interest, the number of boundary elements increases dramatically in the order of 10 elements per wavelength [34]. It is then not useful to employ BEM for such applications. For high frequency problems where the scattering geometry is relatively simple, analytical solutions can be useful since the wavelength is much smaller compared to the size of the scattering obstacle.

Therefore, at high frequencies and for simple geometries such as an infinite plane [103], semi-infinite plane [39] or finite wedges [101], exact analytical scattering solutions can be useful to predict the scattered acoustic field.

3.4. Reflection from an Infinite Plane

The most basic scattering concept is the reflection of acoustic waves by idealized rigid, planar and infinite extent surfaces such as plain walls. Only simple considerations are needed to take a large plane into account when the wavelength λ is much smaller than the length of the scattering obstacle, $\lambda \ll l$.

The common concept is to replace the original boundary-value problem of source-wall configuration by the primary source plus the additional image source but without the wall. The image source is the mirror image of the primary source in all respects [101]. The concept is called the method of images. As seen in Figure 3.9, if the wall corresponds to the plane $z = 0$ and the original source is located at (x, y, h), the image source must be located at $(x, y, -h)$. If a dipole source force strength is (F_x, F_y, F_z), the image source must have $(F_x, F_y, -F_z)$ components. This theory can be applied to various types of sources such as monopole, dipole and arrays typical of a fan. The mirror symmetry of the boundary-value

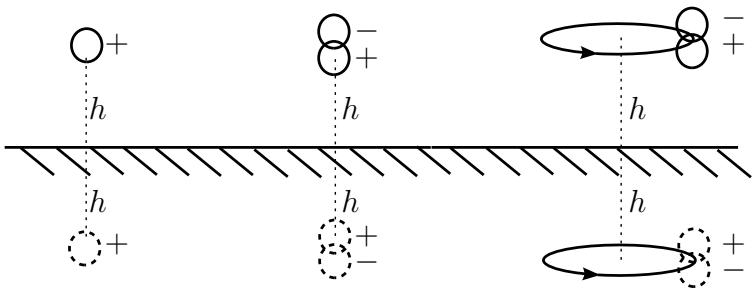

Figure 3.9.: Sketches of the method of images for monopole, dipole and fan noise sources

problem of the original and image sources without the wall doubles the incident pressure on the wall surface and requires the normal component of the acoustic velocity to vanish in the wall plane. The boundary condition appropriate to the original problem is then satisfied with the no wall problem.

As a test case, an axial fan operating parallel to a large rigid flat plate is considered. This problem can be dealt with two methods, the numerical approach described in the Section 3.3 and the exact analytical solution using an image fan. An open rotor, without any upstream stator vanes, with 10 equally spaced blades is selected. The rotational speed is chosen as 3000rpm. The fan radius and the distance of the rotation plane to the wall are fixed to $r = 0.1$ and $z = 0.2$m, respectively. The tip Mach number is then around 0.1, satisfying the low Mach number fan condition. The artificial source strengths defined in Section 2.3 are used for the test case with the same amplitude but with a change in the frequencies, since the blade loading harmonic frequency for the current configuration is now $N/60 = 50$ Hz (see Figure 3.10). The wavelength at the first BPF, $f = 500$ Hz, is then equal to $\lambda = c_0/f = 0.68$m.

The size of the flat plate is selected as $3.5\lambda \times 3.5\lambda$ in order to minimize the effect of the scattering from the free edges. The size of the plate is also limited since the element size used in the BEM model must be at most 1/10 of the acoustic wavelength [35]. 3600 quadrilateral

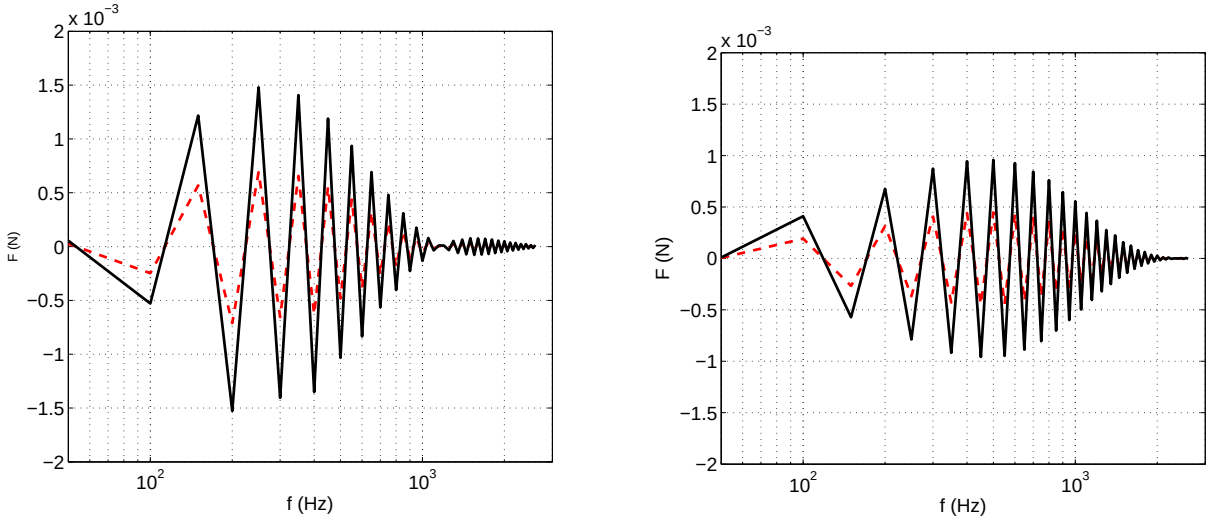

Figure 3.10.: Thrust (plain) and drag (dashed) forces applying on the fan source; real (left) and imaginary (right).

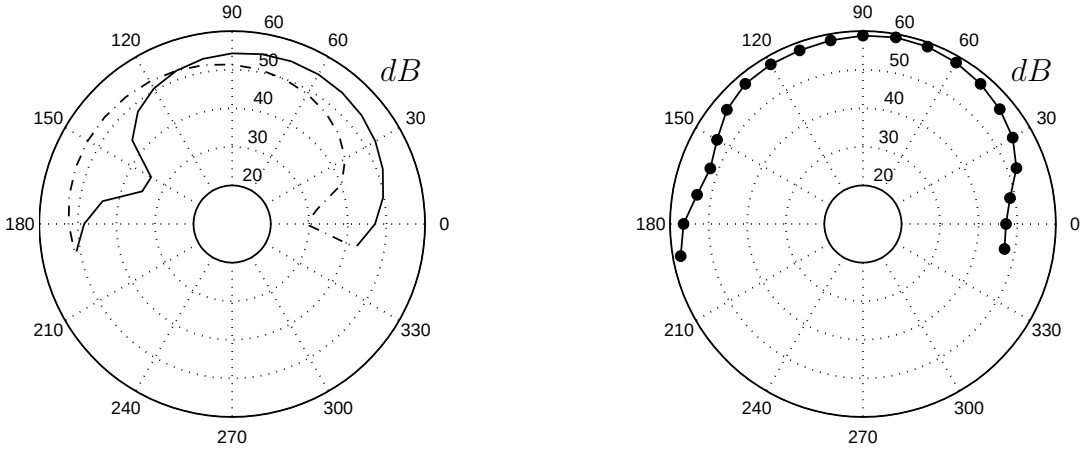

Figure 3.11.: Directivities at $\cong 1.5\lambda$ at $f = 500$ Hz; (left) free-field for primary (plain) and the image fan (dash dot), and (right) scattered field: formulation (2.37) combined with BEM (symbols) and image model (plain).

acoustic boundary elements are used in order to represent the finite plate in Virtual Lab.. Using a larger plate with more acoustic elements would provide a closer approach to the image model but would require higher computational resources to handle large matrices.

Figure 3.11 (left) shows the acoustic free fields of the primary (plain) and the image fans (dash dot) $r \cong 1.5\lambda$ above the primary fan for the first BPF. The near-field formulation (2.37) is used for the consistency of the comparison. It is seen that the acoustic field of two sources alike symmetric since the image source is the mirrored original source. The amplitude obtained from the image source is also slightly lower than the original one, since the propagation distance to the observer is higher. The comparison of the analytical and numerical scattered-field approaches is seen in Figure 3.11 (right). Symbols represent the near-field fan noise formulation (2.37) combined with the BEM model computed in Virtual Lab. [59]. The continuous line represents the near-field tonal fan noise formulation combined with the image model, summing the primary and image sources. A very good agreement is observed between the analytical and numerical approaches. It is also seen that the effect of the free edges is negligible, and the infinite plate assumption can be made for the current plate at the given frequency.

The acoustic field of the fan operating in the vicinity of a large rigid flat plate is shown to be predicted accurately with an exact analytical solution, replacing the numerical mesh with an image fan. However, the image method can be applied to a very limited number of scattering applications. For relatively more complex geometries, other analytical methods have to be considered.

3.5. Scattering by a Rigid Corner

The solution of the diffraction of sound waves by a rigid wedge is a more complex problem to deal with compared to the reflection by a large flat plate. An exact analytical solution is possible using the image sources for limited wedge angles, ϕ. When the wedge index,

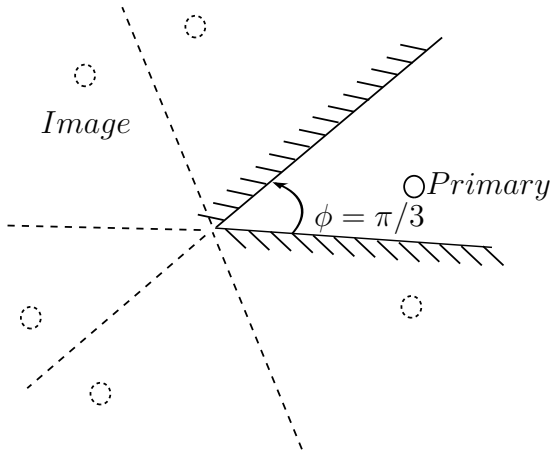

Figure 3.12.: Sketch of the $\phi = \pi/3$ wedge with 5 image sources.

$v_\phi = \pi/\phi$, is an integer and for angles making $v_\phi > 1/2$, it is possible to replace the wedge with $2v_\phi - 1$ image sources [101].

Figure 3.12 shows a sketch of the wedge with the angle $\phi = \pi/3$. The walls can then be changed with $2 \cdot \pi/\phi - 1 = 5$ image sources. The total acoustic pressure is now equal to the summation of the original and the 5 image sources.

A comparison is performed with a monopole located inside a wedge whose apex angle is $\phi = \pi/3$. Table 3.5 shows the positions of the primary source and the image monopoles. ϕ and ϕ_s represent the wedge angle and the source angle, respectively. r_s is the distance to the wedge center. For a monopole, the source and image monopoles have the same phase as seen in Figure 3.9. However, for a dipole source, an additional column for the phase is needed to be included since the orientation of the dipole is required to be taken into account.

Acoustic wave scattering by a rigid wedge is solved with both the image principle and the BEM approach using LMS software Virtual Lab. In the BEM model, the wedge is represented with an acoustic mesh containing 7200 acoustic elements. The field points are located on a circle which is defined from the wedge center with a radius of 3λ, at $f = 1000$ Hz. The source is located at $r_s = 1.5\lambda$ and $\phi_s = \pi/8$. The monopole strength is selected as $q_s = 0.01 + \mathrm{i}0.01 kg/s^2$.

Figure 3.13 shows the directivity of the acoustic field of a point monopole scattered by a $\phi = \pi/3$ wedge. The primary and image sources are sketched as plain and dashed circles, respectively. The plain and symbols represent the BEM model and the image model, respectively. A fair agreement is observed when comparing analytical and numerical directivity

Table 3.1.: Position of the Source and Image monopoles

Name	**Radius**	**Angle**	**Strength**
Primary	r_s	ϕ_s	q_s
Image1	r_s	$2\phi - \phi_s$	q_s
Image2	r_s	$2\phi + \phi_s$	q_s
Image3	r_s	$4\phi - \phi_s$	q_s
Image4	r_s	$4\phi + \phi_s$	q_s
Image5	r_s	$2\pi - \phi_s$	q_s

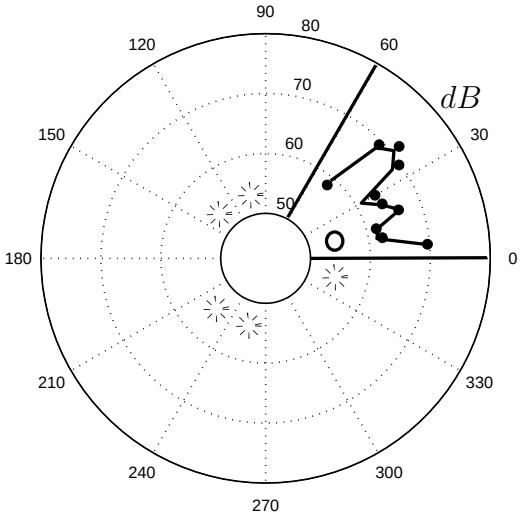

Figure 3.13.: Directivity of a monopole located nearby a $\phi = \pi/3$ wedge at $f = 1000$ Hz; source located at $r_s = 1.5\lambda$ and $\phi_s = \pi/8$, with observer radius of 3λ.

predictions. The differences up to 2 dB between both methods are attributed to effects of the free-edges for the finite wedge geometry considered in the BEM model. The test shows that the source-wedge problem can be easily handled with the image source model. However the image method is limited with certain wedge angles. For the corner case, the wedge index is not an integer, $v_\phi = \pi/(3 \cdot \pi/2) = 2/3$. Therefore, the image method is not applicable anymore.

Another analytical approach proposed here is to treat the scattering problem as a boundary-value problem. A Green's function is derived for the Helmholtz equation with the proper boundary conditions. The derivation must satisfy the rigid-wall boundary condition on the wedge surface and Sommerfeld radiation condition at large distances from the source. The Green's function of the Helmholtz equation around a wedge has been derived first by MacDonald [83]. Spherical coordinates are used in the derivation. As seen in Figure 3.14, the source and observer coordinates are (r_s, ϕ_s, θ_s) and (r_o, ϕ_o, θ_o), respectively. Initial Macdonald's formulation assumed that the source is located in the mid-plane of the rigid wedge, making $\theta_s = \pi/2$.

The Green's function of a wedge with an apex angle ϕ is

$$\begin{aligned} G(\mathbf{r}_s, \mathbf{r}_o) =& \frac{2\pi}{\phi} \sum_{k=0}^{\infty} \sum_{m=0}^{\infty} \varepsilon 2^{m'} (2m' + 4k + 1) \mathrm{e}^{(m'+2k+\frac{1}{2})\frac{1}{2}\pi \mathrm{i}} r_o^{-\frac{1}{2}} r_s^{-\frac{1}{2}} J_{m'+2k+\frac{1}{2}}(\kappa r_<) \\ & K_{m'+2k+\frac{1}{2}}(\mathrm{i}\kappa r_>) \cos(k\pi) \frac{\Pi(m' + k - 1/2)}{\Pi(k)\Pi(-1/2)} P_{m'+2k}^{-m'}(\mu) \cos(\frac{m\pi\phi_o}{\phi}) \cos(\frac{m\pi\phi_s}{\phi}) \end{aligned} \tag{3.17}$$

where ε is 1 for $m = 0$ and 2 for $m > 1$ [101]. $0 < \phi < 2\pi$ and $m' = m\pi/\phi$. $P_{m'+2k}^{-m'}$ stands for the general Legendre functions. J_ν is the Bessel function of the first kind and of order ν. K_ν is the modified Bessel function. Corresponding expressions with $r_>$ and $r_<$ interchange with

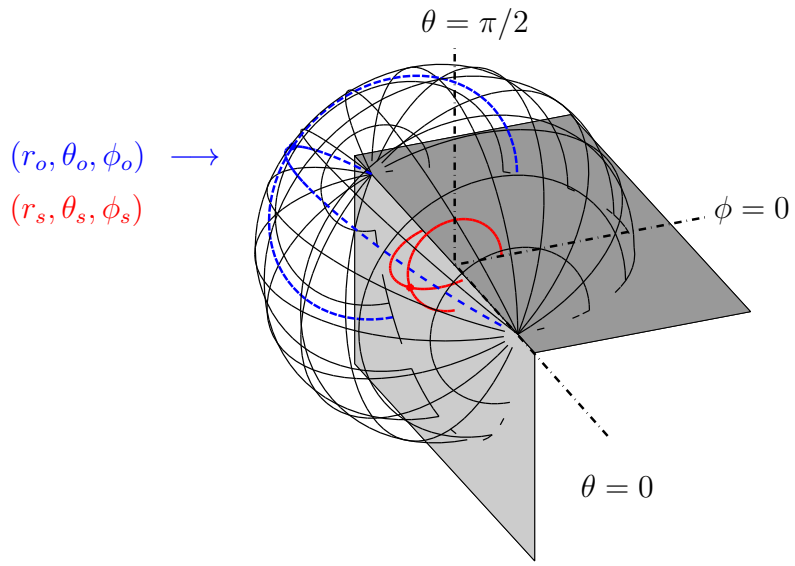

Figure 3.14.: Sketch of the wedge, source and observer positions defined in spherical coordinates

the definition of the source and observer positions, $r_> = max(r_s, r_o)$ and $r_< = min(r_s, r_o)$. κ is equal to $2\pi/\lambda$.

Mel'nik and Podlipenko [84] also proposed an expression for the scattering by a wedge with soft walls for arbitrary source locations, as

$$G(\mathbf{r}_s, \mathbf{r}_o) = \frac{\mathrm{i}\kappa}{\phi} \sum_{m=1}^{\infty} \sin(m'\phi_s) \sin(m'\phi_o) \sum_{n=0}^{\infty} (2(n+m')+1) \frac{\Gamma(n+2m'+1)}{\Gamma(n+1)} \\ P_{m'+n}^{-m'}(cos\theta_s) P_{m'+n}^{-m'}(cos\theta_o) j_{m'+n}(\kappa r_<) h_{m'+n}^{(1)}(\kappa r_>) \tag{3.18}$$

where j_ν and $h_\nu^{(1)}$ are the spherical Bessel and Hankel functions of the first kind and of order ν, respectively. The spherical functions are related to the cylindrical Bessel, J_ν, and Hankel, H_ν, functions via

$$j_{m'+n}(\kappa r_<) = \sqrt{\frac{\pi}{2\kappa r_<}} J_{m'+n+1/2}(\kappa r_<) \tag{3.19}$$

$$h_{m'+n}^{(1)}(\kappa r_>) = \sqrt{\frac{\pi}{2\kappa r_>}} H_{m'+n+1/2}^{(1)}(\kappa r_>). \tag{3.20}$$

The definition of the Green's function according to MacDonald starts from a free-field radiation expressed as $\mathrm{e}^{\mathrm{i}(\omega t - kR)}/R$ which does not involve the factor 4π in the denominator. This and a different choice of the convention for the Fourier transform in Mel'nik and Podlipenko's model explains the complex conjugate and the different amplitude between two approaches. It must be noted that the Hankel function of the first kind ensures outgoing waves if the time dependence is assumed as $\mathrm{e}^{-\mathrm{i}\omega t}$ [129].

Formulation (3.18) considers the scattered field by soft boundary surfaces whereas formulation (3.17) is derived for the hard boundary surfaces. Hence, the Green's function satisfying the condition of normal derivatives at the boundaries relevant for a wedge with rigid walls, is obtained by changing the *sine* functions for *cosine*s as in Equation (3.17).

Combining both derivations, the Green's function of a rigid wedge for arbitrary source and observer positions then becomes

$$G(\mathbf{r}_s, \mathbf{r}_o) = \frac{-\pi \mathrm{i}}{4\phi\sqrt{r_s r_o}} \sum_{m=0}^{\infty} \varepsilon \cos(m'\phi_s)\cos(m'\phi_o) \sum_{k=0}^{\infty} (2m' + 4k + 1) \frac{\Gamma(2m' + 2k + 1)}{\Gamma(2k+1)} \\ P^{-m'}_{m'+2k}(\cos\theta_s) P^{-m'}_{m'+2k}(\cos\theta_o) J_{m'+2k+1/2}(\kappa r_<) H^{(1)}_{m'+2k+1/2}(\kappa r_>). \tag{3.21}$$

The geometrical expansion of the Legendre function $P^{m'}_{m'+k}(\cos\theta)$ [1]

$$P^{-m'}_{m'+2k}(\cos\theta) = \frac{2^{1-m'}(\sin\theta)^{-m'}}{\sqrt{\pi}\Gamma(1/2 - m')} \sum_{n=0}^{\infty} \frac{\Gamma(n + 1/2 - m')\Gamma(2k + n + 1)}{\Gamma(n+1)\Gamma(2k + n + m' + 3/2)} \sin[(2n+1+k)\theta] \tag{3.22}$$

is used for the computations.

Formulation (3.21) is a general solution for acoustic diffraction by a wedge. Replacing the wedge angle ϕ with $3\pi/2$ gives the specific case of a corner. Equation (3.21) then becomes

$$G(\mathbf{r}_s, \mathbf{r}_o) = \frac{-\mathrm{i}}{6\sqrt{r_s r_o}} \sum_{m=0}^{\infty} \varepsilon \ \cos(2m\phi_s/3)\cos(2m\phi_o/3) \sum_{k=0}^{\infty} (4m/3 + 4k + 1) \frac{\Gamma(4m/3 + 2k + 1)}{\Gamma(2k+1)} \\ P^{-2m/3}_{2m/3+2k}(\cos\theta_s) P^{-2m/3}_{2m/3+2k}(\cos\theta_o) J_{2m/3+2k+1/2}(\kappa r_<) H^{(1)}_{2m/3+2k+1/2}(\kappa r_>). \tag{3.23}$$

with

$$P^{-2m/3}_{2m/3+2k}(\cos\theta) = \frac{2^{1-2m/3}(\sin\theta)^{-2m/3}}{\sqrt{\pi}\Gamma(1/2 - 2m/3)} \\ \sum_{n=0}^{\infty} \frac{\Gamma(n + 1/2 - 2m/3)\Gamma(2k + n + 1)}{\Gamma(n+1)\Gamma(2k + n + m' + 3/2)} \sin[(2n + 1 + k)\theta]. \tag{3.24}$$

In the implementations of Equation (3.23), a number of terms included in the series must be decided. It is observed that the series converge easily for any observer positions but for the ones where $\lim |r_s - r_o| \to 0$. The multiplication of the Bessel and Hankel functions does not converge for the observer radii close to the source radius. This was avoided using a first order interpolation between two observer locations $|r_s - r_o| = \epsilon$, where ϵ is an arbitrarily small number.

Equation (3.23) is the exact solution for the acoustic waves scattered by a sharp rigid corner. It was also shown by Crighton, that the rigid corner theory remains unchanged if the corner is smoothed out over any distance that is small compared to the wavelength at the frequency of interest [32]. Formulation (3.23) will then be used to predict the scattered acoustic field of sources located near a rigid corner. For simplicity, a point monopole located on a corner will be investigated first. The theory will then be extended to a point dipole and finally it will be applied to a source representative of a fan.

3.5.1. Scattered-field of a monopole

Once the Green's function is derived for a particular geometry, the acoustic field can then be computed for harmonic sources. The acoustic field of a point monopole located next to a rigid corner is investigated first, knowing that the total acoustic field of a monopole is equal to

$$p(\omega, r) = G(\mathbf{r}_s, \mathbf{r}_o)q(\omega) \tag{3.25}$$

where $q(\omega)$ is the source strength of the point monopole.

In order to compute the scattered acoustic field, a point monopole is located $(1.5\lambda, \pi/2, \pi/16)$ with respect to the origin of the rigid corner. The frequency is selected as $f = 10$ kHz. Figure 3.15 shows instantaneous snapshots of the real part of the Green's function for arbitrary source strength. The motion of the wave patterns is obtained by the multiplication with the factor $\mathrm{e}^{-\mathrm{i}\omega t}$. Different plots refer to different propagation times. The illuminated and shadow zones can be seen clearly in the figure, the intermediate grey standing for the zero fluctuation. In particular, sound extinction is found here along an oblique direction, due to interference between the direct and scattered fields.

A second test is performed in order to check the accuracy of the analytical method. As mentioned above, the BEM theory is able to handle scattered field problems for unbounded domains. The same monopole-corner problem can therefore be solved with the BEM approach. A similar source-corner configuration is used. However, since BEM requires at least 10 elements per wavelength, in order to solve the problem in a reasonable time, the computations are performed at lower frequencies. Two frequencies are then tested, 500 Hz and 1 kHz. The harmonic monopole source is located at $(0.75\lambda, \pi/2, \pi/16)$ at $f = 500$ Hz with a strength of $q(\omega) = (0.01 + \mathrm{i}0.01)kg/s^2$.

In order to minimize the effects of the free edges, a corner is built by associating two $7\lambda \times 7\lambda$ flat plates at $f = 500$ Hz in the BEM model. Total number of acoustic elements is then equal to 7200. The size of the quadrilateral elements, $l \approx 0.06\lambda$, is satisfying the BEM criteria mentioned above [34].

Figure 3.16 shows the directivities of the monopole-corner configurations at both frequencies. The radius of the field point mesh is selected as 3λ at $f = 1$ kHz. The sound pressure levels are plotted in dBs. Analytical and BEM results are represented as lines and symbols, respectively. A very good agreement is observed at both frequencies. The difference for all the directions is less than 1 dB. It may be related to the scattering of the waves from the free edges of the acoustic mesh.

It appears that the scattered field of a point monopole by a rigid infinite corner can be computed accurately with the analytical model. Multiple monopoles can be summed up if needed. However, for a point dipole, a specific development is more appropriate, derived in the following section.

3.5.2. Scattered-field of a dipole

The theory can be extended to a point dipole using the same Green's function defined above. The radiation field of a point dipole is related to the gradient of the Green's function with respect to the source coordinates:

$$p(\omega, r) = \nabla G(\mathbf{r}_s, \mathbf{r}_o) \cdot \mathbf{F}(\omega), \tag{3.26}$$

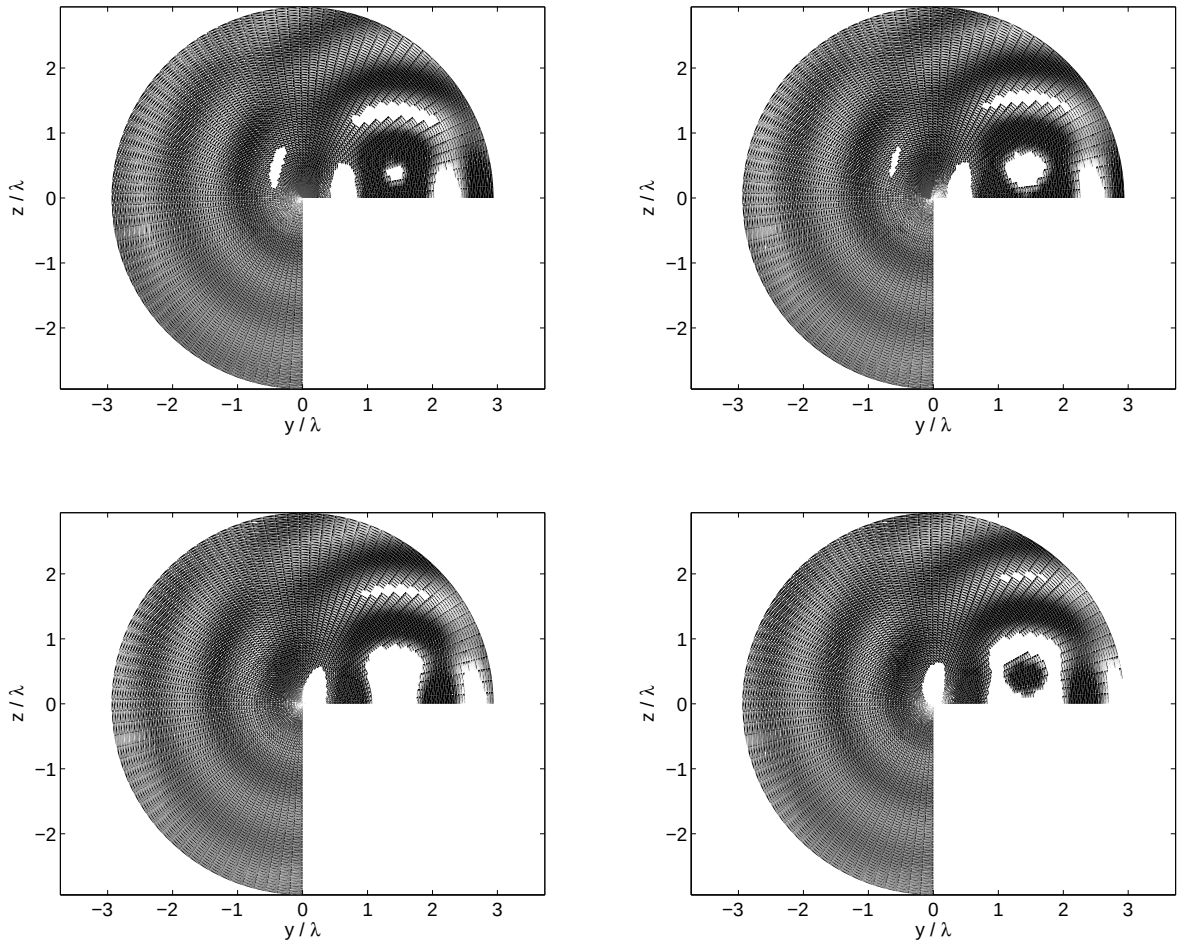

Figure 3.15.: Snapshots of the contour plots of the real part of the Green's function of a monopole nearby a rigid corner at $f = 10$ kHz. The monopole is located at $(1.5\lambda, \pi/2, \pi/16)$.

where $\mathbf{F}(\omega)$ is the source strength of the point dipole.

The gradient of the Green's function defined by Equation (3.21) is

$$\nabla G(\mathbf{r}_s, \mathbf{r}_o) = \left[\frac{\partial}{\partial r_s} \mathbf{e}_{r_s} + \frac{1}{r_s} \frac{\partial}{\partial \phi_s} \mathbf{e}_{\phi_s} + \frac{1}{r_s \sin\theta_s} \frac{\partial}{\partial \theta_s} \mathbf{e}_{\theta_s} \right] G(\mathbf{r}_s, \mathbf{r}_o). \tag{3.27}$$

The first component on the right hand side, $\partial G(\mathbf{r}_s, \mathbf{r}_o)/\partial r_s$ is

$$\begin{aligned} \frac{\partial G(\mathbf{r}_s, \mathbf{r}_o)}{\partial r_s} =& \frac{\pi \mathrm{i}}{4\phi\sqrt{r_o}} \sum_{m=0}^{\infty} \varepsilon \ \cos(m'\phi_s) \cos(m'\phi_o) \sum_{k=0}^{\infty} (2m' + 4k + 1) \\ & P_{m'+2k}^{-m'}(\cos\theta_s) P_{m'+2k}^{-m'}(\cos\theta_o) \frac{\partial}{\partial r_s} \left(\frac{-1}{\sqrt{r_s}} J_{m'+2k+1/2}(\kappa r_<) H_{m'+2k+1}^{(1)}(\kappa r_>) \right). \end{aligned} \tag{3.28}$$

Since the gradient is taken at the source position, two different expansions result depending

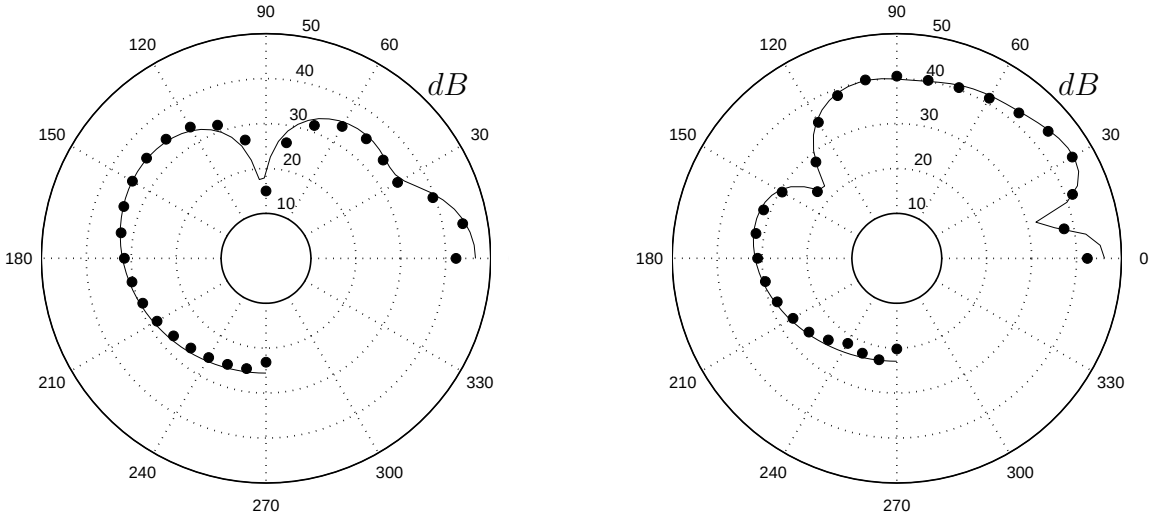

Figure 3.16.: Scattered-field directivity of a monopole by a rigid corner; analytical solution (line) and BEM results (symbols) at $f = 500$ Hz (left) and $f = 1$ kHz (right) for monopole position $(0.75\lambda, \pi/2, \pi/16)$ and observer distance 1.5λ at $f = 500$ Hz.

on the observer locations. For observer positions $r_s < r_o$, the last term on the RHS of the equation reads,

$$\frac{\partial}{\partial r_s}\left(\frac{-1}{\sqrt{r_s}} J_{m'+2k+1/2}(\kappa r_s) H^{(1)}_{m'+2k+1}(\kappa r_o)\right) = H^{(1)}_{m'+2k+1/2}(\kappa r_o)\frac{-1}{2\sqrt{r_s}} \left[\frac{-1}{r_s} J_{m'+2k+1/2}(\kappa r_s) + \kappa\big[J_{m'+2k-1/2}(\kappa r_s) - J_{m'+2k+3/2}(\kappa r_s)\big]\right]. \tag{3.29}$$

At other observer locations, where $r_s > r_o$ the derivative reads

$$\frac{\partial}{\partial r_s}\left(\frac{-1}{\sqrt{r_s}} J_{m'+2k+1/2}(\kappa r_o) H^{(1)}_{m'+2k+1}(\kappa r_s)\right) = J_{m'+2k+1/2}(\kappa r_o)\frac{-1}{\sqrt{r_s}} \left[\frac{-1}{r_s} H^{(1)}_{m'+2k+1/2}(\kappa r_s) + \kappa\big[\mathrm{i}\csc[(m'+2k+1/2)\pi](A_1 - A_2)\big]\right] \tag{3.30}$$

where A_1 and A_2 are defined as

$$\begin{aligned} A_1 &= \mathrm{e}^{-(m'+2k+1)\pi}\left(J_{m'+2k-1/2}(\kappa r_s) - J_{m'+2k+3/2}(\kappa r_s)\right) \\ A_2 &= J_{-m'-2k-3/2}(\kappa r_s) - J_{-m'-2k+1/2}(\kappa r_s). \end{aligned} \tag{3.31}$$

Taking the derivative in the ϕ_s direction, the second component of Equation (3.27) writes

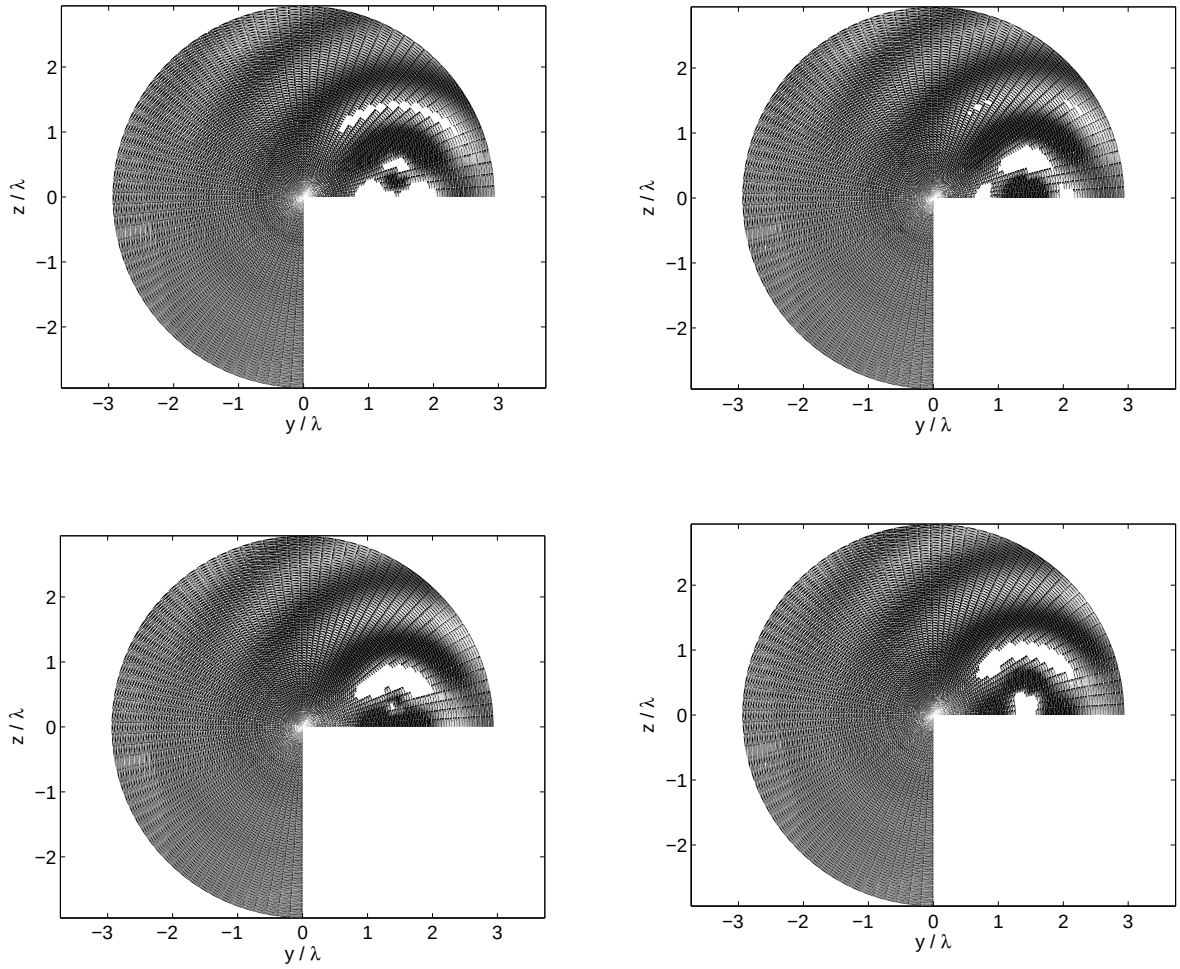

Figure 3.17.: Snapshots of the acoustic potential of a dipole nearby a rigid corner at $f = 10$ kHz. The dipole is located at $(1.5\lambda, \pi/2, \pi/16)$.

$$\frac{\partial G(\mathbf{r}_s, \mathbf{r}_o)}{\partial \phi_s} = \frac{-\pi \mathrm{i}}{4\phi\sqrt{r_s r_o}} \sum_{m=0}^{\infty} \varepsilon \ (-2m') \sin(m'\phi_s) \cos(m'\phi_o) \sum_{k=0}^{\infty} (2m' + 4k + 1) \\ P^{-m'}_{m'+2k}(\cos\theta_s) P^{-m'}_{m'+2k}(\cos\theta_o) J_{m'+2k+1/2}(\kappa r_<) H^{(1)}_{m'+2k+1}(\kappa r_>). \tag{3.32}$$

Finally, the $\partial/\partial\theta_s$ component of Equation (3.27) becomes

$$\frac{\partial G(\mathbf{r}_s, \mathbf{r}_o)}{\partial \theta_s} = \frac{-\pi \mathrm{i}}{4\phi\sqrt{r_s r_o}} \sum_{m=0}^{\infty} \varepsilon \ \cos(m'\phi_s) \cos(m'\phi_o) \sum_{k=0}^{\infty} (2m' + 4k + 1) \\ P^{-m'}_{m'+2k}(\cos\theta_o) J_{m'+2k+1/2}(\kappa r_<) H^{(1)}_{m'+2k+1}(\kappa r_>) \frac{\partial}{\partial \phi_s} \left(P^{-m'}_{m'+2k}(\cos\theta_s) \right) \tag{3.33}$$

where the derivative of the trigonometric Legendre function writes

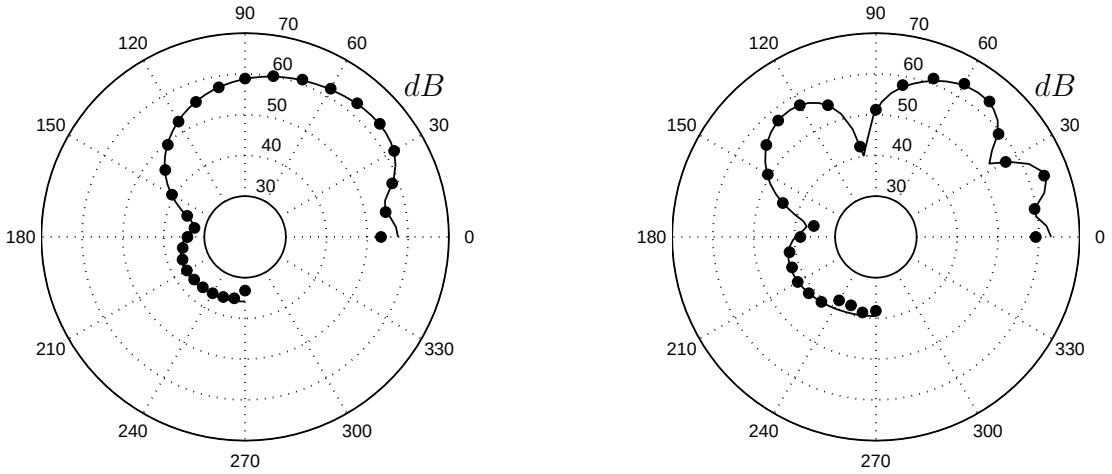

Figure 3.18.: Scattered-field directivity of a dipole by a rigid corner; analytical solution (line) and BEM results (symbols) at $f = 500$ Hz (left) and $f = 1$ kHz (right) for dipole position $(0.75\lambda, \pi/2, \pi/16)$ perpendicular to $\phi = 0$ plane and observer distance 1.5λ at $f = 500$ Hz.

$$\frac{\partial}{\partial\theta_s}\left(P^{-m'}_{m'+2k}(\cos\theta_s)\right) = \frac{2^{1-m'}(\sin\theta_s)^{-m'}}{\sqrt{\pi}\Gamma(1/2-m')} \sum_{n=0}^{\infty} \frac{\Gamma(k+1/2-m')\Gamma(k+n+1)}{\Gamma(k+1)\Gamma(k+n+m'+3/2)}\left(\cot\theta_s + (2n+k+1)\cos[(2n+1+k)\theta_s]\right). \tag{3.34}$$

Combining Equations (3.27) to (3.33), the scattered-field of a dipole by a rigid wedge for arbitrary positions of the source can be obtained. Replacing the wedge angle ϕ with $3\pi/2$ gives again the specific case of a corner. A test is performed using a point dipole located $(1.5\lambda, \pi/2, \pi/16)$ with respect to the origin of the rigid corner at $f = 10$ kHz. The dipole is perpendicular to $\phi = 0$ plane. A typical plot in the $\theta = \pi/2$ plane for the real part of the acoustic potential for a point dipole is seen in Figure 3.17. The dipole-like behavior and the shadow zones are clearly seen in the figure.

In order to check the accuracy of the predictions, the analytical solution is again compared to the numerical model. The comparison is performed as in the monopole case applying the same geometrical parameters in the BEM model. The monopole is just replaced with the perpendicular dipole. The force strength of the dipole is selected as $F_z(\omega) = (0.01 + 0.01\mathrm{i})\mathrm{N}$.

Figure 3.18 shows the corresponding directivity patterns at two frequencies, $f = 500$Hz and $f = 1$kHz. A good agreement is again observed in comparison with the analytical and numerical solutions. The directivity lobes are captured accurately even for a relatively complex directivity. At both frequencies, the difference between the analytical and numerical results is less than 1 dB.

Now validated for a single dipole, the theory can be extended to a fan source introducing the modal structure of tonal fan noise.

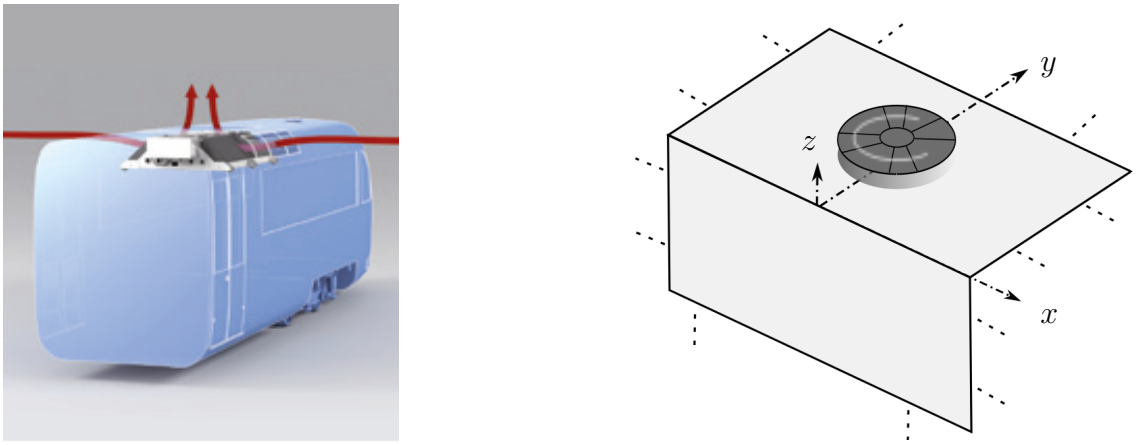

Figure 3.19.: A possible application of the scattered field of tonal fan noise by a rigid corner (left), cooling unit located at the roof of a locomotive [131]. Sketch of the fan-corner configuration, fan operating parallel to the xy-plane (right).

3.5.3. Scattered-field of fan noise

The methods addressing the free-field tonal fan noise mentioned in Chapter 2 are based on the formalism of a rotating dipole which leads to closed form expressions [40, 47, 108]. Introducing the gradient of the Green's function defined above instead of the free-field one, it is not possible anymore to find a closed-form solution expression for the scattered acoustic field of a fan operating next to a rigid corner. However, in order to simulate the rotation of fan source, a circular distribution of phase shifted dipoles can be used as derived in Section 3.5.2.

Introducing Equation (3.26) into Equation (2.44), the total acoustic pressure field of the fan scattered by a rigid corner reads

$$p(\omega, r) = \sum_{N_{dipo}} \nabla G(\mathbf{r}_s(\beta), \mathbf{r}_o) \cdot F(\omega, \beta). \tag{3.35}$$

Since the Green's function of a rigid corner is extended for arbitrary positions of the source with respect to the wedge origin, it can be used for any point dipole of the circular array.

Equation (3.35) is a general solution for a fan operating in the vicinity of a rigid corner. It can therefore be used for different fan-corner configurations. One of the possible application areas is the cooling units of locomotives in parking position (see Figure 3.19 (left)). The noise generated by the cooling unit located on the top of the locomotive and scattered by the corner of the body may result in annoyance for the passengers waiting on the platform. In view of the dimensions and wavelength of interest, the complimentary corner and the front and back ends of the locomotive can be ignored for a first assessment.

The problem is first simplified to a fan operating parallel to a flat surface. Neglecting the scattering by the installation effects such as the presence of any inlet or outlet duct, only the scattering by the corner of the locomotive is addressed. Figure 3.19 (right) shows the sketch of the problem. Only one side of the locomotive is considered for the illustration.

For the benchmark validation case, the artificial low-speed axial fan sources defined in the Section 3.4 are used. The blades are assumed acoustically compact and reduced to point dipoles. The equivalence with a circular array of stationary dipoles is used instead of the rotating dipole formulation [88, 70].

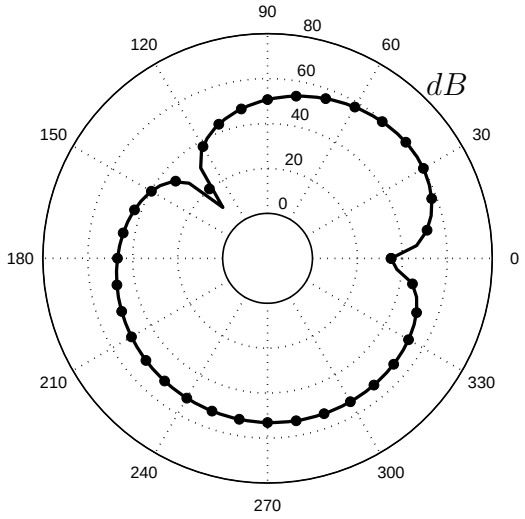

Figure 3.20.: Free-field directivity of tonal fan noise at $f = 500$ Hz at $r = 1.5\lambda$ in the yz-plane; near-field formulation (2.37) and expression (2.44). The fan center is located at $(0.75\lambda, \pi/12, \pi/2)$.

Since the analytical scattered-field model is based on the circular oriented phase shifted dipoles rather than the rotating dipole model, a first test is performed in free-field to determine the number of point dipoles needed for an accurate prediction. Figure 3.20 shows the comparison in free field at the first BPF, $f = 500$ Hz. The observer and source positions are defined with respect to the origin of the corner for consistency, however the scattering effects of the corner are not taken into account. The observers are located at 1.5λ away from the origin of the corner in the yz-plane. The radius of the fan, the distance between the rotation center and the center of the blade surface, is selected as 0.33λ. The center of the fan is located at $(0.75\lambda, \pi/12, \pi/2)$. The continuous line represents the field of the array of 128 phase shifted dipoles whereas symbols represent the near-field formulation (2.37). It is seen that using 128 phase shifted dipoles can capture the sound radiation accurately, hence they are used in the following analytical tests.

Once the number of dipoles in the array is determined, Equation (3.35) can be employed to predict the scattered field of the fan-corner configuration. Two fan source distributions are tested for the validation of the analytical model [70]. The first one (test1) contains only the thrust force component, whereas the second one (test2) contains both drag and thrust force components as in the industrial axial fans in use [108]. The orientation of fans and observers is the same as defined in the free-field comparison. The problem is also dealt with the numerical approach. The same acoustic BEM mesh and field points are used as in the dipole test case for the BEM formulation.

The scattered-field directivities are seen at the first BPF in Figure 3.21. The left and right plots show the scattered field of the first and the second source distributions where lines and symbols represent the numerical and analytical results, respectively. A very good agreement is found in both cases. The difference is again less than 1 dB. It is also seen that adding the drag component to the fan source results in higher acoustic pressure levels in the shadow

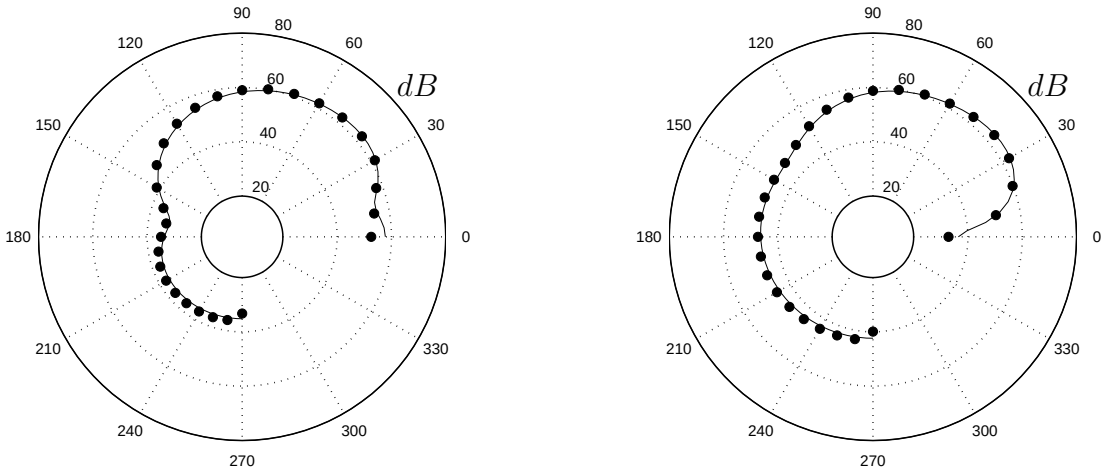

Figure 3.21.: Scattered-field directivity of a fan operating parallel to the xy-plane of a rigid corner; analytical solution (line) and BEM results (symbols) for test1 (left) and test2 (right). The fan center is located at $(0.75\lambda, \pi/2, \pi/12)$ with a radius of 0.33λ. Observers are in the yz-plane with a radius of 3λ, at the first BPF, $f = 500$ Hz.

zone.

Another configuration is encountered with the small wind turbines installed on the roof of a building (see Figure 3.22 (left)). Now the rotation axis is perpendicular to the xy-plane. A sketch of the problem is shown in Figure 3.22 (right). The problem can be dealt with the model described above only considering a new orientation of the fan.

The same benchmark fan source distributions, one with only thrust and one with trust and drag forces, are again selected for the comparison. However, the rotation center is now located at $(0.75\lambda, \pi/2, \pi/12)$ and the fan is operating parallel to the xz-plane. Figure 3.23 shows the directivity patterns. The left and right plots show the first and second tests, respectively. The line and symbols again represent the analytical and BEM predictions, respectively. A very good agreement is again observed. It is seen that adding the drag forces affects the acoustic field around the rotation plane. The effect of the drag forces are up to 20 dB for the given observer locations. It is also seen that for the first test, the dipole-like directivity is captured accurately with the analytical model.

Finally, the analytical model proposed to compute the scattered field of tonal fan noise operating close to a rigid corner is validated against numerical simulations in all tested configurations. As a result, extending the Green's function for arbitrary source positions and combining its gradient with the dipole array model, the scattered field of a low-speed axial fan by a rigid corner is captured accurately. For high frequency problems, where the numerical methods are computationally demanding, the analytical solution can be useful irrespective of any mesh resolution issues.

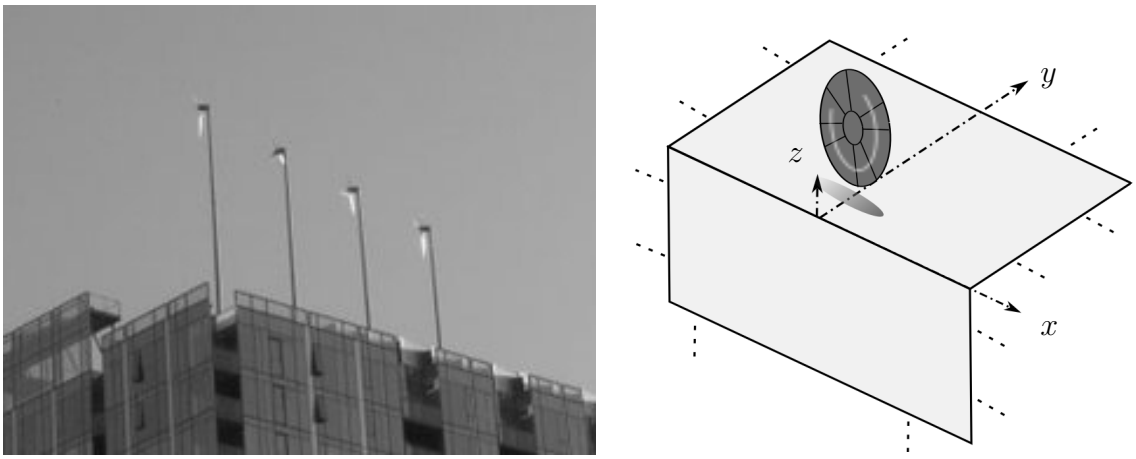

Figure 3.22.: Possible application of the scattered field of tonal fan noise by the rigid corner (left), small wind turbine operating on the roof of a building, photo taken at 17th AIAA/CEAS Aeroacoustics Conference, Portland. Sketch of the fan-corner configuration, fan operating parallel to the xz-plane (right).

3.6. Conclusion

The scattering of the tonal noise generated by a low-speed axial fan has been investigated numerically and analytically. Good agreement is observed in all benchmark validation cases. The effect of near-field terms in the description of the incident field of primary sources is found crucial if the scattering is due to surfaces that are very close to the sources.

On one hand, the numerical approach can be applied to more complex geometries for

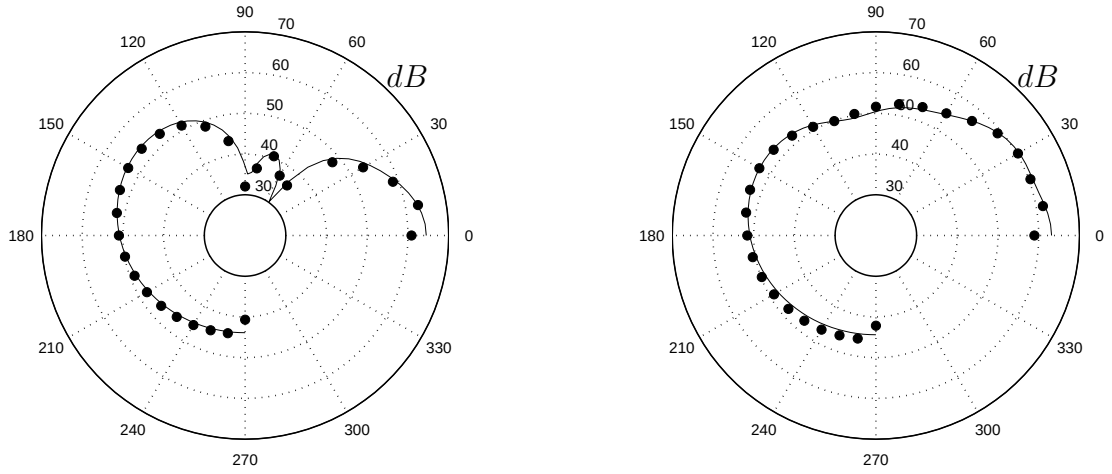

Figure 3.23.: Scattered-field directivity of a fan operating parallel to the xz-plane by the rigid corner: analytical model (line) and BEM results (symbols) for test1 (left) and test2 (right). The fan center is located at $(0.75\lambda, \pi/2, \pi/12)$ with radius 0.33λ. Observers are on the yz-plane with 3λ radius, for the first BPF, $f = 500$ Hz

bounded and unbounded domains. On the other hand, where the numerical methods are computationally demanding, analytical methods can be useful, for relatively simple configurations.

An analytical method combined with non-closed form fan source formalism is proposed in order to compute the scattered acoustic field of a fan by a rigid corner. A very good agreement is obtained in comparison with the numerical solution for different applications.

Only the tonal component of fan noise was addressed in this Chapter. Following chapters will address the broadband noise generated by low-speed axial fans and its scattered field.

Chapter 4.

Free-Field Broadband Fan Noise

Previous chapters dealt with the tonal noise generated by low-speed axial fans and its scattering by obstacles. In case of presence of periodic forces acting on blades, due to upstream guide vanes for example, the noise is generated at the blade passing frequency and harmonics [47, 125]. Besides periodic forces, there may be additional non-periodic forces acting on the blade surface due to turbulence associated with installation effects or blade geometry [86]. Since the source field is random, acoustic response of the fan results in a broadband spectrum rather than a discrete one. A brief scheme about the broadband fan noise source mechanisms was given in Figure 1.1. Only the turbulence interaction noise is addressed in this chapter.

Several approaches, ranging from semi-empirical methods [16] to highly accurate and CPU intensive transient CFD calculations [23, 127] have been proposed to address this problem. Curle [33] extended the pioneering theory of Lighthill [73] on turbulence noise for applications with the presence of solid and stationary surfaces in the flow. Using experimental [114] or computational source field [25], the acoustic field radiated by equivalent dipoles on the surface can then be predicted [128].

Amiet's theory is a well known approach to compute the broadband acoustic field of a stationary airfoil located in turbulent stream [5]. It is a semi-analytical approach to predict the sound level. It is also a hybrid approach and requires the definition of the source-field based on numerical or experimental resolution of the flow disturbances. Although it is widely used in literature [118, 19, 38], Amiet's theory includes some limitations and assumptions in order to deal with the problem in an analytical perspective.

First, the airfoil is simplified to a flat-plate, hence effects of shape, camber and thickness are neglected. The effect of complex shapes of a blade is investigated considering spanwise splitting and parallelogram profiles, for Contra-Rotating Open Rotor applications for example [110]. Other investigations addressing the camber and thickness effects are also found in literature [112, 87].

A second assumption made is on the distance of the observer to the airfoil with respect to the acoustic wavelength at the frequency of interest and spanwise and chordwise extents of the corresponding airfoil. The former, as mentioned in Chapter 2, is dealing with the acoustic near-field effects. In the derivations of Amiet [5], the observer is assumed to be located in the acoustic far-field of the airfoil so that an analytical solution can be obtained. Other two assumptions concern the geometrical near-field of the airfoil. For free-field prediction, where the observer is located far away from the airfoil compared to its span-length, cord-length or the wavelength at the frequency of interest, these approximations are assumed to be valid. However, for free-field predictions where the observer is located close to the airfoil for the given parameters or for scattering problems where the obstacle is located in the near-field of the fan, even if the microphone is located in the far-field, the far-field assumption becomes invalid. This chapter addresses an intermediate level of near-field extension to the theory

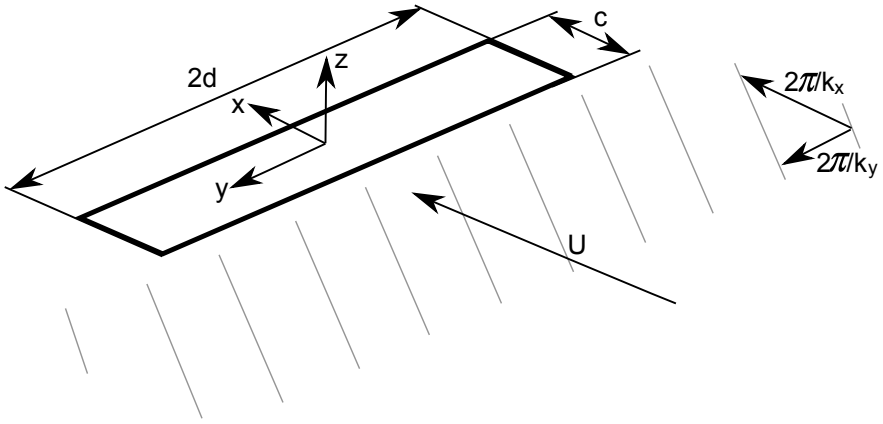

Figure 4.1.: Sketch of the skewed gust impinging to the linearized airfoil.

[64].

Another assumption is that the flow impinging into the airfoil is uniform in the spanwise direction. However, in many industrial applications such as axial fans or helicopter rotors, the airfoil or the blade is subjected to spanwise varying flow conditions. The application of the theory to spanwise varying flow conditions is also investigated in this chapter using different techniques [38, 26, 65].

The last extension of the theory is introducing the rotating motion. Using the far-field approximation of stationary airfoils [5], the rotating motion is taken into account by Paterson and Amiet [98] in order to apply the theory to helicopter blades.

4.1. Generalization of the Semi-Analytical Model

In order to predict the acoustic field of the turbulence-interaction noise, a stationary airfoil of span $2d$ and chord $c = 2b$ is considered in a turbulent stream. Figure 4.1 shows a sketch of an airfoil swept by a single skewed gust. The mean velocity of the turbulent fluid flow is U. The origin of the coordinates is at the center of the airfoil. The x-axis is in the streamwise direction. The y and z-axes are aligned with the spanwise and the crosswise directions, respectively. The wavenumbers k_x and k_y represent chordwise and spanwise Fourier components of the frozen turbulence. As mentioned above, the airfoil is assumed with zero thickness within the scope of a linearized theory, hence the crosswise component of the turbulence k_z is not considered.

The acoustic response of an airfoil subjected to incoming turbulence involves the radiation of distributed dipoles on the airfoil surface. The source and observer coordinates are defined as (x, y, z) and (x_0, y_0), respectively as seen in Figure 4.2.

In presence of a fluid flow in the acoustic radiation field, acoustic waves are affected by convection. Since the airfoil is located in a turbulent stream, the convection needs being taken into account for the turbulence-interaction noise prediction. The propagation distance between the source and the observer is not the linear distance but a corrected distance including the convection effects. Figure 4.3 shows the relation between the convection and the corrected distance term. The source and the observer coordinates are again represented with, $\mathbf{x}$ and $\mathbf{x}_0$, respectively. The linear distance between the source and the observer is equal to $R = |\mathbf{x} - \mathbf{x}_0|$. However, due to the convective flow with the velocity, U, the observer

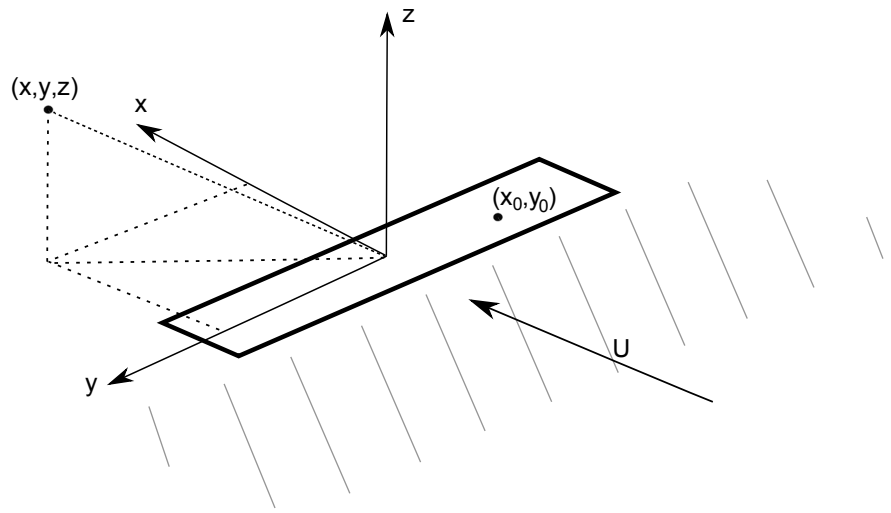

Figure 4.2.: Sketch of the source and observer positions for the flat-plate airfoil planform.

receives the waves which would be received at $\mathbf{x}'$ if there was no convective fluid flow [107]. The distance between $\mathbf{x}'$ and $\mathbf{x}$ is where the sound waves propagated with the convective flow, $|\mathbf{x}-\mathbf{x}'| = U(t_r - t_e)$. t_r and t_e are the reception and emission times of the sound waves, respectively. The difference $\Delta t = t_r - t_e$ is then the time passed during the sound waves travel from $\mathbf{x}_0$ to $\mathbf{x}'$, $\Delta t = \sigma/c_0$. c_0 is the speed of sound. The effect of convection then applies to $|\mathbf{x} - \mathbf{x}'|$ as

$$|\mathbf{x} - \mathbf{x}'| = U(t_r - t_e) = U\frac{\sigma}{c_0} = M\sigma. \tag{4.1}$$

The corrected distance with respect to the source for a convective flow on x-direction is then $((x - x_0) - M\sigma, y - y_0, z)$.

The amplitude of the source-observer distance is thus equal to

$$\sigma = (\sigma_0 - M(x - x_0))/\beta^2 \tag{4.2}$$

with

$$\sigma_0 = \sqrt{(x - x_0)^2 + \beta^2(y - y_0)^2 + \beta^2 z^2}. \tag{4.3}$$

β is the compressibility factor, $\beta = \sqrt{1 - M^2}$.

The acoustic pressure generated by each point dipole located on the linearized airfoil is defined as [33, 42]

$$p(x, y, z, \omega; x_0, y_0) = \frac{\mathrm{i}\omega\mathbf{x} \cdot F(x_0, y_0)\,\mathrm{e}^{\mathrm{i}\omega t}}{4\pi c_0 \sigma_0^2}\,\mathrm{e}^{-\mathrm{i}\omega\sigma/c_0}\left(1 + \frac{1}{\mathrm{i}k\sigma_0}\right). \tag{4.4}$$

$F\,\mathrm{e}^{\mathrm{i}\omega t}$ is the force strength of the dipole. The strength of the wall-normal dipole, or so called the lift component, is obtained from the distribution of the pressure jump across the airfoil [97]. Since the airfoil is assumed to be linearized, the $\mathbf{x} \cdot F(x_0, y_0)\mathrm{e}^{\mathrm{i}\omega t}$ term can be replaced with $zq(x_0, y_0)\,\mathrm{e}^{\mathrm{i}\omega t}$, where q is the lift component of the dipole strength.

The term $(ik\sigma_0)^{-1}$ on the right hand side of Equation (4.4) stands for the acoustic near-field contribution. As mentioned in Chapter 2, this term becomes significant where the observer is close to the source compared to the wavelength at the frequency of interest. At larger values of the source-observer distances, it becomes negligible [64].

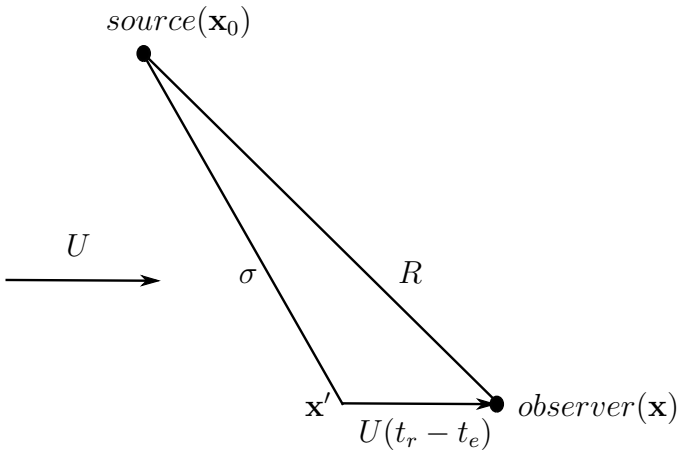

Figure 4.3.: Effect of the convection

The total acoustic pressure field of the airfoil is obtained by integrating the dipole sources on the airfoil surface

$$p(x,y,z,\omega;x_0,y_0) = \int_{-d}^{d}\int_{-c/2}^{c/2} \frac{\mathrm{i}\omega z q(x_0,y_0)\,\mathrm{e}^{\mathrm{i}\omega t}}{4\pi c_0 \sigma_0^2} \mathrm{e}^{-\mathrm{i}\omega\sigma/c_0}\left(1+\frac{1}{\mathrm{i}k\sigma_0}\right)\,\mathrm{d}x_0\mathrm{d}y_0. \tag{4.5}$$

Since turbulence is a random process rather than deterministic [55], it is necessary to work with statistic quantities such as the cross-Power Spectral Density (PSD) rather than deterministic quantities such as the time history of the pressure jump at a source point [5]. The PSD of the sound field at the observer position is obtained by multiplying the acoustic pressure by its complex conjugate, as

$$\begin{aligned} S_{pp}(x,y,z,\omega;x_0,y_0) = \iint_{-d}^{d}\iint_{-c/2}^{c/2} \left(\frac{\omega z}{4\pi c_0}\right)^2 \frac{1}{\sigma_0^2\,\sigma_0'^2} S_{qq}(\omega;x_0,x_0')\mathrm{e}^{-\mathrm{i}\omega(\sigma-\sigma')/c_0} \\ \left(1+\frac{1}{\mathrm{i}k\sigma_0}\right)\left(1+\frac{1}{\mathrm{i}k\sigma_0'}\right)^{*}\,\mathrm{d}x_0\mathrm{d}x_0'\mathrm{d}y_0\mathrm{d}y_0'. \end{aligned} \tag{4.6}$$

The superscript * represents the complex conjugate of the operator. The term S_{qq} is the cross-PSD of the pressure jump at two points on the airfoil surface. It is linked to the incoming gust with the transfer function, $g(x_0,k_x,k_y)$ [5, 6, 7]. Considering a convective sinusoidal gust of the form

$$w_g = w_0 \mathrm{e}^{-\mathrm{i}[k_x(x_0-Ut)+k_y y_0]} \tag{4.7}$$

the pressure jump on the airfoil can be written as

$$q(x_0,y_0,t) = \Delta P(x_0,y_0,t) = 2\pi\rho_0 U w_0 g(x_0,k_x,k_y)\mathrm{e}^{-\mathrm{i}[k_x(x_0-Ut)+k_y y_0]}. \tag{4.8}$$

Accounting for all wavenumber components of the impinging turbulence, the pressure difference becomes

$$\Delta P(x_0, y_0, t) = 2\pi\rho_0 U \iint_{-\infty}^{\infty} \hat{\hat{w}}(k_x, k_y) g(x_0, k_x, k_y) \mathrm{e}^{-\mathrm{i}[k_x(x_0 - Ut) + k_y y_0]} \, \mathrm{d}k_x \mathrm{d}k_y. \tag{4.9}$$

In order to change to the frequency domain from the time domain, the Fourier transform of the pressure difference is applied as

$$\Delta \hat{P}(x_0, y_0, \omega) = \frac{1}{2\pi} \int_{-\infty}^{\infty} 2\pi\rho_0 U \iint_{-\infty}^{\infty} \hat{\hat{w}}(k_x, k_y) g(x_0, k_x, k_y) \mathrm{e}^{-\mathrm{i}[k_x(x_0 - Ut) + k_y y_0]} \mathrm{e}^{-\mathrm{i}\omega t} \, \mathrm{d}k_x \mathrm{d}k_y \mathrm{d}t. \tag{4.10}$$

Grouping the time dependent parameters, the time integral is reduced by products of the Dirac delta function

$$\int_{-\infty}^{\infty} \mathrm{e}^{\mathrm{i}(k_x U - \omega)t} \mathrm{d}t = \frac{2\pi}{U} \delta(k_x U - \omega). \tag{4.11}$$

Equation (4.10) can then be re-written introducing the particular chordwise wave number, $K_x = \omega / U$ as

$$\hat{q}(x_0, y_0, \omega) = \Delta \hat{P}(x_0, y_0, \omega) = 2\pi\rho_0 \int_{-\infty}^{\infty} \hat{\hat{w}}(K_x, k_y) g(x_0, K_x, k_y) \mathrm{e}^{-\mathrm{i}k_y y_0} \, \mathrm{d}k_y. \tag{4.12}$$

Multiplying the source strength with its complex conjugate, the $S_{qq}(\omega; x_0, x_0')$ term of Equation (4.6) writes

$$S_{qq}(x_0, x_0', \omega) = (2\pi\rho_0)^2 \iint_{-\infty}^{\infty} \hat{\hat{w}}(K_x, k_y) \hat{\hat{w}}^*(K_x, k_y) g(x_0, K_x, k_y) g^*(x_0', K_x, k_y') \mathrm{e}^{-\mathrm{i}(k_y y_0 - k_y' y_0')} \, \mathrm{d}k_y \mathrm{d}k_y'. \tag{4.13}$$

The only non-deterministic quantity in Equation (4.13) is $\hat{\hat{w}}$. However, due to the statistical orthogonality of the wave vectors it can be shown that [11]

$$\hat{\hat{w}}(K_x, k_y) \hat{\hat{w}}^*(K_x, k_y') = U \delta(k_y - k_y') \Phi_{ww}(K_x, k_y). \tag{4.14}$$

where $\Phi_{ww}(K_x, k_y)$ is the two-dimensional turbulence energy spectrum.

Introducing Equation (4.14) into Equation (4.13), the final cross-PSD becomes

$$S_{qq}(x_0, x_0', \omega) = (2\pi\rho_0)^2 \int_{-\infty}^{\infty} \Phi_{ww}(K_x, k_y) g(x_0, K_x, k_y) g^*(x_0', K_x, k_y) \mathrm{e}^{-\mathrm{i}k_y(y_0 - y_0')} \, \mathrm{d}k_y. \tag{4.15}$$

Once the cross-PSD of the pressure jump on the airfoil is derived, the final PSD for the acoustic field of an airfoil in a turbulent stream is then predicted introducing Equation (4.15) into Equation (4.6)

$$S_{pp}(x,y,z,\omega;x_0,y_0) = \int_{-d}^{d}\int_{-c/2}^{c/2}\left(\frac{\rho\omega z}{2c_0}\right)^2 \frac{U}{\sigma_0^2\ \sigma_0'^2}\mathrm{e}^{-\mathrm{i}\omega(\sigma-\sigma')/c_0}\left(1+\frac{1}{\mathrm{i}k\sigma_0}\right)\left(1+\frac{1}{\mathrm{i}k\sigma_0'}\right)^* \int_{-\infty}^{\infty}\Phi_{ww}(K_x,k_y)g(x_0,K_x,k_y)g^*(x_0',K_x,k_y)\mathrm{e}^{-\mathrm{i}k_y(y_0-y_0')}\,\mathrm{d}k_y\,\mathrm{d}x_0\mathrm{d}x_0'\mathrm{d}y_0\mathrm{d}y_0'. \tag{4.16}$$

Equation (4.16) is the general solution to predict the acoustic free-field of an airfoil located in a turbulent stream. It applies to geometrical and acoustic near-field of the airfoil, since no assumptions is made on the position of the observer till that point. However, it contains a 5-dimensional integral for which it is difficult to find an exact analytical solution. On the other hand, it is possible to handle the multi-dimensional integral with numerical methods, such as Monte Carlo integration [60, 17, 25].

As mentioned in Chapter 2, it is possible to make assumptions depending on the observer positions. A first assumption is putting the observer in the acoustic far-field of the airfoil, $\sigma \gg \lambda$. Compared to tonal fan noise, broadband noise mostly deals with higher frequencies [96], resulting in smaller wavelengths. It is therefore a valid assumption to consider the observer in acoustic far-field in the high frequency range. The general expression (4.16) can then be re-written as

$$S_{pp}(x,y,z,\omega;x_0,y_0) = \int_{-d}^{d}\int_{-c/2}^{c/2}\left(\frac{\rho\omega z}{2c_0}\right)^2 \frac{U}{\sigma_0^2\ \sigma_0'^2}\mathrm{e}^{-\mathrm{i}\omega(\sigma-\sigma')/c_0} \int_{-\infty}^{\infty}\Phi_{ww}(K_x,k_y)g(x_0,K_x,k_y)g^*(x_0',K_x,k_y)\mathrm{e}^{-\mathrm{i}k_y(y_0-y_0')}\,\mathrm{d}k_y\,\mathrm{d}x_0\mathrm{d}x_0'\mathrm{d}y_0\mathrm{d}y_0'. \tag{4.17}$$

Formulation (4.17) is based on the acoustic far-field assumption but it does not include any geometrical consideration involving the observer position and extent of the airfoil.

4.1.1. Far-field formulation

In order to deal with the 5-dimensional integral in Equation (4.17) analytically, additional assumptions need being considered. First, the observer can be assumed to be located far away from the airfoil compared to its span-length, $\sigma \gg d$, considering a large aspect ratio airfoil, $2d \gg c$. The corrected distance term, σ can then be simplified to obtain a possible analytical solution at the far-field. In Equation (4.17), the distance term appears both at the denominator and in the exponential. The one in the denominator defines the $1/\sigma$ decay for the amplitude modulation and z/σ for the directivity of the corresponding dipole. The one in the exponential accounts approximately for the phase lags between dipoles distributed over an acoustically non-compact airfoil.

For large values of σ, assuming $(y - y_0) \approx y$ and $(x - x_0) \approx x$ is reasonable. The σ_0 term in the denominator can then be simplified to

$$\sigma_0 \approx \sigma_f = \sqrt{x^2 + \beta^2(y^2 + z^2)}. \tag{4.18}$$

Since the new definition of σ is now independent from the source positions, x_0 and y_0, it can be taken out of the spanwise and chordwise integrals. Furthermore, a different procedure

is applied for the one in the phase term in order to obtain a simpler analytical solution for formulation (4.17). Starting from Equation (4.2), the corrected distance term can be extended as

$$\begin{aligned}\sigma =&\big(\sigma_0 - M(x-x_0)\big)/\beta^2\\ =&\sqrt{(x-x_0)^2+\beta^2((y-y_0)^2+z^2)}/\beta^2 - M(x-x_0)/\beta^2\\ =&\sqrt{x^2-2xx_0+x_0^2+\beta^2(y^2-2yy_0+y_0^2+z^2)}/\beta^2 - M(x-x_0)/\beta^2.\end{aligned} \tag{4.19}$$

Neglecting the second-order terms of x_0 and y_0, and adding the negligible $(xx_0+\beta^2yy_0)^2/\sigma_0^4$ term in the square root the corrected distance term in the phase definition reads

$$\begin{aligned}\sigma \approx&\sqrt{x^2-2xx_0+x_0^2+\beta^2(y^2-2yy_0+y_0^2+z^2)}/\beta^2 - M(x-x_0)/\beta^2\\ \approx&\frac{\sigma_f}{\beta^2}\left(1-\frac{xx_0+\beta yy_0}{\sigma_f^2}\right) - M(x-x_0)/\beta^2\\ \approx&\frac{\sigma_f - M(x-x_0)}{\beta^2} - \frac{xx_0+\beta^2yy_0}{\beta^2\sigma_f}.\end{aligned} \tag{4.20}$$

The final approximation of the σ term does not include any integration terms in the square root. It is therefore possible to look for an analytical solution. Introducing definitions (4.18) and (4.20) into Equation (4.17), the PSD reads

$$\begin{aligned}S_{pp}(x,y,z,\omega;x_0,y_0) = &\left(\frac{\rho\omega z}{2c_0}\right)^2\frac{U}{\sigma_f^2\,\sigma_f'^2}\int_{-\infty}^{\infty}\Phi_{ww}(K_x,k_y)\\ &\iint_{-d}^{d}\mathrm{e}^{-\mathrm{i}\left(\frac{\omega y}{c_0\sigma_f}+k_y\right)(y_0-y_0')}\mathrm{d}y_0\mathrm{d}y_0'\\ &\iint_{-c/2}^{c/2}\mathrm{e}^{-\mathrm{i}\frac{\omega(x-M\sigma_f)}{c_0\beta^2\sigma_f}}\,g(x_0,K_x,k_y)g^*(x_0',K_x,k_y)\;\mathrm{d}x_0\mathrm{d}x_0'\mathrm{d}k_y.\end{aligned} \tag{4.21}$$

As seen in Equation (4.21) integrals do not include any terms involving both the spanwise and chordwise positions of the dipoles, such as σ or σ_0 after simplifications. The spanwise and chordwise integrals are then separated and can be solved independently.

The chordwise integral results as

$$\int_{-c/2}^{c/2} g(x_0,K_x,k_y)\mathrm{e}^{-\mathrm{i}\frac{\omega(M\sigma_f-x)}{c_0\beta^2\sigma_f}}\,\mathrm{d}x_0 = \frac{c}{2}\mathcal{L}(x,K_x,k_y). \tag{4.22}$$

where $\mathcal{L}(x,K_x,k_y)$ is the aeroacoustic transfer function linking the impinging gust to the acoustic field of the airfoil [5, 6]. (see Appendix A for further derivations)

Secondly, the spanwise integral reads

$$\int_{-d}^{d} \mathrm{e}^{-\mathrm{i}\left(\frac{\omega y}{c_0\sigma_f}+k_y\right)y_0}\mathrm{d}y_0 = 2d\frac{\sin[(K_y-k_y)d]}{(K_y-k_y)d}. \tag{4.23}$$

where the term $\sin[(K_y - k_y)d]/[(K_y - k_y)d]$ is so called the sine cardinal function with $K_y = \omega y/(c_0\sigma_f)$.

Introducing Equations (4.22) and (4.23) into Equation (4.21), the PSD of the airfoil in its geometrical far-field becomes [5]

$$S_{pp}(x,y,z,\omega) = \left(\frac{\omega\rho_0 z}{c_0\sigma_f^2}\right)^2 U\int_{-\infty}^{\infty}\frac{\sin^2\left[d\left(K_y-k_y\right)\right]}{(K_y-k_y)^2}\left|\mathcal{L}(x,K_x,k_y)\right|^2\Phi_{ww}(K_x,k_y)\,\mathrm{d}k_y. \tag{4.24}$$

Besides the ones mentioned above, another assumption often made in the derivation of the transfer function, g, is considering an arbitrary large aspect ratio, equivalent to an infinite spanwise extent of the airfoil [2]. However at higher frequencies it should not be necessary to make even the large aspect ratio assumption due to the small length scales. As the wavelength of an incident gust decreases, the loading on the airfoil concentrates around the leading edge. The tip then affects a negligible spanwise region of the airfoil [5].

The 5-dimensional integral in Equation (4.17) is now reduced to a 1-dimensional integral. However, Equation (4.24) can be put in a more simplified form, since when the semi-span-length increases the square of the sine cardinal function tends to a delta function,

$$\lim_{d\to\infty}\left(\frac{\sin^2[(K_y-k_y)d]}{[(K_y-k_y)d]^2}\right) = \frac{\pi}{d}\,\delta(K_y-k_y). \tag{4.25}$$

It means that for high values of the span-length, the spanwise wave number k_y is replaced with the particular one, K_y, including the ones in the turbulence spectrum and in the acoustic transfer function. The physical explanation is that the observer only hears the gust producing acoustic wavefronts perpendicular to the line joining the source and the observer. The propagation angle of the sound wave is determined by the trace-velocity of the gust along the leading edge of the airfoil. For any fixed spanwise wave number, if the chordwise one is made large enough, the intersection point of the airfoil with the gust moves supersonically relative to the fluid, similar to the two-dimensional gust problem [5]. Using the similarity rules defined by Graham [49], for $MK_x \gg k_y$ the airfoil response function becomes independent of k_y. Therefore if the value of MK_xd is large, both Φ_{ww} and $\mathcal{L}$ become nearly independent of k_y, allowing them to be taken outside the integral in Equation (4.24). Replacing the spanwise integral with the particular value of the K_y, the PSD for the large-span airfoils then becomes

$$S_{pp}(x,y,z,\omega) = \left(\frac{\omega\rho_0 z}{c_0\sigma_f^2}\right)^2 Ud\;\Phi_{ww}(K_x,K_y)\;\left|\mathcal{L}(x,K_x,K_y)\right|^2. \tag{4.26}$$

In many industrial applications such as the scattering of the acoustic waves generated by the fan blades in a duct, the acoustic pressure (or velocity) used for the scattering computation has to be specified at a short distance from the considered blade – referred to as *spanwise geometrical near-field*. The far-field assumption becomes invalid for such configurations [64]. This motivated the derivation of a more accurate solution.

4.1.2. Spanwise geometrical near-field correction

In the case of large-span airfoils and for observer distances similar to the spanwise extent, supposing that $(x - x_0)^2 \simeq x^2$ can be still quite reasonable while $(y - y_0)^2 \simeq y^2$ may become questionable. An intermediate level of approximation in the spanwise near-field to Equation (4.2) is therefore introduced with

$$\sigma_k \simeq \sqrt{x^2 + \beta^2 (y - y_0)^2 + \beta^2 z^2}\,. \tag{4.27}$$

Using the spanwise near-field approximation in the denominator of Equation (4.21) and the same first-order approximation of the phase variation [5] as detailed above, the spanwise integral (4.23) now becomes

$$\int_{-d}^{d} \frac{1}{\sigma_k^2} \mathrm{e}^{-\mathrm{i}\left(\frac{\omega y}{c_0 \sigma_f} + k_y\right) y_0} \mathrm{d}y_0 = \boldsymbol{K}(x, y, z, K_y, k_y). \tag{4.28}$$

Since the new variable σ_k is a function of y_0, the modified function $\boldsymbol{K}$ is now expressed as a combination of exponential integrals, E_1 [1] (See Appendix E for further derivations)

$$\begin{aligned}
\boldsymbol{K}(x, y, z, K_y, k_y) = {} & \frac{\mathrm{i}\ \mathrm{e}^{\mathrm{i}\,(K_y + k_y) y}}{2\sqrt{x^2 + z^2}} \\
\Big\{ & \mathrm{e}^{-(K_y + k_y)\sqrt{x^2 + z^2}}\, E_1 \left[-(K_y + k_y)\sqrt{x^2 + z^2} - \mathrm{i}\,(K_y + k_y)(d - y) \right] \\
& - \mathrm{e}^{-(K_y + k_y)\sqrt{x^2 + z^2}}\, E_1 \left[-(K_y + k_y)\sqrt{x^2 + z^2} - \mathrm{i}\,(K_y + k_y)(-d - y) \right] \\
& - \mathrm{e}^{(K_y + k_y)\sqrt{x^2 + z^2}}\, E_1 \left[(K_y + k_y)\sqrt{x^2 + z^2} - \mathrm{i}\,(K_y + k_y)(d - y) \right] \\
& + \mathrm{e}^{(K_y + k_y)\sqrt{x^2 + z^2}}\, E_1 \left[(K_y + k_y)\sqrt{x^2 + z^2} - \mathrm{i}\,(K_y + k_y)(-d - y) \right] \Big\}.
\end{aligned} \tag{4.29}$$

Combining the new spanwise integration (4.28) and the chordwise integration (4.22) the incident PSD becomes [64]

$$S_{pp}(x, y, z, \omega) = \left(\frac{\omega \rho_0 z}{2 c_0} \right)^2 U \int_{-\infty}^{\infty} |\boldsymbol{K}(x, y, z, K_y, k_y)|^2\, |\mathcal{L}(x, K_x, k_y)|^2\, \Phi_{ww}(K_x, k_y)\, \mathrm{d}k_y \tag{4.30}$$

which differs from Amiet's classical solution by the modified function $\boldsymbol{K}$.

Equation (4.30) contains a one-dimensional integral as in the far-field formulation (4.24). It therefore requires the same order of computational effort as the far-field solution.

In order to integrate the expression (4.16) analytically different methods are now proposed. However, they all include acoustic and geometrical simplifications. Equation (4.16) can also be integrated numerically using Monte Carlo integration method without any assumptions about the observer position [64]. The Monte Carlo integration method will not be detailed in this thesis for the sake of conciseness. The reader is referred to the related reference [25] for more details. The numerical integration will provide the reference solution for the acoustic response of the airfoil. Furthermore, it allows the verification of the different implementations of near-field hypotheses independently, as illustrated below.

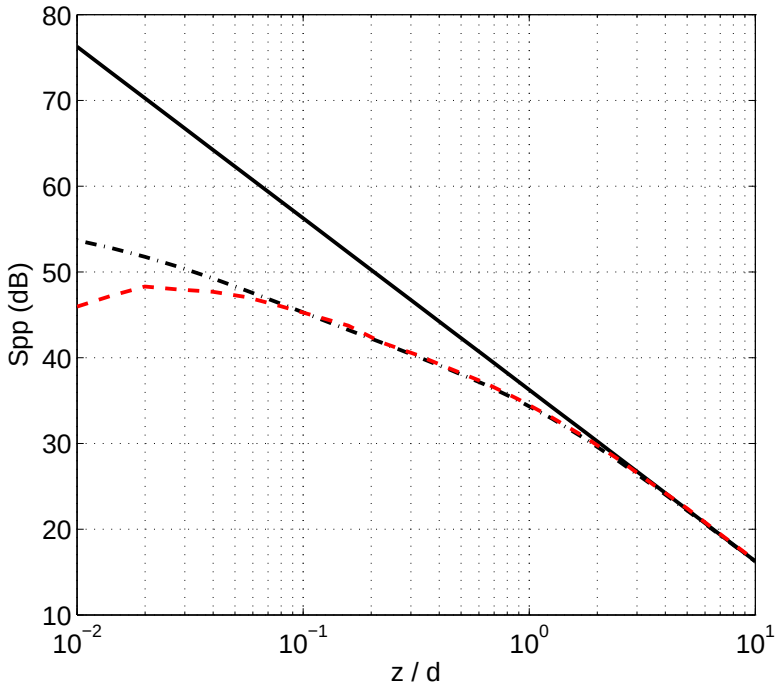

Figure 4.4.: Sound pressure level predicted above the airfoil using Amiet's far-field solution (4.24) (solid line), the geometrical spanwise near-field formulation (4.30) (dash-dotted line) and the direct numerical integration of formulation (4.16) without any geometrical assumption (dashed line)

4.2. Assumption Assessment

The semi-analytical methods described above are compared with analytical and numerical integration techniques in geometrical and acoustic near-field of the stationary airfoil.

4.2.1. Geometrical near-field effects

A numerical test is first performed in order to compare the results provided by the far-field expression (4.24), the spanwise near-field expression (4.30) and the direct numerical integration of formulation (4.21). The sound spectrum emitted by an airfoil subjected to homogeneous turbulence, at various distances z on the line $(x, y) = (0, 0)$ is calculated. A von Karman spectrum model [55] is selected for the turbulent energy spectrum

$$\Phi_{ww}(k_x, k_y) = \frac{4}{9\pi} \frac{\bar{u^2}}{k_e^2} \frac{\hat{k}_x^2 + \hat{k}_y^2}{(1 + \hat{k}_x^2 + \hat{k}_y^2)^{7/3}} \tag{4.31}$$

where

$$k_e = \frac{\sqrt{\pi}}{\Lambda} \frac{\Gamma(5/6)}{\Gamma(1/3)}. \tag{4.32}$$

The turbulence spectrum is modeled using the square root of the r.m.s of the streamwise fluctuations $\bar{u^2}$, and the streamwise integral length scale of the turbulence, Λ. An incoming

velocity $U = 13.2$ m/s, a turbulence intensity $TI = 0.2$, and a turbulent length scale $\Lambda = 0.005$ m are chosen as representative of the experiment described in Section 4.5.2 [27]. The airfoil chord is $c = 0.041$ m, and a large aspect ratio airfoil is assumed by using a span $2d = 40\,c$ [24].

Figure 4.4 shows the variation of the sound power level at a frequency of 2000 Hz ($kc = 1.5$ and $kd = 30.3$) with z. Solid, dash-dots and dashed lines represent the results obtained with solution (4.24), the geometrical spanwise near-field formulation (4.30) and the direct numerical integration of formulation (4.16) without any geometrical assumption, respectively. The results show that all formulations converge for $z/d > 2$, pointing out the limit of application of the far-field formulation (4.24) not taking into account the geometrical near-field effects. The use of the general formulation (4.16) exhibits a first deviation from the far-field approximation at $z/d = 2$ corresponding to the size of the spanwise extent of the airfoil. Between those two points, the evolution of the sound power spectrum is linear (in logarithmic scale) with respect to the observer distance. The new spanwise near-field expression (4.30) shows a good agrement with the reference solution and highly improves the Amiet's far-field solution (4.24). The second deviation around $z/d = 0.08$ between formulations (4.16) and (4.30) corresponds to the chord size of the airfoil. It is seen that the first order approximation in the phase variation of the dipoles provides a reasonable approximation.

4.2.2. Acoustic near-field effects

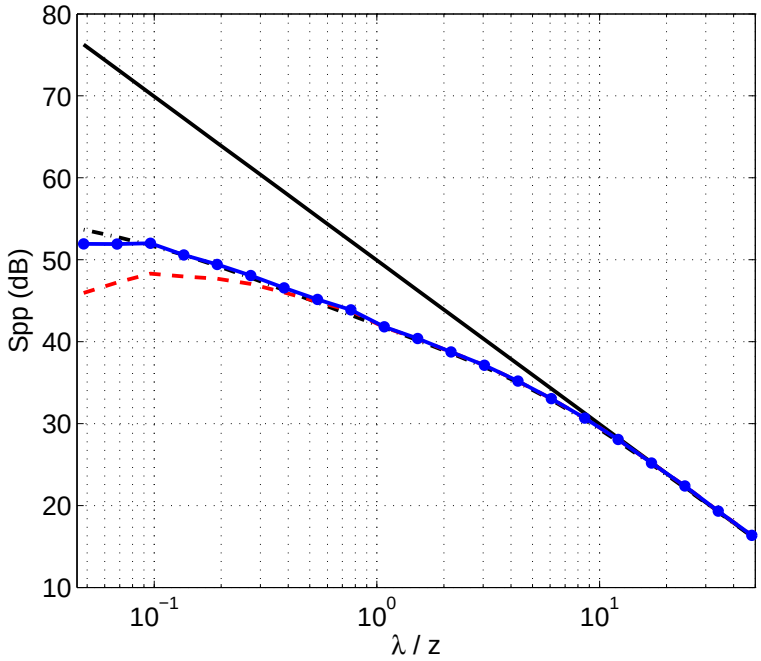

Figure 4.5.: Sound pressure level predicted above the airfoil using Amiet's far-field solution (4.24) (solid line), the geometrical spanwise near-field formulation (4.30) (dash-dotted line), the direct numerical integration of formulation (4.16) without any geometrical assumption (dashed line) and the acoustic near-field terms (symbols-line)

The results presented in previous section are not taking acoustic near-field effects into account, which become significant when the distance z is smaller than the acoustic wavelength. The test used in previous section is considered to evaluate the influence of the acoustic near-field terms.

Figure 4.5 introduces results obtained using Amiet's theory at different observer distances from the airfoil including acoustic near-field terms (symbols line). The deviation is appearing, as expected, at a distance comparable to the acoustic wavelength, λ. The difference observed using acoustic near-field terms on formulation (4.16) is around $6 - 7$ dB for the considered configuration. It should be noted that, the match between results obtained with formulation (4.30) and formulation (4.16) including acoustic near-field terms at lower z/λ values is a coincidence. The former deviates from the reference solution (4.16) neglecting the chordwise position of dipoles on the airfoil surface whereas the latter takes that into account including the $1/\sigma^2$ decay due to the acoustic near-field. Finally, it should be noticed that, at the particular frequency selected for the test ($f = 2000\ Hz$), avoiding the use of acoustic near-field terms in the computation can be acceptable while at lower frequencies, the deviations could increase dramatically as mentioned in tonal fan noise applications.

4.3. Airfoil in Homogeneous Turbulence

Experiments have been conducted for comparing the measured sound pressure levels with broadband noise predictions in free-field. A thin (relative thickness less than 3%) and slightly cambered optimized airfoil is mounted downstream of a wind tunnel in the anechoic chamber of the Ecole Centrale Lyon (ECL) (see Figure 4.24) [112]. The dimensions of the room are 6m × 5m × 4m, and walls, floor and ceiling are covered with acoustic absorbing material. The cut-off frequency of the room is 100 Hz. Sound measurements are taken with Bruel & Kjaer microphones.

Figure 4.6.: Experimental setup showing the airfoil mock-up mounted vertically and the wind tunnel nozzle in the anechoic chamber of ECL.

The isolated airfoil has $2.3c$ span with $c = 0.013$ m. The open end nozzle of the wind

tunnel is rectangular with an outlet size $2.3c \times 1.2c$. The airfoil is placed vertically at zero angle of attack with respect to the mean camber line at leading edge. The flow Mach number is $M \cong 0.09$. In order to create isotropic and homogeneous turbulence impinging onto the airfoil, a square grid is placed upstream of the nozzle [44]. The turbulence generated by the grid-nozzle system at the impingement line has a turbulence rate of 5% and an integral length scale Λ of 0.009 m [112].

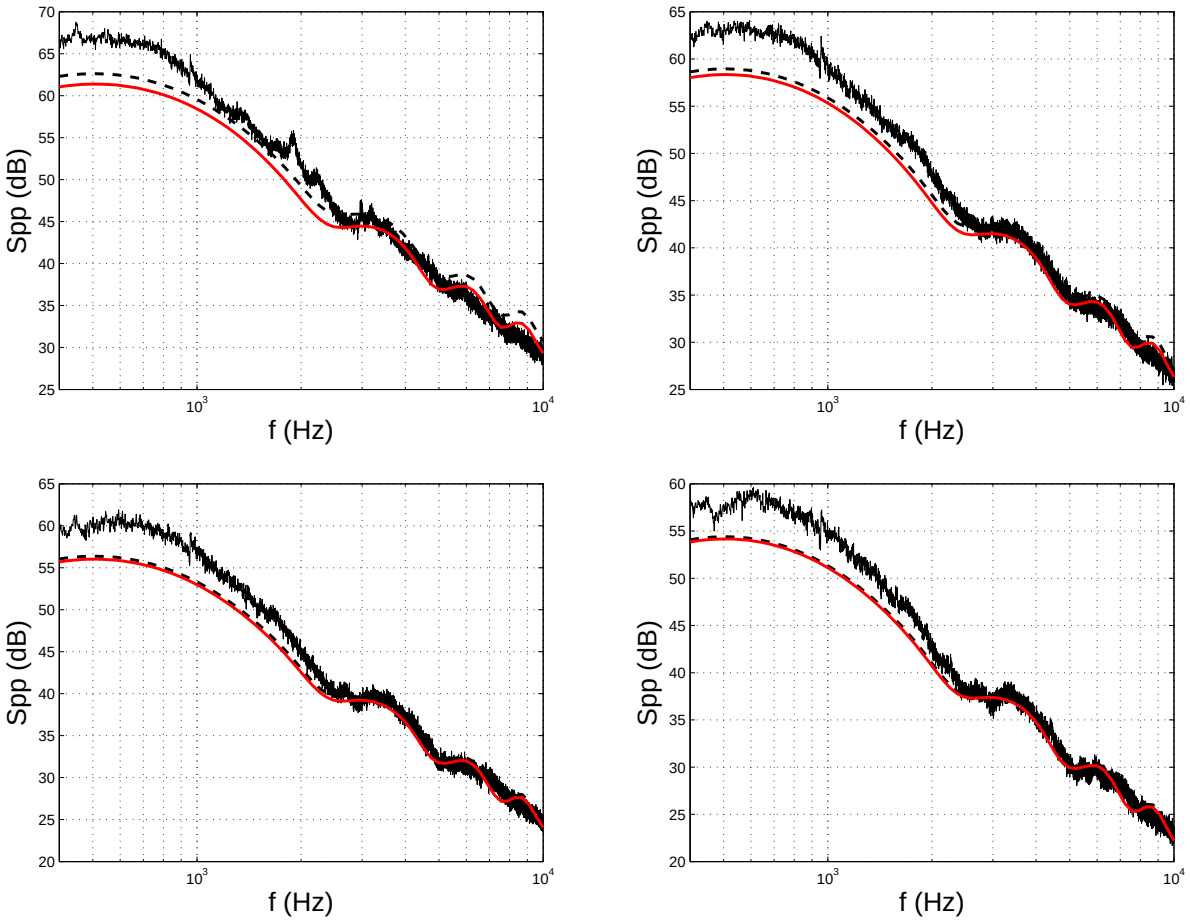

Figure 4.7.: Acoustic spectra at observer locations $4/3, 2, 8/3$ and $10/3$d above the airfoil, measurements (black line), solution (4.24) (dashed line) and solution (4.30) (red line)

Figure 4.7 shows a comparison of the acoustic spectra emitted by the airfoil for observer positions at $4/3, 2, 8/3$ and $10/3$d above the airfoil on the $(x, y) = (0, 0)$ line. Measurements, solution (4.24) and solution (4.30) are represented as black, dashed and red lines, respectively. A good agrement is seen between the measurements and solutions (4.24) and (4.30) in the frequency range of $400 - 10000$ Hz where the differences between two spectra is less than 5 dB. A possible explanation of the discrepancies between solutions (4.24) and (4.30) and the measurements at low frequencies can be related to anisotropic character of the corresponding energetic turbulent scales which is missing in von Karman model [102]. Additionally, the formulation (4.4) neglects the acoustic near-field effects, which may contribute to the sound field at this listener position at the lowest frequencies. On the other hand, the humps and dips in the spectral shape due to the non-compactness of the airfoil are well captured at the

higher frequencies. The reason that the humps and dips being not clear for the measurements at $z = 4/3$ might be due to the scattering of the acoustic waves by the end plates supporting the airfoil.

As seen in Figure 4.7, solutions (4.24) and (4.30) converge at the higher z/d ratios as previously shown in the Figure 4.4. However, at the observer located in the spanwise geometrical near-field of the airfoil (z/d=4/3 here), solution (4.30) provides better agreement with the measurements compared to solution (4.24). The improvement between the two solutions is around 2 dB.

The new near-field expression (4.30) is then attractive for geometrical near-field computation due to its accuracy. Including its facility of implementation and robustness, compared to direct integration which requires higher computational time to obtain a similar accuracy [64] it will then be used in the following sections.

In the experiment described above the airfoil is subjected to homogeneous incoming flow in the spanwise direction. However, this may not be the case for the industrial applications. The effect of spanwise variation of the flow field in the acoustic field is therefore investigated in the next section.

4.4. Spanwise Segmentation

The theory introduced in Section 4.1 considers homogeneous incoming flow field in order to predict the acoustic response of an airfoil. However, most of the industrial applications and the experiment described in Section 4.5 involve non-uniform flow field in the spanwise direction. An approach based on splitting the airfoil into short strips has been applied to implement the spanwise varying incoming flow conditions [24, 38]. Three different segmentation methods are presented in this section as seen in Figure 4.8.

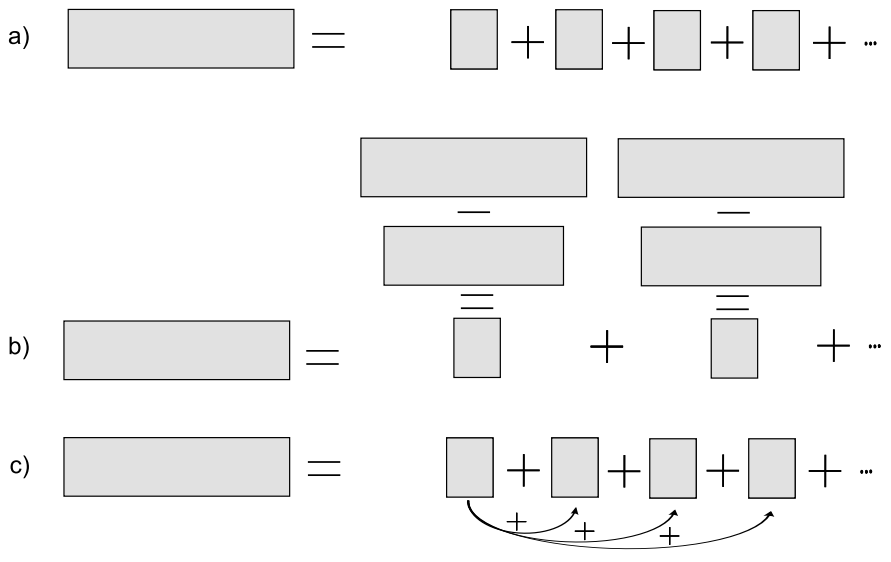

Figure 4.8.: Sketch of segmentation methods, a) Strip theory, b) Inverse strip theory, c) Correlated strips theory

4.4.1. Classical strip theory

The basic spanwise segmentation theory consists in splitting the airfoil into spanwise strips and assume homogeneous flow conditions for each individual strip. The sum of the span-lengths of all strips is equal to the one of the initial large aspect ratio airfoil. The total observed acoustic PSD is then obtained by summing the contributions from the different strips [117, 38], as represented symbolically in Figure 4.8.

A segmentation test is applied to the large aspect ratio airfoil, $d = 20c$, defined in Section 4.2 [27]. The observer is located at $(0, 0, 10c)$. The $z/d = 0.5$ ratio stays in the geometrical near-field of the considered airfoil. Further, since it does not contain a limitation in the spanwise extent of the airfoil the spanwise geometrical near-field solution (4.30) is more suitable rather than the far-field solutions (4.24) and (4.26).

In a first step, identical properties are applied to each segment and compared to the prediction obtained using the entire large aspect ratio airfoil encountering homogeneous conditions. Differences between the two approaches are meant to highlight numerical deficiencies in the segmentation method. Figure 4.9 shows the total acoustic spectra of the segmented and the complete airfoil subjected to the uniform flow conditions as defined in Section 4.2. The solid line represents the large aspect ratio airfoil. The dashed lines represent the summation of 4, 16 and 64 uniform strips. It is seen that increasing the number of strips results in lower spectral level at low frequencies and some damping of the high-frequency humps [24]. However, the influence at low frequencies is higher than the one at high frequencies. In this technique, short strips are uncorrelated and are not able to capture the spanwise correlation associated with large hydrodynamic wavelengths at low frequencies [65], hence the classical strip theory underpredicts the acoustic pressure of the airfoil. Adjacent strips can not be considered as uncorrelated allow spanwise wave number [25]. The effect of large wave lengths are then needs being taken into account [26, 67].

For industrial applications, in which the flow is not uniform in the spanwise direction [117, 116], using the classical strip theory will lead to a poor prediction with a high number of strips. In order to take the effect of the large wavelengths into account a modified strip theory based on the subtraction of two large-span airfoils was proposed [26]. It is called the inverse strip theory.

4.4.2. Inverse strip theory

The inverse strip theory described below was proposed by Christiophe [26, 28]. According to this theory, the acoustic field of a small strip is computed via the subtraction of the contributions of two airfoils of large aspect ratio, the span-length difference of which is equal to the span-length of the strip (see Figure 4.8 (b)). The two contributions then allow including the effects of large hydrodynamic wavelengths.

A similar test is performed for the same generic large aspect ratio airfoil using 64 spanwise segments. The observer is kept at the same spanwise geometrical near-field position at $(0, 0, 10c)$. Figure 4.10 shows the acoustic PSD of the original and segmented airfoils using the same incoming flow profiles as in the classical strip theory. The solid line represents the spectrum of the entire large aspect ratio airfoil. The dashed line and symbols represent the segmented airfoils using classical strip theory and inverse strip theory, respectively. The inverse strip theory minimizes the errors due to the segmentation at all frequencies. The small difference between the entire and segmented airfoils is now due to the effect of the different

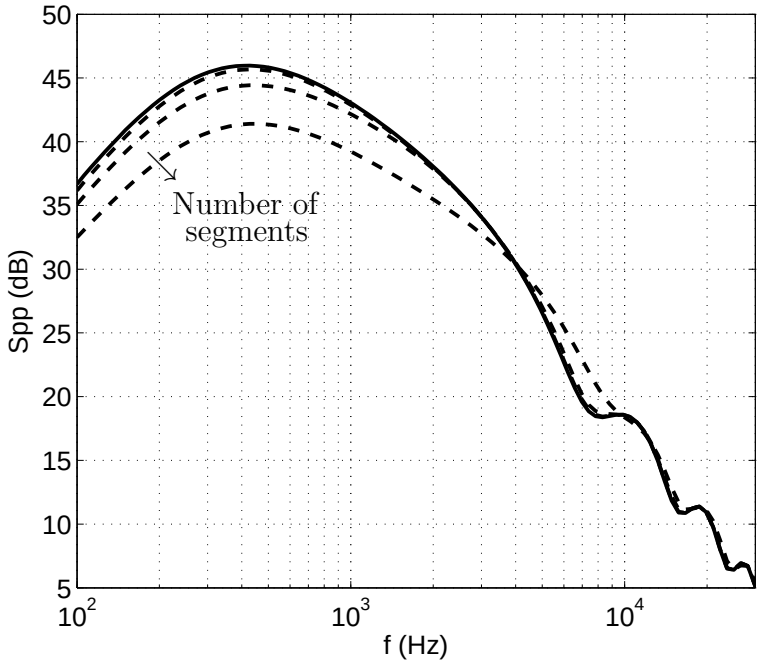

Figure 4.9.: Acoustic PSD of a large aspect ratio airfoil (solid line) and segmented with the strip theory (dashed line) using 4, 16 and 64 strips. $d = 20c$ and observer at $(0, 0, 10c)$.

radiation angles of the dipoles appearing during the subtraction of airfoils. However, the inverse strip theory has been validated elsewhere for observers located in the geometrical far-field where the effect of the directivity of the dipoles is negligible [24]. For far-field predictions, all dipoles are assumed to have the same radiation directivity [25], knowing that the corrected distance value is independent of the position of the dipole in the far-field expression (4.24).

Additionally, since the inverse strip theory is based on subtraction of two large aspect ratio airfoils, Equation (4.26) can be used to compute the PSD of short strips when the observer is located in the geometrical far-field [25]. Hence, a faster solution could be obtained for industrial problems, including spanwise varying impinging flow conditions.

The drawback of the inverse strip theory is that the effect of the directivities of the point dipoles may become significant for observer locations in the near-field. It therefore depends on observer position. Additionally, inverse strip theory simply doubles the computation time since each strip needs being computed twice, first for a large strip and secondly for the truncated one. For free-field problems, the computation time is not an issue whereas for scattered-field computations detailed in the following chapter, the computation time is already a challenge. Independently of observer location, a new segmentation method taking the cross-correlation of the acoustic fields of different strips into account is then proposed.

4.4.3. Correlated-strips theory

Another approach to minimize the aforementioned underprediction of the classical strip theory is to take into account the cross-correlations of the radiated acoustic fields from

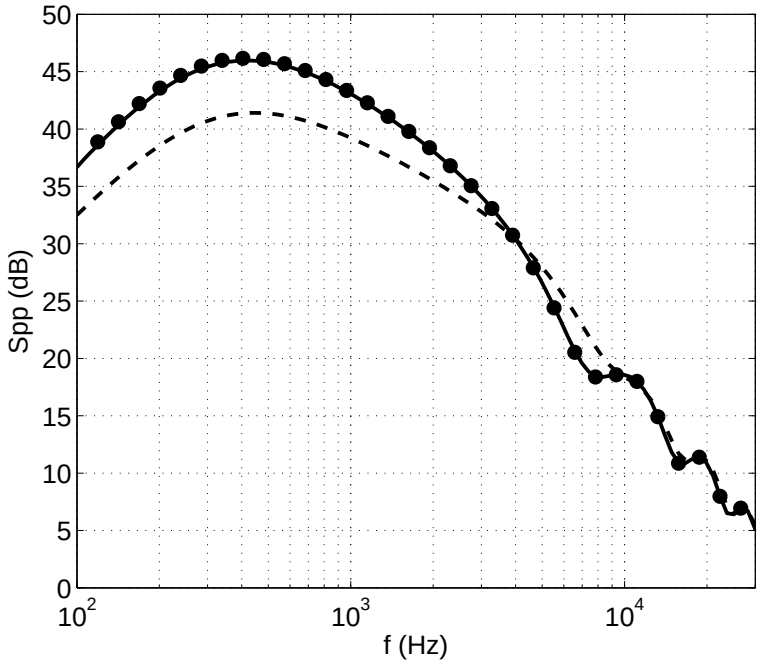

Figure 4.10.: Acoustic PSD of a large aspect ratio airfoil (plain), 64 segments with the strip theory (dotted line) and 64 segments with inverse strip theory (dots); $d = 20c$ and observer at $(0, 0, 10c)$

different strips [65] (see sketch 4.8 (c)). Applying spanwise segmentation to Equation (4.30) leads to the summation of both the auto- and cross-correlations of the acoustic responses of the n strips (see Appendix B for further derivations)

$$S_{pp,total} = \sum_n S_{p_n p_n} = \Big\{ S_{p_1 p_1} + S_{p_1 p_2} + \cdots + S_{p_1 p_n} + S_{p_2 p_1} + S_{p_2 p_2} + \cdots \vdots \quad \ddots \quad \vdots \; S_{p_n p_1} + \quad \cdots \quad + S_{p_n p_n} \Big\}. \tag{4.33}$$

Only summing the auto-correlations of the acoustic PSD of strips, the diagonal terms in Equation (4.33), results in as the classical strip theory defined in Section 4.4.1. Hence, the underprediction can be explained by not taking the cross-correlation terms into account. As mentioned above, the adjacent strips are correlated when the spanwise wave number is low enough [25]. If one wants to consider the correlation between different strips the partially non-homogeneous turbulence field needs being dealt with.

The drawback of this theory is that no analytic definition of partially non-homogeneous turbulence exists to compute the off-diagonal terms in Equation (4.33) to author's knowledge. The proposed approach is to apply a correction in the expansion for homogeneous turbulence.

A method on modeling partially non-homogeneous quantities using homogeneous ones exists in literature [22, 52]. It was proposed to construct the initial conditions for a numerical

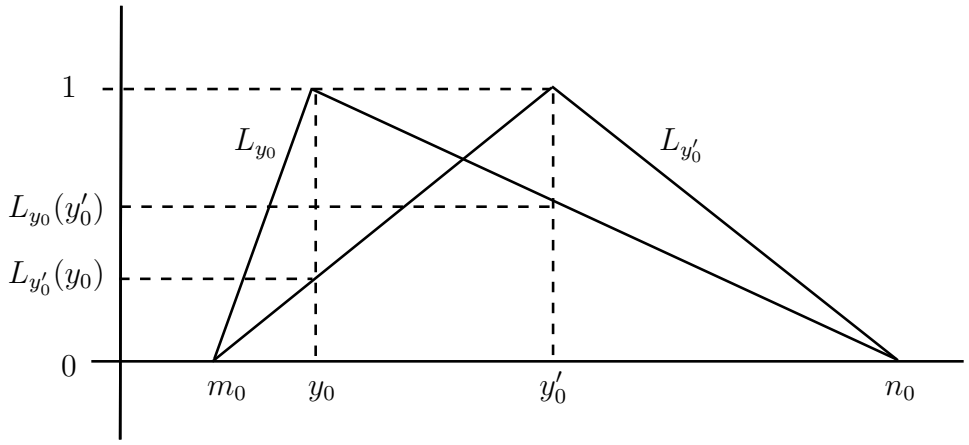

Figure 4.11.: Linear Lebesgue functions [52]

solution of a wall-bounded flow. These conditions were constructed in an intermediate space between physical space and spectral space, so called – quasi-spectral space [22]. The cross-correlation of the turbulence quantities at two points in the partial non-homogeneous flow field is then modeled using a first-order linear correction of the correlation in the homogeneous turbulent field.

The auto- and cross-correlation terms at the right hand side of Equation (4.33) require the definition of the turbulence spectrum Φ_{ww} which is the Fourier transform of the correlation of the upwash velocity at two different points, $R_{ww}(x_0, x'_0, y_0, y'_0) =< w(x_0, y_0)w(x'_0, y'_0) >$ for example. The given correlation function is defined in a 2-dimensional physical space. Assuming the homogeneity is being questioned on the y-component, its transform in the quasi-spectral space can be represented as $\hat{R}_{ww}(K_x, y_0, y'_0)$. Applying a first-order correction, the partially non-homogeneous transformation can be linked to the homogeneous one with [22]

$$\hat{R}_{ww}(K_x, y_0, y'_0) = \hat{R}^H_{ww}(K_x, y_0, y'_0) \cdot L_{y_0}(y'_0) \tag{4.34}$$

where the superscript ^{H} stands for the homogenous turbulence field. L is the first-order correction term.

In order to model the correction term a shape function is used. Linear Lebesgue coefficients were proposed first [22]. Figure 4.11 shows the variation of the linear coefficients with respect to the positions of the sampling points in the physical space. The model was first proposed for wall-bounded turbulent flows, where the parameters m_0 and n_0 represent the walls. Since there is no flow on the wall, the coefficients approach zero at m_0 and n_0. For points y_0 and y'_0 close to each other, the statistics is close to homogeneity (L goes to 1), ensuring a consisting auto-correlation. Using a linear relation between the remaining positions, the distribution of the coefficients becomes as seen in the figure. It is worth to note that, any other shape functions could be used instead, at the price of inclosed complexity.

However, first-order shape functions do not ensure the fundamental equality of the symmetry condition [52]

$$\hat{R}_{ww}(K_x, y_0, y'_0) = \hat{R}_{ww}(K_x, y'_0, y_0). \tag{4.35}$$

A second model was developed in order to enforce this condition [22]. It was based on the position of the sampling point with respect to the most distant wall surface. The model

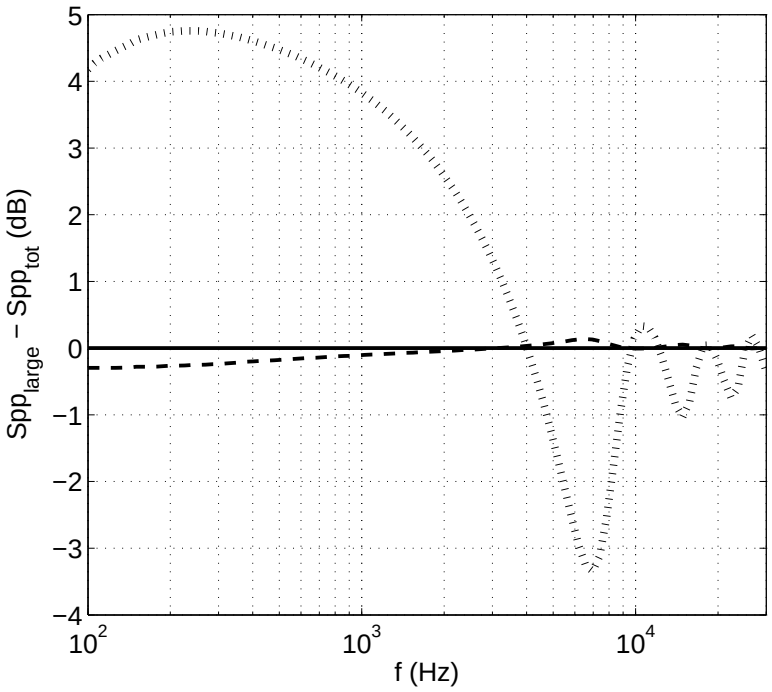

Figure 4.12.: The difference of the acoustic PSD spectra; $d = 20c$ airfoil minus summation of 64 strips. Strip theory (dotted line), inverse strips theory (dashed line) and correlated strips theory (solid line) at $(0, 0, 10c)$.

was named Information by the First Most Distant Point (IFMDP). All the cross-correlation coefficients were then modeled depending on the positions of the sampling points. The partial non-homogeneous turbulence field is modeled using the flow properties taken from the point farthest from the wall as reference.

The theory proposed in [22] was dealing with a wall bounded turbulent flow, an assumption of zero flow at solid boundaries can then be taken as a physically accepted boundary condition. This is not in the present case of interaction of an airfoil with a flow, since there is no wall bounding the airfoil in the spanwise direction. So that, the flow velocity can not be assumed to be zero at the tips of the airfoil. However, a new correction coefficient is defined through the ratio of the impinging mean-flow profiles of the strips instead of the positions in the physical space. Similar to the IFMDP, where the most distant point from the wall has the higher velocity, the ratio of the lower velocity to the higher velocity will now give the new coefficient [65, 67], as.

$$L_{y_0}(y_0') = \frac{\min(U(y_0), U(y_0'))}{\max(U(y_0), U(y_0'))}. \tag{4.36}$$

For the auto-correlation of the velocity field, the coefficient is again equal to 1. Furthermore, the partially non-homogeneous turbulent field is now modeled using the strip subjected to the higher incoming flow velocity as reference.

The initial test is repeated for the $d = 20c$ airfoil using 64 spanwise strips. The observer is located in the spanwise geometrical near-field of the airfoil, $(0, 0, 10c)$. The same identical flow properties are applied to all strips. Therefore the coefficient L becomes $U/U = 1$. Fig-

ure 4.12 shows the difference of the predicted spectra between the actual large aspect ratio airfoil and the segmented one. The dotted line represents the difference with the segmented airfoil using classical strip theory. As mentioned above, the difference is due to the assumption of uncorrelated strips. Although the prediction is improved in the inverse strip theory (dashed line), the effect of the large wavelengths is included imperfectly. There is still a small error. On the other hand, the summation of acoustic PSD obtained employing correlated strips (solid line) provides exactly the same results as the actual airfoil, independently of observer position.

Finally, the spanwise varying flow conditions can be taken into account with different segmentation methods. For the free-field acoustic response of an airfoil located in a turbulent stream, the far-field acoustic PSD can be computed based on the classical strip theory for few segments. When the number of segments increases, using the inverse strip theory is at least required for reliable far-field predictions. On the other hand, using the correlated-strips theory provides corrected acoustic spectra irrespective of the observer positions. Because the inverse strip theory doubles the computation time, the correlated-strips theory will be more efficient especially for computing scattered-fields.

The theories proposed above are used below in a jet-airfoil configuration for validation [120, 28].

4.5. Acoustic Field of a Jet-Airfoil Test-Case

The experiment defined in Section 4.3 includes a stationary airfoil located in a grid generated turbulent field. The impinging turbulent stream was then homogenous and isotropic, hence no spanwise segmentation had been applied. A second set of experiments has also been performed using a jet-airfoil configuration. The airfoil is placed in the developing region of the jet aligned with a diameter, so that the flow profile varies significantly in the spanwise direction [25]. Uniform impinging flow is not a valid assumption anymore. Applying spanwise segmentation is now required for the non-uniform flow.

4.5.1. Numerical setup

The jet-airfoil configuration consists in a NACA 0012 airfoil with chord $c = 0.041$ m and 8.78 c span, placed in the transitional region of a turbulent jet. The jet nozzle is circular with an outlet diameter $D = c$ [27]. The airfoil is placed at zero angle of attack with its leading edge located at 6 c from the nozzle outlet plane as seen in Figure 5.1. The jet exhaust speed is equal to 13.2 m/s. The Mach number $M \cong 0.04$ results in a Reynolds number based on the chord $Re_c = 36,000$. Due to the low Mach number considered, an incompressible LES computation is used to resolve the most energetic content of the flow with the commercial finite volume solver Fluent Rev. 6.3. The mesh contains 2.8 M cells, inlet conditions in the nozzle were imposed and tuned to reproduce the experimental conditions. The cut-off frequency of the computation was estimated at 1 kHz, based on the Power Spectral Density of the streamwise velocity at a location of half a chord upstream the airfoil [25]. Further information on the numerical computation can be found in the related references.

Two hybrid approaches, separating the computation of the sources of sound from the sound propagation itself, are applied in order to compute the acoustic field of the airfoil. The first one is a numerical method using directly the pressure distribution on the airfoil surface

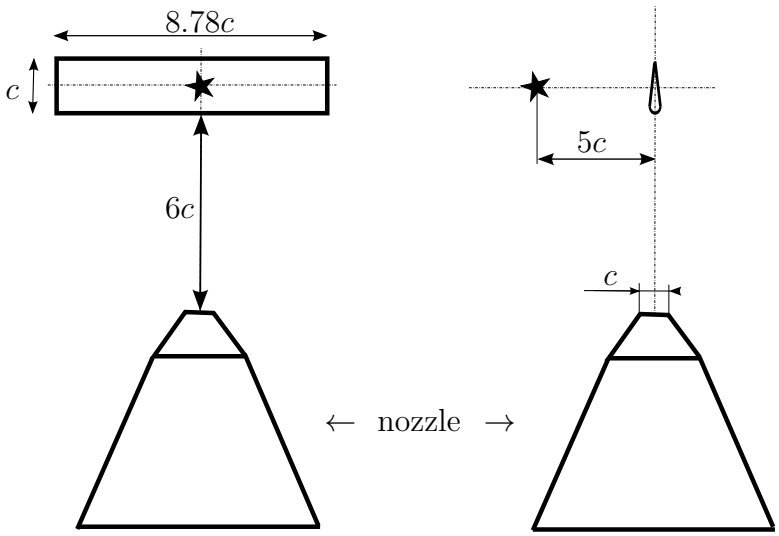

Figure 4.13.: Sketch of the experimental jet-airfoil test case, (left) Front view, (right) Side view

obtained from the unsteady CFD [33, 27]. The second one is a semi-analytical method [5, 64] employing an analytical turbulence model using the flow velocity profile impinging to the airfoil obtained from the same CFD [27].

Both prediction methods, namely Curle's deterministic analogy using formulation (4.4) and formulation (4.30) based on Amiet's theory, are tested on the jet-airfoil case in absence of additional scattering surfaces.

In Curle's deterministic analogy, $F\mathrm{e}^{\mathrm{i}\omega t}$ of Equation (4.4) is obtained through an integration of the unsteady pressure field on the airfoil surface. The airfoil is then reduced to a point dipole. This assumption is only valid if the airfoil is acoustically compact at the frequencies of interest.

An advantage of this numerical method is that the acoustic pressure field can be computed in a deterministic manner, where the amplitude and phase information of the acoustic pressure are known, since the source field is already defined deterministically. This will be related to the acoustic scattering computations detailed in Chapter 5. However, this methodology is limited with the resolution of the numerical mesh of the flow-field computation since in order to predict the acoustic source field at higher frequencies, very fine numerical mesh is required [27].

The necessary input information for both methods is extracted from a numerical computation available in literature [25, 24], on the same test-case geometry. In case of Curle's analogy, the wall-pressure distribution on the complete airfoil is extracted during an acquisition time of $t' = 70$, non-dimensionalized with the jet velocity and the airfoil chord, and a sampling frequency of 100 kHz. The wall-pressure distribution is then integrated over the airfoil surface in order to provide the source strength of the corresponding dipole in formulation (4.4) [66]. Due to the use of an incompressible computation to obtain the acoustic sources, the methodology is valid till the sources remain compact (size of the source region << emitted wavelength). The actual limit of use is around 2.8 kHz based on the jet impacting area. In case of formulation (4.30), the power spectrum of the upwash velocity component Φ_{ww} is modelled using a classical von Karman spectrum [55] modified to be consistent with the rapid distortion theory described in [25] in order to take into account

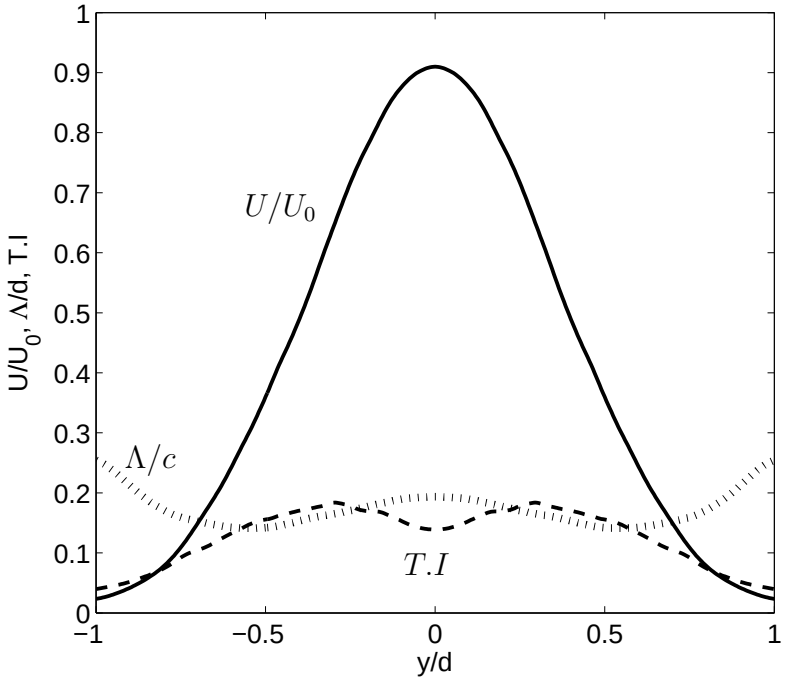

Figure 4.14.: Impinging flow profiles exported at $1c$ upstream of the airfoil: incoming flow velocity (plain), turbulence intensity (dashed) and turbulent length scale (dots)

the non-negligible thickness of the NACA 0012 airfoil. The expansion reads

$$\Phi_{ww}(k_x, k_y) = \frac{9}{36\pi} \frac{\bar{u^2}}{k_e^2} \frac{\hat{k}_x^2 + \hat{k}_y^2}{(1 + \hat{k}_x^2 + \hat{k}_y^2)^{19/6}}. \tag{4.37}$$

This expression is similar to formulation (4.31), but includes a correction of high frequency energy spectrum. The necessary numerical inputs required for the model, namely the streamwise velocity, the turbulence intensity and the integral turbulence length scale, are extracted from the numerical computation upstream of the airfoil.

The incoming turbulent flow profiles obtained from the CFD simulation, extracted 1 c upstream of the leading edge, are seen in the Figure 4.14. The plain, dashed and dots represent the flow velocity, turbulent intensity and length scale, respectively. The velocity is non-dimensionalized with the jet outlet velocity. The turbulent length scale is non-dimensionalized with the chord length. Since the airfoil is located in the development region of the jet and the span-length/jet diameter ratio is large, the impinging flow is strongly non-uniform in the spanwise direction. The center of the airfoil is exposed to the highest impinging flow velocity since it is affected by the core of the jet-flow.

Figure 4.15 shows the comparison of acoustic predictions made with the three segmentation methods using spanwise varying incoming flow conditions obtained from the CFD simulation of Figure 4.14. The observer is located 5 c above the airfoil on the $(x = 0, y = 0)$ line. The airfoil is split into 8 spanwise strips each having the equal span-lengths. The von Karman spectrum defined in Equation (4.31) is employed. The dash-dots spectrum is obtained using the classical strip theory. It is lower than the other two spectra at low frequencies. Additionally, at higher frequencies dips are damped. The difference between the

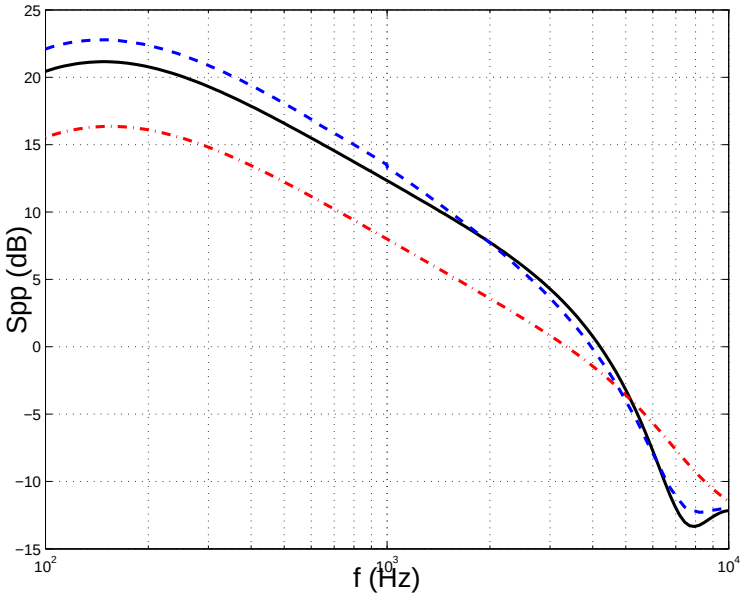

Figure 4.15.: Predicted sound spectra with the segmentation methods for $d = 8.78c$. Flow properties given in Figure 4.14 with von Karman spectrum. Observer located at $(0, 0, 5c)$ for classical strip (dash-dots), inverse strip (dashed) and correlated-strips (plain) theories.

results obtained with the classical strip and inverse strip theories (dashed) is about 7 dB at frequencies below 5000 Hz, pointing the effect of the large hydrodynamic wavelengths mentioned above. Using correlated strips (plain) with the correction coefficients defined in expression (4.36) also considers the effect of large wavelengths. The difference between the spectra corresponding to the inverse strip and correlated-strips theories is less than 2 dB over the entire frequency range. It is concluded that both methods improve the acoustic prediction with respect to the classical strip theory.

4.5.2. Experimental setup

Experiments have been conducted for comparison of the measured sound power levels with the broadband noise predictions in free-field. The jet and the airfoil are placed in the anechoic room of the von Karman Institute for Fluid Dynamics (see Sketch 4.16). The dimensions of the room are 4 m × 3 m × 4 m, and walls, floor and ceiling are covered with acoustic absorbing material. The diameter of the nozzle outlet is equal to $D = 0.041$ m. A 10 bar compressor supplies flow to the settling chamber by the ejectors. In order to prevent swirl, the airflow enters into the nozzle pipe through a honeycomb. The low-turbulence airflow supplied with a high contraction ratio induces laminar boundary-layer at the outlet of the nozzle [120]. The velocity of the jet is adjusted by the static pressure measurement in the stagnation chamber with a water manometer. The velocity is then obtained from the Bernoulli equation using the pressure difference read in the manometer [102].

The cut-off frequency of the room is 350 Hz. Sound measurements are taken with Bruel & Kjaer microphones using a high-pass filter of 100 Hz and a low-pass filter of 12 kHz. The sampling frequency is 2^{19} Hz and measurements are acquired in series of 0.1 s duration.

A first set of measurements is under-taken in order to select the observer position for the

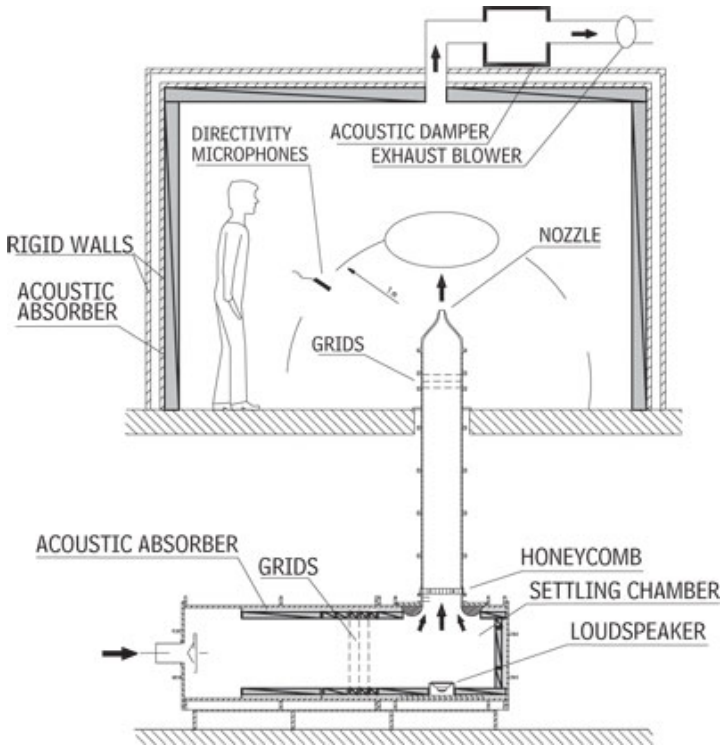

Figure 4.16.: Sketch of the jet in the anechoic chamber

comparisons. The microphone must be out of the incoming jet-flow in order to avoid pseudo sound in the measurements [107]. It is also important that the microphone does not disturb the incoming jet-flow. Additionally, the microphone must be far away from the walls of the room in order to minimize the scattering effects even if the walls are covered with absorbing materials. Since it is known that the free-field acoustic pressure of a dipole source decays like $1/R$ in the far-field [101], R being the linear distance from source to observer, different sets of measurements are taken at 5, 10, 15, 20 and 25c away from the airfoil on the $(x = 0, y = 0)$ line.

Figure 4.17 (left) shows the acoustic PSD of the airfoil at various observer positions. The jet outlet velocity is fixed at 13.2m/s. The point, diamond, square, upper and lower triangles represent the different observer positions given above, respectively. It is seen that all the measurements collapse at -10 dB corresponding to the background noise in the anechoic chamber. The measurements are taken in 5 sets. For each set, the Welch's algorithm is used in MATLAB environment in order to obtaine averaged spectra [130]. Hanning windowing is used with 50% overlapping. The 5 sets are then averaged in order to obtain the final spectrum.

The figure on the right side shows the spectra scaled by the distance z, taking $z = 25$c as reference. It is seen that above 200 Hz, the $1/R$ decay is satisfied for all microphone locations in the acoustic free-field. The disagreement at the lower frequencies is due to the effect of the near-field terms which include a decay like $1/R^2$ [101]. However, these frequencies are already lower than the cut-off frequency of the chamber. Again data do not collapse above 4 kHz due to contamination by the background noise. At these frequencies, the sound measured by the microphone should not be considered in the comparisons. It is therefore decided to select the location $(0, 0, 5c)$ for both free and scattered-field measurements.

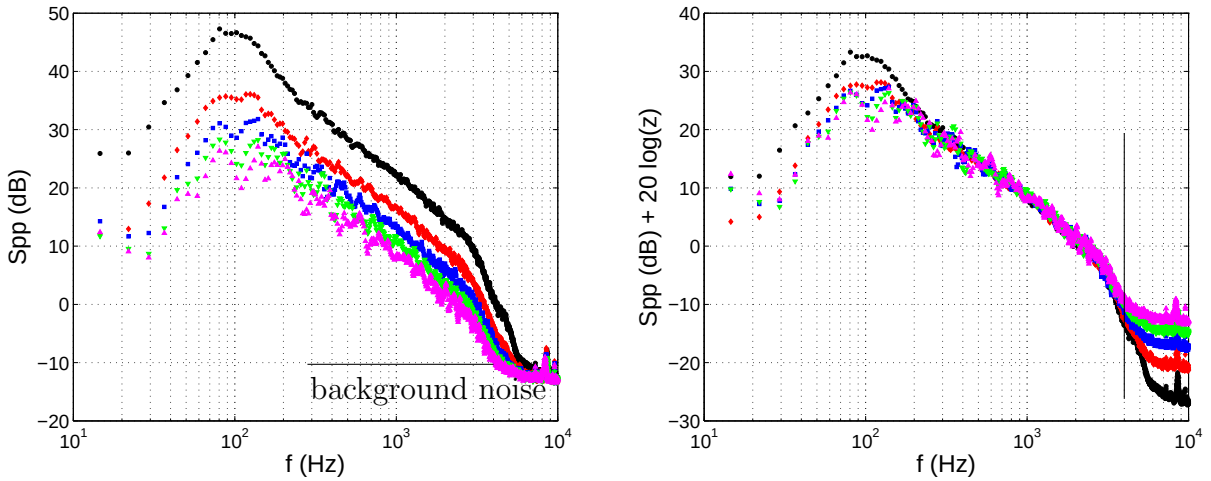

Figure 4.17.: Acoustic measurements of the jet-airfoil mock-up: (left) observer at $z = 5\ c$ (point), 10 c (diamond). 15 c (square), 20 c (upper triangle) and 25 c (lower triangle). (right) spectra scaled to $z = 25\ c$.

Once the flow field is solved and the observer position is defined, the acoustic response of the airfoil located in a turbulent stream can be computed. Integrating the unsteady pressure distribution on the airfoil obtained from the CFD solution provides the wall-normal -or so called lift- force of the source dipole. The LMS software Virtual Lab. is used to compute the compact dipole source [59] using Curle's Analogy, defined in Equation (4.4). The source strength is first imported in a data file to Virtual Lab. in frequency domain. The acoustic pressure field of the harmonic dipole source at the field point is then computed. In order to be consistent with the assumptions of following sections, the effect of the convection is neglected in the acoustic propagation. This is justified because the maximum Mach number of the impinging flow is $M_{max} = 0.03$.

The comparison of the acoustic field emitted by the airfoil for an observer located at $5c = 0.55\ d$ above the airfoil, as obtained from the measurements, a deterministic solution based on Curle's analogy and the solution (4.30) are compared in Figure 4.18. The deterministic hybrid method (thin blue line) provides a reasonable sound prediction up to 1 kHz compared to the experiments (black dots). The limit frequency is the cut-off frequency of the CFD simulation. The effect of the CFD mesh on the cut-off frequency was shown in the related reference [25]. Using a finer mesh would provide a better agreement at higher frequencies, however it will then dramatically increase the required computation time.

On the other hand, solution (4.30) with 8 spanwise segments and with the inverse strip theory is also used to handle the problem analytically (solid red line). The flow field detailed in Figure 4.14 is used. Combining the spanwise geometrical near-field formulation with spanwise segmentation provides a fair agrement with the measurements over the entire frequency range. The differences between the two spectra is less than 5 dB.

As a result, the analytical solution is shown to be applicable at any frequency, independent from the mesh resolution. The effect of the spanwise varying incoming flow condition can also be taken into account with spanwise segmentation. Experiments defined in Sections 4.3 and 4.5.2 finally show that Amiet's theory captures turbulence-interaction noise accurately at the price of some modifications for stationary airfoils. The theory will be now extended

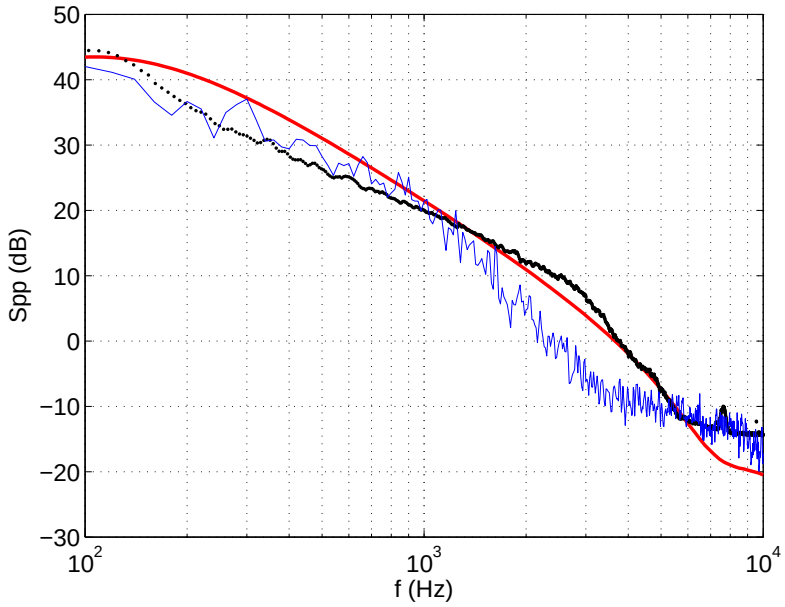

Figure 4.18.: Sound pressure spectra measured (black dots), calculated by Amiet's theory with spanwise segmentation (red solid line) and Curle's deterministic analogy (blue thin line) at (0,0,5c).

in order to deal with rotating blades.

4.6. Implementation of Rotation

The theory mentioned above has been applied to stationary airfoils with relatively simple geometries such as the optimized airfoil and the NACA 0012. However, implementing the theory to industrial rotating machinery requires additional steps. Essentially a blade is split into short strips, and each strip is interpolated by a flat plate of zero thickness.

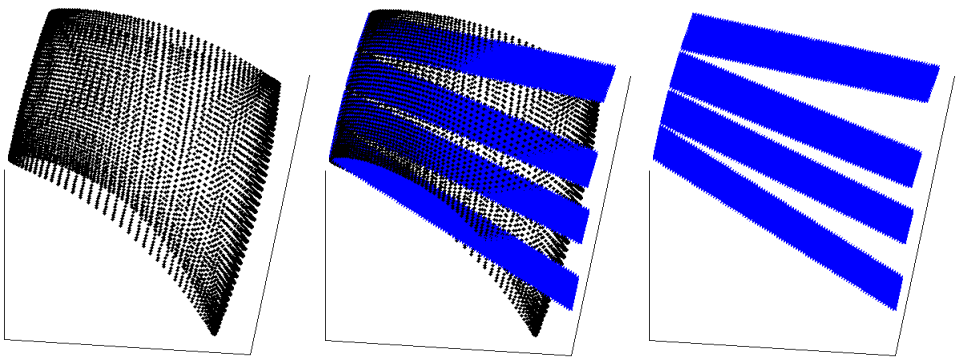

Figure 4.19.: A sketch of segmentation and linearization of a blade.

4.6.1. Linearized blades

Besides its advantage to take spanwise varying flow conditions into account, applying segmentation also provides a better representation of the actual blade geometry in terms of directivities since the blade is converted to a set of linearized strips. Figure 4.19 shows a sketch of the segmentation and linearization process from the point cloud of an actual industrial blade geometry. The blade is divided into four linearized strips for representation. Since the sources are dominant around the leading edge [96] in turbulence-interaction noise problems, it is kept as a reference line. All strips have now different pitch angles with respect to the rotation plane. Knowing that the tangential velocity increases with the radius for a fixed rotational speed, $U_t = \Omega r$, the position and orientation of the strips result in a different impinging flow speed. Figure 4.20 shows the velocity triangles for two strips. Red lines represents the linearized blade strip.

The impinging velocity onto the blade strip is then obtained from the vectorial summation of the tangential velocity and the axial velocity U_z [114].

4.6.2. Coordinate transformation

As in the tonal fan noise computations detailed in Chapter 2, the observer position is defined in a fixed reference frame with respect to the rotation plane and rotation axis by the coordinates $\{X, Y, Z\}$, as seen in Figure 4.21. In order to predict the acoustic field of a blade strip using Equation (4.30), it is required to define the origin in a reference frame attached to the blade strip, as mentioned in the isolated airfoil theory in Section 4.1. The associated coordinates are $\{x, y, z\}$ shown in Figure 4.21. Therefore, a coordinate transformation is required from $\{X, Y, Z\}$ to $\{x, y, z\}$ taking the geometry of the blade into account. Figure 4.21 shows the steps of the coordinate transformation including sweep, pitch and twist angles. It is similar to the one defined in [114] for self-noise investigation, except for the origin on the blade surface. In the self-noise prediction the origin is located at the mid-point of the trailing edge whereas for turbulence-interaction noise prediction the origin is assumed to be at the center of the blade [6, 5].

A first transformation in Figure 4.21 is applied from the fixed coordinate system at the

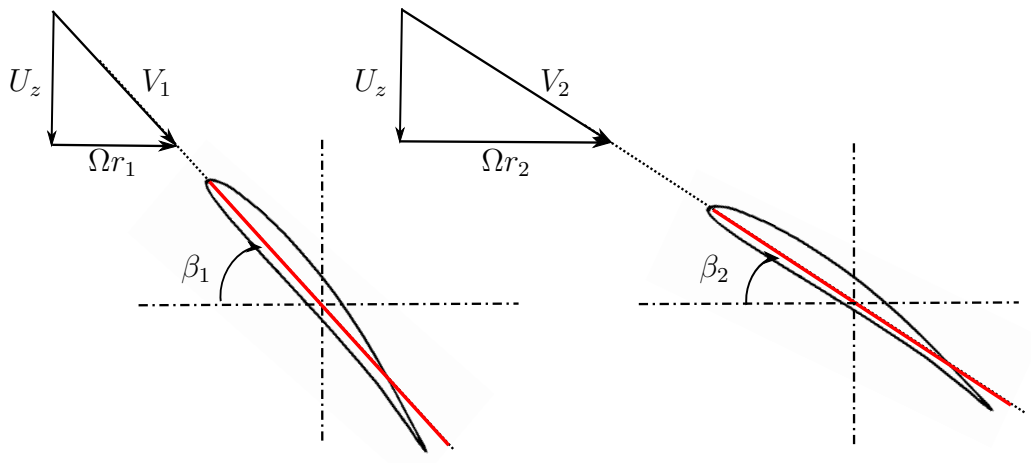

Figure 4.20.: Velocity triangles for the impinging flow

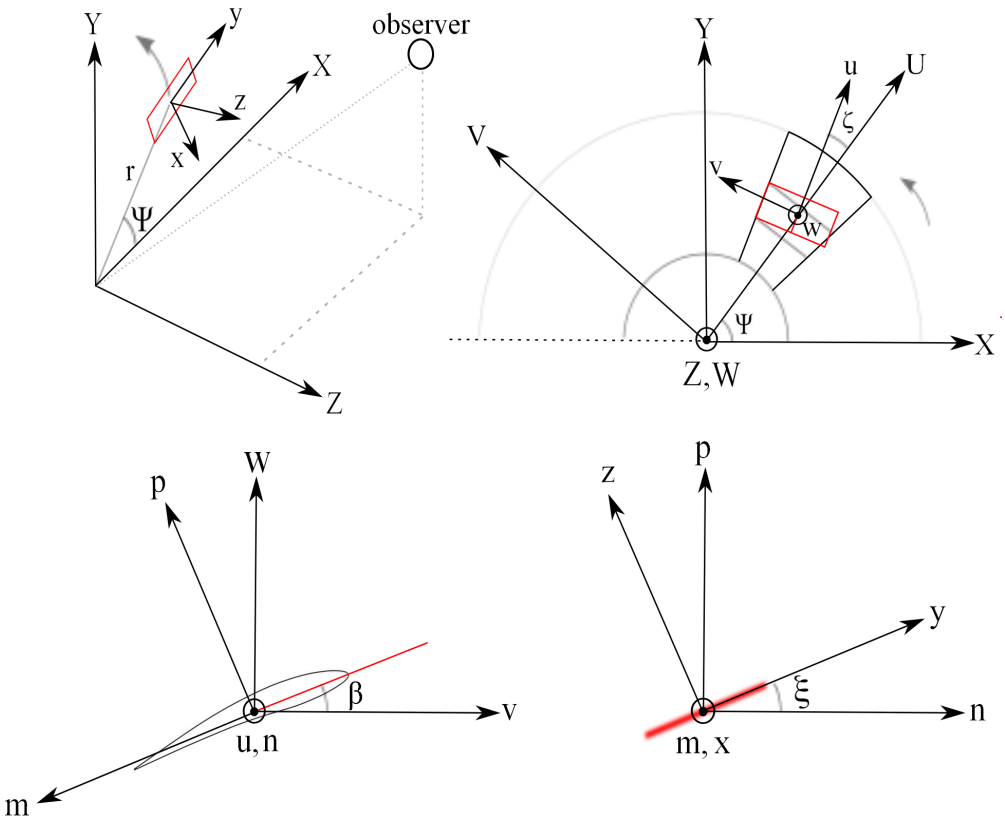

Figure 4.21.: Coordinate transformation steps

rotation center $\{X, Y, Z\}$ to the one at the center of the blade strip [114] $\{U, V, W\}$ keeping the origin fixed as

$$\begin{pmatrix} U \\ V \\ W \end{pmatrix} = M(XYZ \rightarrow UVW) \begin{pmatrix} X \\ Y \\ Z \end{pmatrix} \tag{4.38}$$

where

$$M(XYZ \rightarrow UVW) = \begin{pmatrix} \cos(\Psi) & \sin(\Psi) & 0 \\ -\sin(\Psi) & \cos(\Psi) & 0 \\ 0 & 0 & 1 \end{pmatrix}. \tag{4.39}$$

The transformation on the azimuthal angle Ψ has been performed, keeping the rotation axis fixed $Z = W$. Further, using the definition of angle ζ, a second transformation is performed on the blade strip from $\{U, V, W\}$ to $\{u, v, w\}$. The origin is now shifted from the center of rotation to the center of the blade strip.

$$\begin{pmatrix} u \\ v \\ w \end{pmatrix} = M(UVW \rightarrow uvw) \begin{pmatrix} U \\ V \\ W \end{pmatrix} \tag{4.40}$$

where

$$M(UVW \to uvw) = \begin{pmatrix} \cos(\zeta) & \sin(\zeta) & 0 \\ -\sin(\zeta) & \cos(\zeta) & 0 \\ 0 & 0 & 1 \end{pmatrix}. \tag{4.41}$$

Then, using the definition of the pitch angle β, the new coordinate system $\{m, n, p\}$ becomes

$$\begin{pmatrix} m \\ n \\ p \end{pmatrix} = M(uvw \to mnp) \begin{pmatrix} u \\ v \\ w \end{pmatrix} \tag{4.42}$$

where the transformation matrix is defined as

$$M(uvw \to mnp) = \begin{pmatrix} 0 & -\cos(\beta) & -\sin(\beta) \\ 1 & 0 & 0 \\ 0 & -\sin(\beta) & \cos(\beta) \end{pmatrix}. \tag{4.43}$$

The minus sign appears since the streamwise component is defined from the center to the trailing edge of the blade strip. Finally, taking the twist angle ξ into account, the coordinate system $\{x, y, z\}$ can be obtained from $\{m, n, p\}$ by

$$\begin{pmatrix} x \\ y \\ z \end{pmatrix} = M(mnp \to xyz) \begin{pmatrix} m \\ n \\ p \end{pmatrix} \tag{4.44}$$

where the final transformation matrix is defined as

$$M(mnp \to xyz) = \begin{pmatrix} 1 & 0 & 0 \\ 0 & \cos(\xi) & \sin(\xi) \\ 0 & -\sin(\xi) & \cos(\xi) \end{pmatrix}. \tag{4.45}$$

The position of the observer with respect to the blade strip which fits to the coordinates defined in Section 4.1 then reads

$$\begin{pmatrix} x \\ y \\ z \end{pmatrix} = M(UVW \to xyz) \begin{pmatrix} -r \\ 0 \\ 0 \end{pmatrix} + M(XYZ \to xyz) \begin{pmatrix} X \\ Y \\ Z \end{pmatrix}. \tag{4.46}$$

The transformation matrices are defined as

$$\begin{aligned} M(XYZ \to xyz) =& M(XYZ \to UVW)\ M(UVW \to uvw) \\ & M(uvw \to mnp)\ M(mnp \to xyz) \\ M(UVW \to xyz) =& M(UVW \to uvw)\ M(uvw \to mnp)\ M(mnp \to xyz). \end{aligned} \tag{4.47}$$

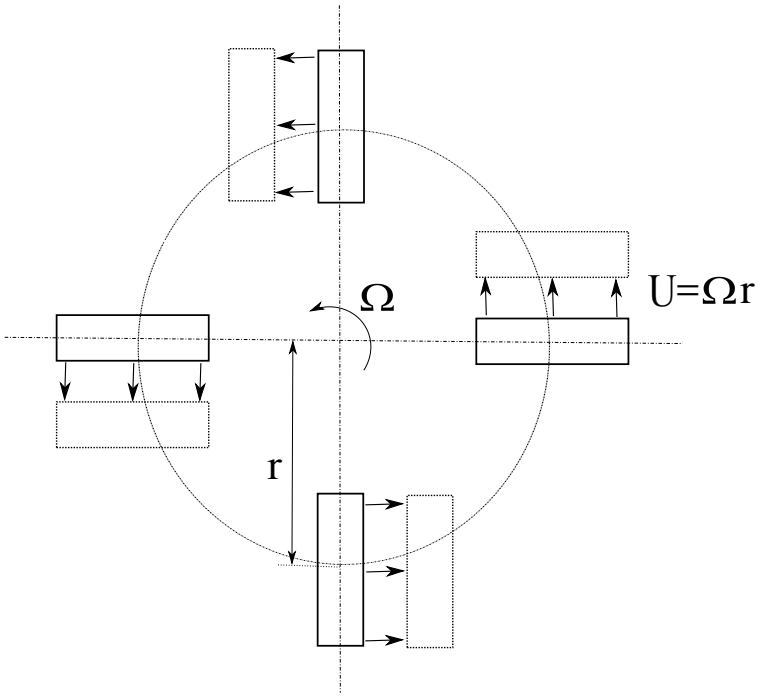

Figure 4.22.: Sketch of the rotation strategy, blades in local tangential motion

4.6.3. The Doppler effect

The turbulence-interaction noise theory for an isolated airfoil [5] has been extended [96] for low Mach number rotor blades. The steady airfoil model has been applied to each blade strip assimilating the circular motion to the locally tangential translation motion (See Figure 4.22). This is acceptable only at sound frequencies much higher than the rotational frequency, $\omega >> \Omega$ [96] for low tip Mach number fans, $M \ll 1$. The strips on the rotor blades are again assumed to be linearized in order to apply the theory described above.

Due to the relative motion between the source and the observer, the emitted frequency ω_e from the blade strip and the observed frequency ω_o are not equal. The frequency shift is known as the Doppler correction factor.

The frequency heard by the observer is equal to the rate of change in the phase definition Θ of the pressure field [4] as

$$\omega_o = \left(\frac{\partial}{\partial t} + c_0 \mathbf{M} \cdot \nabla \right) \Theta \tag{4.48}$$

where $\mathbf{M}$ is the Mach number of the relative motion between the source and the observer. Θ is defined as

$$\Theta = \omega_e \left(t + \frac{Mx - xx_0 - \sigma}{c_0 \beta^2} + \frac{xx_0 + yy_0\beta^2}{c_0 \beta^2 \sigma} \right). \tag{4.49}$$

Introducing another geometrical far-field assumption in order to simplify the derivation, the blade strip is assumed as a point source by neglecting the terms containing x_0 and y_0. The following approximation can be made

$$\Theta \approx \omega_e \left(t + \frac{Mx}{c_0 \beta^2} + \frac{\sigma}{c_0 \beta^2} \right). \tag{4.50}$$

The observed frequency is then related to the emitted frequency with

$$\frac{\omega_o}{\omega_e} = 1 + \frac{M_t \cdot \widehat{OS}}{1 - M_r \cdot \widehat{OS}} \tag{4.51}$$

where M_t and M_r are the tangential and relative Mach numbers, respectively. $\widehat{OS}$ is the unit vector from the observer to the source [114].

$$\begin{aligned} M_t &= -M_t \sin\psi \; i + M_t \cos\psi \; j \\ M_r &= -M_t \sin\psi \; i + M_t \cos\psi \; j - M_z k \\ \overrightarrow{OS} &= (x - x_s) \; i + (y - y_s) \; j + (z - z_s) \; k \\ \widehat{OS} &= \frac{x - x_s}{|\overrightarrow{OS}|} \; i + \frac{y - y_s}{|\overrightarrow{OS}|} \; j + \frac{z - z_s}{|\overrightarrow{OS}|} \; k. \end{aligned} \tag{4.52}$$

Representing the blade strip as a point source which rotates around the $z-$axis with a radius r (See Figure C.2), the observer-source vector components become

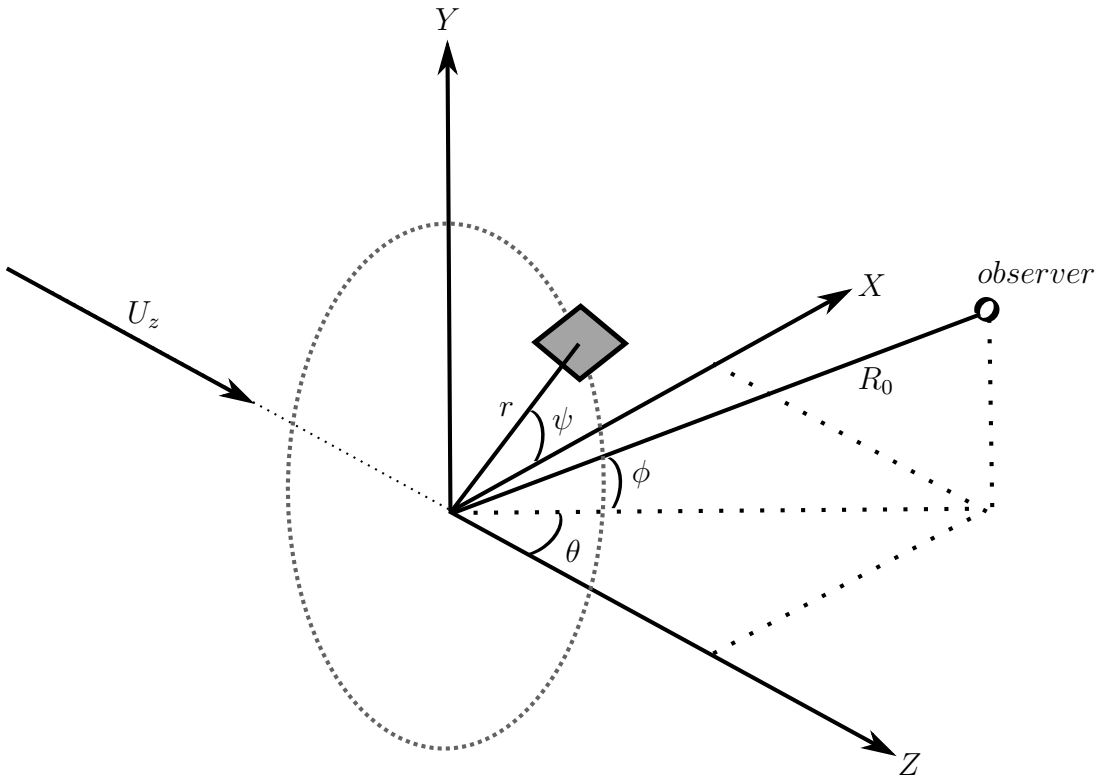

Figure 4.23.: Sketch of the source and the observer for an axial fan.

$$\begin{aligned} x - x_s &= R_0 \cos\phi \sin\theta - r\cos\psi \\ y - y_s &= R_0 \sin\phi - r\sin\psi \\ z - z_s &= R_0 \cos\phi\cos\theta - M_z\ |\overrightarrow{OS}|. \end{aligned} \tag{4.53}$$

For an observer located at any point in the $xyz-$coordinate system, the magnitude of the coordinate vector $\overrightarrow{OS}$ becomes

$$\begin{aligned} &|\overrightarrow{OS}| = \frac{R_0}{1-M_z^2} \\ &\left(-M_z\cos\theta\cos\phi + \sqrt{(M_z^2\cos^2\theta\cos^2\phi + 1 - M_z^2) + (1-M_z^2)\left((\Upsilon - r/R_0)^2 - \Upsilon^2\right)}\right). \end{aligned} \tag{4.54}$$

where $\Upsilon = \cos\phi\sin\theta\cos\psi + \sin\phi\sin\psi$.

Taking the convection in the axial direction and the azimuthal motion into account, the unit vector reads

$$\widehat{OS} = \frac{R_0\cos\phi\sin\theta - r\cos\psi}{|\overrightarrow{OS}|}\ i + \frac{R_0\sin\phi - r\sin\psi}{|\overrightarrow{OS}|}\ j + \left(\frac{R_0\cos\phi\cos\theta}{|\overrightarrow{OS}|} - M_z\right)\ k. \tag{4.55}$$

Combining Equations (4.51), (4.54) and (4.55), the relation between observed and emitted frequencies becomes

$$\frac{\omega_e}{\omega_o} = 1 + \frac{M_t(\cos\phi\sin\theta\sin\psi - \sin\phi\cos\psi)}{\sqrt{(M_z^2\cos^2\phi\cos^2\theta + 1 - M_z^2) + (1-M_z^2)\left((\Upsilon - r/R_0)^2 - \Upsilon^2\right)}}. \tag{4.56}$$

It is seen that, the definition of $\widehat{OS}$ is a function of the radius of the fan. For an observer located in the far-field, $r/R_0 \to 0$, the new formulation converges to the one in the far-field as defined in the related reference [114]

$$\frac{\omega_e}{\omega_o} = 1 + \frac{M_t(\cos\phi\sin\theta\sin\psi - \sin\phi\cos\psi)}{\sqrt{(1 - M_z^2\cos^2\phi\sin^2\theta)}}. \tag{4.57}$$

The relation between observed and emitted frequencies is then a function of the observer position, the axial and the tangential Mach numbers.

The relative motion between the source and the observer and its effect on the acoustic field can also be dealt with considering a fixed source and a moving observer [96]. The acoustic pressure at the moving observer is related to the one for the stationary observer by

$$p^m(t) = p^f\left(\frac{\omega_o}{\omega_e}t\right). \tag{4.58}$$

Superscripts ^{f} and ^{m} represents fixed and moving observers, respectively. The acoustic PSD at the observed then reads (See Appendix C for further derivations.)

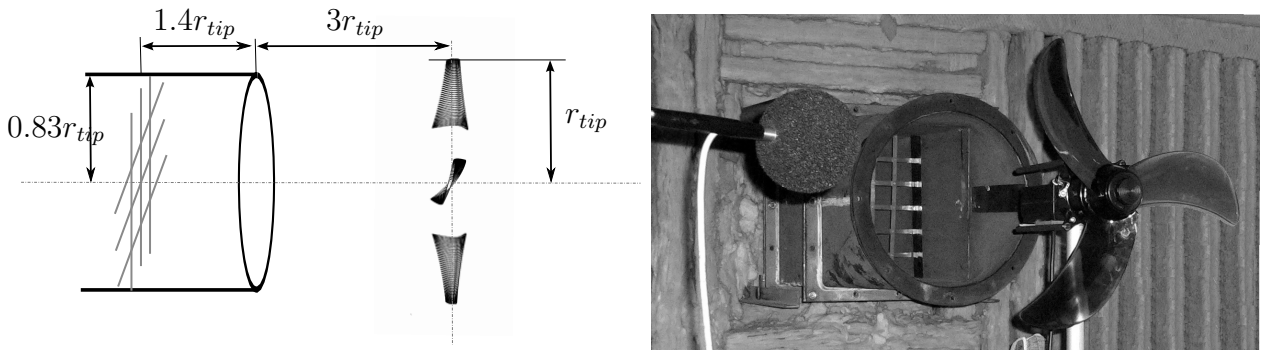

Figure 4.24.: Sketch of the experimental axial fan-wind tunnel setup (left), photo taken in the anechoic chamber (right). The microphone is at 3 r_{tip} downstream and 2.5 r_{tip} away from the rotation axis.

$$Spp^m(\omega_o) = \frac{\omega_e}{\omega_o} Spp^f(\omega_e). \tag{4.59}$$

The rotation is then accounted through an azimuthal averaging including the change of coordinates and the Doppler factor [4].

$$S_{pp}(X, Y, Z, \omega_o) = \frac{B}{2\pi} \int_0^{2\pi} \frac{\omega_e}{\omega_o} \, S^{\psi}_{pp}(x, y, z, \omega_e) \mathrm{d}\psi. \tag{4.60}$$

$\psi = \Omega \, t$ represents the current position of the blade strip as shown in Figure 4.21.

Equation (4.60) is the general solution of the broadband noise emitted by rotating blades accounting the Doppler factor. However, for low-speed fan applications, the Doppler factor has been shown to be negligible [88]. (See Appendix C for the effect of the Doppler factor on the tested configurations.) The rotation effect is finally obtained through a simplified azimuthal averaging as

$$S_{pp}(X, Y, Z, \omega) \approx \frac{B}{2\pi} \int_0^{2\pi} S^{\psi}_{pp}(x, y, z, \omega) \mathrm{d}\psi. \tag{4.61}$$

Formulations (4.60) and 4.61 assume that there is no blade-to-blade correlation and that each fan blade acts independently of the other. This assumption is valid at high frequencies where the same gust is not cut by the succeeding blades [8]. Hence, the number of blades appears as a multiplication factor only. Therefore, doubling B increases the acoustic PSD by $10 \log_{10}(2) = 3$ dB if the fan is assumed to be subjected to the same flow-field.

The one-dimensional integral in Equations (4.60) and (4.61) can be solved using classical numerical methods such as trapezoidal or other Newton-Cotes techniques [118]. However, using Newton-Cotes techniques will result in additional asymmetry in the near-field of the fan, since each azimuthal position of the strips is weighted by different coefficients. Therefore, the trapezoidal method is used in the same order with the Newton-Cotes technique without introducing any additional asymmetry.

The theory for turbulence-interaction noise of a stationary airfoil detailed above is finally implemented to a low-Mach number rotating machinery problem. Equation (4.61) will now be used to predict the free-field of a low-Mach number axial fan.

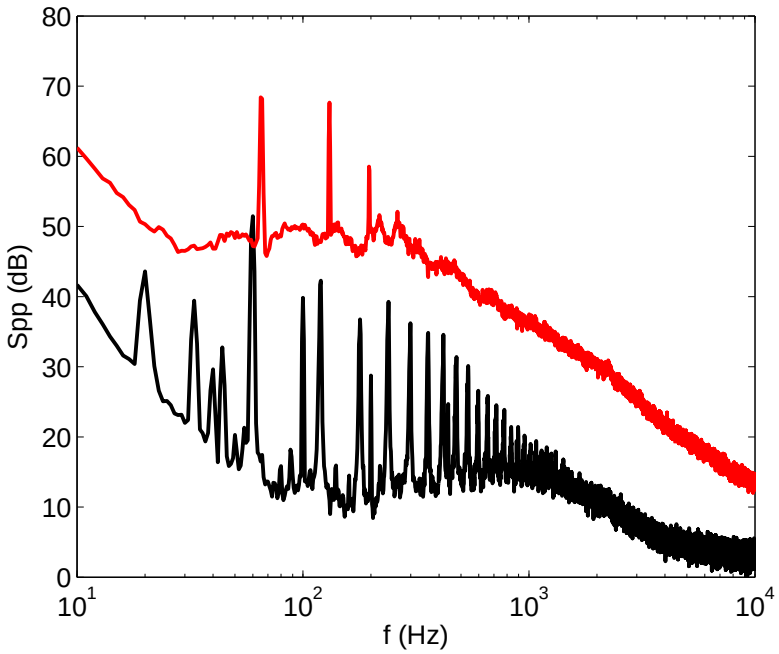

Figure 4.25.: Free-field measurements of the axial fan, operating with (red) and without (black) the turbulent jet-flow at 3 r_{tip} downstream and 2.5 r_{tip} away from the rotation axis.

4.7. Free-Field Broadband Noise of a Low-Speed Axial Fan

In order to measure the acoustic free-field of a fan, a set of experiments is performed in the anechoic chamber at ECL. A low-speed axial cooling fan for home applications is used. Figure 4.24 shows the experimental axial fan-wind tunnel setup.

The rotor consists of 3 uniformly distributed blades and rotates at 1200 rpm. The Blade Passing Frequency (BPF) is then equal to 60 Hz. The tip radius of the blades, $r_{tip} = 0.22$ m makes the tip Mach number around 0.08. The microphone is located at 3 r_{tip} away from the rotation center and 2.5 r_{tip} from the rotation axis. Since the theory described above is related to turbulence-interaction noise, the rotor must be operated in the presence of an upstream turbulent flow. This is achieved by putting the rotor at the exit of a nozzle where the flow is disturbed by an upstream grid (see Figure 4.24) [112]. The rotation plane is located 3 r_{tip} downstream of the nozzle exit. The jet core velocity is fixed to 15 m/s, making jet Mach number equal to 0.04.

Figure 4.25 shows the measured acoustic spectra of the rotor noise in free-field with and without the incoming turbulent flow, represented as red and black lines, respectively. In the absence of turbulence, the tonal component of the fan noise is dominant in the whole frequency range. The tone around 100 Hz and harmonics are generated by the electric motor of the fan. In contrast, operating the fan in the upstream turbulent flow makes the broadband component dominant and only the first three harmonics of BPF emerge. It is also observed from the shift of the BPFs that the incoming flow results in a 100 rpm increase in the rotational speed of the fan, which is also taken into account in the numerical model. The tonal noise of the fan is increased from 51 dB to 69 dB and from 42 dB to 68 dB for the first and second harmonics, respectively. This change in the discrete frequency noise of

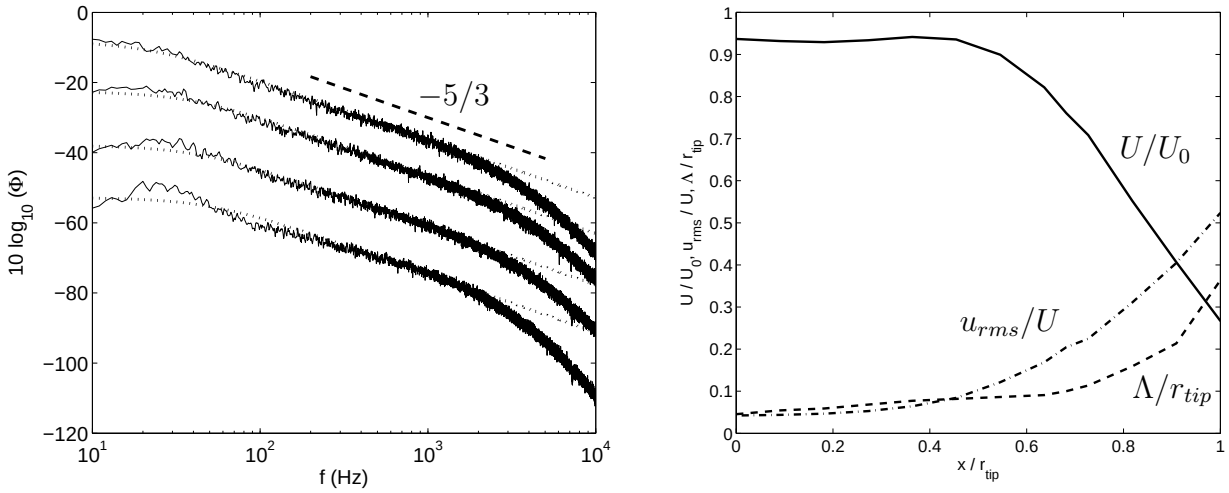

Figure 4.26.: Turbulent spectra (left), measured (solid) and theoretical (dotted) and normalized flow parameters (right), mean velocity (plain), turbulent intensity (dash dot) and turbulent length scale (dashed)

the fan is not addressed in this chapter.

Since the difference of the broadband spectrum is well significant, the noise generated by the fan can then be considered essentially turbulence-interaction noise. Hence the model described above can be applied to predict the acoustic field.

The semi-analytical model requires the description of the incoming flow-field numerically or experimentally. In the stationary airfoil configuration detailed in Section 4.5.2, the flow-field was solved numerically. In the current application, the impinging flow-field is directly measured. The rotor is removed and the turbulent flow field at the location of the rotation plane is measured using a hot-wire anemometry. The measurements are taken on the horizontal line starting from the center of the jet axis till the length of the tip radius of the fan. Once the turbulent spectrum is measured at a given location, using the measured mean flow speed and the turbulent intensity values, the turbulent length scale is then obtained by fitting the von Karman model defined in Equation (4.31) to the measurement [109]. Figure 4.26 (left) shows the measured velocity spectra (plain) at the equivalent center of the strips and the superimposed von Karman spectra (dotted). The slope of the spectra fits with the $-5/3$ power law showing that the turbulent flow can be locally assumed isotropic and homogeneous [102], at least for the sake of the present evaluation of acoustic response of the fan. The plots are shifted from each other by steps of 10 dB for clarity.

All the turbulent flow parameters are shown in Figure 4.26 (right) as functions of the radial position of the probe. The mean flow and the turbulent length scales are non-dimensionalized with the jet outlet velocity and the tip radius of the fan, respectively. The decay of the mean flow at the higher values shows that the blade tip is embedded in the shear layer of the jet. The probe is out of the jet flow at the highest values of the horizontal position since the radius of the nozzle is equal to 83% of the one of the rotor. Considering the position of the rotor with respect to the jet-flow, the turbulent flow impinging is not only due to the grid turbulence but also due to the mixing layer.

Once the flow-field is known, extracting the required parameters, U, u_{rms} and Λ, the acoustic response of the low-speed axial fan can be obtained using Equation (4.61).

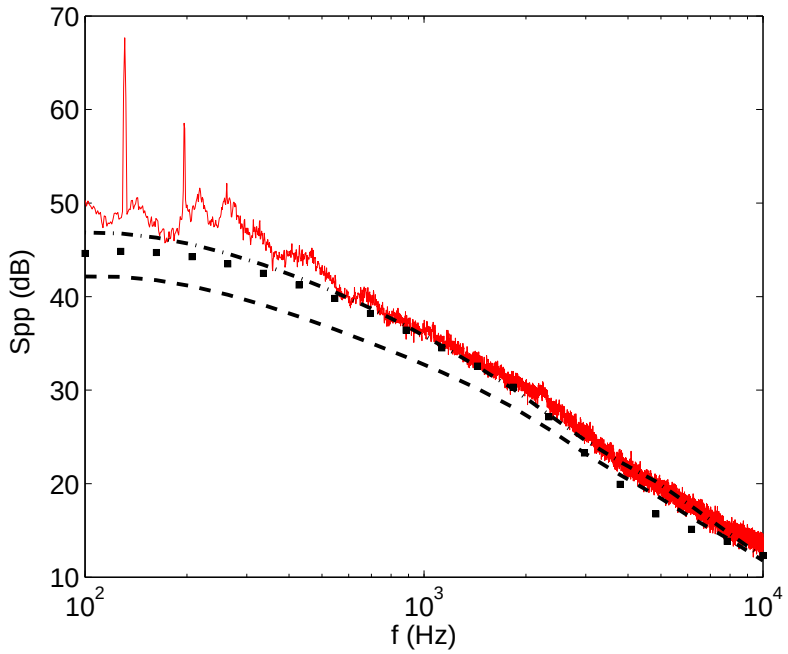

Figure 4.27.: Free-field spectra of the axial fan at 3 radii away from the rotation center and 2.5 radii away from the rotation axis, measurements (red) and using strips (dashed), inverse strips (dash-dots) and correlated strips theory (symbols).

Figure 4.27 shows the measured and computed free-field spectra of the fan at 3 radii away from the rotation center. The blade is split into 4 spanwise segments and the von Karman model spectrum is selected for the numerical simulations. The red line represents the measured spectrum. The dashed line, dash dots and symbols correspond to the model described above using classical strip, inverse strip and correlated-strips theories, respectively [67, 68]. The 5 dB difference between the dashed and symbols addresses the already pointed effect of large hydrodynamic wavelengths. A good agreement is observed with the measurements and the numerical model using classical strip theory at frequencies above 3 kHz. Furthermore, taking the effect of the large wavelengths into account firstly and of the spanwise correlation secondly improves the solution at lower frequencies compared to the classical strip theory. For frequencies higher than 400 Hz, the difference between the measurements and the model is not more than 3 dB. The disagreement at the lowest frequencies can be due to additional sound sources such as stall [122], separation on the blade or the anisotropic behavior of the turbulence developing away from the center of the mixing layer.

As a result, the acoustic free-field response of a low-Mach number axial fan due to impinging turbulent flow can be computed using the semi-analytical method described above. Hence, it is a useful tool to compute the acoustic field of a fan combined with experimental or numerical description of the incoming flow-field.

4.8. Conclusion

It has been shown that, based on a minimum knowledge of the flow-field the acoustic response of a stationary airfoil and of a low-speed axial fan can be computed in a semi-analytical man-

ner. The proposed method has been extended in order to apply to industrial applications.

Considering the observer position with respect to the airfoil span-length, an intermediate level of correction is proposed. The extended formulation provides a more accurate information about the acoustic field. The new formulation is validated against numerical simulations and measurements.

The spanwise varying flow conditions are taken into account with different segmentation techniques. A new technique taking the correlation of adjacent spanwise strips into account has been proposed. Compared to the existing literature, the new method improves the predictions. It is also more efficient in terms of computation time.

Finally, the analytical method has been implemented to a benchmark low-speed fan application. A good agreement has been satisfied in the comparison with the measurements. It is concluded that turbulence-interaction noise generated by a low-speed axial fan can be predicted accurately in the free-field. However, the free-field conditions are far from what is encountered in industrial applications, hence the scattered acoustic field by surrounding surfaces needs being considered. The following chapter will address that point in the context of broadband fan noise.

Chapter 5.

Broadband Fan Noise Scattering

This chapter deals with the broadband noise scattered by an obstacle analytically and experimentally. The application of the scattering techniques to turbulence-interaction noise is focused on.

The scattered-field of discrete-frequency fan noise was addressed in Chapter 3 analytically and experimentally, where the source field was defined in a deterministic manner. However, due to the statistical characterization of turbulence, the numerical method mentioned cannot be applied directly. Hence, the classical solution is re-formulated for the broadband scattering problem in this chapter.

The scattered-field of the turbulence-interaction noise modeled in Chapter 4 is first investigated for the stationary airfoil application. The experiment described in Section 4.5.2 involves an airfoil placed in the development region of a turbulent jet. Prediction of the acoustic free-field of the airfoil was addressed by the approaches described in the corresponding chapter. Acoustic scattering techniques detailed earlier are now employed first for the jet-airfoil test-case in presence of a benchmark scattering obstacle. The model is later implemented to the low-Mach number axial fan described in Section 4.7.

5.1. Broadband Scattering - Stationary Airfoil

The stationary airfoil located in the transitional region of a turbulent jet described in Section 4.5 is considered as the broadband noise source. In order to compute its scattered field, a flat screen is introduced in the existing jet-airfoil installation. The usage of a simple benchmark obstacle also provides simplicity to deal with the scattering problem analytically. Figure 5.1 shows a sketch of the test-case and the screen located in the anechoic chamber.

The screen is $15c$ in width and the airfoil is located facing the middle of it on the horizontal axis. However, due to the supports of the screen, it covers $5c$ downstream the airfoil and $15c$ in the upstream direction on the vertical axis, with a total height of $20c$. In order to observe the effect of the scattered acoustic waves clearly, the screen should be placed close to the airfoil. Therefore a distance of $5c$ has been selected staying in its spanwise geometrical near-field, at $z/d \approx 1.14$. According to the assumptions of the model detailed in Section 4.1, the screen is located in the acoustic far field for most frequencies considered in this case. Additionally, the screen is located away from the turbulent region of the jet in order not to disturb the incoming flow. Hence, the same source data could be used without repeating the CFD simulations.

Experiments have been conducted for comparison of the sound pressure levels with the broadband noise predictions in free-field and including scattering effects. The facility described in Section 4.5.2 is used with the same flow conditions [120, 27]. Figure 5.2 shows the measured free-field (black) and scattered acoustic field (red) of the configuration as seen in sketch 5.1. The thin line represents the background noise. At frequencies higher than

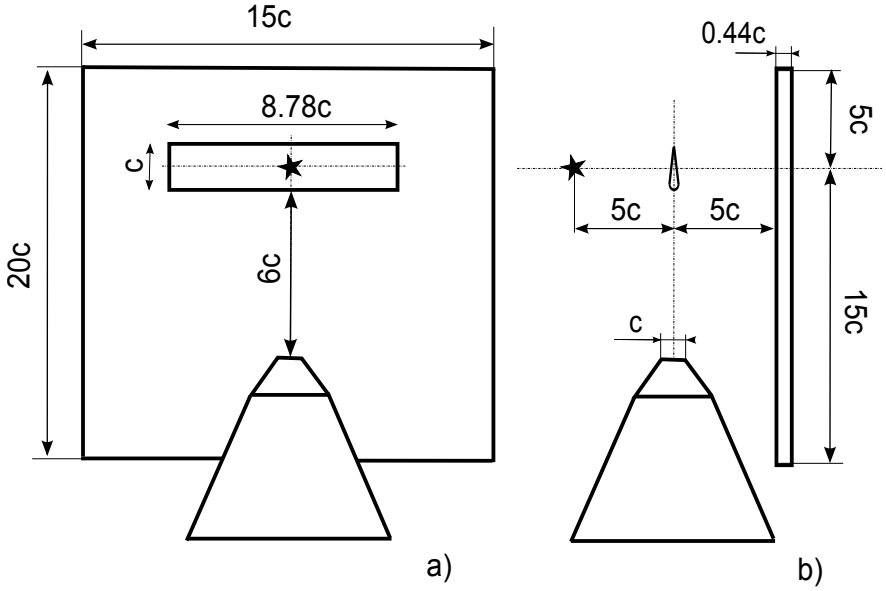

Figure 5.1.: Sketch of the experimental jet-airfoil test-case including the scattering screen, a) Front view, b) Side view

6 kHz, the sound measured by the microphone is disturbed by the background noise and should not be considered in the comparisons. The interference fringes due to the scattering obstacle result in a wave-like spectrum with respect to the free-field one. The effect of the obstacle is less than 5 dB at the frequencies of interest.

Using the methods detailed in Chapters 3, the acoustic scattering could be handled with numerical and analytical methods. The numerical methods are investigated first.

5.1.1. Numerical broadband scattering techniques

In order to compute the scattered field of deterministic sources, BEM is a useful tool especially when the fluid domain is unbounded [34]. Therefore the same method as used for tonal fan noise can be employed for the current problem using the deterministic source field obtained from the unsteady CFD simulation. It is worth noting that in the BEM formulation the fluid is assumed at rest. The effect of convection is not taken into account in the scattering problems. In the applications described in this chapter, the Mach number does not exceed 0.08. Therefore neglecting the convection effects is reasonable.

5.1.1.1. Boundary Element Method

It was shown in Equation 3.1 that in order to compute the total pressure field of a source, that field is first decomposed into incident and scattered contributions. Using the deterministic source described in Section 4.5.2 [25], the incident field pressure p_i can be obtained from Equation (4.4) [33]. The scattered pressure p_s is then computed using the Indirect Boundary Element Method, where the rigid Neumann boundary conditions are imposed on the scattering surface [35].

Figure 5.3 shows the incident (thick) and scattered (thin) acoustic fields of the jet-airfoil and flat screen test-case. Both computations are performed in LMS software Virtual Lab. [59], using the harmonic source strength provided from the CFD simulation [27]. The airfoil

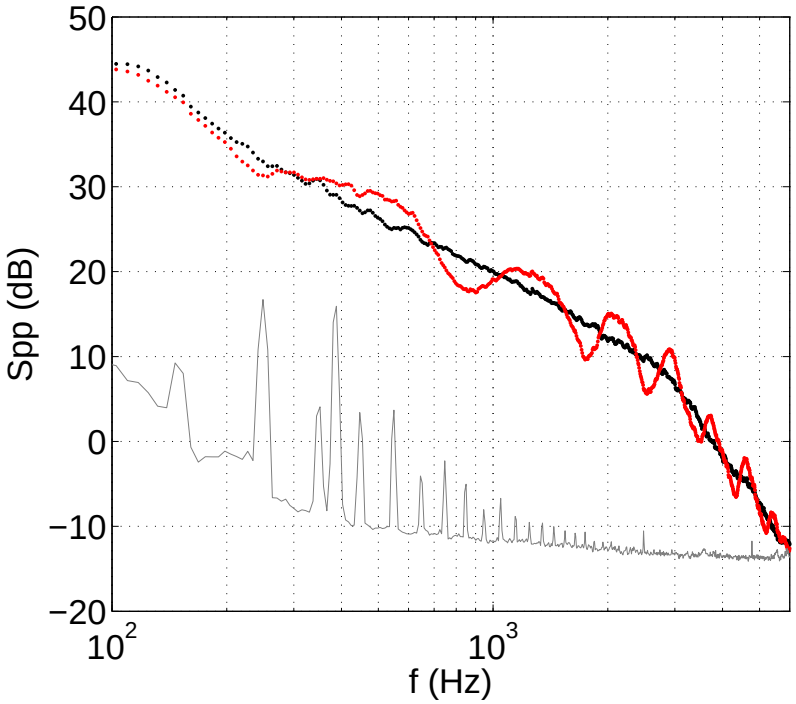

Figure 5.2.: Sound pressure spectra measured in free-field (black dots), with the screen (red dots) and the background noise (thin line) at $(0, 0, 5c)$ with the screen parallel to the airfoil at $z = 5c$.

is reduced to a point dipole assuming it is acoustically compact at the frequencies of interest. The difference between both computed spectra addressing scattered-field effects is less than 5 dB.

However, since the broadband noise model described in Section 4.1 is based on a statistical description of the source field [102], rather than a deterministic one, the BEM formulation employed is not capable to handle this problem directly. The deterministic BEM problem [34, 63] is therefore re-formulated.

5.1.1.2. Acoustic Transfer Vectors approach

In the proposed approach, the acoustic pressure field is first decomposed into incident and scattered components as showed in Equation 3.1. The total PSD then becomes

$$S_{pp} = S_{p_i p_i} + S_{p_i p_s} + S_{p_s p_i} + S_{p_s p_s} \tag{5.1}$$

where the first term on the right hand side of the equation is the free-field response of the airfoil which can be solved with Equations (4.24), (4.30) and (4.26) depending on the problem addressed. Remaining terms are solved by the BEM methodology [34]. In this BEM framework, an Acoustic Transfer Vector (ATV) formulation [45] is employed to relate the acoustic pressure at a listener point to the wall-normal velocity of the elements that discretize the surface of the scattering body

$$p_s(\omega) = \{\mathbf{ATV}(\omega)\} \cdot \{v_{n_s}(\omega)\}. \tag{5.2}$$

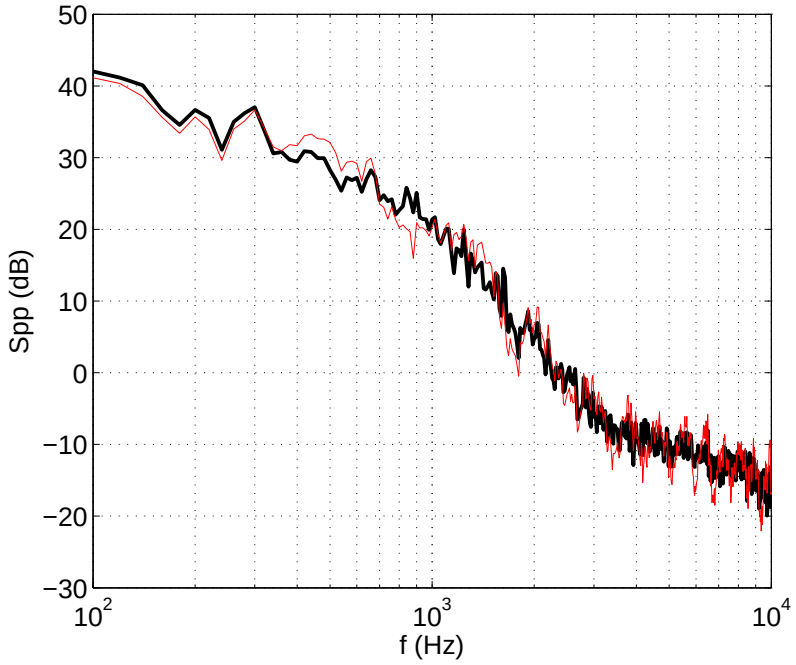

Figure 5.3.: Acoustic pressure spectra computed with the Curle's analogy for free-field (black) and Curle's analogy combined with BEM (thin red line) at $(0, 0, 5c)$.

$\{\mathbf{ATV}(\omega)\}$ is the Acoustic Transfer Vector obtained by solving the BEM problem with unit normal velocities on the acoustic mesh. In order to satisfy the rigid Neumann boundary condition on the acoustic mesh [35], the velocities $\{v_{n_s}(\omega)\}$ in Equation (5.2) are the opposite projection of the incident velocity, $v_{n_s} = -v_{n_i}$.

The incident velocity term, v_{n_i}, is computed from the gradient of the incident pressure defined in Equation (4.5)

$$v_{n_i}(\mathbf{x}, \omega) = \frac{\mathrm{i}}{\rho_0 \omega} \frac{\partial p(\mathbf{x}, \omega)}{\partial n}. \tag{5.3}$$

In order to be consistent in between the assumptions, the same acoustic far-field approximation is made in the derivations of v_{n_i}. Therefore it applies to the position of the scattering surface next to the source, as for the listener position.

Combining Equations (5.1) to (5.3), the total acoustic PSD becomes [123]

$$S_{pp} = S_{pp,i} - S_{pv} \cdot \mathbf{ATV}^T - \mathbf{ATV}^* \cdot S_{vp} + \mathbf{ATV}^* \cdot S_{vv} \cdot \mathbf{ATV}^T \tag{5.4}$$

where S_{pv} and S_{vp} are the cross-power spectra of the incident velocity evaluated over the acoustic mesh and the incident acoustic pressure at the listener point. The S_{vv} is the auto and cross-power spectra of the incident velocities over the acoustic mesh. The $\{\mathbf{ATV}(\omega)\}$ is now a matrix composed of the Acoustic Transfer Vectors for each listener point. The superscripts ^{T} and * stand for the matrix transpose and the complex conjugate operator, respectively. A detailed derivation of Equation (5.4) is given in Appendix E.

Since Equation (5.4) is represented with the incident acoustic field variables, using the derivation of the incident acoustical velocity detailed in Appendix E, the cross-correlation

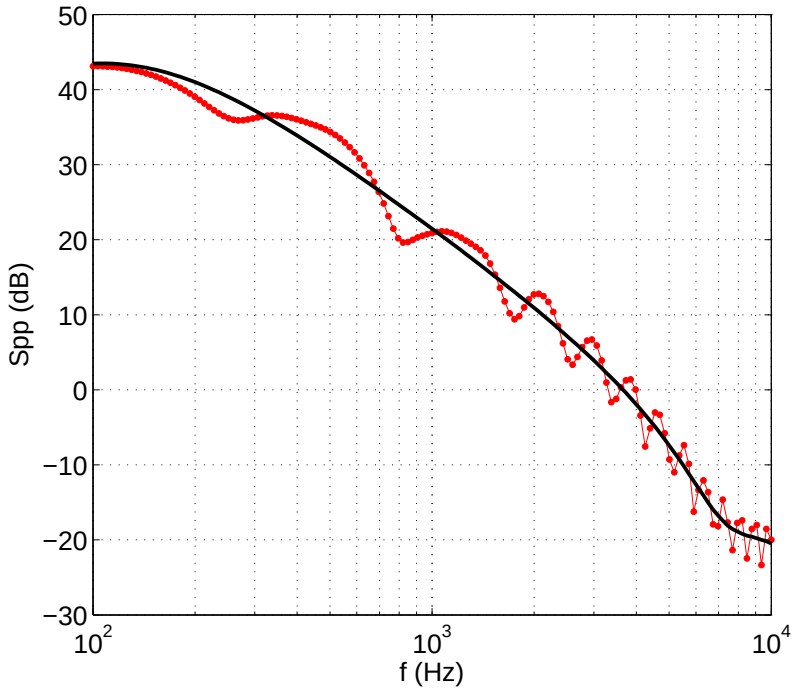

Figure 5.4.: Acoustic PSD computed with Amiet's formulation in free-field (black) and Amiet's formulation combined with ATV technique (symbols line) at $(0, 0, 5c)$.

terms of the velocity and pressure fields and the auto- and cross-correlation of the incident velocity field can be computed.

In order to compute the **ATV**s, the BEM model of the problem is first defined in LMS software Virtual Lab. considering the frequencies of interest. Once the mesh quality, 10 elements per wavelength as a rule of thumb [35], is satisfied, the Acoustic Transfer Vector Analysis case is solved in Virtual Lab. for the pre-defined observer points. The case file is then imported to Sysnoise and the **ATV**s are exported at the frequency of interest. It can be seen that **ATV**s are functions of the properties of the propagation medium (such as density or speed of sound), acoustic mesh, field point and the frequency of interest. They are independent of the source position. Hence, the same **ATV**s can be used for different source positions in the same geometrical problem.

Once the auto- and cross correlation matrices defined in Equation (5.4) are computed and the **ATV**s are exported, the scattered acoustic field due to turbulence-interaction noise can be predicted. Figure 5.4 shows the application of the theory described above to the current jet-airfoil configuration in presence of the flat plate. The source field detailed in Section 4.5 is again used including 8 spanwise strips obtained with inverse strip theory. The spanwise geometrical near-field correction is also considered in the model. The line and symbols represent the free and scattered fields of the broadband noise generated by the interaction of the turbulent jet flow and the stationary airfoil obtained via the the semi-analytical model combined with the **ATV** analogy of BEM framework, respectively. Similar to the ones showed in Figures 5.2 and 5.3, the total spectrum oscillates around the one in free-field conditions with differences less than 5 dB.

It is shown that the scattered field of the broadband noise generated by the jet-airfoil test-

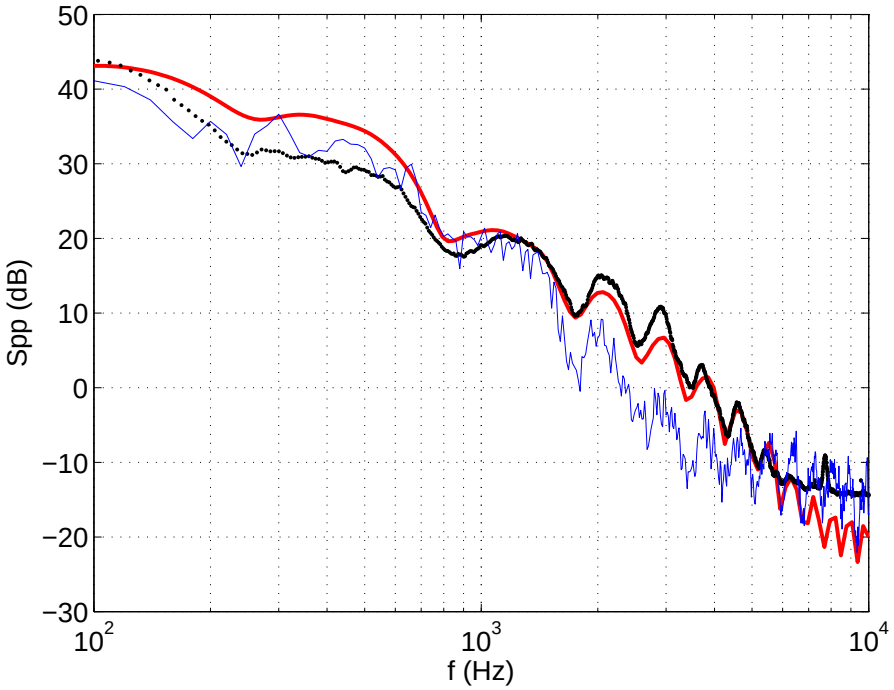

Figure 5.5.: Sound pressure spectrum computed with the ATV model (thick) using 8 segments, Curle's deterministic analogy combined with BEM (thin blue line) compared with the measurements (dots) at (0,0,5c).

case can be dealt with numerical scattering techniques using the deterministic and statistical definitions of the source field. Figure 5.5 shows the comparison of the numerical methods and the measurements. The thick and thin lines represent the semi-analytical model combined with the ATV theory and Curle's approach combined with the classical BEM approach, respectively. Black dots represent the measurements performed in the anechoic chamber. Both numerical methods capture the interference fringes due to scattering at frequencies between 100 Hz and 7500 Hz. Higher frequencies are disturbed by the background noise. Both methods provide a good agreement up to 1 kHz, where the difference is less than 5 dB. However, Curle's method combined with the BEM methodology fails at frequencies more than 1 kHz, as in Figure 4.18. Since the scattered-field computations are based on the ones in the free-field, the deviation again starts from the cut-off frequency of the CFD [27]. However, the ATV method combined with the semi-analytical model provides a good agreement in the entire frequency range of interest. Since it does not depend on the mesh resolution, the semi-analytical model is a useful tool for computing scattered fields.

Finally, Figure 5.6 shows the difference between the scattered-field and free-field spectra shown in Figure 5.5 and 4.18. The solid line, symbols and dashed line represent the deterministic BEM method, ATV approach and measurements, respectively. Both numerical models are able to handle the effects of the scattering screen. Both amplitude and fringes are captured accurately compared with measurements.

It is concluded that the effects of the scattering obstacle can be computed using numerical techniques. Since the numerical methods are based on BEM formulation, using deterministic or statistical source definitions, the acoustic scattering including complex geometries can be

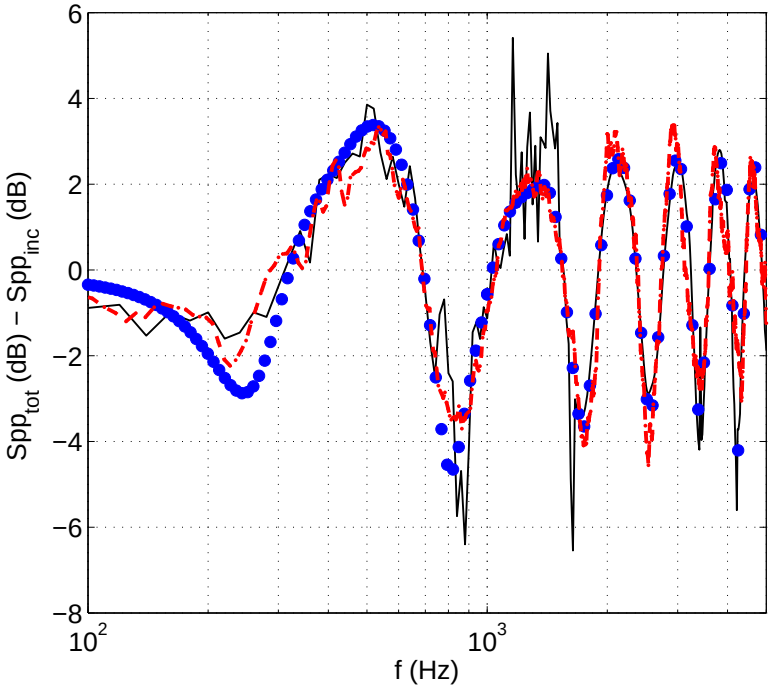

Figure 5.6.: Ratio of the total acoustic PSD to the incident one, Curle's formulation with indirect BEM (solid line), Amiet's analogy with ATV (symbols) and experiments (dashed line).

addressed.

Furthermore, since the scattering obstacle is a flat screen, the analytical scattering methods defined in Chapter 3, can also be employed.

5.1.2. Analytical scattering techniques

Relatively simple scattering problems can be dealt with analytical methods including some simplifications [101]. Since the scattering obstacle considered here is a finite flat screen, the methods described in Chapter 3 are able to handle the problem at high frequencies. First, the image model is applied to the same configuration.

5.1.2.1. Method of images

At higher frequencies, where the wavelength is much smaller than the width and height of the scattering screen, the screen can be assumed infinite. It can therefore be replaced by an image source. The deterministic source is obtained directly from the unsteady pressure fluctuations on the airfoil surface extracted from the CFD simulation. Assuming the airfoil is acoustically compact, both the primary and image sources become point dipoles. The image dipole has then the same source strength but with the opposite phase.

In the semi-analytical approach mentioned in Section 4.1, the image source becomes an image airfoil, which is represented as spanwise and chordwise distributed dipoles. The total acoustic field is then equal to the summation of the primary and image sources, $p = p_{pr} + p_{im}$. Subscripts pr and im indicates the primary and the image sources, respectively. Introducing

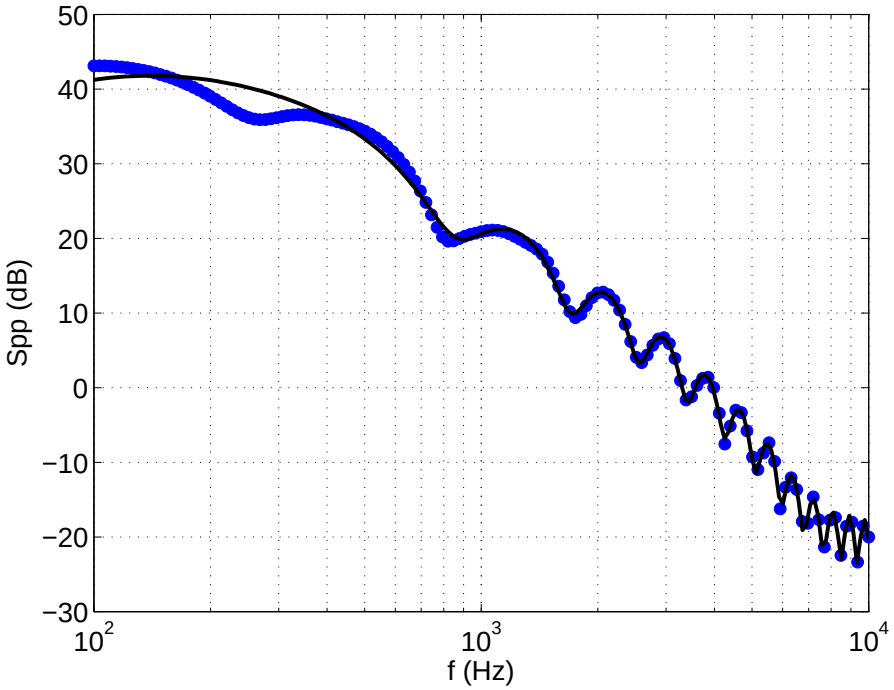

Figure 5.7.: Sound pressure spectrum computed with the image method (solid line) and ATV model (circles) using 8 segments at (0,0,5c).

the contribution of the image source, the far-field acoustic pressure defined in Equation (4.4) becomes

$$p(x,y,z,\omega;x_0,y_0) = \frac{\mathrm{i}\omega \mathbf{x}_o \cdot F(x_{0,pr},y_{0,pr})\,\mathrm{e}^{\mathrm{i}\omega t}}{4\pi c_0 \sigma_{pr}^2}\mathrm{e}^{-\mathrm{i}\omega\sigma_{pr}/c_0} + \frac{\mathrm{i}\omega \mathbf{x}_{im} \cdot F(x_{0,im},y_{0,im})\mathrm{e}^{\mathrm{i}(\omega t+\pi)}}{4\pi c_0 \sigma_{im}^2}\mathrm{e}^{-\mathrm{i}\omega\sigma_{im}/c_0} \tag{5.5}$$

The phase shift for the image source is considered in the exponential term, $\mathrm{e}^{i\pi} = -1$. One can then show that the total PSD including the contribution of the image source becomes similar to the Equation (5.1)

$$S_{pp} = S_{p_{pr}p_{pr}} + S_{p_{pr}p_{im}} + S_{p_{im}p_{pr}} + S_{p_{im}p_{im}} \tag{5.6}$$

Introducing the definition of the acoustic field in Equation (5.5) into Equation (5.6), the total PSD reads

$$
\begin{aligned}
S_{pp}(x,y,z,\omega;\mathbf{x}_{0,pr},\mathbf{x}_{0,im}) = \Bigg(& \int_{-\infty}^{\infty} \Phi_{ww}(K_x,k_y) \\
& \left(\frac{\rho\omega z_{pr}}{2c_0}\right)^2 \frac{U}{\sigma_{pr}^2\ \sigma_{pr}'^2} \iint_{-d}^{d} \mathrm{e}^{-\mathrm{i}\frac{\omega y_{pr}}{c_0\sigma_{f,pr}}(y_{0,pr}-y'_{0,pr})}\mathrm{d}y_{0,pr}\mathrm{d}y'_{0,pr} \\
& \iint_{-c/2}^{c/2} \mathrm{e}^{-\mathrm{i}\frac{\omega(x_{pr}-M\sigma_{f,pr})}{c_0\beta^2\sigma_{f,pr}}} g(x_{0,pr},K_x,k_y)g^*(x'_{0,pr},K_x,k_y)\ \mathrm{d}x_{0,pr}\mathrm{d}x'_{0,pr} - ... \\
& \left(\frac{\rho\omega}{2c_0}\right)^2 \frac{U z_{pr} z_{im}}{\sigma_{pr}^2\ \sigma_{im}^2} \int_{-d}^{d} \mathrm{e}^{-\mathrm{i}\frac{\omega y_{pr}}{c_0\sigma_{f,pr}}(y_{0,pr})}\mathrm{d}y_{0,pr} \int_{-d}^{d} \mathrm{e}^{-\mathrm{i}\frac{-\omega y_{im}}{c_0\sigma_{f,im}}y_{0,im}}\mathrm{d}y_{0,im} \\
& \int_{-c/2}^{c/2} \mathrm{e}^{-\mathrm{i}\frac{\omega(x_{pr}-M\sigma_{f,pr})}{c_0\beta^2\sigma_{f,pr}}} g(x_{0,pr},K_x,k_y)\ \mathrm{d}x_{0,pr} \\
& \int_{-c/2}^{c/2} \mathrm{e}^{-\mathrm{i}\frac{\omega(x_{im}-M\sigma_{f,im})}{c_0\beta^2\sigma_{f,im}}} g^*(x_{0,im},K_x,k_y)\mathrm{d}x_{pr,im}\mathrm{d}k_y - ... \\
& \left(\frac{\rho\omega}{2c_0}\right)^2 \frac{U z_{im} z_{pr}}{\sigma_{im}^2\ \sigma_{pr}^2} \int_{-d}^{d} \mathrm{e}^{-\mathrm{i}\frac{\omega y_i m}{c_0\sigma_{0,im}}(y_{0,im})}\mathrm{d}y_{0,im} \int_{-d}^{d} \mathrm{e}^{-\mathrm{i}\frac{-\omega y_{pr}}{c_0\sigma_{f,pr}}y_{0,pr}}\mathrm{d}y_{0,pr} \\
& \int_{-c/2}^{c/2} \mathrm{e}^{-\mathrm{i}\frac{\omega(x_{im}-M\sigma_{f,im})}{c_0\beta^2\sigma_{0,im}}} g(x_{0,im},K_x,k_y)\ \mathrm{d}x_{0,im} \\
& \int_{-c/2}^{c/2} \mathrm{e}^{-\mathrm{i}\frac{\omega(x_{pr}-M\sigma_{f,pr})}{c_0\beta^2\sigma_{0,pr}}} g^*(x'_{0,pr},K_x,k_y)\mathrm{d}x_{0,pr} + ... \\
& \left(\frac{\rho\omega z_{im}}{2c_0}\right)^2 \frac{U}{\sigma_{im}^2\ \sigma_{im}'^2} \iint_{-d}^{d} \mathrm{e}^{-\mathrm{i}\frac{\omega y_{im}}{c_0\sigma_{f,i}}(y_{0,im}-y'_{0,im})}\mathrm{d}y_{0,im}\mathrm{d}y'_{0,im} \\
& \iint_{-c/2}^{c/2} \mathrm{e}^{-\mathrm{i}\frac{\omega(x_{im}-M\sigma_{f,im})}{c_0\beta^2\sigma_{0,im}}} g(x_{0,im},K_x,k_y)g^*(x'_{0,im},K_x,k_y)\ \mathrm{d}x_{0,im}\mathrm{d}x'_{0,im}\mathrm{d}k_y \Bigg).
\end{aligned}
\tag{5.7}
$$

For an observer located on the scattering plane, where $z_{im} = -z_{pr}$ and $\sigma_{im} = \sigma_{pr}$, all four components of the equation are equal. Hence, the total PSD is equal four times the incident one of the primary source, $S_{pp} = 4S_{p_{pr}p_{pr}}$. The total acoustic pressure then becomes twice the incident one, with a total velocity equal to zero on the boundary surface.

Assuming that the flat screen is infinite and replacing it with a phase shifted airfoil symmetrical to it, the contribution of the flat scattering screen described above can now be computed with the infinite plane approximation. The same configuration described in Section 4.5 is employed using 8 spanwise segments for both auto- and cross-PSD of the primary

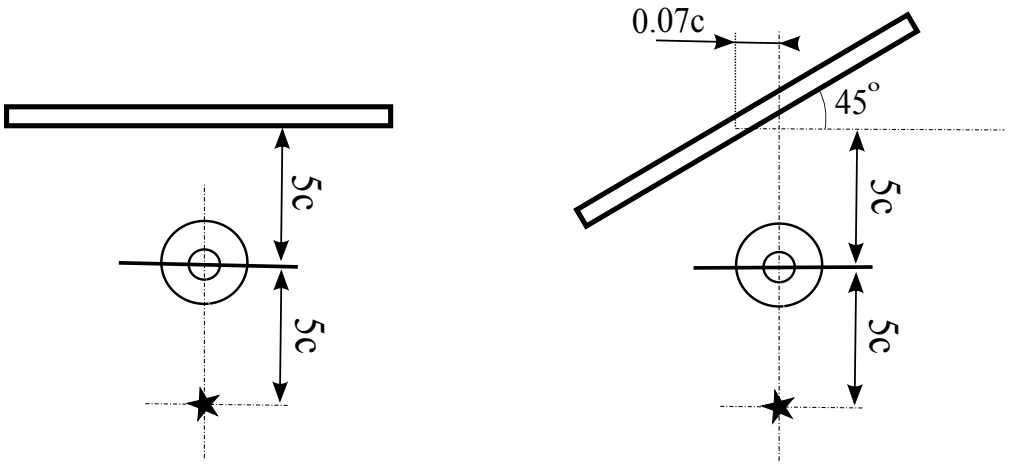

Figure 5.8.: Sketches of the experimental set-ups: parallel plate (left) and 45^o rotated plate (right).

and image airfoils. Inverse strip theory is used in order to take the large hydrodynamic wavelengths into account.

Figure 5.7 shows the acoustic pressure spectra computed with the ATV theory and the image method. The image method approach converges to the numerical solution at frequencies beyond 700 Hz. It can therefore be used to compute the scattered field at higher frequencies, where the number of elements required in BEM increases dramatically [35]. The difference between spectra below 700 Hz is due to the effects of the scattered acoustic waves by the edges of the screen. Since the BEM model accounts for the exact size of the scattering obstacle, it is able to consider the effect of the free edges [34]. However, the image model assumes the plate is infinite and neglects this effect [101]. For the values making $\ell/\lambda < 0.6$, ℓ being the distance to the closest edge, the free edge effects are significant and needed being taken into account.

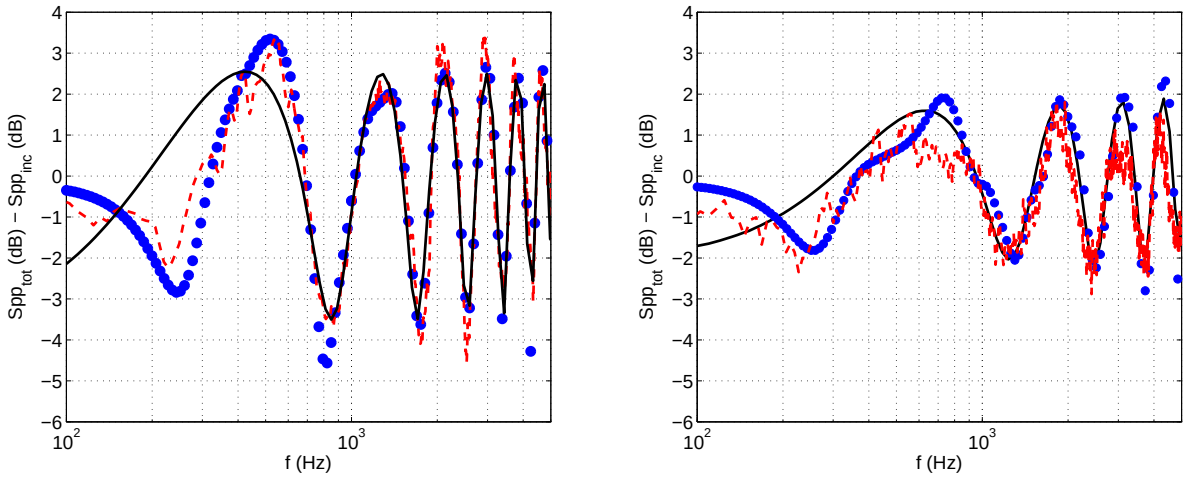

Figure 5.9.: Ratio of the scattered sound pressure spectrum to the free-field one, image model (solid line), ATV model (circles) and experiments (dashed line), (a) parallel plate, (b) 45 degrees rotated plate.

In the comparison addressed above and the application given in Section 4.5, the scattering screen is located parallel to the airfoil. In order to check the consistency of the derivations of the ATV method and image model, the screen is rotated and shifted arbitrarily. A non-parallel airfoil-screen configuration is considered. The experiments addressed above are repeated. The screen is rotated 45 degrees on its vertical axis. Due to the supports of the screen in the experiments and the jet nozzle, the screen is shifted in the spanwise direction. Figure 5.8 shows the sketches of the tested arrangements.

Since the field point-acoustic mesh orientation has changed, the acoustic transfer vectors used for the parallel configuration cannot be used for the rotated one. ATVs are then re-computed and re-exported. For the image model, the position of the image airfoil is reconsidered for the new position of the scattering screen. Since the screen is rotated by $\alpha = 45$ degrees, the image airfoil is rotated by $2\alpha = 90$ degrees. The spanwise axis of the image airfoil is now located perpendicular to the one of the primary airfoil.

Figure 5.9 shows the ratio of the scattered acoustic PSD to the free-field one in logarithmic scale for parallel (left) and 45 degrees rotated screen (right). Solid line, circles and dashed line represent the image model, ATV model and the measurements, respectively. The effect of the screen is captured accurately by the ATV model in both configurations. It can be seen that the image model converges to the ATV model at frequencies higher than 700 Hz. The difference is due to the free edge effects as pointed above. It can be said that the ATV model is robust with arbitrary positions of the scattered obstacle. It is also seen that the scattered-field of the finite plate can be computed using the image source approach where the source-edge distance $\ell/\lambda > 0.6$ in both configurations.

On one hand, the image model is ideal and neglects the effects of the waves scattered by the free edges of the flat screen. On the other hand, the ATV method takes the effects of the free edges into account. Since it is based on BEM, it can be applied to complex geometries. For the current configuration, the scattered field by the finite screen can also be handled with first-order corrections using a semi-infinite plate approximation [39] or the Green's function of a corner described in Section 3.5.

5.1.2.2. Scattering by the edge of the screen

The analytical model mentioned in Section 5.1.2.1 is based on assuming the flat screen is infinite, hence the effect of the free edges are neglected. Taking the position of the observer with respect to the source and scattering screen into account, the closest edge of the finite screen must be included in the modelling for a better physical consistency. In this section the edge is considered that of a finite corner. Note that, due to the orientation, the effect of thickness becomes negligible for the considered observer position. The infinite plane assumption then applies at other three edges. Only the airfoil parallel to the scattering screen is considered. Using the deterministic source given above and representing the airfoil as a point dipole, Equation (3.27) can then be employed. Figure 5.10 shows the scattered spectra for the current configuration using the deterministic Curle's analogy with the source field [27] obtained with the image model (thick) and the analytical corner model (thin). The difference is now due to the effect of the scattered waves by the closest edge. It is seen that both methods converge above 700 Hz. The frequency limit is again due to the relation of the distance of the edge with the wavelength at the frequency of interest.

The effect of waves scattered by the assumed corner is seen in Figure 5.11. Red thick and blue thin lines represent the ratio of the scattered spectra to the incident one for the corner

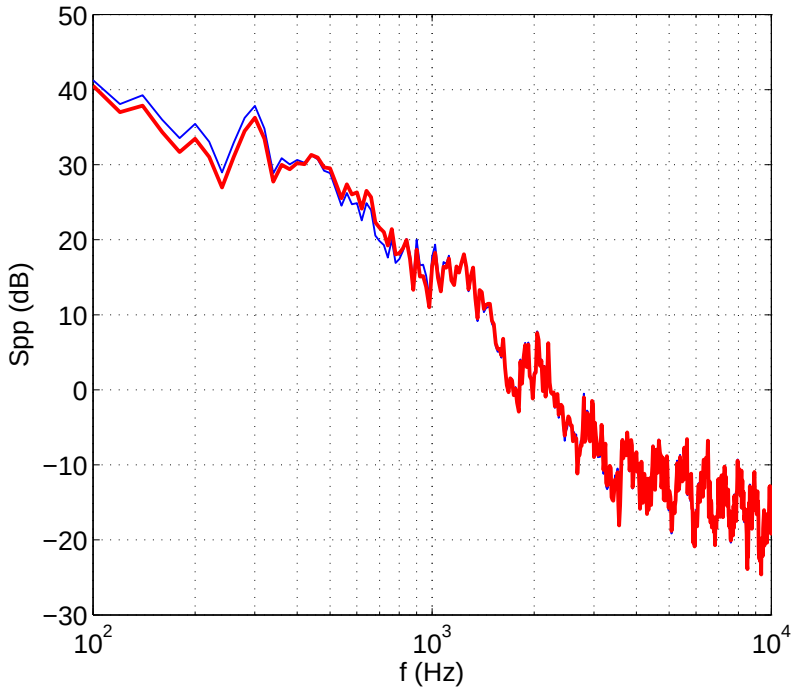

Figure 5.10.: Acoustic PSD computed with the deterministic source terms, using Curle's analogy with image model (thick), using the Green's function of a corner (thin) at (0,0,5c).

and image models. The measured ratio is plotted with dashed line. Both analytical models are able to capture the effects of the scattering screen at higher frequencies. The effect of the finite extent of the scattering screen, the first deep in the experimental spectrum, is only captured with the corner approximation. However, as seen in Figure 5.9, the effect of the free edges can be accurately captured with the numerical methods such as the BEM and the ATV theory. Hence, the analytical solutions are more suitable for high frequency scattered field problems containing simple scattering obstacles in the acoustic field. It is worth noting that in the case using the half-plane Green's function would lead to similar results.

The broadband scattered field of a stationary airfoil due to turbulence-interaction is now predicted with several methods. The analytical and numerical models are next implemented for rotating machinery for low-Mach number applications.

5.2. Scattered-Field of a Low-Speed Axial Fan

The derivation of the semi-analytical method and its implementation to the low-speed fan noise free-field given in Section 4.6 is now modified to include the effect of a scattering obstacle.

The theory described above is implemented in numerical and experimental validation cases. The former assumes an ideal case where there is no fan-induced main flow and the model fan is placed parallel to a finite scattering plate. The ATV results are then compared to the analytical results assuming the plate is infinite. On the other hand, the latter compares the semi-analytical method combined with scattered-field theory to the measurements.

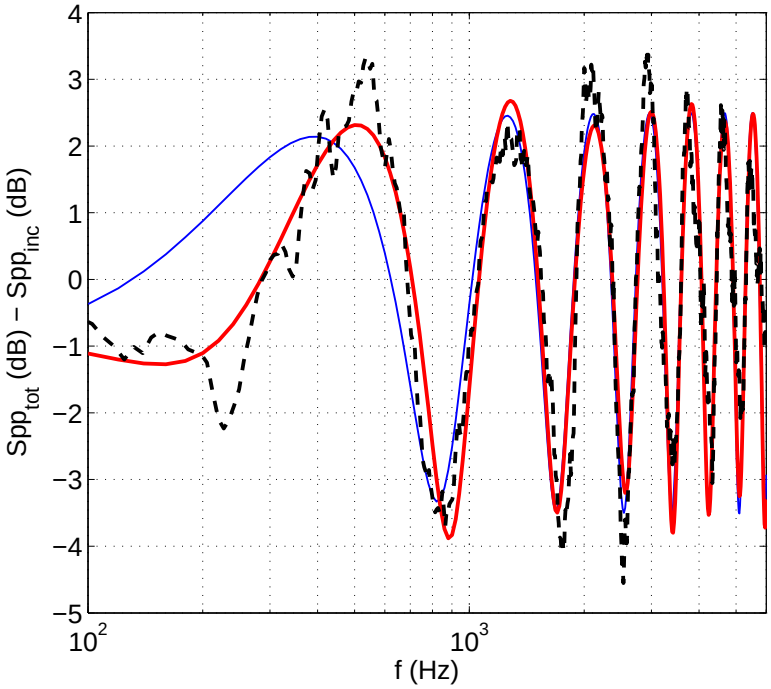

Figure 5.11.: Ratio of scattered to free-field acoustic PSD, image model (thick), Green's function of a corner (thin) and experiments (dashed line).

5.2.1. Image fan model

In order to prove the ability to predict the scattered-field of a low-speed axial fan, a flat plate is introduced parallel to the rotation plane of a model fan. The parallel orientation of the fan and the plate maximizes the observed scattered acoustic field due to the dipolar nature of the leading-edge noise sources [5, 33]. A $7.5r_{tip} \times 7.5r_{tip}$ plate is used in the comparison. The observer is located 1.5 tip radius from the fan on the rotation axis. The plate is mounted at the same distance parallel to the rotation plane but on the other side of the fan with respect to the observer (see the sketch in Figure 5.12).

A primary theoretical comparison is performed considering a benchmark low-speed axial fan with 4 blades. The rotational speed of the fan is selected as, $\Omega = 3000$ rpm. The tip and hub radii are 0.14 and 0.06 m, respectively. The axial flow velocity, U_z, is selected as zero. The blade is split into 4 spanwise segments and all segments are linearized to rectangular plates (as seen in Figure 4.19). The chord length of the blade segments are constant along the span. The Mach number of the segments varies from 0.08 to 0.15. Turbulence intensity and length scale are assumed constant in the spanwise direction. They are selected as 20% and 0.005 m, respectively. For this benchmark problem, the spanwise variation of the incoming flow is only taken into account with the impinging velocity. The velocity is computed as a function of the radius and pitch angle of the blade segment [114]. For the azimuthal integration in Equation (4.61), an 8−point trapezoidal method is chosen.

Figure 5.12 shows the comparison of the free (solid line) and scattered-field (symbols) spectra of the low-speed axial fan calculated with the ATV model. The free-field spectrum is smoother and the effect of interference fringes due to scattering results in a wavelike envelope.

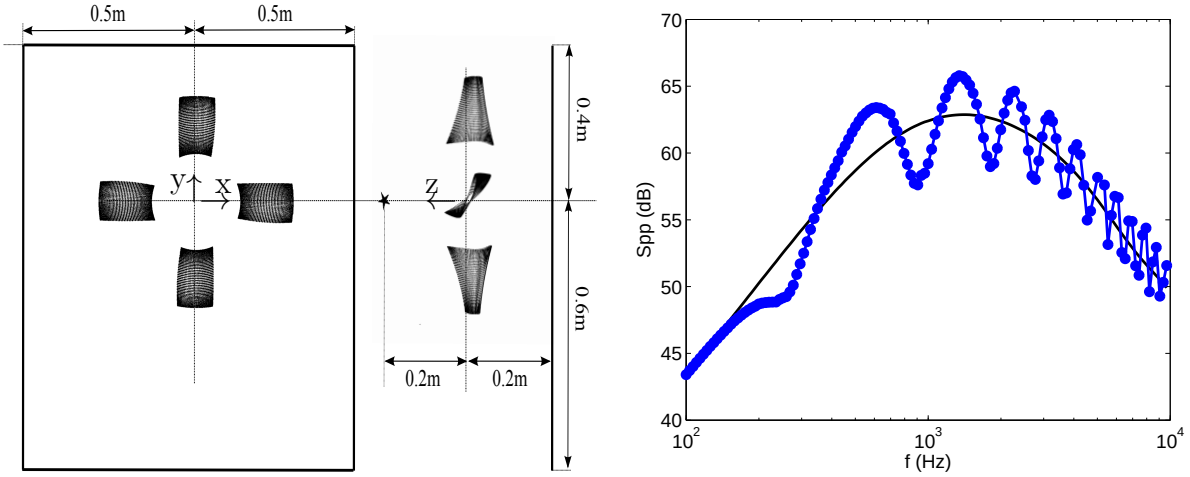

Figure 5.12.: Sketch of the axial fan problem (left) and free (solid line) and scattered-field (circles) spectra of the fan computed with the ATV theory (right) at $(0, 0, 1.5r)$.

The contribution of the flat scattering screen can also be calculated with the image model by replacing the screen by a phase-shifted fan symmetrical to the screen. However, this case is ideal and neglects the effects of the sound waves scattered by the free edges of the finite screen. Figure 5.13 shows the comparison of both methods applied to the scattering problem. Both the image (solid line) and ATV (symbols) methods capture the same interference fringes at frequencies above 800 Hz. However, the ATV model captures one additional deep at low frequencies, which can be addressed as the scattering of the large waves from the free edges. This exercise is a cross-validation of the numerical and analytical scattering techniques. The ATV theory now will be applied to the experimental test-case of the low-speed axial fan defined in Section 4.7.

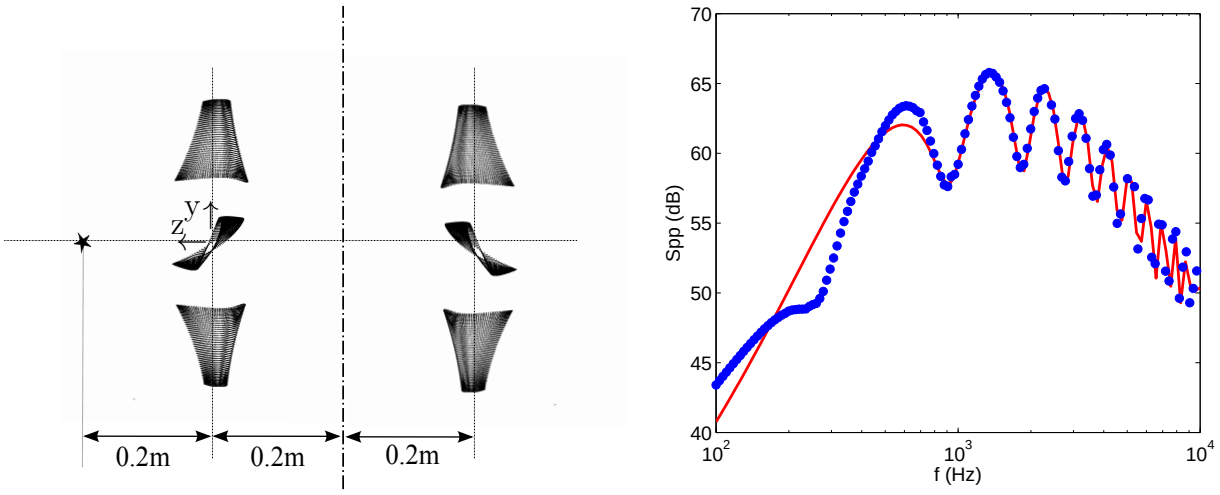

Figure 5.13.: Sketch of the image model (left), scattered-field spectra (right), ATV theory (circles) and image model (solid line) at $(0, 0, 1.5r)$.

Figure 5.14.: Experimental axial fan-scattering screen configuration in the anechoic chamber.

5.2.2. Experimental validation

The low-speed axial cooling fan described in Section 5.1.1.2 is now operated in the vicinity of a flat plate. Figure 5.14 shows the experimental set-up in the anechoic chamber.

In order to compute the effect of a benchmark scattering obstacle, a 1m × 1m plexiglass flat plate is placed 1.5 r_{tip} away from the rotation axis perpendicular to the rotation plane (see Figure 4.24). On the one hand, the plate is located in the geometrical near-field of the rotor. On the other hand, the selected distance of the plate should be far enough for not disturbing the incoming flow. The center of the plate is located 0.03 m upstream and 0.1 m below the rotation center. Figure 5.15 shows measured free and scattered-field spectra of the benchmark fan. The difference between spectra is less than 3 dB at frequencies considered.

Figure 5.16 next shows the difference between the scattered and incident-field spectra in terms of dBs. The red line and the symbols stand for the measurements and the theory described in Section 5.1.1.2, respectively. Correlated-strips theory is employed with 4 spanwise strips. The interference fringes due to the presence of the scattering screen are captured using the model described above combined with the ATV approach at frequencies above 400 Hz. The difference with the measurements is less than 1 dB at these frequencies. The disagreement at the lowest frequencies may be due to the scattering of other source mechanisms [122] as mentioned in Chapter 4.

5.3. Conclusions

Predicting the broadband noise emitted by low-Mach number axial fans in a turbulent stream is an essential issue for applications such as cooling fans or wind turbines. Amiet's theory provides an interesting approach to deal with this problem, and has been used by a number of works in the literature, especially for configurations where the free-field assumptions are

reasonable. In cases where the installation effects are significant in the vicinity of the fan, the scattering of the generated broadband noise has been considered in this Chapter.

First a numerical methods has been employed. The scattered acoustic field of a stationary airfoil by a finite plate has been computed with the indirect BEM method using a deterministic source field. In order to compute the scattered acoustic field using analytical turbulence models, a method based on the ATV approach, obtained by means of a commercial BEM solver, has been proposed.

Addressing the effects of the free-edges of a finite plate, the analytical scattering techniques have been compared to numerical and experimental results. Following a first order consideration, the scattering from the edge of the plate has been obtained with the Green's function of a corner, for the airfoil-screen configuration.

The combined model including the semi-analytical solution and the ATV theory has been compared with the analytical solutions and experiments performed in an anechoic chamber. A good agreement has been found between all models. It has been shown that the semi-analytical method provides better results at higher frequencies where Curle's method is limited due to the cut-off frequency of the CFD mesh as shown in Chapter 4.

The scattered acoustic field of an industrial low-speed axial cooling fan operating in a turbulent stream has been also investigated. A benchmark problem has been first solved for an axial fan operating parallel to a flat plate. The ATV model for a fan has been first compared with the analytical solution. Interference fringes have been very well captured with the ATV model.

Finally, a good agreement has been observed in comparison with experimental data gath-

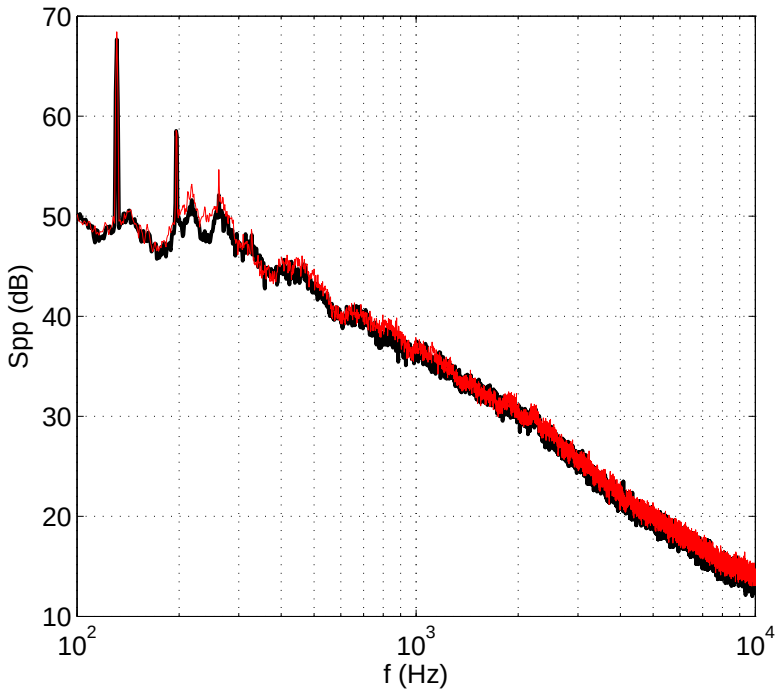

Figure 5.15.: Free (black) and scattered-field (red) spectra measured for the low-speed axial fan at 3 r_{tip} downstream and 2.5 r_{tip} away from the rotation axis. The flat plate is placed 1.5 r_{tip} away from the rotation axis.

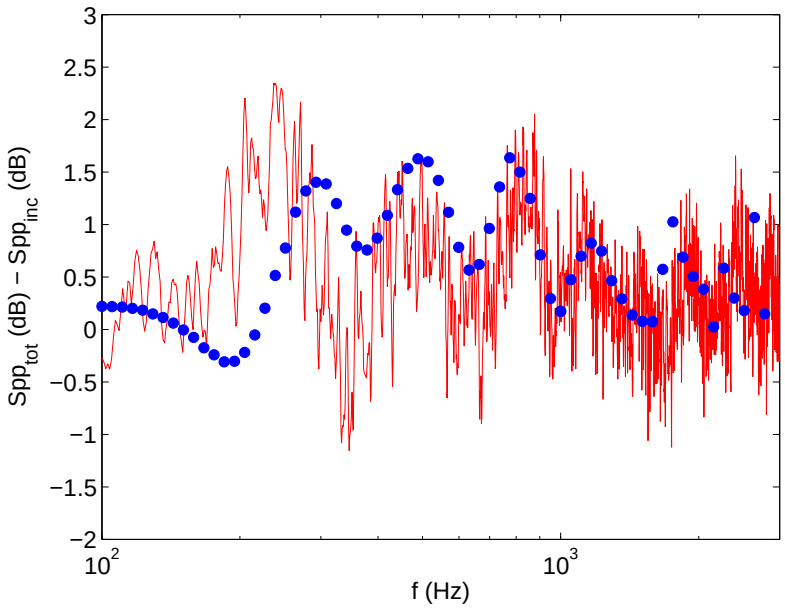

Figure 5.16.: Difference between the scattered-field and free-field acoustic spectra, ATV theory (symbols) and measurements (solid line).

ered in the anechoic room. The effect of the broadband scattering has been captured at the frequencies of interest using the ATV approach. Since the ATV model can be applied to arbitrary scattering geometries, it has been proved to be a useful tool for realistic scattering problems where the source field is random.

Chapter 6.

Conclusions and Perspective

This thesis proposed to compute the aerodynamic noise generated by low-speed fans in presence of surrounding surfaces. Both numerical and analytical acoustic scattering techniques and their applications to low-speed fan noise have been investigated.

6.1. Conclusions

Closed-form exact analytical solutions existing in literature involve some simplifications in order to solve the propagation problem in an analytical manner. One assumption is consideration of an observer located in acoustic and geometrical far-field. This may be a valid assumption when the free-field propagation takes place and the observer-source distance is greater than the acoustic wavelength and geometrical extent of the source. However, most of industrial applications involve a fan operating in presence of surrounding surfaces, such as ducts or cooling units. Acoustic quantities then need being computed in the near-field. This thesis investigates near-field effects for different applications.

First, tonal fan noise has been investigated. Employing both near and far-field closed-form analytical solutions, free-field response of a benchmark open rotor has been computed. Additionally, another methodology considering circular array of phase shifted stationary dipoles has been introduced. After the number of stationary dipoles representing the equivalent fan source has been determined by an iterative procedure, the acoustic response of the fan has been computed. Since the dipole array approach includes the acoustic near-field terms in the dipole radiation and handles the geometrical near-field with the summation of the dipoles, it provides the reference solution. A very good agreement has been obtained with the closed-form analytical near-field solution. It has been concluded that for free-field tonal fan noise applications, the near-field solution provides accurate prediction of acoustic field when the source-observer distance is comparable to the wavelength at the frequency of interest.

Secondly, the scattered-field of tonal fan noise has been investigated numerically. The closed-form analytical solutions mentioned above have been combined with BEM formulation using commercial solvers. A low-speed axial fan operating in a finite duct downstream of a stator has been investigated. Employing the unsteady blade loading harmonics, the scattered acoustic field has been computed using two analytical approaches combined with BEM. A good agrement has been observed in comparison with the measurements and the near-field formulation. Near-field terms have been shown to be significant if the scattering surface is located in the immediate neighborhood of the source.

However, the BEM formulation is known to be a more suitable method for low frequency problems in terms of computational efficiency. For high frequency problems, the number of elements required for an accurate prediction increases dramatically. For relatively simple scattering problems such as configurations involving a flat plate or a corner, analytical methods can be useful at higher frequencies. The reflection and scattering of sound waves

emitted from an axial fan by a flat plate has been computed using an image fan symmetrical to the scattering surface. A very good agreement has been observed in comparison with the BEM solution containing a large flat plate. A more complex problem is computing the tonal fan noise scattered by a corner in an analytical perspective. In this thesis, an analytical approach based on solution of the Helmholtz equation for exact boundary conditions for a corner has been considered. The solution has been re-formulated for arbitrary source positions and extended for fan noise applications combined with the phase shifted dipole array approach. A very good agreement has been satisfied in comparison with the BEM solution at the frequency of interest.

One key point addressed in this thesis is the prediction of broadband noise generated by first a stationary airfoil and second a low-speed axial fan. Several source mechanisms exist resulting broadband noise due to their random characteristics. This thesis focuses on turbulence-interaction noise. Amiet's theory provides an interesting semi-analytical approach to the turbulence-interaction problem for stationary airfoils and rotor blades. It is a hybrid method considering homogeneous turbulence acting on the airfoil. However, due to the simplifications in the analytical model, the solution is limited with assumptions. One of them is consideration of an observer located in far-field. As mentioned above, the far-field assumption might be significant for acoustic problems when the observer or scattering surfaces are located in the near-field. The effect of far-field approximation has been investigated using an exact numerical integration of the theory as reference. An intermediate level of correction accounting for observers located in the geometrical near-field of the airfoil has been proposed. The new solution has highly improved the Amiet's model where the observer-source distance is comparable to the span-length of the airfoil. In the numerical validation test case, the spanwise geometrical near-field formulation has provided a correction to the far-field solution up to 10 dB.

Another assumption in Amiet's theory is the turbulent flow impinging onto the airfoil is considered as uniform. However, in most of the industrial applications and the experimental jet-airfoil configuration detailed, the flow is varying in the spanwise direction. An approach already in use in literature is splitting the airfoil into short strips in the spanwise direction and assuming homogeneous flow properties for each strips, called classical strip theory. The overall sound is obtained then summing the sound emitted from each strips. The tests have showed that with the increasing number of strips, the overall spectrum underpredicts the reference one. This has been addressed as the effect of large hydrodynamic wavelengths due to the lack of correlation between strips. Another method existing in the literature is the inverse strip theory, considering the reconstruction of the strip from a subtraction of truncated airfoil from a large span airfoil. Hence, it is capable of taking the large wavelength effects into account in far-field. In the geometrical near-field, due to the different directivities of the dipoles appearing during substraction, the overall spectrum does not match exactly with the reference solution but it highly improves the solution compared to the classical strip theory. Further, it doubles the computation time since each strip needs being calculated using two large-span airfoils. A new segmentation method has been proposed in this thesis considering the cross-correlation of the adjacent strips. For the author's knowledge, there is not an exact solution for partially non-homogeneous turbulent field. However, it can be modeled employing homogeneous turbulent models using a method proposed in literature. A first order correction has been proposed using a shape function. Compared to the classical strip theory, the new method has improved the solution due to the cross-correlation of strips. Further, it has been found being computationally less demanding than the inverse

strip theory since each strip is computed once and only the cross-correlation is introduced.

Combining the extension of Amiet's theory and the segmentation techniques, the acoustic response of a NACA0012 airfoil located in the developing region of a jet has been computed. The flow field was obtained through an LES solution existing in the literature. Using the incoming flow profile from the LES solution and employing a von Karman spectrum modified with rapid distortion theory, the spectrum has been obtained with the semi-analytical model. Besides, using the unsteady pressure distribution on the airfoil surface directly, the acoustic pressure at the observer has also been computed with Curle's analogy. A good agreement has been satisfied compared to the measurements performed in the anechoic chamber. The Curle's analogy has been found to be able to predict the acoustic field at frequencies up to the cut-off frequency of the CFD whereas Amiet's model is able to predict over the entire frequency range. Later, the theory proposed for stationary airfoils has been implemented for rotor blades applying an azimuthal averaging. Acoustic free-field of a fan with a tip Mach number around 0.08 operated in turbulent stream has been computed with the model. A good agreement has been satisfied with the measurements and the model using classical strip theory at frequencies higher than 3 kHz. The effect of large wavelengths have also been introduced using different segmentation methods. The predictions are improved and a better agreement has been obtained at frequencies higher than 400 Hz.

Another key point of this thesis is the prediction of the scattering of the broadband noise. A deterministic numerical scattering method and analytical approaches have been detailed in the chapter considering the scattered-field of the tonal fan noise. However, due to the statistical characterization of the turbulent spectrum employed in the semi-analytical model, the deterministic BEM solution can not be used directly. In order to deal with the scattered field of random sound sources, the BEM solution has been re-formulated. The Acoustic Transfer Vector (ATV) approach which links the acoustic incident velocity on the scattering surface to the incident acoustic pressure at the observer point has been employed. The semi-analytical solution has been re-derived in order to compute the acoustic velocity contribution. ATVs have been obtained by solving the BEM problem partially in Virtual Lab. and exported from Sysnoise. Combining the derivations with the ATVs exported, scattered field of the turbulence-interaction noise of the stationary airfoil by a flat screen has been computed. Similar to the free-field computations, the deterministic Curle's analogy has been combined with the classical BEM formulation in order to deal with the same problem using the unsteady pressure distribution on the airfoil surface directly. A very good agreement has been satisfied capturing the interference fringes due to the scattering using both deterministic and non-deterministic scattering methods. Since the scattered-field derivations are based on the ones in free-field, the deterministic method is limited with the cut-off frequency of the CFD. However, the semi-analytical method combined with the ATV approach predicts the scattered-field spectrum accurately over the entire frequency range. The convenience of the ATV methodology has also been compared with measurements considering an arbitrary orientation of the scattering surface.

The analytical scattering methods applied to the tonal fan noise have also been employed for the scattering of broadband noise. The same stationary airfoil problem has been dealt with the image method using both deterministic and semi-analytical approaches. A very good agreement has been obtained at higher frequencies compared with measurements. Due to the waves scattered by the free-edges of the finite scattering surface, the analytical solution deviates from the measurements and numerical solution at low frequencies. The effect of the closest edge has also been examined by treating the scattering problem as a corner. A better

agreement has been observed compared to the image method. The scattering techniques for broadband noise are finally applied to low-Mach number axial fans operating in the vicinity of a scattering screen. A benchmark test is first performed considering a low-speed axial fan operating parallel to a scattering screen. Due to simplicity of the problem, the screen has been replaced with an image fan. The results obtained with the image method are converged to the ones obtained with the ATV model. Finally, a flat screen has been introduced to the acoustic radiation field of the low-speed axial fan in the experimental setup. An agreement has been obtained in the comparison with the semi-analytical model combined with the ATV approach and the measurements performed at frequencies higher than 400 Hz. Both alignment and magnitude of interference fringes are captured accurately. The analytical solutions have been shown to be applicable also for broadband scattering problems for relatively simple scattering obstacles. However, since the ATV approach is based on BEM, it is also applicable for more complex geometries.

6.2. Future Work and Perspectives

Both tonal and broadband components of low-speed fan noise have been investigated. Satisfying results are obtained in both free and scattered acoustic field in the comparison with numerical, analytical and experimental methods. Further improvements can be made on the following sections,

- The free-field radiation of turbulence-interaction noise takes convection of the acoustic waves with the fluid flow into account. However, in the scattered field computations, the effect of convection of the scattered waves is neglected. Introducing the uniform flow to the BEM formulation [10] and exporting the ATVs later, the convected waves can be taken into account. For the investigated configurations the Mach number is less than 0.1 hence the effect of convection is negligible. For higher Mach number applications, the convective effect of fluid flow in acoustic propagation needs being considered.

- The effect of the Doppler factor has been shown to be negligible for the broadband noise emitted from low-speed fans [88]. It can be easily considered for free-field computations. However, due to the cross-correlation at the two different acoustic points, it is not possible to take the Doppler effect into account in the current scattered-field formulation. Using further numerical models, accounting the Doppler effect will result a more elegant solution for the scattered-field problems.

- In the correlated-strips theory, the cross-correlation of segments has been taken into account using a shape function, depending on the impinging flow velocity only. The first order correction using shape functions improves the solution compared to the classical strips theory. However, using additional empirical methodology, the shape function, hence the total sound spectrum can be improved.

- Implementation of the ATV theory to the broadband airfoil and fan noise has been proposed. Only the turbulence-interaction noise has been investigated in this thesis. However, other broadband source mechanisms, such as self-noise [6], can also be combined with the ATV approach. The sound emitted by an airfoil or a fan due to the self-noise and its scattered-field by an obstacle can be computed.

- The exact-analytical solution addressing the scattered-field of the noise emitted from a monopole by a rigid corner has been extended for a dipole. The extended dipole-corner solution has been later combined with the continuous array of phase shifted dipoles approach

to obtain equivalent of a fan source operating next to the corner. Further derivations can address the scattered-field of a quadrupole by the corner. Such formulation can be employed in the scattered-field of sound field generated by wakes next to the flap side-edge in aeronautical applications [70].

Appendix A.

Derivation of the Acoustic Transfer Function

As mentioned in Chapter 4, the airfoil is considered as a linearized flat plate with zero thickness and camber. The plate is located on $z = 0$ plane with zero angle of attack. In the derivations, the origin is considered on the leading edge of the airfoil, hence the plate is located on $0 \leq x \leq 2b$ on the streamwise direction, b being the half-chord length of the airfoil [5]. The flow speed impinging to the airfoil is represented as U with the corresponding Mach number, M for the speed of sound equal to c_0. Using these definitions, the linearized wave equation for the velocity potential ϕ is

$$\left[\nabla^2 - \frac{1}{c_0^2}\frac{\mathrm{D}^2}{\mathrm{D}t^2}\right]\phi(\mathbf{x}, t) = 0. \tag{A.1}$$

The differentiation $\mathrm{D}/\mathrm{D}t$ on the streamwise direction reads

$$\frac{\mathrm{D}}{\mathrm{D}t} = \frac{\partial}{\partial t} + U\frac{\partial}{\partial x}. \tag{A.2}$$

Introducing Equation (A.2) into Equation (A.1) then results

$$\begin{aligned}
0 &= \frac{\partial^2\phi}{\partial x^2} + \frac{\partial^2\phi}{\partial y^2} + \frac{\partial^2\phi}{\partial z^2} - \frac{1}{c_0^2}\left[\frac{\partial^2\phi}{\partial t^2} + 2U\frac{\partial^2\phi}{\partial t\partial x} + U^2\frac{\partial^2\phi}{\partial x^2}\right] \\
&= \left(1 - \frac{U^2}{c_0^2}\right)\frac{\partial^2\phi}{\partial x^2} + \frac{\partial^2\phi}{\partial y^2} + \frac{\partial^2\phi}{\partial z^2} - \frac{1}{c_0^2}\frac{\partial^2\phi}{\partial t^2} - \frac{2U}{c_0^2}\frac{\partial^2\phi}{\partial t\partial x} \\
&= \left(1 - M^2\right)\frac{\partial^2\phi}{\partial x^2} + \frac{\partial^2\phi}{\partial y^2} + \frac{\partial^2\phi}{\partial z^2} - \frac{1}{c_0^2}\frac{\partial^2\phi}{\partial t^2} - \frac{2U}{c_0^2}\frac{\partial^2\phi}{\partial t\partial x} \\
&= \beta^2\frac{\partial^2\phi}{\partial x^2} + \frac{\partial^2\phi}{\partial y^2} + \frac{\partial^2\phi}{\partial z^2} - \frac{1}{c_0^2}\frac{\partial^2\phi}{\partial t^2} - \frac{2U}{c_0^2}\frac{\partial^2\phi}{\partial t\partial x}.
\end{aligned} \tag{A.3}$$

where $\beta = \sqrt{1 - M^2}$ is the compressibility factor. The Fourier domain velocity potential ϕ can be defined as

$$\phi(\mathbf{x}, t) = \varphi(\mathbf{x})\ \mathrm{e}^{\mathrm{i}\omega t}\ \mathrm{e}^{\mathrm{i}kM/\beta^2}\mathrm{e}^{-\mathrm{i}k_y y} \tag{A.4}$$

for the further derivations. k is the wave number defined as $k = \omega/c_0$. Introducing the definition of the velocity potential, one can show the terms on the right hand side of the Equation (A.3) as

$$
\begin{aligned}
\beta^2\frac{\partial^2\phi}{\partial x^2} &= \beta^2\left(\frac{\partial^2\phi}{\partial x^2}+\frac{2\mathrm{i}kM}{\beta^2}\frac{\partial\phi}{\partial x}-\frac{k^2M^2}{\beta^4}\varphi\right)\mathrm{e}^{\mathrm{i}\omega t}\mathrm{e}^{\mathrm{i}kM/\beta^2}\mathrm{e}^{-\mathrm{i}k_y y}\\
\frac{\partial^2\phi}{\partial y^2} &= -k_y^2\varphi\ \mathrm{e}^{\mathrm{i}\omega t}\mathrm{e}^{\mathrm{i}kM/\beta^2}\mathrm{e}^{-\mathrm{i}k_y y}\\
\frac{\partial^2\phi}{\partial z^2} &= \frac{\partial^2\varphi}{\partial z^2}\ \mathrm{e}^{\mathrm{i}\omega t}\mathrm{e}^{\mathrm{i}kM/\beta^2}\mathrm{e}^{-\mathrm{i}k_y y}\\
\frac{1}{c_0^2}\frac{\partial^2\phi}{\partial t^2} &= -k^2\varphi\ \mathrm{e}^{\mathrm{i}\omega t}\mathrm{e}^{\mathrm{i}kM/\beta^2}\mathrm{e}^{-\mathrm{i}k_y y}\\
\frac{2U}{c_0^2}\frac{\partial^2\phi}{\partial t\partial x} &= \left(\frac{2U\omega\mathrm{i}}{c_0^2}\frac{\partial\varphi}{\partial x}-\frac{2U\omega kM}{\beta^2c_0^2}\varphi\right)\ \mathrm{e}^{\mathrm{i}\omega t}\mathrm{e}^{\mathrm{i}kM/\beta^2}\mathrm{e}^{-\mathrm{i}k_y y}.
\end{aligned}
\tag{A.5}
$$

Using the terms in Equation (A.5) and without considering the exponential terms, formulation (A.3) can be simplified to

$$
\beta^2\frac{\partial^2\phi}{\partial x^2}+\left(\frac{k^2}{\beta^2}-k_y^2\right)\varphi+\frac{\partial^2\phi}{\partial z^2}=0. \tag{A.6}
$$

In order to non-dimensionalize the problem, the geometrical parameters are divided by the semi chord length, b. Introducing the compressibility factor, the non-dimensional geometrical parameters writes

$$
\bar{x}=\frac{x}{b},\quad \bar{y}=\beta\frac{y}{b},\quad \bar{z}=\beta\frac{z}{b}. \tag{A.7}
$$

The non-dimensional form of Equation (A.6) is

$$
\frac{\partial^2\phi}{\partial\bar{x}^2}+\frac{b^2}{\beta^2}\left(\frac{k^2}{\beta^2}-k_y^2\right)\varphi+\frac{\partial^2\phi}{\partial\bar{z}^2}=0. \tag{A.8}
$$

Introducing the definition of the chordwise wavenumber defined in Chapter 4, $k_x=\omega/U$, the wave number k results as $k=Mk_x$. Non-dimensionalizing the wave numbers as $\bar{k}_i=bk_i$, Equation (A.8) reads

$$
\frac{\partial^2\phi}{\partial\bar{x}^2}+\left(\frac{M^2\bar{k}_x^2}{\beta^4}-\frac{\bar{k}_y^2}{\beta^2}\right)\varphi+\frac{\partial^2\phi}{\partial\bar{z}^2}=0. \tag{A.9}
$$

Defining the new parameters, $\mu=M\bar{k}_x/\beta^2$ and $\kappa^2=\mu^2-\bar{k}_y^2/\beta^2$, Equation (A.9) can be written in the form of a Helmholtz equation as

$$
\frac{\partial^2\phi}{\partial\bar{x}^2}+\frac{\partial^2\phi}{\partial\bar{z}^2}+\kappa^2\varphi=0. \tag{A.10}
$$

The velocity potential for an incident velocity perturbation

$$
w=w_0\ \mathrm{e}^{\mathrm{i}(\omega t-k_x x-k_y y)} \tag{A.11}
$$

must be zero upstream the airfoil

$$
\varphi(\mathbf{x},t)=0,\quad x\leq 0,\ z=0. \tag{A.12}
$$

Hence, after non-dimensonalizing with the half chord-length

$$\varphi(\bar{x},t)=0,\quad \bar{x}\leq 0,\ z=0. \tag{A.13}$$

Additionally, the normal velocity is equal to zero on the plate

$$\frac{\partial\varphi}{\partial z}(\mathbf{x})=-w,\quad 0<x<2b,\ z=0. \tag{A.14}$$

which can be written in the non-dimensional form using the definition of the velocity potential

$$\begin{aligned}
\frac{\partial\phi}{\partial z}(\mathbf{x}) =& -w,\quad 0<\bar{x}<2b,\ z=0\\
\frac{\partial\varphi}{\partial z}(\mathbf{x}) =& -w_0\ \mathrm{e}^{-\mathrm{i}k_x x}\ \mathrm{e}^{-\mathrm{i}kMx/\beta^2}\\
\frac{\partial\varphi}{\partial\bar{z}}(\bar{\mathbf{x}}) =& -\frac{w_0 b}{\beta}\mathrm{e}^{-\mathrm{i}k_x\bar{x}/\beta^2},\quad 0<\bar{x}<2,\ z=0.
\end{aligned} \tag{A.15}$$

Finally, according to the Kutta condition [85] the pressure difference between the suction and the pressure side is equal to zero for the streamwise position above the trailing edge.

$$\frac{\mathrm{D}\varphi}{\mathrm{D}z}=0,\quad x\geq 2b. \tag{A.16}$$

Using the definition of the velocity potential and the definition of the differentiation, the non-dimensional form of the equation becomes

$$\begin{aligned}
0 =& \frac{\mathrm{D}\phi}{\mathrm{D}z},\quad x\geq 2b.\\
=& \frac{\partial\phi}{\partial t}+U\frac{\partial\phi}{\partial x}\\
=& \mathrm{i}\ \omega\ \varphi\mathrm{e}^{\mathrm{i}\omega t}\mathrm{e}^{\mathrm{i}kM/\beta^2}\mathrm{e}^{-\mathrm{i}k_y y}+U\mathrm{e}^{\mathrm{i}\omega t}\mathrm{e}^{-\mathrm{i}k_y y}\left(\frac{\partial\varphi}{\partial x}+\frac{\mathrm{i}kM}{\beta^2}\mathrm{e}^{\mathrm{i}kM/\beta^2}\varphi\right)\\
=& \mathrm{i}(k_x+\frac{kM}{\beta^2})\varphi+\frac{\partial}{\partial x}\varphi\\
=& \mathrm{i}(k_x+\frac{k_xM^2}{\beta^2})\varphi+\frac{\partial}{\partial\bar{x}}\varphi\\
=& \mathrm{i}b\left(k_x+\frac{k_xM^2}{\beta^2}\right)\varphi+\frac{\partial}{\partial\bar{x}}\varphi\\
=& \left(\mathrm{i}\frac{\bar{k}_x}{\beta^2}+\frac{\partial}{\partial\bar{x}}\right)\varphi.
\end{aligned} \tag{A.17}$$

Combining the Equations (A.10), (A.13), (A.15) and (A.17), the solution set of the potential field can be computed. However, the solution differs with the sign of κ^2. For the values of the spanwise wave number $\bar{k}_y<\bar{k}_xM/\beta^2$, the equation becomes hyperbolic and the gust is said to be supercritical. Supercritical gusts are known to be radiate efficiently [113].

For other values of the spanwise wave number making $\bar{k}_y>\bar{k}_xM/\beta^2$ the equation behaves elliptically. The gust is then said subcritical and is less efficient in terms of acoustic radiation [113]. However if the span is finite, subcritical gusts need being taken into account. Since

the supercritical gusts are dominant compared to the subcritical gusts in terms of acoustic radiation, only the supercritical gusts are considered in the derivations.

A solution for the hyperbolic function (A.10) can be written as

$$\varphi^0(\bar{\mathbf{x}}) = \alpha \ \mathrm{e}^{\gamma\bar{x}-\mathrm{i}\sqrt{\kappa^2+\gamma^2}\bar{z}}. \tag{A.18}$$

Constants α and γ are computed using the boundary condition defined in Equation (A.15) as

$$\begin{aligned}
-\frac{w_0 b}{\beta}\mathrm{e}^{-\mathrm{i}k_x\bar{x}/\beta^2} =& \frac{\partial\varphi^0}{\partial\bar{z}}(\bar{\mathbf{x}}) \\
-\frac{w_0 b}{\beta}\mathrm{e}^{-\mathrm{i}k_x\bar{x}/\beta^2} =& \alpha\mathrm{e}^{\gamma\bar{x}}\frac{\partial}{\partial\bar{z}}\mathrm{e}^{\mathrm{i}\sqrt{\kappa^2+\gamma^2}\bar{z}} \\
-\frac{w_0 b}{\beta}\mathrm{e}^{-\mathrm{i}k_x\bar{x}/\beta^2} =& \alpha\mathrm{e}^{\gamma\bar{x}}(-\mathrm{i}\sqrt{\kappa^2+\gamma^2})\mathrm{e}^{\mathrm{i}\sqrt{\kappa^2+\gamma^2}\bar{z}}
\end{aligned} \tag{A.19}$$

with

$$\begin{aligned}
\mathrm{e}^{-\mathrm{i}k_x\bar{x}/\beta^2} =& \alpha \ \mathrm{e}^{\gamma\bar{x}}, \quad \bar{z}=0 \\
-\frac{w_0 b}{\beta} =& -\mathrm{i}\alpha\sqrt{\kappa^2+\gamma^2}.
\end{aligned} \tag{A.20}$$

Replacing the definition of κ, one can obtain the parameters as

$$\begin{aligned}
\alpha =& -\frac{w_0 b}{\sqrt{\bar{k}_x^2+\bar{k}_y^2}} \\
\gamma =& -\mathrm{i}\frac{\bar{k}_x}{\beta^2}.
\end{aligned} \tag{A.21}$$

Introducing the definitions above, the solution of the velocity potential becomes

$$\varphi^0(\bar{\mathbf{x}}) = -\frac{w_0 b}{\sqrt{\bar{k}_x^2+\bar{k}_y^2}}\mathrm{e}^{-(\mathrm{i}\bar{k}_x\bar{x}+\sqrt{\bar{k}_x^2+\bar{k}_y^2}\bar{z})/\beta^2}. \tag{A.22}$$

The boundary condition defined in Equation (A.15) is now satisfied. In order to satisfy the first boundary condition defined in Equation (A.13), the corrected potential $\varphi^1 = \varphi^0 + \varphi^c$ is must be computed. Replacing the parameter φ in Equations (A.10) and (A.13) and since the derivative of the correction potential φ^c in the streamwise direction is equal to zero for the values $\bar{x} > 0$, the problem can be re-written as the Schwarzchild statement [121]

$$\begin{aligned}
\frac{\partial^2\varphi}{\partial X^2}+\frac{\partial^2\varphi}{\partial Y^2}+\kappa^2\varphi =& 0 \\
\varphi(\mathbf{X}) =& f(X), \quad X \geq 0 \\
\frac{\partial\varphi}{\partial Y}(\mathbf{X}) =& 0, \quad X < 0.
\end{aligned} \tag{A.23}$$

with the solution for $X < 0$ and $Z = 0$ given as

$$\varphi(X,0) = \frac{1}{\pi}\int_0^\infty G(X,\xi,0)f(\xi)\ \mathrm{d}\xi. \tag{A.24}$$

The function G is defined as

$$G(X,\xi,0) = \sqrt{\frac{-X}{\xi}}\frac{\mathrm{e}^{-\mathrm{i}\kappa(\xi-X)}}{\xi - X}. \tag{A.25}$$

Converting the problem set to the Schwarzschild problem, one can obtain

$$\begin{aligned}\varphi^c(\bar{\mathbf{x}}) &= -\frac{1}{\pi}\int_0^\infty \sqrt{\frac{\bar{x}}{\xi}}\frac{\mathrm{e}^{-\mathrm{i}\kappa(\xi+\bar{x})}}{\xi+\bar{x}}\varphi^0(-\xi,0)\ \mathrm{d}\xi \\ &= \frac{w_0 b}{\pi\sqrt{\bar{k}_x^2+\bar{k}_y^2}}\mathrm{e}^{-\mathrm{i}\kappa\bar{x}}\int_0^\infty \sqrt{\frac{\bar{x}}{\xi}}\frac{\mathrm{e}^{-\mathrm{i}\xi(\kappa-\bar{k}_x/\beta^2)}}{\xi+\bar{x}}\ \mathrm{d}\xi\end{aligned} \tag{A.26}$$

Knowing that the integral on the right hand side of the equation reads [48]

$$\int_0^\infty \sqrt{\frac{A}{\xi}}\frac{\mathrm{e}^{-\mathrm{i}B\xi}}{\xi+A}\ \mathrm{d}\xi = \pi\mathrm{e}^{\mathrm{i}BX}\left(1 - \frac{\mathrm{e}^{\mathrm{i}\pi/4}}{\sqrt{\pi}}\int_0^{BX}\frac{\mathrm{e}^{-\mathrm{i}t}}{\sqrt{(t)}}\ \mathrm{d}t\right), \tag{A.27}$$

Equation (A.28) can be computed as

$$\varphi^c(\bar{\mathbf{x}}) = \frac{w_0 b}{\sqrt{\bar{k}_x^2+\bar{k}_y^2}}\mathrm{e}^{-\mathrm{i}\bar{k}_x\bar{x}/\beta^2}\left(1 - (1+\mathrm{i})\int_0^{(\kappa-\bar{k}_x/\beta^2)}\frac{\mathrm{e}^{-\mathrm{i}t}}{\sqrt{2\pi t}}\ \mathrm{d}t\right). \tag{A.28}$$

The integral can be converted to the Fresnel integrals $E(x) = C(x) + iS(x)$ defined as

$$E(x) = \int_0^x \frac{\mathrm{e}^{\mathrm{i}t}}{\sqrt{2\pi t}}\ \mathrm{d}t. \tag{A.29}$$

using the transformation

$$(1-\mathrm{i})E(x) = (1+\mathrm{i})E^*(-x) \tag{A.30}$$

where the superscript * represents the complex conjugate operator. Introducing the Fresnel integrals, the Equation (A.28) results

$$\varphi^c(\bar{\mathbf{x}}) = \frac{w_0 b}{\sqrt{\bar{k}_x^2+\bar{k}_y^2}}\mathrm{e}^{-\mathrm{i}\bar{k}_x\bar{x}/\beta^2}\left(1 - (1-\mathrm{i})E\left[(-\kappa+\bar{k}_x/\beta^2)\bar{x}\right]\right). \tag{A.31}$$

The corrected velocity field is then obtained via adding Equation (A.31) to (A.22) as

$$\varphi^1(\bar{\mathbf{x}}) = -\frac{w_0 b}{\sqrt{\bar{k}_x^2+\bar{k}_y^2}}\mathrm{e}^{-\mathrm{i}\bar{k}_x\bar{x}/\beta^2}(1-\mathrm{i})E\left[(-\kappa+\bar{k}_x/\beta^2)\bar{x}\right]. \tag{A.32}$$

Introducing the formulation (A.32) into Equation (A.4), the velocity potential in dimensional form then reads

$$\phi(\mathbf{x}) = -\frac{w_0}{\sqrt{k_x^2+k_y^2}}\mathrm{e}^{\mathrm{i}(Uk_xt-k_xx-k_yy)}(1-\mathrm{i})E\big[\frac{x}{b}(-\kappa+\bar{k}_x/\beta^2)\big]. \tag{A.33}$$

Since the velocity potential is linked to the surface pressure as

$$p(x,y,0,t) = -\rho_0\frac{\mathrm{D}\phi}{\mathrm{D}t} \tag{A.34}$$

where the particular differentiation defined in Equation A.2. Hence the surface pressure is computed via

$$p(x,y,0,t) = -\rho_0\left(\frac{\partial\phi}{\partial t}+U\frac{\partial\phi}{\partial x}\right). \tag{A.35}$$

The derivations of the velocity potential defined in expression (A.33) appearing in the Equation (A.35) are computed as

$$\begin{aligned}\frac{\partial\phi}{\partial t} =& -\frac{w_0}{\sqrt{k_x^2+k_y^2}}\mathrm{e}^{-\mathrm{i}(k_xx+k_yy)}(1-\mathrm{i})E\big[\frac{x}{b}(-\kappa+\bar{k}_x/\beta^2)\big]\frac{\partial}{\partial t}\left(\frac{\partial\phi}{\partial t}\mathrm{e}^{\mathrm{i}Uk_xt}\right)\\ =& -\frac{w_0}{\sqrt{k_x^2+k_y^2}}(1-\mathrm{i})E\big[\frac{x}{b}(-\kappa+\bar{k}_x/\beta^2)\big]\mathrm{i}Uk_x\mathrm{e}^{\mathrm{i}(Uk_xt-k_xx-k_yy)}\end{aligned} \tag{A.36}$$

and

$$\begin{aligned}\frac{\partial\phi}{\partial x} =& -\frac{w_0}{\sqrt{k_x^2+k_y^2}}(1-\mathrm{i})\mathrm{e}^{\mathrm{i}(Uk_xt-k_yy)}\frac{\partial}{\partial x}\left(\mathrm{e}^{-\mathrm{i}k_xx}E\big[\frac{x}{b}(-\kappa+\bar{k}_x/\beta^2)\big]\right)\\ =& -\frac{w_0}{\sqrt{k_x^2+k_y^2}}(1-\mathrm{i})\mathrm{e}^{\mathrm{i}(Uk_xt-k_yy)}\Bigg[(-\mathrm{i}k_x)\mathrm{e}^{-\mathrm{i}k_xx}E\big[\frac{x}{b}(-\kappa+\bar{k}_x/\beta^2)\big]+\\ &\mathrm{e}^{-\mathrm{i}k_xx}\frac{\partial}{\partial x}\left(E\big[\frac{x}{b}(-\kappa+\bar{k}_x/\beta^2)\big]\right)\Bigg].\end{aligned} \tag{A.37}$$

It is seen that multiplying the first term in the brackets of Equation (A.37) with U as defined in expression (A.35) results in minus the right Equation (A.36). Hence the surface pressure is computed only using the second part of the expression (A.37)

$$p(x,y,0,t) = \rho_0\frac{w_0}{\sqrt{k_x^2+k_y^2}}\mathrm{e}^{\mathrm{i}(Uk_xt-k_xx-k_yy)}U(1-\mathrm{i})\frac{\partial}{\partial x}\left(E\big[\frac{x}{b}(-\kappa+\bar{k}_x/\beta^2)\big]\right). \tag{A.38}$$

The derivation of the Fresnel integral is now obtained employing the Leibniz rule [1]

$$\frac{\partial}{\partial\alpha}\int_{a(\alpha)}^{b(\alpha)}f(x,a)\mathrm{d}x = \frac{\mathrm{d}b(\alpha)}{\mathrm{d}\alpha}f(b(\alpha,\alpha)) - \frac{\mathrm{d}a(\alpha)}{\mathrm{d}\alpha}f(a(\alpha,\alpha)) + \int_{a(\alpha)}^{b(\alpha)}\frac{\partial}{\partial\alpha}f(x,a)\mathrm{d}x. \tag{A.39}$$

Finally, the surface pressure results as

$$p(x,y,0,t) = \rho_0w_0U\frac{\mathrm{e}^{-\mathrm{i}\pi/4}}{\sqrt{\pi(\beta^2\kappa+k_xb)x/b}}\mathrm{e}^{\mathrm{i}(Uk_xt-(k_x+(\kappa-k_x/\beta^2)/b)x-k_yy)}. \tag{A.40}$$

The pressure jump on the profile can be written as

$$\Delta P(x,0,t) = 2\pi\rho_0 U\ w_0\ g(x,k_x,k_y)\mathrm{e}^{\mathrm{i}\omega t} \tag{A.41}$$

where $P(x,0,t)$ is linked to the surface pressure $p(x,y,0,t)$ via

$$p(x,y,0,t) = P(x,0,t)\mathrm{e}^{-\mathrm{i}k_y y}. \tag{A.42}$$

Since the thickness and the camber is infinitely small, the pressure jump on the profile is assumed to be twice the pressure fluctuations on one face of the profile. Combining the last three formulations above, one can obtain the relation between the transfer function g and the surface pressure as p as

$$g(x,k_x,k_y) = \frac{p(x,y,0,t)\mathrm{e}^{-\mathrm{i}(\omega t - k_y y)}}{\pi\rho_0 U w_0}. \tag{A.43}$$

The transfer function g can now be computed with this equation. The origin of the coordinate axis is defined on the leading edge where the streamwise position of the profile is located between $0 < \bar{x} < 2$. However, for the derivations defined in Chapter 4 the origin is located at the center of the airfoil, making $-1 < \bar{x} < 1$. Hence, changing $\bar{x}$ with $\bar{x} - 1$, the transfer function can be computed as

$$g(\bar{x},k_x,k_y) = \frac{\mathrm{e}^{-\mathrm{i}\pi/4}}{\pi\sqrt{\pi(\bar{k}_x+\beta^2\kappa)(\bar{x}+1)}}\mathrm{e}^{-\mathrm{i}(\kappa-\bar{k}_x M^2/\beta^2)(\bar{x}+1)}. \tag{A.44}$$

For readers infirmation, the backscattering component from the trailing edge [111] in the derivations of the transfer function is not considered since high frequencies are addressed [96].

The aeroacoustic transfer function $\mathcal{L}(\mathbf{x},k_x,k_y)$ is then obtained via the chordwise integration

$$\mathcal{L}(x,k_x,k_y) = \int_{-1}^{1} g(\xi,k_x,k_y)\ \mathrm{e}^{-\mathrm{i}k_x M(M-x/\sigma_0)\xi/\beta^2}\mathrm{d}\xi \tag{A.45}$$

where ξ is the chordwise position of the dipole on the surface. Introducing the definition of g into Equation (A.45)

$$\begin{aligned}\mathcal{L}(x,k_x,k_y) =& \frac{1-\mathrm{i}}{\pi\sqrt{\bar{k}_x+\beta^2\kappa}} \\ & \int_{-1}^{1} frac1\sqrt{2\pi(\bar{x}_0+1)}\mathrm{e}^{-\mathrm{i}[(\kappa-M^2\bar{k}_x/\beta^2)(\bar{x}_0+1)]}\mathrm{e}^{-\mathrm{i}\mu\bar{x}_0(M-x/\sigma_0)}\mathrm{d}\bar{x}\end{aligned} \tag{A.46}$$

with $\mu = \bar{k}_x M/\beta^2$. The subscript zero, x_0, indicates the dipole position. The integral is then solved as

$$\begin{aligned}\mathcal{L}(x,k_x,k_y) =& \frac{1-\mathrm{i}}{\pi\sqrt{\bar{k}_x+\beta^2\kappa}}\int_0^2 \frac{1}{\sqrt{2\pi(\bar{x}_0)}}\mathrm{e}^{-\mathrm{i}[(\kappa-M^2\bar{k}_x/\beta^2)\bar{x}_0]}\mathrm{e}^{-\mathrm{i}\mu(\bar{x}_0-1)(M-x/\sigma_0)}\mathrm{d}\bar{x}_0 \\ =& \frac{(1-\mathrm{i})\mathrm{e}^{\mathrm{i}\mu(M-x/\sigma_0)}}{\pi\sqrt{\bar{k}_x+\beta^2\kappa}}\int_0^2 \frac{\mathrm{e}^{-\mathrm{i}\bar{x}_0}\Theta_1}{\sqrt{2\pi\bar{x}_0}}\mathrm{d}\bar{x}_0 \\ =& \frac{\mathrm{e}^{\mathrm{i}\Theta_2}}{\pi}\sqrt{\frac{2}{\bar{k}_x+\beta^2\kappa}}\int_0^2 \frac{\mathrm{e}^{-\mathrm{i}\bar{x}_0}\Theta_1}{\sqrt{2\pi\bar{x}_0}}\mathrm{d}\bar{x}_0 \end{aligned} \tag{A.47}$$

where the new parameters are $\Theta_1 = \kappa - \mu x/\sigma_0$ and $\Theta_2 = \mu(M - x/\sigma_0) - \pi/4$. Using the definition of Fresnel integrals, the last term on the right hand side becomes

$$\int_0^2 \frac{\mathrm{e}^{-\mathrm{i}\bar{x}_0}\Theta_1}{\sqrt{2\pi\bar{x}_0}}\mathrm{d}\bar{x}_0 = \frac{E^*(2\Theta_1)}{\sqrt{\Theta_1}}. \tag{A.48}$$

Hence, the aeroacoustic transfer function finally reads

$$\mathcal{L}(x,k_x,k_y) = \frac{1}{\pi}\sqrt{\frac{2}{(\bar{k}_x+\beta^2\kappa)\Theta_1}}E^*(2\Theta_1)\mathrm{e}^{\mathrm{i}\Theta_2}. \tag{A.49}$$

Following a similar procedure, the second transfer function $\mathcal{L}'(x,k_x,k_y)$ appearing in the scattered field derivations in Chapter 5 can be integrated as

$$\begin{aligned}\mathcal{L}'(x,k_x,k_y) =& \int_{-1}^1 g(\bar{x}_0,k_x,k_y)\mathrm{e}^{-\mathrm{i}\mu\bar{x}_0(M-x/\sigma_0)}\mathrm{d}\bar{x}_0\ \bar{x}_0 \\ =& \frac{1-\mathrm{i}}{\pi\sqrt{\bar{k}_x+\beta^2\kappa}}\int_{-1}^1 \frac{1}{\sqrt{2\pi(\bar{x}_0+1)}}\mathrm{e}^{-\mathrm{i}[(\kappa-M^2\bar{k}_x/\beta^2)(\bar{x}_0+1)]}\mathrm{e}^{-\mathrm{i}\mu\bar{x}_0(M-x/\sigma_0)}\bar{x}_0\ \mathrm{d}\bar{x} \\ =& \frac{1-\mathrm{i}}{\pi\sqrt{\bar{k}_x+\beta^2\kappa}}\int_0^2 \frac{1}{\sqrt{2\pi(\bar{x}_0)}}\mathrm{e}^{-\mathrm{i}[(\kappa-M^2\bar{k}_x/\beta^2)\bar{x}_0]}\mathrm{e}^{-\mathrm{i}\mu(\bar{x}_0-1)(M-x/\sigma_0)}(\bar{x}_0-1)\ \mathrm{d}\bar{x}_0 \\ =& \frac{\mathrm{e}^{\mathrm{i}\Theta_2}}{\pi}\sqrt{\frac{2}{\bar{k}_x+\beta^2\kappa}}\left[\int_0^2 \frac{\mathrm{e}^{-\mathrm{i}\bar{x}_0}\Theta_1}{\sqrt{2\pi\bar{x}_0}}\bar{x}_0\mathrm{d}\bar{x}_0 - \int_0^2 \frac{\mathrm{e}^{-\mathrm{i}\bar{x}_0}\Theta_1}{\sqrt{2\pi\bar{x}_0}}\mathrm{d}\bar{x}_0\right] \\ =& \frac{\mathrm{e}^{\mathrm{i}\Theta_2}}{\pi}\sqrt{\frac{2}{\bar{k}_x+\beta^2\kappa}}\left[\left[\sqrt{\frac{\bar{x}_0}{2\pi}}\mathrm{e}^{-\mathrm{i}\bar{x}_0\Theta_1}\right]_0^2 - \left(1+\frac{\mathrm{i}}{2\Theta_1}\right)\int_0^2 \frac{\mathrm{e}^{-\mathrm{i}\bar{x}_0}\Theta_1}{\sqrt{2\pi\bar{x}_0}}\mathrm{d}\bar{x}_0\right] \end{aligned} \tag{A.50}$$

and finally

$$\mathcal{L}'(x,k_x,k_y) = \frac{\mathrm{e}^{\mathrm{i}\Theta_2}}{\pi}\sqrt{\frac{2}{\bar{k}_x+\beta^2\kappa}}\left[\frac{\mathrm{i}\mathrm{e}^{-2\mathrm{i}\Theta_1}}{\sqrt{\pi}\Theta_1} - \left(1+\frac{\mathrm{i}}{2\Theta_1}\right)\frac{E^*(2\Theta_1)}{\sqrt{\Theta_1}}\right]. \tag{A.51}$$

Appendix B.

Derivation of the Spanwise Segmentation

Using the definition of acoustic pressure radiated from the point dipoles given in Equation (4.4) and integrating explicitly the distribution of dipoles over the airfoil surface the acoustic PSD is calculated as

$$\begin{aligned} S_{pp}(x,y,z,\omega) = &(\frac{\omega z}{4\pi c_0})^2 \\ &\int_{d_1}\int_{d_2}\int_{b_1}\int_{b_2}\int_{-\infty}^{\infty}(2\pi\rho_0)^2 g^*(x_1,K_x,k_y)g^*(x_2,K_x,k_y)U\Phi_{ww}(K_x,k_y) \\ &\frac{1}{\sigma_{y_1}^2}\frac{1}{\sigma_{y_2}^2}\mathrm{e}^{-\mathrm{i}(\frac{\omega y}{c_0\sigma_0}+k_y)y_1}\mathrm{e}^{-\mathrm{i}\omega\frac{x_1}{c_0\beta^2}(M-\frac{x}{\sigma_0})}\mathrm{e}^{\mathrm{i}(\frac{\omega y}{c_0\sigma_0}+k_y)y_2}\mathrm{e}^{\mathrm{i}\omega\frac{x_2}{c_0\beta^2}(M-\frac{x}{\sigma_0})}\mathrm{d}k_y\mathrm{d}x_2\mathrm{d}x_1\mathrm{d}y_2\mathrm{d}y_1. \end{aligned} \tag{B.1}$$

where $\sigma_{yn} = \sqrt{x^2+\beta^2(y-y_n)^2+\beta^2z^2}$ and $\sigma_0 = \sqrt{x^2+\beta^2y^2+\beta^2z^2}$ defined in Equation (4.27). Using such an intermediate far-field assumption allows the chordwise integrals to be solved analytically [5]

$$\mathcal{L}_n(x,K_x,k_y) = \int_b g^*(x_n,K_x,k_y)\mathrm{e}^{-\mathrm{i}\omega\frac{x_n}{c_0\beta^2}(M-\frac{x}{\sigma_0})}\mathrm{d}x_n. \tag{B.2}$$

Introducing Equation (B.2) into Equation (B.1), the PSD becomes

$$\begin{aligned} S_{pp}(x,y,z,\omega) = (\frac{\rho_0\omega z}{2c_0})^2 &\int_{-\infty}^{\infty}\int_{d_1}\frac{1}{\sigma_{y_1}^2}\mathrm{e}^{-\mathrm{i}(\frac{\omega y}{c_0\sigma_0}+k_y)y_1}\mathcal{L}_1^*(x,K_x,k_y)\mathrm{d}y_1 \\ &\int_{d_2}\frac{1}{\sigma_{y_2}^2}\mathrm{e}^{\mathrm{i}(\frac{\omega y}{c_0\sigma_0}+k_y)y_2}\mathcal{L}_2(x,K_x,k_y)\mathrm{d}y_2 \;\; U\Phi_{ww}(K_x,k_y)\mathrm{d}k_y \end{aligned} \tag{B.3}$$

The acoustic transfer function $\mathcal{L}$ is a function of incoming flow velocity U as defined in Equation (A.49) and since the incoming flow velocity varies in the spanwise direction, $\mathcal{L}$ is kept in the spanwise integrals.

The parameter $S_n(x,y,z;y_n) = 1/(\sigma_{y_n}^2)\mathrm{e}^{\mathrm{i}(\frac{\omega y}{c_0\sigma_0}+k_y)y_n}$ is defined in order to simplify the notation. The acoustic PSD then writes

$$\begin{aligned} S_{pp}(x,y,z,\omega) = (\frac{\rho_0\omega z}{2c_0})^2 &\int_{-\infty}^{\infty}\int_{d_1} S_1(x,y,z;y_1)\mathcal{L}_1^*(x,K_x,k_y)\mathrm{d}y_1 \\ &\int_{d_2} S_2(x,y,z;y_2)\mathcal{L}_2(x,K_x,k_y)\mathrm{d}y_2 \;\; U\Phi_{ww}(K_x,k_y)\mathrm{d}k_y \end{aligned} \tag{B.4}$$

Since the integral limits can be distributed using (for $-a<b<a$)

$$\int_{-a}^{a} f(x)\mathrm{d}x = \int_{-a}^{b} f(x)\mathrm{d}x + \int_{b}^{a} f(x)\mathrm{d}x, \tag{B.5}$$

the spanwise segmentation is performed for the acoustic PSD as

$$\begin{aligned} S_{pp}(x,y,z,\omega) = (\frac{\rho_0 \omega z}{2c_0})^2 \int_{-\infty}^{\infty} \\ \left(\int_{-d}^{d_1} S_1(y_1)^* \mathcal{L}_1^*(x,K_x,k_y)\mathrm{d}y_1 + \ldots + \int_{d_n}^{d} S_1(y_1)^* \mathcal{L}_1^*(x,K_x,k_y)\mathrm{d}y_1 \right) \\ \left(\int_{-d}^{d_1} S_2(y_2) \mathcal{L}_2(x,K_x,k_y)\mathrm{d}y_2 + \ldots + \int_{d_n}^{d} S_2(y_2) \mathcal{L}_2(x,K_x,k_y)\mathrm{d}y_2 \right) \\ U\Phi_{ww}(K_x,k_y)\mathrm{d}k_y \end{aligned} \tag{B.6}$$

for $-d < d_1 < ... < d_n < d$. Solving the spanwise integrals and defining the new parameter $P_n = \int_{d_{n-1}}^{d_n} S_n \cdot \mathcal{L}_n \mathrm{d}y_n$,

$$S_{pp}(x,y,z,\omega) = (\frac{\rho_0 \omega z}{2c_0})^2 \tag{B.7}$$

$$\begin{aligned} \Big(\int_{-\infty}^{\infty} P_1^* P_1 (U\Phi_{ww})_{1,1}\mathrm{d}k_y + \cdots + \int_{-\infty}^{\infty} P_1^* P_n (U\Phi_{ww})_{1,n}\mathrm{d}k_y + \\ \int_{-\infty}^{\infty} P_2^* P_1 (U\Phi_{ww})_{2,1}\mathrm{d}k_y + \ \cdots \\ \vdots \qquad\qquad \ddots \qquad\qquad \vdots \\ \int_{-\infty}^{\infty} P_n^* P_1 (U\Phi_{ww})_{n,1}\mathrm{d}k_y + \cdots + \int_{-\infty}^{\infty} P_n^* P_n (U\Phi_{ww})_{n,n}\mathrm{d}k_y \Big) \end{aligned} \tag{B.8}$$

the total PSD becomes equal to the summation of the auto- and cross-correlation of the strips.

The applications including spanwise segmentation in the literature [27, 38, 118] consider strips with distinct centers. The initial gust-airfoil interaction problem is then changed. Since the observer hears the gust perpendicular to the line joining the source to the observer [5] this may lead deviation from the original problem. In the segmentation procedure detailed above, the observer position is kept the same for the initial large aspect ratio airfoil and small strips. Only the spanwise integration limits are change on each strips. The initial gust-airfoil problem is then preserved.

Appendix C.

Application of the Doppler Factor to Broadband Fan Noise

C.1. Application to Free-Field Problems

The relative motion between the source and observer can be dealt with for moving sources and stationary observer or stationary source and moving observer due to the reciprocity property [101]. The latter is considered for the simplicity of derivations [96]. The relation between the acoustic pressure at the moving observer and the fixed one was shown in Equation (4.58) as $p^m(t) = p^f(\alpha t)$. Superscripts ^{m} and ^{f} represent the moving and the fixed observers, respectively. The ratio of emitted and observed frequencies, $\alpha = \omega_o/\omega_e$ is used for the derivations. Knowing that the acoustic PSD at a fixed observer is the Fourier transform of the auto-correlation function of the acoustic pressure

$$Spp^f(\omega_o) = \frac{1}{2\pi}\int_{-\infty}^{\infty} Rpp^f(\tau)\mathrm{e}^{-i\omega_o\tau}\mathrm{d}\tau \tag{C.1}$$

where the auto-correlation function at the fixed observer is defined as

$$Rpp^f(\tau) = \frac{1}{2T}\int_{-T}^{T} p^f(t)p^f(t+\tau)\mathrm{d}t. \tag{C.2}$$

Similarly, at the moving observer case, the autocorrelation function reads

$$Rpp^m(\tau) = \frac{1}{2T}\int_{-T}^{T} p^m(t)p^m(t+\tau)\mathrm{d}t, \tag{C.3}$$

Using the transformation between p^f and p^m defined in Equation (4.58), the auto-correlation function of the moving observer can be represented with the fixed ones

$$Rpp^m(\tau) = \frac{1}{2T}\int_{-T}^{T} p^f(\alpha t)p^f(\alpha(t+\tau))\mathrm{d}t. \tag{C.4}$$

Applying the change of the integration parameter the correlation function at the moving observer becomes

$$Rpp^m(\tau) = \frac{1}{2\alpha T}\int_{-\alpha T}^{\alpha T} p^f(t)p^f(t+\alpha\tau))\mathrm{d}t. \tag{C.5}$$

Finally the relation between correlation functions at fixed and moving observers is obtained as

$$Rpp^m(\tau) = Rpp^f(\alpha\tau). \tag{C.6}$$

Taking the Fourier transform of the Rpp^m, the acoustic PSD computed at the moving observer then becomes

$$\begin{aligned} Spp^m(\omega_o) =& \frac{1}{2\pi}\int_{-\infty}^{\infty} Rpp^m(\tau)\mathrm{e}^{-i\omega_o\tau}\mathrm{d}\tau, \\ =& \frac{1}{2\pi}\int_{-\infty}^{\infty} Rpp^f(\alpha\tau)\mathrm{e}^{-i\omega_o\tau}\mathrm{d}\tau, \\ =& \frac{1}{\alpha 2\pi}\int_{-\infty}^{\infty} Rpp^f(\tau)\mathrm{e}^{-i\omega_o\tau/\alpha}\mathrm{d}\tau, \\ =& \frac{1}{\alpha} Spp^f\left(\frac{\omega_o}{\alpha}\right). \end{aligned} \tag{C.7}$$

Introducing the definition of α, the acoustic PSD at the moving observer becomes

$$Spp^m(\omega_o) = \frac{\omega_e}{\omega_o} Spp^f(\omega_e). \tag{C.8}$$

C.2. Application to the Benchmark Problem

Equation 4.60 is used in order to compute the broadband noise generated by rotating blades. It includes the Doppler frequency shift. However, for the implementation of the scattering methods addressed in Chapter 5, it is not possible to take the frequency shift into account. Therefore its effect on the benchmark fan is investigated. It was shown in [88], for a low-speed axial fan, the observed frequency converges to the emitted frequency

$$\lim_{M\to 0}\left(\frac{\omega_e}{\omega_o}\right) \to 1 \tag{C.9}$$

hence the Doppler factor becomes negligible.

A test is performed using the low-speed axial fan described in Section 4.7 in order to address the effect of the Doppler shift. The observers are located at 5 radii away from the fan center. Three observer positions are tested $\theta = \pi/8, \pi/4, 0$. The far-field equation (4.26) is employed for the test-case using inverse strip theory with 4 segments.

Figure C.1 shows the sound spectra at three observer positions located in the far field of the fan. The spectra are shifted 10 dB from each other for clarity. The plain line and symbols represent the spectra with and without the Doppler effect. The difference of the spectra due to the Doppler effect is less than 1 dB, since the maximum Mach number is less than 0.08. Therefore, the Doppler effect is shown to be negligible for the low-speed axial fan of interest.

C.3. Application to Scattered-Field Problems

The free-field computations are based on the transformation of the auto-correlation function only, however in the scattered-field problems, the cross-correlation of the observer and acoustic mesh points is also a point of interest. One of the parameters appearing in the final Doppler factor formulation is the geometrical orientation of the acoustic point (field point and acoustic mesh) with respect to the moving source. Since the positions of any field point

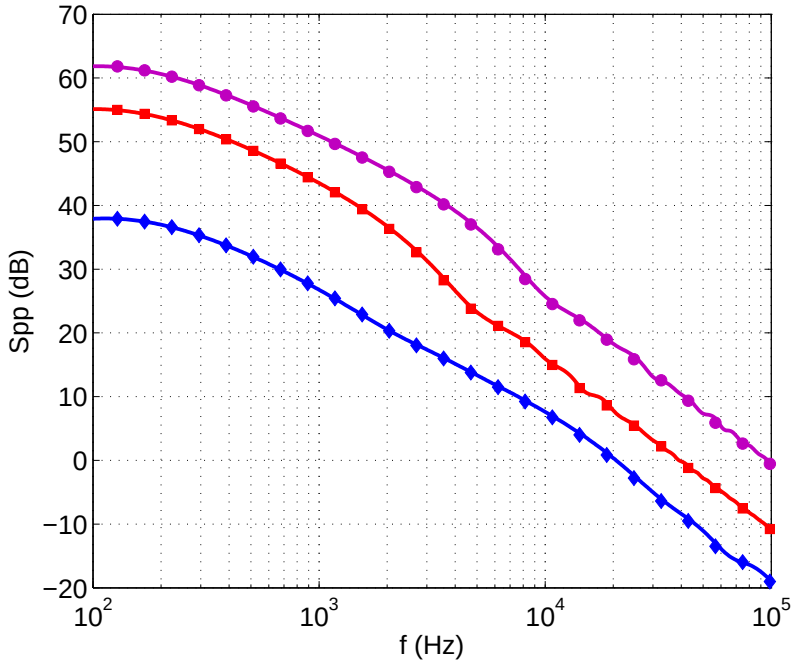

Figure C.1.: Acoustic PSD spectra of the low-Mach number axial fan at $\theta = \pi/8, \pi/4, 0$, (plain) with and (symbols) without the Doppler effect.

and acoustic mesh points are different, two different factors appear in the derivations for the cross-correlation terms. Using the transformation between fixed and moving observers, the acoustic pressures read $p_1^m(t) = p_1^f(\alpha_1 t)$ and $p_2^m(t) = p_2^f(\alpha_2 t)$ for two acoustic points. Reminding $\alpha_1 \neq \alpha_2$ unless they are not located at the same position in space, (see Figure C.2). Equation (C.4) then becomes

$$Rpp^m(\tau) = \frac{1}{2T}\int_{-T}^{T} P_1^f(\alpha_1 t) P_2^f(\alpha_2(t+\tau))\mathrm{d}t. \tag{C.10}$$

Unlike Equation (C.5), the correlation term $Rpp^m(\tau)$ can not be represented as a function of $Rpp^f(\tau), \alpha_1$ and α_2.

The problem faced is the implementation of the turbulence spectrum for the scattered-field computations. The Doppler factor is the ratio of the emitted and the observed frequencies resulting from the relative motion between the source and the observer. Since there is no relative motion between the observer and the acoustic mesh (unless the mesh is not moving with the source), a fixed observed frequency applies for both field and acoustic points. Fixing the observed frequency simplifies the computation and application of the ATV theory, however due to the different positions of acoustic and field point elements,

$$\begin{aligned} \omega_{o,1} &= \omega_{o,2} \\ \frac{\omega_{e,1}}{\alpha_1} &= \frac{\omega_{e,2}}{\alpha_2} \\ \alpha_1 &\neq \alpha_2 \\ \omega_{e,1} &\neq \omega_{e,2} \end{aligned} \tag{C.11}$$

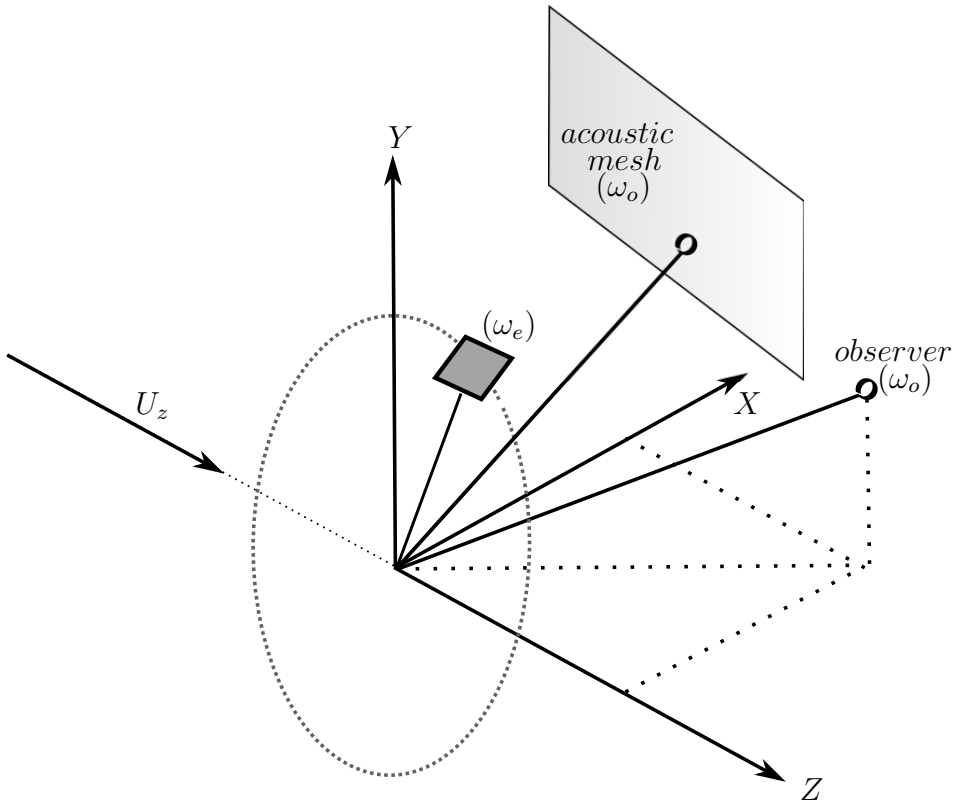

Figure C.2.: Sketch of the source, observer and the acoustic mesh for the broadband scattering problem.

the emitted frequency from the source is not unique. The semi-analytical method employed in Sections 4.6 and 5.2 is based on the statistical definition of the source field. For turbulence-interaction noise model, the source field is Fourier transform of the surface pressure jump of the airfoil [5],

$$\Delta P_T(x,y,t) = 2\pi\rho_0 U \int\int_{-\infty}^{\infty} \widehat{\widehat{w}}_R(k_x,k_y) g(x,k_x,k_y) \mathrm{e}^{i(k_y y - k_x U t)} \mathrm{d}k_x \mathrm{d}k_y \tag{C.12}$$

$$\Delta \hat{P}_T(x,y,\omega) = \rho_0 U \int\int_{-\infty}^{\infty} \widehat{\widehat{w}}_R(k_x,k_y) g(x,k_x,k_y) \mathrm{e}^{ik_y y} \int_{\infty}^{\infty} \mathrm{e}^{-i(\omega+Uk_x)t} \mathrm{d}t \mathrm{d}k_x \mathrm{d}k_y. \tag{C.13}$$

The time integral in the transformation tends to a delta function,

$$\int_{\infty}^{\infty} \mathrm{e}^{i(-\omega-Uk_x)t} \mathrm{d}t \rightarrow 2\pi\delta(\omega + Uk_x) \tag{C.14}$$

meaning that only one particular chordwise turbulence wave number yields in the pressure jump. The particular wave number is $K_x = \omega/U$.

The scattered-field problem is solved by means of auto- and cross-correlation of the acoustic quantities at the observer and acoustic mesh points. Introducing the relative motion between the source and the acoustic point, the observed frequency becomes different than the emitted one. Considering that the acoustic and scattering obstacle are located in a fixed position in space, the observed frequency becomes unique for all the acoustic points. Hence, as shown

in Equation (C.11), at different acoustic points in the space, different emitted frequencies apply. In the cross-correlation term of two acoustic mesh points on the scattering surface for example, two different chordwise turbulence wave numbers then apply, $K_{x,1}$ and $K_{x,2}$ where $K_{x,1} \neq K_{x,2}$. Since the turbulent spectrum is related with,

$$E[\widehat{\widehat{w}}_R(K_{x,1}, k_y)\widehat{\widehat{w^*}}_R(K_{x,2}, k'_y)] = \frac{R}{\pi}\delta(k_y - k'_y)\delta(K_{x,1} - K_{x,2})\Phi_{ww}(K_x, k_y) \tag{C.15}$$

if $K_{x,1} \neq K_{x,2}$, due to the statistical orthogonality of the wave vectors, the expected value of the auto-correlation of the source term is zero. Hence, the contribution of the Doppler factor cannot be taken into account with the current formulation. Nevertheless, it was shown above that the Doppler effect is assumed to be negligible for the low-speed axial fan tested [88]. It is therefore not taken into account for the scattered field problems. The aforementioned issue would be a concern for high-speed applications.

Appendix D.

Scattered-Field due to Broadband Noise Sources

The time history of the acoustic pressure at the field point is first decomposed to incident pressure p_i and the scattered pressure p_s as

$$p(t) = p_i(t) + p_s(t). \tag{D.1}$$

The PSD of the acoustic pressure at the observer point is obtained via the Fourier transform of the auto-correlation matrix

$$Spp = \int_{-\infty}^{\infty} Rpp(\tau)\ \mathrm{e}^{-\mathrm{i}\omega\tau}\ \mathrm{d}\tau \tag{D.2}$$

where the auto-correlation matrix is given as

$$Rpp(\tau) = \lim_{T_0\to\infty} \frac{1}{2T_0} \int_{-T_0}^{T_0} p(t)\ p^T(t+\tau)\ \mathrm{d}t. \tag{D.3}$$

Introducing Equation (D.1) into Equation (D.3), the auto-correlation term of the scattered acoustic field can be represented as the auto-and cross correlation of the incident and scattered acoustic fields as

$$Rpp(\tau) = Rpp(\tau) + Rp_ip_i(\tau) + Rp_ip_s(\tau) + Rp_sp_i(\tau) + Rp_sp_s(\tau). \tag{D.4}$$

The correlation terms are then [123]

$$\begin{aligned}
Rp_ip_i(\tau) &= \lim_{T_0\to\infty} \frac{1}{2T_0} \int_{-T_0}^{T_0} p_i(t)\ p_i^T(t+\tau)\ \mathrm{d}t \\
Rp_ip_s(\tau) &= \lim_{T_0\to\infty} \frac{1}{2T_0} \int_{-T_0}^{T_0} p_i(t)\ p_s^T(t+\tau)\ \mathrm{d}t \\
Rp_sp_i(\tau) &= \lim_{T_0\to\infty} \frac{1}{2T_0} \int_{-T_0}^{T_0} p_s(t)\ p_i^T(t+\tau)\ \mathrm{d}t \\
Rp_sp_s(\tau) &= \lim_{T_0\to\infty} \frac{1}{2T_0} \int_{-T_0}^{T_0} p_s(t)\ p_s^T(t+\tau)\ \mathrm{d}t.
\end{aligned} \tag{D.5}$$

As defined in Equation (D.2), the Fourier transform of the autocorrelation matrix of the scattered acoustic field decomposed as,

$$Spp(\omega) = Sp_ip_i + Sp_ip_s + Sp_sp_i + Sp_sp_s. \tag{D.6}$$

with

$$
\begin{aligned}
Sp_ip_i &= \int_{-\infty}^{\infty} Rp_ip_i(\tau)\ \mathrm{e}^{-\mathrm{i}\omega\tau}\ \mathrm{d}\tau \\
Sp_ip_s &= \int_{-\infty}^{\infty} Rp_ip_s(\tau)\ \mathrm{e}^{-\mathrm{i}\omega\tau}\ \mathrm{d}\tau \\
Sp_sp_i &= \int_{-\infty}^{\infty} Rp_sp_i(\tau)\ \mathrm{e}^{-\mathrm{i}\omega\tau}\ \mathrm{d}\tau \\
Sp_sp_s &= \int_{-\infty}^{\infty} Rp_sp_s(\tau)\ \mathrm{e}^{-\mathrm{i}\omega\tau}\ \mathrm{d}\tau.
\end{aligned} \tag{D.7}
$$

The term Sp_ip_i term is the free-field acoustic PSD of the source which can be computed using the Equations defined in Chapter 4. The terms containing the subscript $_s$, appearing due to the effects of the scattering obstacle, need being computed in order to obtain the PSD of the scattered acoustic field. Introducing Equation (D.5) into Equation (D.8) the PSD reads [123]

$$
\begin{aligned}
Sp_ip_i &= \int_{-\infty}^{\infty} \lim_{T_0\to\infty} \frac{1}{2T_0} \int_{-T_0}^{T_0} p_i(t)\ p_i^T(t+\tau)\mathrm{d}t\ \mathrm{e}^{-\mathrm{i}\omega\tau}\ \mathrm{d}\tau \\
Sp_ip_s &= \int_{-\infty}^{\infty} \lim_{T_0\to\infty} \frac{1}{2T_0} \int_{-T_0}^{T_0} p_i(t)\ p_s^T(t+\tau)\mathrm{d}t\ \mathrm{e}^{-\mathrm{i}\omega\tau}\ \mathrm{d}\tau \\
Sp_sp_i &= \int_{-\infty}^{\infty} \lim_{T_0\to\infty} \frac{1}{2T_0} \int_{-T_0}^{T_0} p_s(t)\ p_i^T(t+\tau)\mathrm{d}t\ \mathrm{e}^{-\mathrm{i}\omega\tau}\ \mathrm{d}\tau \\
Sp_sp_s &= \int_{-\infty}^{\infty} \lim_{T_0\to\infty} \frac{1}{2T_0} \int_{-T_0}^{T_0} p_s(t)\ p_s^T(t+\tau)\mathrm{d}t\ \mathrm{e}^{-\mathrm{i}\omega\tau}\ \mathrm{d}\tau.
\end{aligned} \tag{D.8}
$$

In order to compute the scattered acoustic pressure $p_s(t)$ the ATV analogy in the BEM framework is used as [45],

$$
p_s(t) = \int_{-\infty}^{\infty} ATV(\tau)v_n(t-\tau)\ \mathrm{d}\tau. \tag{D.9}
$$

where v_n is the acoustical normal velocity at the position of the boundary element. Since the obstacle is assumed to be solid, the Neumann boundary conditions are satisfied on the boundary element [35]. The zero acoustic velocity normal to the element is obtained

$$
v_i(\tau) + v_n(\tau) = 0. \tag{D.10}
$$

where the incident acoustic velocity is obtained via the gradient of the incident pressure field. Combining Equations (D.9) and (D.10), the scattered pressure is then linked to the acoustic incident velocity,

$$
p_s(t) = -\int_{-\infty}^{\infty} ATV(\tau)v_i(t-\tau)\ \mathrm{d}\tau. \tag{D.11}
$$

Introducing Equation (D.11) into Equation (D.8), the auto and cross-correlation PSD becomes [123]

$$
\begin{aligned}
Sp_ip_i &= \int_{-\infty}^{\infty} \lim_{T_0\to\infty} \frac{1}{2T_0} \int_{-T_0}^{T_0} p_i(t)\ p_i^T(t+\tau)\ \mathrm{d}t\ \mathrm{e}^{-\mathrm{i}\omega\tau}\ \mathrm{d}\tau \\
Sp_ip_s &= -\int_{-\infty}^{\infty} \lim_{T_0\to\infty} \frac{1}{2T_0} \int_{-T_0}^{T_0} \left(\int_{-\infty}^{\infty} v_i^T(t+\tau-\tau_2) ATV^T(\tau_2)\ \mathrm{d}\tau_2\right) \\
&\quad p_i(t)\mathrm{d}t\ \mathrm{e}^{-\mathrm{i}\omega\tau}\ \mathrm{d}\tau \\
Sp_sp_i &= -\int_{-\infty}^{\infty} \lim_{T_0\to\infty} \frac{1}{2T_0} \int_{-T_0}^{T_0} \left(\int_{-\infty}^{\infty} ATV(\tau_1) v_i(t-\tau_1)\ \mathrm{d}\tau_1\right) \\
&\quad p_i^T(t+\tau)\ \mathrm{d}t\ \mathrm{e}^{-\mathrm{i}\omega\tau}\ \mathrm{d}\tau \\
Sp_sp_s &= \int_{-\infty}^{\infty} \lim_{T_0\to\infty} \frac{1}{2T_0} \int_{-T_0}^{T_0} \left(\int_{-\infty}^{\infty} ATV(\tau_1) v_i(t-\tau_1)\ \mathrm{d}\tau_1\right) \\
&\quad \left(\int_{-\infty}^{\infty} v_i^T(t+\tau-\tau_2) ATV^T(\tau_2)\mathrm{d}\tau_2\right)\ \mathrm{d}t\ \mathrm{e}^{-\mathrm{i}\omega\tau}\ \mathrm{d}\tau.
\end{aligned} \tag{D.12}
$$

Changing the integration parameters $t' = t - \tau_1$, Equation (D.12) yields

$$
\begin{aligned}
Sp_ip_i &= \int_{-\infty}^{\infty} \lim_{T_0\to\infty} \frac{1}{2T_0} \int_{-T_0}^{T_0} p_i(t)\ p_i^T(t+\tau)\ \mathrm{d}t\ \ \mathrm{e}^{-\mathrm{i}\omega\tau}\ \mathrm{d}\tau \\
Sp_ip_s &= -\int_{-\infty}^{\infty}\int_{-\infty}^{\infty} \lim_{T_0\to\infty} \frac{1}{2T_0} \int_{-T_0}^{T_0} p_i(t') v_i^T(t'+\tau-\tau_2)\ \mathrm{d}t' ATV^T(\tau_2)\ \ \mathrm{e}^{-\mathrm{i}\omega\tau}\ \mathrm{d}\tau\ \mathrm{d}\tau_2 \\
Sp_sp_i &= -\int_{-\infty}^{\infty} ATV(\tau_1) \int_{-\infty}^{\infty} \lim_{T_0\to\infty} \frac{1}{2T_0} \int_{-T_0}^{T_0} v_i(t') p_i^T(t'+\tau+\tau_1)\ \mathrm{d}t'\ \ \mathrm{e}^{-\mathrm{i}\omega\tau}\ \mathrm{d}\tau\ \mathrm{d}\tau_1 \\
Sp_sp_s &= \int_{-\infty}^{\infty}\int_{-\infty}^{\infty} ATV(\tau_1) \int_{-\infty}^{\infty} \lim_{T_0\to\infty} \frac{1}{2T_0} \int_{-T_0}^{T_0} v_i(t') v_i^T(t'+\tau+\tau_1-\tau_2)\ \mathrm{d}t' ... \\
&\quad ATV^T(\tau_2)\ \ \mathrm{e}^{-\mathrm{i}\omega\tau}\ \mathrm{d}\tau\ \mathrm{d}\tau_1\ \mathrm{d}\tau_2.
\end{aligned} \tag{D.13}
$$

Introducing the definition of the auto- and cross-correlation terms of incident pressure and velocity, similar to the ones defined in Equation (D.5) into Equation (D.13) writes

$$
\begin{aligned}
Sp_ip_i &= \int_{-\infty}^{\infty} Rp_ip_i(\tau)\ \ \mathrm{e}^{-\mathrm{i}\omega\tau}\ \mathrm{d}\tau \\
Sp_ip_s &= -\int_{-\infty}^{\infty}\int_{-\infty}^{\infty} Rp_iv_i(t+\tau-\tau_2)\ ATV^T(\tau_2)\ \ \mathrm{e}^{-\mathrm{i}\omega\tau}\ \mathrm{d}\tau\ \mathrm{d}\tau_2 \\
Sp_sp_i &= -\int_{-\infty}^{\infty} ATV(\tau_1) \int_{-\infty}^{\infty} Rv_ip_i(t+\tau+\tau_1)\ \ \ \mathrm{e}^{-\mathrm{i}\omega\tau}\ \mathrm{d}\tau\ \mathrm{d}\tau_1 \\
Sp_sp_s &= \int_{-\infty}^{\infty}\int_{-\infty}^{\infty} ATV(\tau_1) \int_{-\infty}^{\infty} Rv_iv_i(t+\tau+\tau_1-\tau_2)\ ATV^T(\tau_2) \\
&\quad \mathrm{e}^{-\mathrm{i}\omega\tau}\ \mathrm{d}\tau\ \mathrm{d}\tau_1\ \mathrm{d}\tau_2.
\end{aligned} \tag{D.14}
$$

Similar to $\mathrm{e}^{-\mathrm{i}\omega\tau} = \mathrm{e}^{\mathrm{i}\omega\tau_1}\ \mathrm{e}^{-\mathrm{i}\omega(\tau+\tau_1)}$, decomposing the exponential term,

$$
\begin{aligned}
Sp_ip_i &= \int_{-\infty}^{\infty} Rp_ip_i(\tau)\ \ \mathrm{e}^{-\mathrm{i}\omega\tau}\ \mathrm{d}\tau \\
Sp_ip_s &= -\int_{-\infty}^{\infty} Rp_iv_i(t_{pv})\ \mathrm{e}^{-\mathrm{i}\omega t_{pv}}\ \mathrm{d}t_{pv} \int_{-\infty}^{\infty} ATV^T(\tau_2)\ \ \mathrm{e}^{-\mathrm{i}\omega\tau_2}\ \mathrm{d}\tau_2 \\
Sp_sp_i &= -\int_{-\infty}^{\infty} ATV(\tau_1)\mathrm{e}^{\mathrm{i}\omega\tau_1}\ \mathrm{d}\tau_1 \int_{-\infty}^{\infty} Rv_ip_i(t_{vp})\ \ \mathrm{e}^{-\mathrm{i}\omega t_{vp}}\ \mathrm{d}t_{vp} \\
Sp_sp_s &= \int_{-\infty}^{\infty} ATV(\tau_1)\mathrm{e}^{\mathrm{i}\omega\tau_1}\ \mathrm{d}\tau_1 \int_{-\infty}^{\infty} Rv_iv_i(t_{vv})\ \mathrm{e}^{-\mathrm{i}\omega t_{vv}}\ \mathrm{d}t_{vv} \\
&\qquad \int_{-\infty}^{\infty} ATV^T(\tau_2)\ \ \mathrm{e}^{-\mathrm{i}\omega\tau_2}\ \mathrm{d}\tau\ \mathrm{d}\tau_2.
\end{aligned} \tag{D.15}
$$

with

$$
\begin{aligned}
t_{pv} &= t + \tau - \tau_2 \\
t_{vp} &= t + \tau + \tau_1 \\
t_{vv} &= t + \tau + \tau_1 - \tau_2.
\end{aligned} \tag{D.16}
$$

The final auto and cross-correlation terms of the PSD then become

$$
\begin{aligned}
Sp_ip_i &= Sp_ip_i(\omega) \\
Sp_ip_s &= -Sp_iv_i(\omega)ATV^T(\omega) \qquad \text{(D.17)} \\
Sp_sp_i &= -ATV^*(\omega)Sv_ip_i(\omega) \\
Sp_sp_s &= ATV^*(\omega)Sv_iv_i(\omega)ATV^T(\omega). \qquad \text{(D.18)}
\end{aligned}
$$

The total PSD defined in Equation (D.6) finally becomes [123]

$$
\begin{aligned}
S_{pp}(\omega) =& Sp_ip_i(\omega) \\
&- Sp_iv_i(\omega)ATV^T(\omega) - ATV^*(\omega)Sv_ip_i(\omega) + ATV^*(\omega)Sv_iv_i(\omega)ATV^T(\omega).
\end{aligned} \tag{D.19}
$$

Appendix E.

Derivations of Spv, Svp and Svv

In order to obtain the scattered field matrices Spv, Svp and Svv, one needs to derive incident velocity at the acoustic mesh point. The relation between the incident velocity and the incident pressure was given in Equation (5.3). Using the acoustical far-field definition of the acoustic pressure of a dipole,

$$p(x,y,z,\omega;x_1,y_1) \approx \frac{\mathrm{i}\omega z}{4\pi c_0 \sigma_k^2}(F\mathrm{e}^{\mathrm{i}\omega t})\mathrm{e}^{\mathrm{i}\omega(\frac{M(x-x_1)-\sigma_f}{c_0\beta^2}+\frac{xx_1+\beta^2 yy_1}{c_0\beta^2\sigma_f})} \tag{E.1}$$

where σ_f and σ_k are defined as

$$\sigma_f = \sqrt{x^2+\beta^2(y^2+z^2)}$$
$$\sigma_k = \sqrt{x^2+\beta^2(y-y_1)^2+\beta^2 z^2}$$

where the subscript $_1$ represents the position of the point dipole on the airfoil surface.

The gradient of the incident pressure in cartesian coordinates is needed. Starting from the streamwise component,

$$\frac{\partial p}{\partial x} = \frac{\mathrm{i}\omega}{4\pi c_0}(F\mathrm{e}^{\mathrm{i}\omega t})\frac{\partial}{\partial x}\left(\frac{z}{\sigma_k^2}\mathrm{e}^{\mathrm{i}\omega(\frac{M(x-x_1)-\sigma_f}{c_0\beta^2}+\frac{xx_1+\beta^2 yy_1}{c_0\beta^2\sigma_f})}\right). \tag{E.2}$$

The derivation of the exponential term reads

$$\frac{\partial}{\partial x}(e^{\mathrm{i}\omega(\frac{M(x-x_1)-\sigma_f}{c_0\beta^2}+\frac{xx_1+\beta^2 yy_1}{c_0\beta^2\sigma_f})}) = \mathrm{e}^{\mathrm{i}\omega(\frac{M(x-x_1)-\sigma_f}{c_0\beta^2}+\frac{xx_1+\beta^2 yy_1}{c_0\beta^2\sigma_f})}$$
$$\mathrm{i}\omega\left(\frac{M}{c_0\beta^2}-\frac{x}{c_0\beta^2\sigma_f}+x_1\left(\frac{1}{c_0\beta^2\sigma_f}-\frac{x^2}{c_0\beta^2\sigma_f^3}\right)+y_1\left(\frac{-xy}{c_0\sigma_f^3}\right)\right). \tag{E.3}$$

Grouping the terms in the parenthesis with respect to x_1 and y_1,

$$\frac{M}{c_0\beta^2}-\frac{x}{c_0\beta^2\sigma_f}+x_1(\frac{1}{c_0\beta^2\sigma_f}-\frac{x^2}{c_0\beta^2\sigma_f^3})+y_1(\frac{-xy}{c_0\sigma_f^3}) = B_{1x}+B_{2x}x_1+B_{3x}y_1 \tag{E.4}$$

with

$$
\begin{aligned}
B_{1x} &= \frac{M}{c_0\beta^2} - \frac{x}{c_0\beta^2\sigma_f} \\
B_{2x} &= \frac{1}{c_0\beta^2\sigma_f} - \frac{x^2}{c_0\beta^2\sigma_f^3} \\
B_{3x} &= \frac{-xy}{c_0\sigma_f^3}.
\end{aligned} \tag{E.5}
$$

The derivative in Equation (E.2) results

$$
\begin{aligned}
&\frac{\partial}{\partial x}\left(\frac{z\mathrm{e}^{\mathrm{i}\omega(\frac{M(x-x_1)-\sigma_f}{c_0\beta^2}+\frac{xx_1+\beta^2yy_1}{c_0\beta^2\sigma_f})}}{x^2+\beta^2(y-y_1)^2+\beta^2z^2}\right) = \frac{e^{\mathrm{i}\omega(\frac{M(x-x_1)-\sigma_f}{c_0\beta^2}+\frac{xx_1+\beta^2yy_1}{c_0\beta^2\sigma_f})}}{(x^2+\beta^2(y-y_1)^2+\beta^2z^2)^2} \\
&\Big(\mathrm{i}\omega zB_{1x}x^2+\mathrm{i}\omega zB_{2x}x_1x^2+\mathrm{i}\omega zB_{3x}y_1x^2+ \\
&\mathrm{i}\omega zB_{1x}\beta^2(y-y_1)^2+\mathrm{i}\omega zB_{2x}x_1\beta^2(y-y_1)^2+\mathrm{i}\omega zB_{3x}y_1\beta^2(y-y_1)^2+ \\
&\mathrm{i}\omega zB_{1x}\beta^2z^2+\mathrm{i}\omega zB_{2x}x_1\beta^2z^2+\mathrm{i}\omega zB_{3x}y_1\beta^2z^2-2xz\Big).
\end{aligned} \tag{E.6}
$$

Grouping Equation (E.6) with respect to the spanwise position of the dipole on the airfoil surface reads

$$
\begin{aligned}
&\frac{\partial}{\partial x}\left(\frac{z\mathrm{e}^{\mathrm{i}\omega(\frac{M(x-x_1)-\sigma_f}{c_0\beta^2}+\frac{xx_1+\beta^2yy_1}{c_0\beta^2\sigma_f})}}{x^2+\beta^2(y-y_1)^2+\beta^2z^2}\right) = \\
&\quad A\big(\mathrm{i}\omega zB_{1x}x^2+\mathrm{i}\omega zB_{3x}y_1x^2+\mathrm{i}\omega zB_{1x}\beta^2(y-y_1)^2+ \\
&\qquad \mathrm{i}\omega zB_{3x}y_1\beta^2(y-y_1)^2+i\omega zB_{1x}\beta^2z^2+\mathrm{i}\omega zB_{3x}y_1\beta^2z^2-2xz\big)+ \\
&\quad A\big(\mathrm{i}\omega zB_{2x}x^2+\mathrm{i}\omega zB_{2x}\beta^2(y-y_1)^2+\mathrm{i}\omega zB_{2x}\beta^2z^2\big)x_1
\end{aligned} \tag{E.7}
$$

with

$$
A = \frac{\mathrm{e}^{\mathrm{i}\omega(\frac{M(x-x_1)-\sigma_f}{c_0\beta^2}+\frac{xx_1+\beta^2yy_1}{c_0\beta^2\sigma_f})}}{(x^2+\beta^2(y-y_1)^2+\beta^2z^2)^2}. \tag{E.8}
$$

Terms in the parenthesis are named as C_x and D_x for simplicity in the further derivations.

$$
\begin{aligned}
C_x(y_1) =& \mathrm{i}\omega zB_{1x}x^2+\mathrm{i}\omega zB_{3x}y_1x^2+\mathrm{i}\omega zB_{1x}\beta^2(y-y_1)^2+ \\
&\mathrm{i}\omega zB_{3x}y_1\beta^2(y-y_1)^2+\mathrm{i}\omega zB_{1x}\beta^2z^2+\mathrm{i}\omega zB_{3x}y_1\beta^2z^2-2xz \\
D_x(y_1) =& \mathrm{i}\omega zB_{2x}x^2+\mathrm{i}\omega zB_{2x}\beta^2(y-y_1)^2+\mathrm{i}\omega zB_{2x}\beta^2z^2
\end{aligned} \tag{E.9}
$$

Combining the definitions of the new parameters, Equation (E.2) can now be simplified as

$$\frac{\partial}{\partial x}\left(\frac{z\mathrm{e}^{i\omega(\frac{M(x-x_1)-\sigma_f}{c_0\beta^2}+\frac{xx_1+\beta^2yy_1}{c_0\beta^2\sigma_f})}}{x^2+\beta^2(y-y_1)^2+\beta^2z^2}\right)=A\cdot C_x(y_1)+A\cdot D_x(y_1)x_1 \tag{E.10}$$

Introducing the spanwise and chordwise integrals, the streamwise derivative of the Equation (4.16) becomes,

$$\begin{aligned}\frac{\partial\dot{P}}{\partial x}=\ &\mathrm{e}^{\mathrm{i}\omega(\frac{Mx-\sigma_f}{c_0\beta^2})}\int_{-d}^{d}\frac{\mathrm{e}^{\mathrm{i}\omega\frac{yy_1}{c_0\sigma_f}}}{(x^2+\beta^2(y-y_1)^2+\beta^2z^2)^2}C_x(y_1)\mathrm{d}y_1\\ &\int_{-b}^{b}\mathrm{e}^{-\mathrm{i}\omega(\frac{M}{c_0\beta^2}-\frac{x}{c_0\beta^2\sigma_f})x_1}g(x_1)\mathrm{d}x_1+\\ &\mathrm{e}^{\mathrm{i}\omega(\frac{Mx-\sigma_f}{c_0\beta^2})}\int_{-d}^{d}\frac{\mathrm{e}^{\mathrm{i}\omega\frac{yy_1}{c_0\sigma_f}}}{(x^2+\beta^2(y-y_1)^2+\beta^2z^2)^2}D_x(y_1)\mathrm{d}y_1\\ &\int_{-b}^{b}\mathrm{e}^{-\mathrm{i}\omega(\frac{M}{c_0\beta^2}-\frac{x}{c_0\beta^2\sigma_f})x_1}g(x_1)x_1\mathrm{d}x_1\end{aligned} \tag{E.11}$$

The term $\dot{P}$ is the part of the acoustic pressure containing the corresponding parameters for the derivations. The remaining terms will be introduced later.

Replacing the chordwise integrals with the acoustic transfer functions described in Appendix A, Equation (E.11) becomes

$$\begin{aligned}\frac{\partial\dot{P}}{\partial x}=\ &\mathrm{e}^{\mathrm{i}\omega(\frac{Mx-\sigma_f}{c_0\beta^2})}\int_{-d}^{d}\frac{\mathrm{e}^{\mathrm{i}\omega\frac{yy_1}{c_0\sigma_f}}}{(x^2+\beta^2(y-y_1)^2+\beta^2z^2)^2}C_x(y_1)\mathcal{L}\ \mathrm{d}y_1+\\ &\mathrm{e}^{\mathrm{i}\omega(\frac{Mx-\sigma_f}{c_0\beta^2})}\int_{-d}^{d}\frac{\mathrm{e}^{\mathrm{i}\omega\frac{yy_1}{c_0\sigma_f}}}{(x^2+\beta^2(y-y_1)^2+\beta^2z^2)^2}D_x(y_1)\mathcal{L}'\ \mathrm{d}y_1\end{aligned} \tag{E.12}$$

Grouping $C_x(y_1)$ and $D_x(y_1)$ on the spanwise position of the dipoles on the airfoil, y_1, as

$$\begin{aligned}C_x(y_1)=&(\mathrm{i}\omega zB_{1x}x^2+\mathrm{i}\omega zB_{1x}\beta^2y^2+\mathrm{i}\omega z\beta^2z^2-2xz)+\\ &y_1(\mathrm{i}\omega zB_{3x}x^2-2i\omega B_{1x}\beta^2y+\mathrm{i}\omega zB_{3x}\beta^2z^2+\mathrm{i}\omega zB_{3x}\beta^2z^2)+\\ &y_1^2(\mathrm{i}\omega zB_{1x}\beta^2-2\mathrm{i}\omega zB_{3x}\beta^2y)+\\ &y_1^3(\mathrm{i}\omega zB_{3x}\beta^2)\\ D_x(y_1)=&(\mathrm{i}\omega zB_{2x}x^2+\mathrm{i}\omega zB_{2x}\beta^2y^2+\mathrm{i}\omega zB_{2x}\beta^2z^2)+\\ &y_1(-2\mathrm{i}\omega B_{2x}\beta^2y)+\\ &y_1^2(\mathrm{i}\omega z\beta^2B_{2x}).\end{aligned} \tag{E.13}$$

Decomposing $C_x(y_1)=C_{0x}+C_{1x}y_1+C_{2x}y_1^2+C_3y_1^3$ and $D_x(y_1)=D_{0x}+D_{1x}y_1+D_{2x}y_1^2$ as defined above, Equation (E.11) becomes

$$\begin{aligned}\frac{\partial \dot{P}}{\partial x} = \mathrm{e}^{\mathrm{i}\omega(\frac{Mx-\sigma_f}{c_0\beta^2})}\Bigg(&\int_{-d}^{d} \frac{\mathrm{e}^{\mathrm{i}\omega\frac{yy_1}{c_0\sigma_f}}}{(x^2+\beta^2(y-y_1)^2+\beta^2z^2)^2} C_{0x}\mathcal{L}\ \mathrm{d}y_1 + \\ &\int_{-d}^{d} \frac{\mathrm{e}^{\mathrm{i}\omega\frac{yy_1}{c_0\sigma_f}}}{(x^2+\beta^2(y-y_1)^2+\beta^2z^2)^2} C_{1x}y_1\mathcal{L}\ \mathrm{d}y_1 + \\ &\int_{-d}^{d} \frac{\mathrm{e}^{\mathrm{i}\omega\frac{yy_1}{c_0\sigma_f}}}{(x^2+\beta^2(y-y_1)^2+\beta^2z^2)^2} C_{2x}y_1^2\mathcal{L}\ \mathrm{d}y_1 + \\ &\int_{-d}^{d} \frac{\mathrm{e}^{\mathrm{i}\omega\frac{yy_1}{c_0\sigma_f}}}{(x^2+\beta^2(y-y_1)^2+\beta^2z^2)^2} C_{3x}y_1^3\mathcal{L}\ \mathrm{d}y_1 + \\ &\int_{-d}^{d} \frac{\mathrm{e}^{\mathrm{i}\omega\frac{yy_1}{c_0\sigma_f}}}{(x^2+\beta^2(y-y_1)^2+\beta^2z^2)^2} D_{0x}\mathcal{L}'\ \mathrm{d}y_1 + \\ &\int_{-d}^{d} \frac{\mathrm{e}^{\mathrm{i}\omega\frac{yy_1}{c_0\sigma_f}}}{(x^2+\beta^2(y-y_1)^2+\beta^2z^2)^2} D_{1x}y_1\mathcal{L}'\ \mathrm{d}y_1 + \\ &\int_{-d}^{d} \frac{\mathrm{e}^{\mathrm{i}\omega\frac{yy_1}{c_0\sigma_f}}}{(x^2+\beta^2(y-y_1)^2+\beta^2z^2)^2} D_{2x}y_1^2\mathcal{L}'\ \mathrm{d}y_1\Bigg)\end{aligned} \tag{E.14}$$

Introducing the spanwise wave numbers, k_y, the integral on the spanwise position of the dipoles become

$$\begin{aligned} I_0 &= \int_{-d}^{d} \mathrm{e}^{\mathrm{i}(\frac{\omega y}{c_0\sigma_f}+k_y)y_1} \frac{1}{(x^2+\beta^2(y_1-y)^2+\beta^2z^2)^2}\mathrm{d}y_1 \\ I_1 &= \int_{-d}^{d} \mathrm{e}^{\mathrm{i}(\frac{\omega y}{c_0\sigma_f}+k_y)y_1} \frac{y_1}{(x^2+\beta^2(y_1-y)^2+\beta^2z^2)^2}\mathrm{d}y_1 \\ I_2 &= \int_{-d}^{d} \mathrm{e}^{\mathrm{i}(\frac{\omega y}{c_0\sigma_f}+k_y)y_1} \frac{y_1^2}{(x^2+\beta^2(y_1-y)^2+\beta^2z^2)^2}\mathrm{d}y_1 \\ I_3 &= \int_{-d}^{d} \mathrm{e}^{\mathrm{i}(\frac{\omega y}{c_0\sigma_f}+k_y)y_1} \frac{y_1^3}{(x^2+\beta^2(y_1-y)^2+\beta^2z^2)^2}\mathrm{d}y_1 \end{aligned} \tag{E.15}$$

Repeating the derivations for y and z components, one can obtain the parameters

$$\begin{aligned} C_y(y_1) =&(\mathrm{i}\omega z B_{1y}\sigma_f^2 - 2z\beta^2 y) + \\ &y_1(\mathrm{i}\omega z B_{3y}\sigma_f^2 - 2\mathrm{i}\omega B_{2y}\beta^2 y + 2z\beta^2) + \\ &y_1^2(\mathrm{i}\omega z B_{1y}\beta^2) - 2\mathrm{i}\omega z B_{3y}\beta^2 y) + \\ &y_1^3(\mathrm{i}\omega z B_{3y}\beta^2) \\ D_y(y_1) =&(\mathrm{i}\omega z B_{2y}\sigma_f^2) + \\ &y_1(-2\mathrm{i}\omega B_{2y}\beta^2 y) + \\ &y_1^2(\mathrm{i}\omega z\beta^2 B_{2y}). \end{aligned} \tag{E.16}$$

$$
\begin{aligned}
C_z(y_1) =&(\sigma_f^2 + \mathrm{i}\omega z B_{1z}\sigma_f^2 - 2\beta^2 z^2)+ \\
&y_1(\mathrm{i}\omega z B_{3z}\sigma_f^2 - 2\beta^2 y 2i\omega B_{1z}\beta^2 y)+ \\
&y_1^2(\beta^2 + i\omega z B_{1z}\beta^2 - 2zi\omega B_{3z}\beta^2 y)+ \\
&y_1^3(\mathrm{i}\omega z B_{3z}\beta^2) \\
D_z(y_1) =&(\mathrm{i}\omega z B_{2z}\sigma_f^2)+ \\
&y_1(-2\mathrm{i}\omega B_{2z}\beta^2 y)+ \\
&y_1^2(\mathrm{i}\omega B_{2z}\beta^2).
\end{aligned} \tag{E.17}
$$

The normal velocity is then computed with the incident acoustic velocity components

$$
\begin{aligned}
v_x &\propto \frac{\partial \dot{P}}{\partial x} \\
&\propto \mathrm{e}^{\mathrm{i}\omega(\frac{Mx-\sigma_f}{c_0\beta^2})} \\
&\quad ((C_{0x}\mathcal{L} + D_{0x}\mathcal{L}')I_0 + (C_{1x}\mathcal{L} + D_{1x}\mathcal{L}')I_1 + (C_{2x}\mathcal{L} + D_{2x}\mathcal{L}')I_2 + C_{3x}\mathcal{L}I_3)
\end{aligned} \tag{E.18}
$$

$$
\begin{aligned}
v_y &\propto \frac{\partial \dot{P}}{\partial y} \\
&\propto \mathrm{e}^{\mathrm{i}\omega(\frac{Mx-\sigma_f}{c_0\beta^2})} \\
&\quad ((C_{0y}\mathcal{L} + D_{0y}\mathcal{L}')I_0 + (C_{1y}\mathcal{L} + D_{1y}\mathcal{L}')I_1 + (C_{2y}\mathcal{L} + D_{2y}\mathcal{L}')I_2 + C_{3y}\mathcal{L}I_3)
\end{aligned} \tag{E.19}
$$

$$
\begin{aligned}
v_z &\propto \frac{\partial \dot{P}}{\partial z} \\
&\propto \mathrm{e}^{\mathrm{i}\omega(\frac{Mx-\sigma_f}{c_0\beta^2})} \\
&\quad ((C_{0z}\mathcal{L} + D_{0z}\mathcal{L}')I_0 + (C_{1z}\mathcal{L} + D_{1z}\mathcal{L}')I_1 + (C_{2z}\mathcal{L} + D_{2z}\mathcal{L}')I_2 + C_{3z}\mathcal{L}I_3)\,.
\end{aligned} \tag{E.20}
$$

The relation between the incident acoustical velocity and the dipole positions is derived above. The definition of the derivation of the acoustic transfer functions are given in Appendix A. The only remaining term is then the computation of the spanwise integrals. As mentioned in Section 4.1.2, the spanwise position of the dipole is introduced for the geometrical near-field correction. The integration is then different from the one defined in reference [5].

The spanwise integral I_0 defined above can be first simplified as

$$
I_0 = A\int_{-d-y}^{d-y} \mathrm{e}^{\mathrm{i}By_1}\frac{1}{((y_1)^2 + C)^2}\mathrm{d}y_1 \tag{E.21}
$$

where

$$
\begin{aligned}
A =& \frac{\mathrm{e}^{\mathrm{i}(\frac{\omega y}{c_0\sigma_f}+k_y)y}}{\beta^4} \\
B =& \frac{\omega y}{c_0\sigma_f} + k_y \\
C =& \frac{x^2}{\beta^2} + z^2.
\end{aligned} \tag{E.22}
$$

Introducing the Exponential integrals E_1 [1]

$$
E_1(\mu) = \int_{\mu}^{\infty} \frac{\mathrm{e}^{-t}}{t}\mathrm{d}t, \qquad (|\arg\mu| < \pi). \tag{E.23}
$$

the integral I_0 results

$$
\begin{aligned}
I_0 =& \frac{A}{4C^{3/2}} \frac{2\sqrt{C}\mathrm{e}^{\mathrm{i}Bx}x}{x^2+C} + \\
& \frac{A\mathrm{i}}{4C^{3/2}} \Big[(B\sqrt{C})(\mathrm{e}^{-B\sqrt{C}}E_1(-B\sqrt{C}-\mathrm{i}Bx) + \mathrm{e}^{B\sqrt{C}}E_1(B\sqrt{C}-\mathrm{i}Bx)) + \\
& (\mathrm{e}^{-B\sqrt{C}}E_1(-B\sqrt{C}-\mathrm{i}Bx) - \mathrm{e}^{B\sqrt{C}}E_1(B\sqrt{C}-\mathrm{i}Bx)) \Big].
\end{aligned} \tag{E.24}
$$

If the limits of the integration (E.21) have opposite signs, a removable singularity around 0 appears. In order to remove the singularity around 0, the integral is calculated as for opposite sign integrals in the neighborhood of 0, decomposing the integration interval as

$$
\int_{-d}^{d} \frac{\mathrm{e}^{ix}}{a^2+x^2}\mathrm{d}x \equiv \int_{-d}^{0^-} \frac{\mathrm{e}^{ix}}{a^2+x^2}\mathrm{d}x + \int_{0^+}^{d} \frac{\mathrm{e}^{ix}}{a^2+x^2}\mathrm{d}x. \tag{E.25}
$$

The arbitrarily small number is selected as $0^+ = 10^{-10}$ for the computations detailed in the related chapter.

The second spanwise integral I_1 using the same A,B and C parameters is computed as

$$
\begin{aligned}
I_1 =& yI_0 + \\
& \frac{AB}{4\sqrt{C}} \left(\mathrm{e}^{-B\sqrt{C}}E_i(B\sqrt{C}+\mathrm{i}Bx) - \mathrm{e}^{B\sqrt{C}}E_i(-B\sqrt{C}+\mathrm{i}Bx) - \frac{2\sqrt{C}\mathrm{e}^{\mathrm{i}Bx}}{B(x^2+C)} \right)
\end{aligned} \tag{E.26}
$$

which can be converted to introducing the definition of I_0,

$$
I_1 = yI_0 - \frac{A\mathrm{e}^{\mathrm{i}Bx}}{2(x^2+C)} - \frac{AB}{4\sqrt{C}} \left(\mathrm{e}^{-B\sqrt{C}}E_1(-B\sqrt{C}-\mathrm{i}Bx) - \mathrm{e}^{B\sqrt{C}}E_1(B\sqrt{C}-\mathrm{i}Bx) \right). \tag{E.27}
$$

Similarly, I_2 and I_3 results,

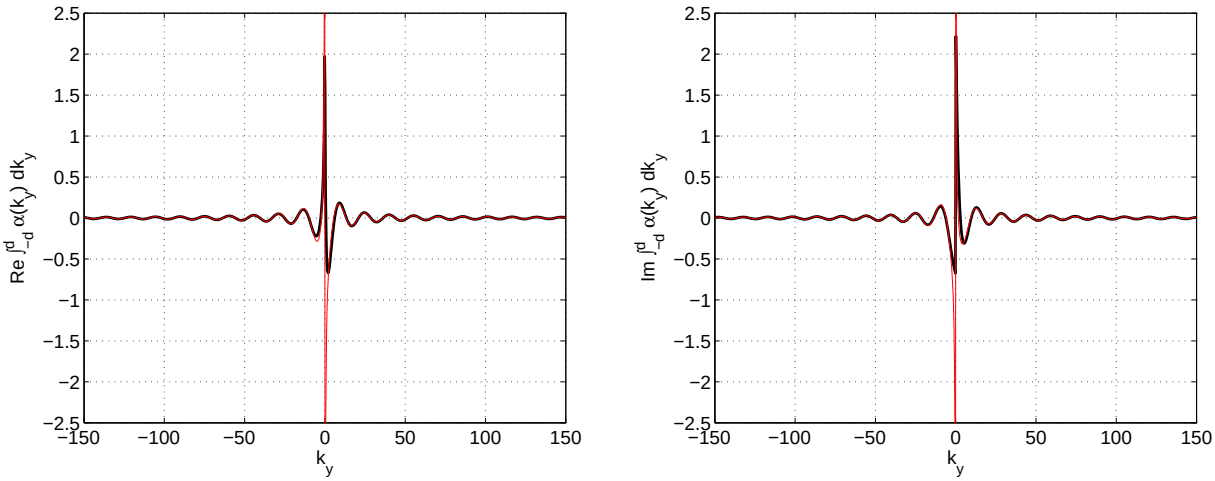

Figure E.1.: Real (left) and imaginary (right) components of the spanwise integral I_0

$$I_2 = \frac{A\mathrm{i}}{4\sqrt{C}}\Big[- B\sqrt{C}(\mathrm{e}^{-B\sqrt{C}}E_1(-B\sqrt{C} - \mathrm{i}Bx) + \mathrm{e}^{B\sqrt{C}}E_1(B\sqrt{C} - \mathrm{i}Bx))+ \\ (\mathrm{e}^{-B\sqrt{C}}E_1(-B\sqrt{C} - \mathrm{i}Bx) - \mathrm{e}^{B\sqrt{C}}E_1(B\sqrt{C} - \mathrm{i}Bx)) + \frac{2\mathrm{i}\sqrt{C}x\mathrm{e}^{\mathrm{i}Bx}}{(x^2 + C)}\Big] \qquad \text{(E.28)}$$

$$I_3 = \frac{A}{4}\Big[B\sqrt{C}(\mathrm{e}^{-B\sqrt{C}}E_1(-B\sqrt{C} - \mathrm{i}Bx) - \mathrm{e}^{B\sqrt{C}}E_1(B\sqrt{C} - \mathrm{i}Bx))- \\ 2(\mathrm{e}^{-B\sqrt{C}}E_1(-B\sqrt{C} - iBx) + \mathrm{e}^{B\sqrt{C}}E_1(B\sqrt{C} - \mathrm{i}Bx)) + \frac{2C\mathrm{e}^{\mathrm{i}Bx}}{(x^2 + C)}\Big] \qquad \text{(E.29)}$$

The Exponential integral used in the computation of spanwise integrals can be obtained with a series expansion [1]

$$E_1(\mu) = -\gamma - \ln\mu - \sum_{n=1}^{\infty}\frac{(-1)^n\mu^n}{nn!}, \qquad (|\arg\mu| < \pi). \qquad \text{(E.30)}$$

where $\gamma = 0.5772156649$ is Euler's constant. The computation of the Exponential integral is performed with the MATLAB routine, '*expint*'. However, for large values of μ the series expansion could be replaced with the asymptotic approach. Hence, the asymptotic definition of the Exponential integral is used for the larger values of μ [1]. The limit between series and asymptotic approaches is selected for the values around $\mu = 20$ in the computations.

$$E_1\mu \sim \left(1 - \frac{1}{\mu} + \frac{1(1+1)}{\mu^2} - \frac{1(1+1)(1+2)}{\mu^3} + ...\right) \qquad (|\arg\mu| < \frac{3\pi}{2}). \qquad \text{(E.31)}$$

Since the terms including the exponential integral terms are in the form of $\mathrm{e}^a E_1(-a - \mathrm{i}x)$ and $\mathrm{e}^a E_1(a - \mathrm{i}x)$

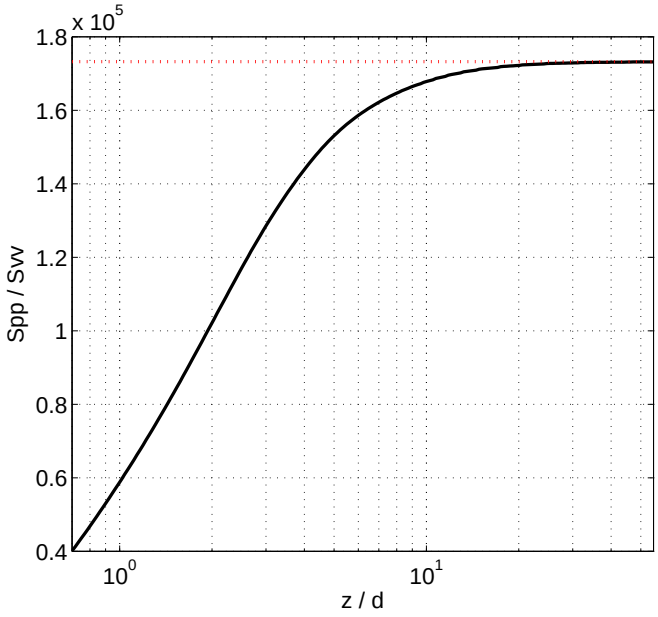

Figure E.2.: Ratio of the Spp and Svv matrices

$$\begin{aligned} \mathrm{e}^{-a}E_1(-a-\mathrm{i}x) &= \mathrm{e}^{-a}\mathrm{e}^{a+\mathrm{i}x}\left(\frac{1}{-a-\mathrm{i}x}-\frac{1}{(-a-\mathrm{i}x)^2}+...\right) \\ \mathrm{e}^{a}E_1(a-\mathrm{i}x) &= \mathrm{e}^{a}\mathrm{e}^{-a+\mathrm{i}x}\left(\frac{1}{a-\mathrm{i}x}-\frac{1}{(a-\mathrm{i}x)^2}+...\right) \end{aligned} \tag{E.32}$$

neglecting second and higher order terms in the parenthesis, one can show that

$$\mathrm{e}^{-a}E_1(-a-\mathrm{i}x)-\mathrm{e}^{a}E_1(a-\mathrm{i}x) \approx -2a\frac{\mathrm{e}^{\mathrm{i}x}}{a^2+x^2}. \tag{E.33}$$

Similarly, $\mathrm{e}^{-a}E_1(-a-\mathrm{i}x)+\mathrm{e}^{a}E_1(a-\mathrm{i}x)$ becomes

$$\mathrm{e}^{-a}E_1(-a-\mathrm{i}x)+\mathrm{e}^{a}E_1(a-\mathrm{i}x) \approx 2\mathrm{i}\frac{\mathrm{e}^{\mathrm{i}x}x}{a^2+x^2}. \tag{E.34}$$

Introducing the asymptotic expressions (E.33) and (E.34) into Equations (E.24), (E.27), (E.28) and (E.29), one can show that the asymptotic results of spanwise integrals

$$\begin{aligned} I_0 &\approx -\frac{A\mathrm{i}\mathrm{e}^{\mathrm{i}Bx}}{2BC(x^2+C)} \\ I_1 &\approx yI_0 \\ I_2 &\approx -\frac{A\mathrm{i}\mathrm{e}^{\mathrm{i}Bx}}{2B(x^2+C)}\big(2y(I_1-yI_0)+y^2I_0\big) = y^2I_0^2C \\ I_3 &\approx -\frac{Ax\mathrm{i}\mathrm{e}^{\mathrm{i}Bx}}{B(x^2+C)}\big(3y(I_2-y(I_1-yI_0))+3y^2(I_1-yI_0)+y^3I_0\big) = 2xyI_2(3I_0C+1) \end{aligned} \tag{E.35}$$

Figure E.1 shows the result of the spanwise integral with respect to different k_y values. Since the observer located on the $y = 0$ line, the parallel gust, $k_y = 0$ reaches its highest value. It is seen that both models converge for the higher values of $|k_y|$ where as for the lower values, the asymptotic approach deviates from the series one. Since the series expansion is accurate for the lower values and asymptotic approach is faster to converge for the higher values, both methods are combined in order to obtain a more accurate and faster solution.

Finally, introducing the spanwise integrals, the aeroacoustic transfer function and the source terms, one can obtain the scattered field matrices required for Equation (5.4).

Once all matrices are derived, a primary test is performed for the far-field knowing that the acoustic pressure converges to acoustic velocity with $p = \rho c_0 v$. Since the convection is taken into account for the derivation of the acoustical velocity, the ratio becomes

$$\lim_{z \to \infty} \frac{Spp}{Svv} \approx (\beta \rho c_0)^2 \tag{E.36}$$

A test is performed using the flow profiles defined in Section 4.5.2 at $f = 1$ kHz. As seen in the Figure E.2, the ratio between the incident acoustic pressure PSD converges to the auto-correlation of the acoustic velocity PSD at the far-field of the airfoil. Hence, the acoustic velocity derivations are validated in the far-field.

The matrices derived are then used for the scattered field of the broadband noise for the jet-airfoil mock-up and the low speed axial fan located in a turbulent stream in Chapter 5.

Bibliography

[1] M. Abramowitz and I. A. Stegun. *Handbook of mathematical functions*. New York, 1970. 36, 55, 114, 134, 135

[2] J.J. Adamczyk. The passage of an infinite swept airfoil through an oblique gust. *Jou. of Aircraft*, 11, 1974. 54

[3] H. Allik, R.N. Dees, and S.W. Moore. Efficient structural acoustic analysis using finite and infinite elements. *Proceedings of Design Engineering Technical Conference*, 3 (B):87–95, 1995. 22

[4] R.K. Amiet. Frame of reference considerations for the forward flight noise problem. *United Technologies Research Center Report N212775-1*, 1974. 76, 79

[5] R.K. Amiet. Acoustic radiation from an airfoil in a turbulent stream. *Jou. of Sound and Vib.*, 41 (4):407–420, 1975. 4, 5, 47, 48, 50, 53, 54, 55, 67, 73, 76, 97, 109, 117, 118, 122, 133

[6] R.K. Amiet. Noise due to turbulent flowpast a trailing edge. *Jou. of Sound and Vib.*, 47 (3):387–393, 1976. 50, 53, 73, 106

[7] R.K. Amiet. Effect of the incident surface pressure field on noise due to turbulent flow past a trailing edge. *Jou. of Sound and Vib.*, 57 (2):305–306, 1978. 50

[8] R.K. Amiet. Noise produced by turbulent flow into a rotor: Theory manual for noise calculations. *NASA Report TR-CR 17763*, 1989. 4, 5, 79

[9] A. Ashraf and C. Rajakumar. *The Boundary Element Method: Applications in Sound and Vibration*. Netherlands, 2004. 22

[10] R. Astley and J. Bain. A three-dimesional Boundary Element Scheme for acoustic radiation in low mach number flows. *Jou. of Sound and Vib.*, 109 (3):445–465, 1986. 106

[11] C. Bailly and G. Comte-Bellot. *Turbulence*. Paris, 2003. 51

[12] A. Bayliss, M. Gunzburger, and E. Turkel. Boundary conditions for the numerical solution of elliptic equations in exterior regions. *SIAM J. Appl. Math.*, 42:430–450, 1982. 22

[13] A. Bayliss and E. Turkel. Radiation boundary conditions for wave-like equations. *Comm. Pure Appl. Math.*, 33:707–725, 1980. 22

[14] C. Bogey, C. Bailly, and D. Juve. Noise investigation of a high subsonic, moderate reynolds number jet using a compressible LES. *Theoretical and Computational Fluid Dynamics*, 16 (4):273–297, 2003. 1

[15] K.S. Brentner. Numerical algorithms for acoustic integrals with examples for rotor noise prediction. *AIAA Journal*, 35 (4):625–630, 1997. 2

[16] T.F. Brooks, M.A. Marcolini, and D.S. Pope. Airfoil trailing edge flow measurements. *AIAA Journal*, 24 (8):1245–1251, 1986. 4, 47

[17] R.E. Caflisch. Monte Carlo and quasi-Monte Carlo methods. *Acta Numerica*, 7:1–49, 1998. 52

[18] S. Caro and S. Moreau. Aeroacoustic modeling of low pressure axial flow fans. *AIAA paper*, AIAA-2000-22094, 2000. 1

[19] T. Carolus, M. Schneider, and H. Reese. Axial flow broad-band noise and prediction. *Jou. of Sound and Vib.*, 300:50–70, 2007. 4, 47

[20] J. Casper and F. Farassat. Broadband trailing edge noise predictions in the time domain. *Jou. Sound and Vib.*, 271:159–176, 2004. 2

[21] A.H.D. Cheng and D.T. Cheng. Heritage and early history of the boundary element method. *Eng. Analysis with Boundary Elements*, 29:268–302, 2005. 21

[22] M.O. Cherkaoui-Malki and S. Sayouri. Quasi spectral data construction in two points in partially nonhomogenous turbulence. *Elec. Jou. of Diff. Eq.*, 11:103–108, 2004. 63, 64, 65

[23] M. Choudhari, M. Khorrami, D. Lockard, H. Atkins, and G. Lilley. Slat cove noise modeling: A posteriori analysis of unsteady RANS simulations. *AIAA paper 2002-2468*, 2002. 4, 47

[24] J. Christophe. Airfoil noise: Hybrid approaches. *von Karman Institute for Fluid Dynamics Lecture Series: In Aero-dynamic Noise from Wall-Bounded Flows*, 2009. 57, 60, 61, 62, 67

[25] J. Christophe. Appllication of hybrid methods to high frequency aeroacoustics. *PhD Dissertation, von Karman Institute for Fluid Dynamics*, 2011. 47, 52, 55, 61, 62, 63, 66, 67, 71, 86

[26] J. Christophe, J. Anthoine, and S. Moreau. Amiet's theory in spanwise varying flow conditions. *AIAA Journal Technical Notes*, 47 (3):788–790, 2009. 48, 61

[27] J. Christophe, J. Anthoine, P. Rambaud, and S. Moreau. Numerical issues in the application of an amiet model for spanwise-varying incoming turbulence. *AIAA paper 2008-2865*, 2008. 57, 61, 66, 67, 85, 86, 90, 95, 118

[28] J. Christophe, J. Anthoine, P. Rambaud, C. Schram, F. Matley, and S. Moreau. Prediction of incoming turbulent noise using a combined numerical / semi-empirical method and experimental validation. *AIAA paper 2001-3468*, 2007. 61, 66

[29] T. Colonius, S.K. Lele, and P. Moin. Boundarry condition for direct computation of aerodynamic sound generation. *AIAA Journal*, 31 (9):1574–1582, 2003. 1

[30] W.T.W. Cory. *Fans and Ventilation: A Practical Guide.* Amsterdam, 2005. 2, 3, 151

[31] J.P. Coyette. Validation of a new wave envelope formulation for handling exterior acoustic and elasto-acoustic problems in the frequency domain. *Proceedings of the DGLR/AIAA 14th Aeroacoustics Conference, edited by DGLR*, pages 421–427, 1992. 22

[32] D.G. Crighton and F.G. Leppington. On the scattering of aerodynamic noise. *Jou. Fluid Mech.*, 46 (3):577–597, 1971. 36

[33] N. Curle. The influence of solid boundaries upon aerodynamic sound. *Proc. R. Soc. Lond.*, 231:505–514, 1955. 1, 4, 8, 47, 49, 67, 86, 97

[34] W. Desmet. Boundary Element Modeling for acoustics. *In Lecture Notes of the ISAAC21 Course. K.U.Leuven, Leuven, Belgium*, September 2010. 4, 22, 23, 25, 28, 30, 37, 86, 87, 94

[35] W. Desmet and P. Sas. Introduction to numerical acoustics. *In Lecture Notes of the ISAAC21 Course. K.U.Leuven, Leuven, Belgium*, September 2010. 4, 21, 22, 24, 28, 30, 31, 86, 88, 89, 94, 126

[36] W. Desmet and D. Vandepitte. Finite element modeling for acoustics. *In Lecture Notes of the ISAAC21 Course. K.U.Leuven, Leuven, Belgium*, September 2010. 4, 22, 25

[37] F. Farassat. Derivation of formulations 1 and 1a of farassat. *NASA Report/TM-2007-214853*, March 2007. 2

[38] D. Fedala, S. Kouidri, F. Bakir, and R. Rey. Modeling of broadband noise radiated by an airfoil application to an axial fan. *Int. Jou. of Vehicle Noise and Vib.*, 3 (1):106–117, 2007. 47, 48, 60, 61, 118

[39] J.E. Ffowcs-Williams and L.H. Hall. Aerodynamic sound generation by turbulent flow in the vicinity of a scattering half plane. *Jou. Fluid Mech.*, 40 (4):657–670, 1970. 4, 30, 95

[40] J.E. Ffowcs-Williams and D.L. Hawkings. Sound generation by turbulence and surfaces in arbitrary motion. *Proc. Royal Soc. London*, 264:321–342, 1968. 1, 8, 13, 25, 42

[41] J.E. Ffowcs-Williams and D.L. Hawkings. Noise of rotating machinery. *AIAA Journal*, 10 (1):10–21, 1969. 2, 9, 10, 13, 26

[42] I.E. Garrick and C.E. Watkins. A theoretical study of the effect of forward speed on the free-space sound pressure-field around propellers. *NACA Report*, 1198, 1953. 49

[43] A.R. George and S.T. Chou. Helicopter tail rotor noise analysis. NASA Technical Report under Grant NAG-1-590, January 1986. 1

[44] W.K. George. The decay of homogeneous isotropic turbulence. *Phys. of Fluids*, 4 (7):1492–1509, 1992. 59

[45] F. Gerard, M. Tournour, N.E. Masri, L. Cremers, M. Felice, and A. Selmane. Numerical modeling of engine noise radiation through the use of acoustic transfer vectors: A case study. *SAE paper, 2001-01-1514*, 2001. 87, 126

[46] S.A.L. Glegg, S.M. Baxter, and A.G. Glendinning. The prediction of broadband noise from wind turbines. *Jou. Sound and Vib.*, 118 (2):217–239, 1987. 1

[47] M.E. Goldstein. *Aeroacoustics*. New York, 1976. 2, 8, 9, 12, 21, 25, 42, 47

[48] I.S. Gradshteyn and I.M. Ryzhik. *Table of Integrals, Series and Products, Corrected and Enlarged Edition*. San Diego, 1980. 113

[49] J.M.R. Graham. Similarity rules of thin aerofoils in non-stationary subsonic flows. *Jou. Fluid Mech.*, 43 (4):753–766, 1970. 54

[50] A. Guedel. *Fan Acoustics: Noise Generation and Control Methods*. Air Movement and Control Association International, 2007. 1, 4

[51] L. Gutin. On the sound field of a rotating propeller. *Phys. Z. Sow. Un. (Translated NACA Tech Memo 1195(1948))*, 9 (57), 1936. 2, 10, 12

[52] M. Hamadiche. Analyse spectrale des mechanismes lineaires des ecoulements turbulents inhomogenes. *L'Universite Claude-Bernard-Lyon 1*, 1985. 63, 64, 153

[53] D.B. Hanson. Compressible helicoidal surface theory for propeller aerodynamics and noise. *AIAA Journal*, 21 (6):881–889, 1983. 1, 13

[54] D.B. Hanson and M.R. Fink. The importance of quadrupole sources in prediction of transonic tip speed propeller noise. *Jou. Sound and Vib.*, 62 (1):19–38, 1979. 2, 8

[55] J.O. Hinze. *Turbulence*. New York, 1975. 50, 56, 67

[56] G.F. Homicz and S.A. George. Broadband and discrete frequency radiation from subsonic rotors. *Jou. Sound and Vib.*, 36 (2):151–177, 1974. 4

[57] M.S. Howe. A review of the theory of trailing edge noise. *Jou. of Sound and Vib.*, 61 (3):437–465, 1965. 4

[58] LMS International. Virtual Lab: Numerical acoustics theoretical manual,. 2006. 22, 25

[59] LMS International. Virtual Lab Rev 9: User manual,. 2009. 9, 23, 25, 26, 32, 71, 86

[60] F. James. Monte Carlo theory and practice. *Rep. Prog. Phys.*, 43, 1980. 52

[61] W.H. Jeon, S.J. Baek, and C. J. Kim. Analysis of the aeroacoustic characteristics of the centrifugal fan in a vacuum cleaner. *Jou. Sound and Vib.*, 268:1025–1035, 2003. 1

[62] H.K. Johnson and W.M. Katz. Investigation of the vortex noise produced by a helicopter rotor. *USAAMRDL Technical Report 72-2*, 1972. 3

[63] S. Kirkup. *The Boundary Element Method in Acoustics*. Integrated Sound Software, 1998. 22, 23, 87

[64] K. Kucukcoskun, J. Christophe, C. Schram, J. Anthoine, and M. Tournour. An extension of amiet's theory for spanwise varying incoming turbulence noise and broadband noise scattering using bem. *AIAA paper 2010-3987*, 2010. 4, 48, 49, 54, 55, 60, 67

[65] K. Kucukcoskun, J. Christophe, C. Schram, J. Anthoine, and M. Tournour. A geometrical near-field extension of amiet's theory for spanwise varying incoming turbulence noise and broadband noise scattering. *ISMA paper 2010-690*, 2010. 4, 48, 61, 63, 65

[66] K. Kucukcoskun, J. Christophe, C. Schram, and M. Tournour. Broadband scattering of the turbulence-interaction noise of a stationary airfoil: Experimental validation of the semi-analytical model. *submitted to: Int. Jou. of Aeroacoustics*. 67

[67] K. Kucukcoskun, J. Christophe, C. Schram, and M. Tournour. A semi-analytical approach on the turbulence interaction noise of a low-speed axial fan including broadband scattering. *AIAA paper 2011-2714*, 2011. 4, 61, 65, 82

[68] K. Kucukcoskun, J. Christophe, C. Schram, and M. Tournour. Free and scattered acoustic field predictions of the broadband noise generated by a low-speed axial fan. *FAN2012 paper 2012-21, Senlis*, 2012. 82

[69] K. Kucukcoskun, T. Deconinck, and F. Presezniak. Acoustic field generated by a low-speed ducted fan: Experimental validation of the numerical model. *accepted to ISMA2012, Leuven*, 2012. 8, 25, 26, 28

[70] K. Kucukcoskun and M. Roger. On the scattering of aerodynamic noise by a rigid corner. *AIAA paper 2012-2113*, 2012. 42, 43, 107

[71] S. Lee, K.S. Brentner, and P. J. Morris. Acoustic scattering in the time domain using an equivalent source method. *AIAA Journal*, 48 (12):2772–2780, 2010. 4, 21

[72] H. Liebowitz and F. Farassat. *Research on Helicopter Rotor Noise*. Washington DC, 1979. 1

[73] J. Lighthill. On sound generated aoerdynamically. i. general theory. *Proc. R. Soc. Lond. Series A, Mathematical and Physical Sciences*, 211 (1102):564–587, 1952. 1, 7, 47

[74] J. Lighthill. On sound generated aerodynamically. ii. turbulence as a source of sound. *Proc. R. Soc. Lond. Series A, Mathematical and Physical Sciences*, 222(1148):1–32, 1954. 1

[75] R.G. Loewy and S.G. Sandler. A theory for predicting the rotational and vortex noise of lifting rotors in hover and forward flight. *NASA Report CR-1333*, 1969. 3

[76] M.V. Lowson and J.B. Ollerhead. A theoretical study of helicopter rotor noise. *Jou. Sound and Vib.*, 9 (2):197–222, 1969. 2

[77] M.W. Lowson. The sound field for singularities in motion. *Proc. R. Soc. Lond. Series A*, 286:559–572, 1965. 2, 10

[78] K. Luo and H. Lai. *Direct and Large-Eddy Simulation VI: A Hybrid LES-Acoustic Analogy Method for Computational Aeroacoustics*. Dordrecht, 2006. 2

[79] R.H. Lyon. *Statistical Energy Analysis of Dynamical Systems*. Boston, 1975. 4, 21

[80] R.H. Lyon and R.G. DeJong. *Theory and application of statistical energy analysis - second edition*. Boston, 1995. 4

[81] A.S. Lyrintzis. Surface integral methods in computational aeroacousticsfrom the (cfd) near-field to the (acoustic) far-field. *Intl. Jou. of Aeroacoustics*, 2 (2):95–128, 2003. 3

[82] A. Maaloum, S. Kouidri, F. Bakir, and R. Rey. Effect of inlet duct contour and lack thereof on the noise generated of an axial flow fan. *Applied Acoustics*, 64:999–1010, 2003. 2

[83] H.M. MacDonald. A class of diffraction problems. *Proc. London Math. Soc.*, 14:410–427, 1915. 5, 21, 34

[84] P. Mel'nik and Y.K. Podlipenko. On green's function for the helmholtz equation in a wedge. *Ukranian Mathematical Jou.*, 45 (9):1471–1474, 1993. 35

[85] J. Moran. *An Introduction to Theoretical and Computational Aerodynamics*. New York, 1984. 111

[86] S. Moreau and M. Roger. Axial flow compressor noise studies. *AIAA Journal*, 45 (1):48–57, 2007. 47

[87] S. Moreau, M. Roger, and V. Jurdic. Effect of angle of attack and airfoil shape on turbulence-interaction noise. *AIAA paper 2005-2973*, 2005. 47

[88] C.L. Morfey. Rotating pressure patterns in ducts: Their generation and transmission. *Jou. of Sound and Vib.*, 1 (1):60–87, 1964. 14, 21, 42, 79, 106, 120, 123

[89] P.J. Morris, T.E Scheidegger L.N. Long, and S. Boluriaan. Simulations of supersonic jet noise. *International Jou. of Aeroacoustics*, 1 (1):17–41, 2002. 1

[90] P.M. Morse and K.U. Ingard. *Theoretical Acoustics*. New Jersey, 1986. 4

[91] B.D. Mugridge. The noise of cooling fans used in heavy automotive vehicles. *Jou. Sound and Vib.*, 44 (3):349–367, 1976. 1

[92] W. Neise. Review of fan noise generation mechansims and control method. *Fan Noise 1992*, 1992. 2, 8

[93] A.M. Ondet and J. Babry. Modeling of sound propagation in fitted workshops using ray tracing. *Jou. Acoust. Soc. Am.*, 85:787–796, 1989. 4, 21

[94] N.C. Ovenden and S.W. Rienstra. Mode-matching strategies in slowly varying engine ducts. *AIAA Journal*, 42 (9):1832–1840, 2004. 1, 3, 13, 21

[95] A. Pagano, M. Barbarino, D. Casalino, and L.Federico. Tonal and broadband noise calculations for aeroacoustic optimization of a pusher propeller. *Jou. of Aircraft*, 47 (3):835–848, 2010. 2, 8

[96] R.W. Paterson and R.K. Amiet. Noise of a model helicopter rotor due to ingestion of turbulence. 4, 52, 73, 76, 78, 115, 119

[97] R.W. Paterson and R.K. Amiet. Acoustic radiation and surface pressure characteristics of an airfoil due to incident turbulence. *NASA Report TR-CR 2733*, 1976. 4, 49

[98] R.W. Paterson and R.K. Amiet. Noise and surface pressure response of an airfoil to incident turbulence. *Jou. of Aircraft*, 14 (8):729–736, 1977. 48

[99] N. Peake and D.G. Chrighton. An asymptotic theory on propeller acouistics. *Jou. of Fluid Mech.*, 232:285–301, 1991. 3

[100] F. Perot, M.S. Kim, S. Moreau, M. Henner, and D. Neal. Direct aeroacoustics prediction of a low speed axial fan. *AIAA paper 2010-3887*, 2010. 1

[101] A. Pierce. *Acoustics: An Introduction to Its Physical Principles and Applications*. New York, 1989. 4, 7, 27, 30, 33, 34, 70, 91, 94, 119

[102] S.B. Pope. *Turbulent Flows*. Cambridge, 2010. 59, 69, 81, 87

[103] A. Powell. Aerodynamic noise and the plane boundary. *Jou. Acoust. Soc. Am.*, 32 (8):982–990, 1960. 4, 21, 30

[104] G. Reboul, C. Polacsek, S. Lewy, and S. Heibs. Aeroacoustic computation of ducted fan broadband noise using LES data. *Acoustics-08 Conference*, pages 4077–4082, 2008. 10, 26

[105] S.K. Richards, X.X. Chen, X. Huang, and X. Zhang. Computation of fan noise radiation through an engine exhaust geometry with flow. *Int. Journal of Aeroacoustics*, 6 (3):223–241, 2007. 3, 13, 21

[106] S. W. Rienstra and A. Hirschberg. An introduction to acoustics. *Lecture Notes, Eindhoven University of Technolog*, 2003. 8

[107] M. Roger. Noise from moving surfaces. *von Karman Institute for Fluid Dynamics Lecture Series: In Computational Aeroacoustics*, 2006. 49, 70

[108] M. Roger. Near-field fan noise modeling and installation effects due to scattering surfaces. *Fan Noise 2007*, 2007. 3, 13, 21, 25, 26, 42, 43

[109] M. Roger. On broadband jet-ring interaction noise and aerofoil turbulence-interaction noise predictions. *Jou. of Fluid Mech.*, 653:337–364, 2010. 81

[110] M. Roger and A. Carazo. Blade geometry considerations in analytical gust-airfoil interaction noise models. *AIAA paper 2010-3799*, 2010. 47

[111] M. Roger and S. Moreau. Back-scattering correction and further extensions of amiets trailing-edge noise model. part 1: Theory. *Jou. of Sound and Vib.*, 286:477–506, 2005. 115

[112] M. Roger and S. Moreau. Extentions and limitations of analytical airfoil broadband noise models. *Int. Jou. of Aeroacoustics*, 9 (3):273–305, 2010. 47, 58, 59, 80

[113] M. Roger, S. Moreau, and M. Wang. An analytical model for predicting airfoil self-noise using wall-pressure statistics. *Annual Research Brief, Center for Turbulence Research, Stanford University*, pages 405–414, 2002. 111

[114] Y. Rozenberg. Modelisation analytique du bruit aerodynamique a large bande des machines tournantes: utilisation de calculs moyennes de mecanique des fluides. *PhD Dissertation, Ecole Centrale Lyon*, 2007. 47, 73, 74, 77, 78, 97

[115] Y. Rozenberg, S. Moreau, M. Henner, and S.C. Morris. Fan trailing-edge *AIAA paper 2010-3720*, 2010. 2, 8

[116] Y. Rozenberg, S. Moreau, M. Henner, and S.C. Morris. Fan trailing-edge noise prediction using RANS simulations. *AIAA paper 2010-3720*, 2010. 61

[117] Y. Rozenberg, M. Roger, A. Guedel, and S. Moreau. Rotating blade self-noise: Experimental validation of analytical models. *AIAA paper 2007-3709*, 2007. 61

[118] Y. Rozenberg, M. Roger, and S. Moreau. Rotating blade trailing-edge noise: Experimental validation of analytical model. *AIAA Journal*, 48 (5):951–962, 2010. 47, 79, 118

[119] R.H. Schlinker and R.K. Amiet. Helicopted rotor trailing edge noise. *NASA Report TR-CR 3470*, 1981. 1, 4

[120] C. Schram, W. Coenen, J. Anthoine, and A. Hirschberg. Aerodynamic moise generated by an airfoil in a turbulent jet flow. *In Proc. of 12th International Cong. on Sound and Vib.*, 2005. 66, 69, 85

[121] K. Schwartzschild. Die beugung und polarisation des lichts durch einen spalt. *Mathematische Annalen*, 55:177–247, 1902. 112

[122] I.J. Sharland. Sources of noise in axial flow fans. *Jou. of Sound and Vib.*, 1 (3):302–322, 1964. 82, 99

[123] M. Tournour. Scattered random field. *Unpublished work*, 2009. 88, 125, 126, 128

[124] M. Tournour, Z. El Hachemi, A. Read, F. Barone, and P. Durello. Investigation of the tonal noise radiated by subsonic fans using the aero-acoustic analogy. *Fan Noise 2003*, 2003. 1

[125] J.M. Tyler and T.G. Sofrin. Axial flow compressor noise studies. *SAE Trans.*, 70:309–332, 1962. 27, 28, 47

[126] S. Vilmin, E. Lorrain, C. Hirsch, and M. Swoboda. Unsteady flow modeling across the rotor/stator interface using the nonlinear harmonic method. *Proceedings of GT2006 ASME Turbo Expo 2006: Power for Land, Sea and Air: GT2006-90210*, 2006. 26, 27

[127] C. Wagner, T. Hutti, and P. Sagaut. *Large-Eddy Simulation for Acoustics*. Cambridge, 2007. 47

[128] M. Wang, J.B. Freund, and S.K. Lele. Computational prediction of flow generated sound. *Annual Rev. Fluid Mech.*, 38:483–512, 2006. 2, 47

[129] G.N. Watson. *A Treatise on the Theory of Bessel Functions*. Vermont, 1995. 35

[130] P.D. Welch. The use of fast fourier transform for the estimation of power spectra: A method based on time averaging over short, modified periodograms. *IEEE Trans. Audio Electroacoustics*, AU-15:70–73, 1967. 70

[131] www.voith.com. 42, 152

[132] J. Yin and A. Stuermer. Coupled URANS and FW-H analysis of installed pusher propeller aircraft configurations. *AIAA paper 2009-3332*, 2009. 26

List of Tables

List of Figures

ÉCOLE CENTRALE LYON — Direction de la recherche

Liste des personnes Habilitées à Diriger des Recherches en poste à l'Ecole Centrale de Lyon

Nom-Prénom	Corps grade	Laboratoire ou à défaut département ECL	Etablissement
BEROUAL Abderrahmane	professeur	AMPERE	ECL
BURET François	professeur	AMPERE	ECL
JAFFREZIC-RENAULT Nicole	directeur de recherche	AMPERE	CNRS/ECL
KRÄHENBÜHL Laurent	directeur de recherche	AMPERE	CNRS/ECL
NICOLAS Alain	professeur	AMPERE	ECL
NICOLAS Laurent	directeur de recherche	AMPERE	CNRS/ECL
SCORLETTI Gérard	professeur	AMPERE	ECL
SIMONET Pascal	directeur de recherche	AMPERE	CNRS/ECL
VOLLAIRE Christian	professeur	AMPERE	ECL

Nbre Ampère 9

HELLOUIN Yves	maître de conférences	DER EEA	ECL

Nbre DER EEA 1

GUIRALDENQ Pierre	professeur émérite	DER STMS	ECL
VINCENT Léo	professeur	DER STMS	ECL

Nbre DER STMS 2

LOHEAC Jean-Pierre	maître de conférences	ICJ	ECL
MAITRE Jean-François	professeur émérite	ICJ	ECL
MARION Martine	professeur	ICJ	ECL
MIRONESCU Elisabeth	professeur	ICJ	ECL
MOUSSAOUI Mohand	professeur	ICJ	ECL
MUSY François	maître de conférences	ICJ	ECL
ZINE Abdel-Malek	maître de conférences	ICJ	ECL

Nbre ICJ 7

DAVID Bertrand	professeur	ICTT	ECL

Nbre ICTT 1

CALLARD Anne-Ségolène	professeur	INL	ECL
CLOAREC Jean-Pierre	maître de conférences	INL	ECL
GAFFIOT Frédéric	professeur	INL	ECL
GAGNAIRE Alain	maître de conférences	INL	ECL
GARRIGUES Michel	directeur de recherche	INL	CNRS/ECL
GENDRY Michel	directeur de recherche	INL	CNRS/ECL
GRENET Geneviève	directeur de recherche	INL	CNRS/ECL
HOLLINGER Guy	directeur de recherche	INL	CNRS/ECL
KRAWCZYK Stanislas	directeur de recherche	INL	CNRS/ECL
LETARTRE Xavier	chargé de recherche	INL	CNRS/ECL
O'CONNOR Ian	professeur	INL	ECL
PHANER-GOUTORBE Magali	professeur	INL	ECL

ROBACH Yves	*professeur*	INL	ECL
SAINT-GIRONS Guillaume	*chargé de recherche*	INL	CNRS/ECL
SEASSAL Christian	*directeur de recherche*	INL	CNRS/ECL
SOUTEYRAND Eliane	*directeur de recherche*	INL	CNRS/ECL
TARDY Jacques	*directeur de recherche*	INL	CNRS/ECL
VIKTOROVITCH Pierre	*directeur de recherche*	INL	CNRS/ECL

Nbre INL 18

CHEN Liming	*professeur*	LIRIS	ECL

Nbre LIRIS 1

BAILLY Christophe	*professeur*	LMFA	ECL
BERTOGLIO Jean-Pierre	*directeur de recherche*	LMFA	CNRS/ECL
BLANC-BENON Philippe	*directeur de recherche*	LMFA	CNRS/ECL
BOGEY Christophe	*chargé de recherche*	LMFA	CNRS/ECL
CAMBON Claude	*directeur de recherche*	LMFA	CNRS/ECL
CARRIERE Philippe	*directeur de recherche*	LMFA	CNRS/ECL
CHAMPOUSSIN J-Claude	*professeur émérite*	LMFA	ECL
COMTE-BELLOT geneviève	*professeur émérite*	LMFA	ECL
FERRAND Pascal	*directeur de recherche*	LMFA	CNRS/ECL
GALLAND Marie-Annick	*professeur*	LMFA	ECL
GODEFERD Fabien	*directeur de recherche*	LMFA	CNRS/ECL
GOROKHOVSKI Mikhail	*professeur*	LMFA	ECL
HENRY Daniel	*directeur de recherche*	LMFA	CNRS/ECL
JEANDEL Denis	*professeur*	LMFA	ECL
JUVE Daniel	*professeur*	LMFA	ECL
LE RIBAULT Catherine	*chargée de recherche*	LMFA	CNRS/ECL
LEBOEUF Francis	*professeur*	LMFA	ECL
PERKINS Richard	*professeur*	LMFA	ECL
ROGER Michel	*professeur*	LMFA	ECL
SCOTT Julian	*professeur*	LMFA	ECL
SHAO Liang	*directeur de recherche*	LMFA	CNRS/ECL
SIMOENS Serge	*chargé de recherche*	LMFA	CNRS/ECL
TREBINJAC Isabelle	*maître de conférences*	LMFA	ECL

Nbre LMFA 23

BENAYOUN Stéphane	*professeur*	LTDS	ECL
CAMBOU Bernard	*professeur*	LTDS	ECL
COQUILLET Bernard	*maître de conférences*	LTDS	ECL
DANESCU Alexandre	*maître de conférences*	LTDS	ECL
FOUVRY Siegfrid	*chargé de recherche*	LTDS	CNRS/ECL
GEORGES Jean-Marie	*professeur émérite*	LTDS	ECL
GUERRET Chrystelle	*chargé de recherche*	LTDS	CNRS/ECL
HERTZ Dominique	*past*	LTDS	ECL
ICHCHOU Mohamed	*professeur*	LTDS	ECL
JEZEQUEL Louis	*professeur*	LTDS	ECL
JUVE Denyse	*ingénieur de recherche*	LTDS	ECL
KAPSA Philippe	*directeur de recherche*	LTDS	CNRS/ECL
LE BOT Alain	*directeur de recherche*	LTDS	CNRS/ECL
LOUBET Jean-Luc	*directeur de recherche*	LTDS	CNRS/ECL
MARTIN Jean-Michel	*professeur*	LTDS	ECL
MATHIA Thomas	*directeur de recherche*	LTDS	CNRS/ECL
MAZUYER Denis	*professeur*	LTDS	ECL
PERRET-LIAUDET Joël	*maître de conférences*	LTDS	ECL
SALVIA Michelle	*maître de conférences*	LTDS	ECL

SIDOROFF François	*professeur*	LTDS	ECL
SINOU Jean-Jacques	*professeur*	LTDS	ECL
STREMSDOERFER Guy	*professeur*	LTDS	ECL
THOUVEREZ Fabrice	*professeur*	LTDS	ECL
TREHEUX Daniel	*professeur*	LTDS	ECL
VINCENS Eric	*maître de conférences*	LTDS	ECL
		Nbre LTDS 25	
	Total HdR ECL	91	

dernière page de la thèse

AUTORISATION DE SOUTENANCE

Vu les dispositions de l'arrêté du 7 août 2006,

Vu la demande du Directeur de Thèse

Monsieur M. ROGER

et les rapports de

Monsieur A. GUEDEL
Docteur-Ingénieur - Chargé d'étude à la Direction Scientifique - CETIAT Domaine Scientifique de la Doua
25 avenue des Arts - BP 52042 - 69603 Villeurbanne cedex

Monsieur S. MOREAU
Professeur - GAUS - Université de Sherbrooke - 2500 bd de l'Université - Sherbrooke (Québec)
Canada J1K 2R1

Monsieur T. CAROLUS
Professeur - Institüt für Fluid und Thermodynamik Universität Siegen - Paul-Bonatz-Str. 9-11
57076 SIEGEN - Allemagne

Monsieur KUCUKCOSKUN Korcan

est autorisé à soutenir une thèse pour l'obtention du grade de **DOCTEUR**

Ecole doctorale MECANIQUE, ENERGETIQUE, GENIE CIVIL ET ACOUSTIQUE

Fait à Ecully, le 16 mars 2012

P/Le directeur de l'E.C.L.
La directrice des Etudes

M-A. GALLAND